FABRICATION AND PERFORMANCE EVALUATION OF ANODE-SUPPORTED PLANAR SOLID OXIDE FUEL CELLS VIA TAPECASTING AND CO-SINTERING TECHNIQUE

by

Ayşenur Eslem Kısa

B.S., Chemistry, Middle East Technical University, 2012

M.S., Chemistry, Boğaziçi University, 2015

Submitted to the Institute for Graduate Studies in
Science and Engineering in partial fulfillment of
the requirements for the degree of
Doctor of Philosophy

Graduate Program in Chemistry

Boğaziçi University

2023

ACKNOWLEDGEMENTS

If only one paragraph of this gets read, I have to thank all those who have shaped who I am today and those who continue to do so. I wouldn't even be writing the following if it weren't all of that, and more. Throughout my life, I have had the blessed opportunity to get to know some very amazing people and build strong bonds with many of them. I want to thank each and every one of you from the bottom of my heart.

I certainly must give my appreciation to Assoc. Prof. Oktay Demircan, as my thesis advisor. I carry with me a lasting imprint of his enthusiasm for science. I hope to one day stand in his position at the head of a class, emitting the same passion for teaching and showing concern for the progress of the students. Also, he deserves acknowledgements for allowing me the wonderful experience to work as his assistant, to offer my input, and just a pleasure the opportunity has been. Finally, many thanks to my thesis committee members, Prof. Amitav Sanyal, Assoc. Prof. Damla Eroğlu Pala, Assoc. Prof. Aligül Büyükaksoy, and Prof. Emren Nalbant for being generous with their time and knowledge. I also have to express my gratitude to every one of the Boğaziçi academics and staff, as well as others, who have assisted me in my study.

I am grateful to my parents for their unwavering support and encouragement to follow my dreams. They have never given me anything but love and patience throughout my whole life, and they still set the highest standard for how to live, treat others, put in a lot of effort, endure, find strength in my darkest times, and make the most out of any circumstance. They recognize that everyone makes mistakes, that plans don't always work out, and that our really selves are shown in the ways we bounce back from setbacks and go on. That has been an excellent lesson for me during my study at Boğaziçi. They made me realize that *things aren't always fair in life*, and my family and I had our fair share of difficult times. Thank you also to my sisters Erva and Hümeyra for everything, being a constant source of sarcastic humor, even the teasing :) I believe in addition to all the gratitude I owe, I just want to say, I did eventually graduate, and it was definitely a team effort.

I have met a lot of people at Boğaziçi who are worthy of acknowledgment. They made the years I spent more enjoyable despite all the work. I genuinely believe I studied with some of the greatest people I've ever met, and I'm grateful for these connections as I go through life. I'm grateful to everyone who helped me escape the lab and was reminded that life isn't really about science. Science is only the thread that linked us all together in the first place; life is about the experiences, connections, and interactions we have along the road.

I certainly must give my thanks and appreciation to the Inorganic Chemistry lab students, who I TAed for the fall terms of several academic years. I never imagined that I would have so much fun and would be able to connect with so many students. To all of those who regularly stopped by my office, or even made an effort to say hello outside of the classroom, you made me feel like all the effort and all the time I committed was worth every moment. I wish you all the very best as you continue through Boğaziçi and beyond, and nothing but success in the rest of your lives. I encourage you to find something you love doing and run with it—many of you will go on to do great things. Though I have long had the suspicion that I would love teaching, the opportunity to serve as teaching assistant, and the students and their personalities, have more confirmed my belief.

I truly believe there are many deserving of my thanks, and probably many I failed to mention here. I understand that words are not the proper way to show appreciation that can only be accomplished through actions. However, this space provides me the opportunity to express my gratitude and document some of the experiences I have had at Boğaziçi. That said, I again say thank you to all those that have shared this experience with me.

Finally, this study was supported by the grant numbers of TÜBİTAK - 214Z094 and 112M279, and BAP - 19B05D5, 22B05D5 and 23BP1. I hope you will enjoy reading this thesis as much as I have enjoyed writing it.

ABSTRACT

FABRICATION AND PERFORMANCE EVALUATION OF ANODE-SUPPORTED PLANAR SOLID OXIDE FUEL CELLS VIA TAPECASTING AND CO-SINTERING TECHNIQUE

Interest in solid oxide fuel cells has increased due to their ability to combine flexible fuel gas composition with efficient energy production. The most important goals include the long-term durability and performance of the cells. This is determined by three loss mechanisms: ohmic, polarization and activation polarization losses. To date, further development of anode-supported cells has been hampered by an incomplete understanding of the origin of the individual loss processes and their contribution to the internal resistance of the cell. Therefore, the primary goal of this dissertation was the clear identification and simultaneous physical interpretation of all polarization processes occurring in an anode-supported cell. Vanadium and Gadolinium doped four cathode samples ($La_{0.595}V_{0.005}Sr_{0.4}CoO_{3-\partial}$ (LV05SC), $La_{0.50}Gd_{0.10}Sr_{0.4}CoO_{3-\partial}$ (LG10SC), $La_{0.57}V_{0.03}Sr_{0.4}FeO_{3-\partial}$ (LV3SF), $La_{0.595}V_{0.005}Sr_{0.4}MnO_{3-\partial}$ (LV05SM)) were synthesized using sol-gel method. Their crystal structure and elemental analysis were investigated by XRD and XPS techniques. The anode-supported cells were prepared using tape-casting method. Both YSZ (Yttria-stabilized Zirconia) and GDC (Gadolinium-doped Ceria) were used as electrolyte layers in different combinations. The surface and cross-section morphology of the sintered cells were studied with SEM analysis. For electrochemical characterization of the electrodes, Linear Sweep Voltammetry (LSV) and Electrochemical Impedance Spectroscopy (EIS) were performed. The analysis of the measured impedance required the use of four (RQ) circuits in series in the equivalent circuit model. All loss processes that contribute to the overall resistance of the individual cell were clearly identified. Up to six loss processes were identified by specifically analyzing the Distribution of Relaxation Time (DRT) while varying the operating conditions. Of the four cathodes, the LG10SC on GDC (35 μm)/YSZ showed the highest performance with 415 mW/cm^2. The much higher electrode performance was clearly due to its much higher oxygen ion conductivity and high catalytic activity.

ÖZET

ANOT DESTEKLİ PLANAR KATI OKSİT YAKIT HÜCRELERİNİN ŞERİT DÖKÜM VE SİNTERLEME YÖNTEMLERİYLE ÜRETİMİ VE PERFORMANS DEĞERLENDİRİLMESİ

Katı oksit yakıt hücrelerine olan ilgi, esnek yakıt gazı kompozisyonunu verimli enerji üretimiyle birleştirme yeteneklerinden dolayı artmıştır. En önemli hedefler hücrelerin uzun vadeli dayanıklılığı ve performansını içerir. Bu üç kayıp mekanizması ile belirlenir: ohmik, polarizasyon ve aktivasyon kayıpları. Bugüne kadar, anot destekli hücrelerin daha fazla geliştirilmesi, bireysel kayıp süreçlerinin kökeninin ve bunların hücrenin iç direncine katkılarının tam olarak anlaşılmaması nedeniyle sekteye uğramıştır. Bu nedenle, bu tezin temel amacı anot destekli bir hücrede meydana gelen tüm polarizasyon süreçlerinin açık bir şekilde tanımlanması ve eşzamanlı fiziksel yorumlanmasıdır. Vanadyum ve Gadolinyum katkılı katot örnekleri ($La_{0.595}V_{0.005}Sr_{0.4}CoO_{3-\partial}$ (LV05SC), $La_{0.50}Gd_{0.10}Sr_{0.4}CoO_{3-\partial}$ (LG10SC), $La_{0.57}V_{0.03}Sr_{0.4}FeO_{3-\partial}$ (LV3SF), $La_{0.595}V_{0.005}Sr_{0.4}MnO_{3-\partial}$ (LV05SM)) sol-gel yöntemi kullanılarak sentezlenmiştir. Kristal yapısı ve elemental analizleri XRD ve XPS teknikleriyle araştırılmıştır. Anot destekli hücreler, şerit döküm yöntemi kullanılarak hazırlanmıştır. Hem YSZ (Yttria ile stabilize edilmiş Zirkonyum) hem de GDC (Gadolinyum katkılı Seryum) farklı kombinasyonlarda elektrolit katmanı olarak kullanılmıştır. Sinterlenen hücrelerin yüzey ve kesit morfolojisi SEM analizi ile incelenmiştir. Elektrotların elektrokimyasal karakterizasyonu için Doğrusal Tarama Voltametresi (LSV) ve Elektrokimyasal Empedans Spektroskopisi (EIS) yapıldı. Ölçülen empedansın analizi, eşdeğer devre modelinde seri olarak dört (RQ) devrenin kullanılması gerektirdi. Tek bir hücrenin genel direncine katkıda bulunan tüm kayıp süreçleri açıkça belirlendi. Çalışma koşulları değiştirilerek, Gevşeme Süresi Dağılımı (DRT) ayrıntılı analizi edilip en fazla altı kayıp süreci olduğu tespit edildi. Dört katot arasında, GDC (35 μm)/YSZ elektrolit malzemeleriyle üretilmiş LG10SC katodu, 415 mW/cm^2 ile en yüksek performansı gösterdi. Yüksek elektrot performansı, daha iyi oksijen iyon iletkenliği ve katalitik aktivitesinden kaynaklanmaktadır.

TABLE OF CONTENTS

ACKNOWLEDGEMENTS iii

ABSTRACT v

ÖZET vi

LIST OF FIGURES xi

LIST OF TABLES xxii

LIST OF SYMBOLS xxiv

LIST OF ACRONYMS/ABBREVIATIONS xxv

1. INTRODUCTION 1

1.1. Introduction to Fuel Cells 1

1.2. Types of Fuel Cells 3

1.2.1 Polymer Electrolyte Fuel Cells 3

1.2.2. Direct Methanol Fuel Cells 4

1.2.3. Alkaline Fuel Cells 4

1.2.4. Phosphoric Acid Fuel Cells (PAFC) 4

1.2.5. Molten Carbonate Fuel Cell (MCFC) 5

1.3. Solid Oxide Fuel Cells 5

1.3.1. Thermodynamics of SOFC 7

1.3.2. Kinetics 8

1.3.3. Overall Efficiency 9

1.3.4. Voltage Losses (Polarization) in SOFCs 11

1.3.5. Current and Voltage Characteristics 13

1.4. Experimental and Preparative Techniques 15

1.4.1. X-Ray Diffraction (XRD) 15
1.4.2. X-Ray Photoelectron Spectroscopy (XPS) 16
1.4.3. Extended X-Ray Absorption Fine Structure (EXAFS) 17
1.4.4. Electrochemical Impedance Spectroscopy (EIS) 18
1.4.4.1. Equivalent Circuit Elements. 20
1.4.4.2. Analysis of the EIS Using the Distribution of Relaxation Times (DRT) 22
1.4.5. Tape Casting 24
1.5. Solid Oxide Fuel Cell Materials 25
1.5.1. Anode 25
1.5.2. Electrolyte 25
1.5.3. Cathode 26
1.5.3.1. Oxygen Reduction Reaction 27
1.5.3.2. State-of-the-art Cathode Materials 28
1.5.3.3. Perovskite Materials 29
2. SCOPE OF THE THESIS 36
3. SYNTHESIS, CHARACTERIZATION AND PERFORMANCE ANALYSIS OF $La_{0.595}V_{0.005}Sr_{0.4}CoO_{3-\partial}$ (LV05SC) CATHODE SAMPLE 38
3.1. Introduction 38
3.2. Material Synthesis 41
3.3. Characterization, Electrochemical Measurements and Fabrication Procedures 41
3.4. Results and Discussion 43
3.4.1. Phase Compositions and Structure 43
3.4.2. EXAFS Analysis 44

3.4.3. XPS Analysis 47

3.4.4. Fabrication of Anode-Supported Electrolyte via Tape casting/ Lamination/Co-firing 51

3.4.5. Surface Morphology Analysis of the Cell 52

3.4.6. Single Cell Performances 58

3.5. Conclusion 72

4. SYNTHESIS, CHARACTERIZATION AND PERFORMANCE ANALYSIS OF $La_{0.50}Gd_{0.10}Sr_{0.4}CoO_{3-\partial}$ (LG10SC) CATHODE SAMPLE 74

4.1. Introduction 74

4.2. Material Synthesis 75

4.3. Characterization, Electrochemical Measurements and Fabrication Procedures 76

4.4. Results and Discussion 77

4.4.1. Phase Composition and Structure 77

4.4.2. XPS Analysis 78

4.4.3. Fabrication of Anode-Supported Electrolyte via Tape casting/ Lamination/ Co-firing 82

4.4.4. Surface Morphology Analysis of the Cell 83

4.4.5. Single Cell Performances 87

4.5. Conclusion 100

5. SYNTHESIS, CHARACTERIZATION AND PERFORMANCE ANALYSIS OF $La_{0.57}V_{0.03}Sr_{0.4}FeO_{3-\partial}$ (LV3SF) CATHODE SAMPLE 102

5.1. Introduction 102

5.2. Material Synthesis 103

5.3. Characterization, Electrochemical Measurements and Fabrication Procedures 103

5.4. Results and Discussion 105

5.4.1. Phase Composition and Structure 105

5.4.2. XPS Analysis 106

5.4.3. Fabrication of Anode-Supported Electrolyte via Tape casting/ Lamination/ Co-firing 109

5.4.4. Surface Morphology Analysis of the Cell 110

5.4.5. Single Cell Performances 114

5.5. Conclusion 128

6. SYNTHESIS, CHARACTERIZATION AND PERFORMANCE ANALYSIS OF $La_{0.595}V_{0.005}Sr_{0.4}MnO_{3-\partial}$ (LV05SM) CATHODE SAMPLE 130

6.1. Introduction 130

6.2. Material Synthesis 131

6.3. Characterization, Electrochemical Measurements and Fabrication Procedures 132

6.4. Results and Discussion 133

6.4.1. Phase Composition and Structure 133

6.4.2. XPS Analysis 134

6.4.3. Fabrication of Anode-Supported Electrolyte via Tape casting/ Lamination/ Co-firing 137

6.4.4. Surface Morphology Analysis of the Cell 138

6.4.5. Single Cell Performances 142

6.5. Conclusion 156

7. CONCLUDING REMARKS 158

REFERENCES 162

LIST OF FIGURES

Figure 1.1. Illustration of the principle of a Solid Oxide Fuel Cell (SOFC). 6

Figure 1.2. Cell potential as function of current density of a fuel cell. 12

Figure 1.3. The Voltage - Current density and Power density relations for a fuel cell... 14

Figure 1.4. Schematic of XRD diffraction..... 16

Figure 1.5. Schematic representation of the X-Ray absorption spectrum. 17

Figure 1.6. AC impedance of a SOFC unit under small amplitude perturbations..... 19

Figure 1.7. Nyquist diagram of impedance Z and related equivalent circuit. 19

Figure 1.8. Impedance spectra and the corresponding DRT plot. 23

Figure 1.9. (a) Perovskite unit cell (b) the anions on the edges, the B-cations in the corners, and the A-cation in the center. 31

Figure 1.10. Molecular orbital diagram for an ABO_3 perovskite crystal structure. 33

Figure 1.11. Bulk oxygen transport process. 34

Figure 3.1. A schematic representation of the experimental SOFC setup. 42

Figure 3.2. XRD data of $La_{0.595}V_{0.005}Sr_{0.4}Co_{3-\partial}$ cathode powder. 44

Figure 3.3. (a) Raw and calculated Co K-edge X-ray absorption spectrum of LV05SC perovskite, (b) Normalized, back-ground subtracted, and k^3-

weighted Co-EXAFS spectrum, (c) Radial structure function obtained by Fourier Transform of $k^3X(k)$..... 46

Figure 3.4. XPS survey spectra of (a) LV05SC perovskite, (b) La3d3/2 and La3d5/2, (c) V2p1/2 and V2p3/2, (d) Sr3d3/2 and Sr3d5/2, (e) Co2p1/2 and Co2p3/2, (f) O1s..... 48

Figure 3.5. Pictures of the green tapes of (a) YSZ electrolyte, (b) NiOYSZ anode layers. 52

Figure 3.6. SEM images of (a)YSZ-NiOYSZ half-cell cross section, (b) closer look to interfaces, (c) YSZ electrolyte, and (d) NiOYSZ anode. 53

Figure 3.7. SEM images of (a) GDC-NiOGDC half-cell cross section, (b) closer look to interfaces, (c) GDC electrolyte, and (d) NiOGDC anode. 53

Figure 3.8. SEM images of (a) GDC (35 µm)-YSZ-NiOYSZ half-cell cross section, (b) closer look to interfaces, (c) GDC electrolyte, (d) YSZ electrolyte, and (e) NiOYSZ anode..... 54

Figure 3.9. SEM images of (a) GDC (5 µm)-YSZ-NiOYSZ half-cell cross section, (b) closer look to interfaces, (c) GDC electrolyte, (d) YSZ electrolyte, and (e) NiOYSZ anode..... 54

Figure 3.10. XRD analysis from electrolyte layer of (a) YSZ-NiOYSZ, (b) GDC-NiOGDC, (c) GDC (35 µm)-YSZ-NiOYSZ, and (d) GDC (5 µm)-YSZ-NiOYSZ half-cells. 55

Figure 3.11. SEM images of LV05SC-YSZ-NiOYSZ fuel cell, (a) cross section, (b) closer look to interfaces, (c) LV05SC cathode, (d) YSZ electrolyte, and (e) NiOYSZ anode. 55

Figure 3.12. SEM images of LV05SC-GDC-NiOGDC fuel cell, (a) cross section, (b) closer look to interfaces, (c) LV05SC cathode, (d) GDC electrolyte, and (e) NiOGDC anode. 56

Figure 3.13. SEM images of LV05SC-GDC (35 μm)-YSZ-NiOYSZ fuel cell, (a) cross section, (b) closer look to interfaces, (c) LV05SC cathode, (d) GDC electrolyte, (e) YSZ electrolyte, and (f) NiOYSZ anode. 57

Figure 3.14. SEM images of LV05SC-GDC (5 μm)-YSZ-NiOYSZ fuel cell, (a) cross section, (b) closer look to interfaces, (c) LV05SC cathode, (d) GDC electrolyte, (e) YSZ electrolyte, and (f) NiOYSZ anode. 57

Figure 3.15. XRD analysis from cathode side of (a) LV05SC-GDC (35 μm)-YSZ-NiOYSZ, (b) LV05SC-GDC (5 μm)-YSZ-NiOYSZ fuel cells. 58

Figure 3.16. I-V curves and output power density of single cell with LV05SC-YSZ-NiYSZ at different temperatures. 59

Figure 3.17. (a) Nyquist plots of LV05SC-YSZ-NiYSZ cell at OCV conditions, inset: Equivalent circuit model, (b) DRT curve of impedance spectra as a function of operating temperature at 500 - 800 °C. 59

Figure 3.18. (a) Nyquist plots of LV05SC-YSZ-NiYSZ cell, (b) DRT patterns under different applied voltages at 800 °C. 62

Figure 3.19. I-V curves and output power density of single cell with LV05SC-GDC-NiGDC at different temperatures. 63

Figure 3.20. (a) Nyquist plots of LV05SC-GDC-NiGDC cell at OCV conditions, inset: Equivalent circuit model, (b) DRT curve of impedance spectra as a function of operating temperature at 500 - 800 °C. 64

Figure 3.21. (a) Nyquist plots of LV05SC-GDC-NiGDC cell, (b) DRT patterns under different applied voltages at 700 ºC. 66

Figure 3.22. I-V curves and output power density of single cell with LV05SC- GDC (35 µm)-YSZ-NiYSZ at different temperatures. 66

Figure 3.23. (a) Nyquist plots of LV05SC-GDC (35 µm)-YSZ-NiYSZ cell at OCV conditions, inset: Equivalent circuit model, (b) DRT curve of impedance spectra as a function of operating temperature at 500 - 800 ºC. 67

Figure 3.24. (a) Nyquist plots of LV05SC-GDC (35 µm)-YSZ-NiYSZ cell, (b) DRT patterns under different applied voltages at 800 ºC. 69

Figure 3.25. I-V curves and output power density of single cell with LV05SC- GDC (5 µm)-YSZ-NiYSZ at different temperatures. 70

Figure 3.26. (a) Nyquist plots of LV05SC-GDC (5 µm)-YSZ-NiYSZ cell at OCV conditions, inset: Equivalent circuit model, (b) DRT curve of impedance spectra as a function of operating temperature at 500 - 800 ºC. 70

Figure 3.27. (a) Nyquist plots of LV05SC-GDC (5 µm)-YSZ-NiYSZ cell, (b) DRT patterns under different applied voltages at 800 ºC. 71

Figure 4.1. XRD data of $La_{0.5}Gd_{0.1}Sr_{0.4}Co_{3-\partial}$ cathode powder. 78

Figure 4.2. XPS survey spectra of (a) LG10SC perovskite, (b) La3d3/2 and La3d5/2, (c) Gd4d3/2 and Gd4d5/2, (d) Sr3d3/2 and Sr3d5/2, (e) Co2p1/2 and Co2p3/2, (f) O1s. 80

Figure 4.3. Pictures of the green tapes of (a) GDC electrolyte, (b) NiOGDC anode layers. 83

Figure 4.4. SEM images of LG10SC-YSZ-NiOYSZ fuel cell, (a) cross section, (b) closer look to interfaces, (c) LG10SC cathode, (d) YSZ electrolyte, and (e) NiOYSZ anode. 84

Figure 4.5. SEM images of LG10SC-GDC-NiOGDC fuel cell, (a) cross section, (b) closer look to interfaces, (c) LG10SC cathode, (d) GDC electrolyte, and (e) NiOGDC anode. 84

Figure 4.6. SEM images of LG10SC-GDC-NiGDC fuel cell after reduction by H_2, (a) cross section, (b) closer look to interfaces, (c) LG10SC cathode, (d) GDC electrolyte, and (e) NiGDC anode. 85

Figure 4.7. SEM images of LG10SC-GDC (35 μm)-YSZ-NiOYSZ fuel cell, (a) cross section, (b) closer look to interfaces, (c) LG10SC cathode, (d) GDC electrolyte, (e) YSZ electrolyte, and (f) NiOYSZ anode. 85

Figure 4.8. SEM images of LG10SC-GDC (5 μm)-YSZ-NiOYSZ fuel cell, (a) cross section, (b) closer look to interface, (c) LG10SC cathode, (d) GDC electrolyte, (e) YSZ electrolyte, and (f) NiOYSZ anode. 86

Figure 4.9. XRD analysis from cathode side of (a) LG10SC-GDC (35 μm)-YSZ-NiOYSZ, (b) LG10SC-GDC (5 μm)-YSZ-NiOYSZ fuel cells. 87

Figure 4.10. I-V curves and output power density of single cell with LG10SC-YSZ-NiYSZ at different temperatures. 88

Figure 4.11. (a) Nyquist plots of LG10SC-YSZ-NiYSZ cell at OCV conditions, inset: Equivalent circuit model, (b) DRT curve of impedance spectra as a function of operating temperature at 500 - 800 ^{o}C. 88

Figure 4.12. (a) Nyquist plots of LG10SC-YSZ-NiYSZ cell, (b) DRT patterns under different applied voltages at 800 ^{o}C. 91

Figure 4.13. I-V curves and output power density of single cell with LG10SC-GDC-NiGDC at different temperatures. 92

Figure 4.14. (a) Nyquist plots of LG10SC-GDC-NiGDC cell at OCV conditions, inset: Equivalent circuit model, (b) DRT curve of impedance spectra as a function of operating temperature at 500 - 800 ºC. 93

Figure 4.15. (a) Nyquist plots of LG10SC-GDC-NiGDC cell, (b) DRT patterns under different applied voltages at 800 ºC. 94

Figure 4.16. I-V curves and output power density of single cell with LG10SC-GDC (35 µm)-YSZ-NiYSZ at different temperatures. 95

Figure 4.17. (a) Nyquist plots of LG10SC-GDC (35 µm)-YSZ-NiYSZ cell at OCV conditions, inset: Equivalent circuit model, (b) DRT curve of impedance spectra as a function of operating temperature at 500 - 800 ºC. 96

Figure 4.18. (a) Nyquist plots of LG105SC-GDC (35 µm)-YSZ-NiYSZ cell, (b) DRT patterns under different applied voltages at 800 ºC. 97

Figure 4.19. I-V curves and output power density of single cell with LG10SC-GDC (5 µm)-YSZ-NiYSZ at different temperatures. 98

Figure 4.20. (a) Nyquist plots of LG10SC-GDC (5 µm)-YSZ-NiYSZ cell at OCV conditions, inset: Equivalent circuit model, (b) DRT curve of impedance spectra as a function of operating temperature at 500 - 800 ºC. 99

Figure 4.21. (a) Nyquist plots of LG10SC-GDC (5 µm)-YSZ-NiYSZ cell, (b) DRT patterns under different applied voltages at 700 ºC. 100

Figure 5.1. XRD data of $La_{0.57}V_{0.03}Sr_{0.4}FeO_{3-\partial}$ cathode powder. 105

Figure 5.2. XPS survey spectra of (a) LV3SF perovskite, (b) La3d3/2 and La3d5/2, (c) V2p1/2 and V2p3/2, (d) Sr3d3/2 and Sr3d5/2, (e) Fe2p1/2 and Fe2p3/2, (f) O1s. 107

Figure 5.3. Pictures of the YSZ/NiOYSZ half cells from (a) top and (b) bottom, fuel cells after cathode sample brush-painted on electrolyte layer (c) LV3SF-YSZ-NiOYSZ, (d) LV3SF-GDC-NiOGDC, (e) LV3SF-GDC (35 μm)-YSZ-NiOYSZ, and (f) LV3SF-GDC (5μm)-YSZ-NiOYSZ. ... 110

Figure 5.4. SEM images of LV3SF-YSZ-NiOYSZ fuel cell, (a) cross section, (b) closer look to interfaces, (c) LV3SF cathode, (d) YSZ electrolyte, and (e) NiOYSZ anode. 111

Figure 5.5. SEM images of LV3SF-GDC-NiOGDC fuel cell, (a) cross section, (b) closer look to interfaces, (c) LV3SF cathode, (d) GDC electrolyte, and (e) NiOGDC anode. 112

Figure 5.6. SEM images of LV3SF-GDC (35 μm)-YSZ-NiOYSZ fuel cell, (a) cross section, (b) closer look to interfaces, (c) LV3SF cathode, (d) GDC electrolyte, (e) YSZ electrolyte, and (f) NiOYSZ anode. 112

Figure 5.7. SEM images of LV3SF-GDC (5 μm)-YSZ-NiOYSZ fuel cell, (a) cross section, (b) closer look to interfaces, (c) LV3SF cathode, (d) GDC electrolyte, (e) YSZ electrolyte, and (f) NiOYSZ anode. 113

Figure 5.8. XRD analysis from cathode side of (a) LV3SF-GDC (35 μm)-YSZ-NiOYSZ fuel cell, (b) LV3SF-GDC (5 μm)-YSZ-NiOYSZ fuel cell..... 114

Figure 5.9. I-V curves and output power density of single cell with LV3SF-YSZ-NiYSZ at different temperatures. 115

Figure 5.10. (a) Nyquist plots of LV3SF-YSZ-NiYSZ cell at OCV conditions, inset: Equivalent circuit model, (b) DRT curve of impedance spectra as a function of operating temperature at 500 - 800 ºC..... 115

Figure 5.11. (a) Nyquist plots of LV3SF-YSZ-NiYSZ cell, (b) DRT patterns under different applied voltages at 800 ºC. 117

Figure 5.12. I-V curves and output power density of single cell with LV3SF-GDC-NiGDC at different temperatures. 119

Figure 5.13. (a) Nyquist plots of LV3SF-GDC-NiGDC cell at OCV conditions, inset: Equivalent circuit model, (b) DRT curve of impedance spectra as a function of operating temperature at 500 - 800 ºC..... 120

Figure 5.14. (a) Nyquist plots of LV3SF-GDC-NiGDC cell, (b) DRT patterns under different applied voltages at 800 ºC. 121

Figure 5.15. I-V curves and output power density of single cell with LV3SF-GDC (35 µm)-YSZ-NiYSZ at different temperatures..... 122

Figure 5.16. (a) Nyquist plots of LV3SFC-GDC (35 µm)-YSZ-NiYSZ cell at OCV conditions, inset: Equivalent circuit model, (b) DRT curve of impedance spectra as a function of operating temperature at 500 - 800 ºC. 123

Figure 5.17. (a) Nyquist plots of LV3SF-GDC (35 µm)-YSZ-NiYSZ cell, (b) DRT patterns under different applied voltages at 800 ºC. 124

Figure 5.18. I-V curves and output power density of single cell with LV3SF-GDC (5 µm)-YSZ-NiYSZ at different temperatures. 125

Figure 5.19. (a) Nyquist plots of LV3SF-GDC (5 µm)-YSZ-NiYSZ cell at OCV conditions, inset: Equivalent circuit model, (b) DRT curve of impedance spectra as a function of operating temperature at 500 - 800 ºC. 125

Figure 5.20. (a) Nyquist plots of LV3SF-GDC (5 μm)-YSZ-NiYSZ cell, (b) DRT patterns under different applied voltages at 800 ºC. 127

Figure 6.1. XRD data of $La_{0.595}V_{0.005}Sr_{0.4}MnO_{3-\partial}$ cathode powder. 133

Figure 6.2. XPS survey spectra of (a) LV05SM perovskite, (b) La3d3/2 and La3d5/2, (c) V2p1/2 and V2p3/2, (d) Sr3d3/2 and Sr3d5/2, (e) Mn2p1/2 and Mn2p3/2, (f) O1s. 135

Figure 6.3. Pictures of the fuel cell attached to a zirconia tube set-up. 138

Figure 6.4. SEM images of LV05SM-YSZ-NiOYSZ fuel cell, (a) cross section, (b) closer look to interfaces, (c) LV05SM cathode, (d) YSZ electrolyte, and (e) NiOYSZ anode. 139

Figure 6.5. SEM images of LV05SM-GDC-NiOGDC fuel cell, (a) cross section, (b) closer look to interfaces, (c) LV05SM cathode, (d) GDC electrolyte, and (e) NiOGDC anode. 140

Figure 6.6. SEM images of LV05SM-GDC (35 μm)-YSZ-NiOYSZ fuel cell, (a) cross section, (b) closer look to interfaces, (c) LV05SM cathode, (d) GDC electrolyte, (e) YSZ electrolyte, and (f) NiOYSZ anode. 140

Figure 6.7. SEM images of LV05SM-GDC (5 μm)-YSZ-NiOYSZ fuel cell, (a) cross section, (b) closer look to interfaces, (c) LV05SM cathode, (d) GDC electrolyte, (e) YSZ electrolyte, and (f) NiOYSZ anode. 141

Figure 6.8. XRD analysis from cathode side of (a) LV05SM-GDC (35 μm)-YSZ-NiOYSZ fuel cell, (b) LV05SM-GDC (5 μm)-YSZ-NiOYSZ fuel cell. 141

Figure 6.9. I-V curves and output power density of single cell with LV05SM-YSZ-NiYSZ at different temperatures. 142

Figure 6.10. (a) Nyquist plots of LV05SM-YSZ-NiYSZ cell at OCV conditions, inset: Equivalent circuit model, (b) DRT curve of impedance spectra as a function of operating temperature at 500 - 800 °C. 143

Figure 6.11. (a) Nyquist plots of LV05SM-YSZ-NiYSZ cell, (b) DRT patterns under different applied voltages at 800 °C. 145

Figure 6.12. I-V curves and output power density of single cell with LV05SM-GDC-NiGDC at different temperatures. 147

Figure 6.13. (a) Nyquist plots of LV05SM-GDC-NiGDC cell at OCV conditions, inset: Equivalent circuit model, (b) DRT curve of impedance spectra as a function of operating temperature at 500 - 800 °C. 148

Figure 6.14. (a) Nyquist plots of LV05SM-GDC-NiGDC cell, (b) DRT patterns under different applied voltages at 800 °C. 149

Figure 6.15. I-V curves and output power density of single cell with LV05SM-GDC (35 µm)-YSZ-NiYSZ at different temperatures. 150

Figure 6.16. (a) Nyquist plots of LV05SM-GDC (35 µm)-YSZ-NiYSZ cell at OCV conditions, inset: Equivalent circuit model, (b) DRT curve of impedance spectra as a function of operating temperature at 500 - 800 °C. 151

Figure 6.17. (a) Nyquist plots of LV05SM-GDC (35 µm)-YSZ-NiYSZ cell, (b) DRT patterns under different applied voltages at 600 °C. 153

Figure 6.18. I-V curves and output power density of single cell with LV05SM-GDC (5 µm)-YSZ-NiYSZ at different temperatures. 154

Figure 6.19. (a) Nyquist plots of LV05SM-GDC (5 µm)-YSZ-NiYSZ cell at OCV conditions, inset: Equivalent circuit model, (b) DRT curve of impedance spectra as a function of operating temperature at 500 - 800 °C. 154

Figure 6.20. (a) Nyquist plots of LV05SM-GDC (5 μm)-YSZ-NiYSZ cell, (b) DRT patterns under different applied voltages at 800 ºC. 156

LIST OF TABLES

Table 1.1. List of the top six qualities shared by the five most popular fuel cell types, the alkaline FC, the direct methanol FC, the polymer electrolyte membrane FC, phosphoric acid FC, molten carbonate FC and solid oxide FC. 5

Table 1.2. Equivalent Circuit Elements Used in Modelling. 21

Table 3.1. Structural parameters of $La_{0.595}V_{0.05}Sr_{0.4}CoO_{3-\partial}$ sample derived from Co - XAS analysis..... 47

Table 3.2. EIS Fitting values of LV05SC-YSZ-NiYSZ fuel cell at 500-800°C..... 61

Table 3.3. EIS Fitting values of LV05SC-GDC-NiGDC fuel cell at 500-800°C..... 65

Table 3.4. EIS Fitting values of LV05SC-GDC (35 µm)-YSZ-NiYSZ cell at 500 - 800°C..... 68

Table 3.5. EIS Fitting values of LV05SC-GDC (5 µm)-YSZ-NiYSZ fuel at 500 – 800°C..... 71

Table 4.1. EIS Fitting values of LG10SC-YSZ-NiYSZ fuel cell at 500-800°C. 90

Table 4.2. EIS Fitting values of LG10SC-GDC-NiGDC fuel cell at 500-800°C..... 94

Table 4.3. EIS Fitting values of LG10SC-GDC (35 µm)-YSZ-NiYSZ fuel cell at 500-800°C. 97

Table 4.4. EIS Fitting values of LG10SC-GDC (5 µm)-YSZ-NiYSZ fuel cell at 500-800°C. 100

Table 5.1. EIS Fitting values of LV3SF-YSZ-NiYSZ fuel cell at 500-800ºC. 116

Table 5.2. EIS Fitting values of LV3SF-GDC-NiGDC fuel cell at 500-800ºC. 120

Table 5.3. EIS Fitting values of LV3SF-GDC (35 μm)-YSZ-NiYSZ fuel cell at 500-800ºC. 123

Table 5.4. EIS Fitting values of LV3SF-GDC (5 μm)-YSZ-NiYSZ fuel cell at 500-800ºC. 126

Table 6.1. EIS Fitting values of LV05SM-YSZ-NiYSZ fuel cell at 500-800ºC..... 144

Table 6.2. EIS Fitting values of LV05SM-GDC-NiGDC fuel cell at 500-800ºC. ... 149

Table 6.3. EIS Fitting values of LV05SM-GDC (35 μm)-YSZ-NiYSZ fuel cell at 500-800ºC. 152

Table 6.4. EIS Fitting values of LV05SM-GDC (5 μm)-YSZ-NiYSZ fuel cell at 500-800ºC. 155

Table 7.1. Comparison of relative surface concentration of the perovskite-type catalysts. 160

LIST OF SYMBOLS

C	Capacitance
f	Frequency
F	Faraday constant
G	Gibbs energy
I	Current
k	Boltzmann constant or effective surface rate constant
L_b	Inductance
OCV	Open-circuit voltage
Q	Constant phase element
R	Ideal gas constant or resistance
R_{bulk}	Ohmic resistance
R_p	Polarization resistance
V_{cell}	Cell voltage
$V_O^{\bullet\bullet}$	Oxygen vacancy
Z_{imag}	Imaginary part of the complex impedance
Z_{real}	Real part of the complex impedance
α	Charge transfer coefficient
ΔH^0	Enthalpy change at standard temperature and pressure, kJ/mol
δ	Oxygen non-stoichiometry
ε	Efficiency
η	Electrode overpotential (polarization)
λ	Regularization parameter
ϕ	Phase shift
ω	Angular frequency

LIST OF ACRONYMS/ABBREVIATIONS

ASR	Area Specific Resistance
DRT	Distribution of Relaxation Time
EIS	Electrochemical Impedance Spectroscopy
GDC	Gadolinia-doped Ceria
HF	High Frequency Feature in Impedance Spectra
IT	Intermediate Temperature
I	Current
LF	Low Frequency Feature in Impedance Spectra
LSC	Lanthanum Strontium Cobaltate (La,Sr)$CoO_{3-\partial}$
LSCF	Lanthanum Strontium Cobalt Iron Oxide (La,Sr)(Co,Fe)$O_{3-\partial}$
LSF	Lanthanum Strontium Ferrate (La,Sr)$FeO_{3-\partial}$
LSM	Lanthanum Strontium Manganite (La,Sr)$MnO_{3-\partial}$
LSV	Linear Sweep Voltammetry
MF	Medium Frequency Feature in Impedance Spectra
MIEC	Mixed Ionic Electrical Conductor
OCV	Open-Circuit Voltage
SEM	Scanning Electron Microscopy
SOFC	Solid Oxide Fuel Cell
TEC	Thermal Expansion Coefficient
TPB	Triple Phase Boundary
V	Voltage
XRD	X-ray Diffraction
XPS	X-ray Photoelectron Spectroscopy
YSZ	Yttria-stabilized Zirconia (Y_2O_3-doped ZrO_2)

1. INTRODUCTION

1.1. Introduction to Fuel Cells

As our understanding of global warming and its negative climatological, ecological, and impacts on society expand quickly, the development of new energy technologies has become of increasing importance [1, 2]. Over the past century, internal combustion engines have powered nearly all forms of transportation, but as fossil fuel reserves are depleting and environmental awareness is growing, interest has increased in technologies that either use renewable energy sources or more effectively use the fossil fuels [3]. The idea of a world where energy generated from sustainable sources can be preserved in the form of hydrogen has been made possible as a result of this drive for sustainable energy technology. An effective converter, that is required by modern civilization, is a crucial component of such an energy system. A fuel cell is an energy conversion device that does not require direct combustion as an intermediate step in the process, instead converting chemical energy from a fuel directly into electrical energy. Furthermore, a fuel cell may be used as an electrolyzer in reverse, converting water into oxygen and hydrogen while drawing power from any other source [4, 5]. Compared to traditional thermo-mechanical processes, it provides substantially better conversion efficiencies. Fuel cells use an electrochemical combination of reactants, much like batteries do, in order to produce power. In a fuel cell, an oxidant gas (such as oxygen in the air) and a gaseous fuel (such as hydrogen or hydrocarbon fuels) travels via electrodes and undergo a half-cell rection, with the primary charge carrier species passing through an ion-conducting, gas-tight, electrically insulating electrolyte layer. The electrons generated at the fuel electrode must be carried through an external circuit – along which the electrical power is gained- for the entire reaction to be completed [6].

A fuel cell does not need to be recharged, though, unlike a battery. A fuel cell is an environmentally friendly device that functions as long as the electrodes are supplied with both fuel and oxidant. Fuel cells come in a variety of forms now, but they all work on the same principles. The reduction of oxygen (the cathode-air electrode) and the oxidation of fuel (the anode-fuel electrode), respectively, are accommodated by two electrodes on either side of the electrolyte [7, 8].

Although they have a contemporary, high-tech design, fuel cells have been studied by researchers for more than 150 years. Fuel cells have been the focus of significant study and development, especially since World War II. Sir William Grove, who gained the fame for creating a wet-cell battery in 1838, showed that fuel cells may one day become a reality [9]. The “Grove cell”, as it become known, produced around 12 amps of current at roughly 1.8 V using a platinum electrode submerged in nitric acid and a zinc electrode in zinc sulfate. Grove found that a continuous current would flow between two platinum electrodes if one end of each electrode was placed in a sulfuric acid container and the other end was placed in an oxygen or hydrogen container, respectively. It was observed that the water level increased in both tubes as the current passed, indicating that the sealed containers stored water in addition to the gases [10].

Nicholson and Carlisle first documented the use of electricity to split water into hydrogen and oxygen in 1800. Grove, however, claimed that mixing the gases to generate electricity and water was - a step further than any so far recorded. Grove came to the conclusion that by connecting numerous sets of these electrodes in a series circuit, it might be “effect the splitting of water by means of its composition”. It was quickly achieved this feat using the first fuel cell, which is called a “battery of gas” [11]. Ludwig Mond, a chemist, spent the most of his career producing industrial chemical technologies for industries like soda manufacturing and nickel refining. Mond and his colleague Carl Langer published a report on their studies with a hydrogen-oxygen fuel cell in 1889. This cell was able to produce 6 amps per square foot of electrode surface area at 0.73 V [12]. The electrodes of Mond and Langer’s cell were made of thin, perforated platinum. It is observed challenges employing liquid electrolytes, absorbed by a porous non-conducting substance, in a manner similar to that used in the so-called dry stacks and batteries [13]. A considerable amount of the theoretical knowledge related to the operation of fuel cells was contributed by Friedrich Wilhelm Ostwald, a pioneer in the field of physical chemistry. Some experiments were conducted by him in 1893 to ascertain the interrelated functions of the fuel cell’s numerous parts, including the electrodes, electrolyte, oxidizing and reducing agents [14, 15].

Grove has hypothesized that the activity in his gas battery took place where the electrode, gas and the electrolyte came into contact, but was at a loss for additional explanation. Ostwald found the solution to Grove’s gas battery mystery by building on his

innovative research connecting physical qualities and chemical processes. It was paved the way for later fuel cell researchers with these investigations of the underlying chemistry of fuel cells [16].

When Nernst creates a “glower” towards the end of the 19th century, the history of solid oxide electrolytes can be said to have started. Nernst discovered that adding a few different oxides might significantly lower the extremely high electrical resistance of pure solid-oxides. The most effective of these oxides mostly contained Zirconia (ZrO_2) with minor levels of Yttria (Y_2O_3). In Solid Oxide Fuel Cells (SOFC), this is still the electrolyte material (Yttria stabilized Zirconia - YSZ) that is most frequently worked with [17, 18]. During the first part of the 20th century, Swiss scientist Emil Baur conducted extensive research on several fuel cell types. The work of Baur comprised high temperature devices (using molten silver as an electrolyte material) and a device that employed a solid electrolyte of clay and metal oxides, employing stabilized zirconia as the electrolyte and coke and magnetite as the fuel and oxidant, respectively. The cell potential was 0.65 V at a current density of around 0.3 mA/cm^2. Although the first SOFC’s functionality had been proven, its current output was too low for actual use [19, 20].

1.2. Types of Fuel Cells

1.2.1. Polymer Electrolyte Fuel Cells

An ion-exchange membrane (fluorinated sulfonic acid polymer or any such polymer), which is a good proton conductor, serves as the electrolyte in this type of fuel cell. The cell must function in circumstances where the waste water does not evaporate more quickly than it is produced since the polymer membrane has to be kept hydrated in order to function efficiently. A Hydrogen rich gas with less than 10 ppm CO – poisoned the catalyst– is employed due to the polymer’s restriction on the working temperature, which is typically less than 120 °C. This restriction is caused by issues with water balance. Both electrodes must have higher catalyst loadings (Pt in most situations) than those utilized in PAFCs. The ideal uses for these cells are lightweight construction materials, automobiles, and even smaller items like portable equipment [21–23].

1.2.2. Direct Methanol Fuel Cells

A relatively recent member of the fuel cell family, the direct-methanol fuel cell (DMFC) is similar to the PEM cell in that it employs a polymer membrane as the electrolyte. However, the DMFC does not require a fuel reformer since a catalyst on the anode extracts hydrogen from liquid methanol [24, 25].

1.2.3. Alkaline Fuel Cells

This electrolyte of alkaline fuel cell is either more concentrated – 85 wt% KOH – when operating at higher temperatures (~ 250 °C) or less concentrated – 35-50 wt% KOH – at lower operating temperatures (~ 120 °C). A variety of electrocatalysts, including Ni, Ag, metal oxides, spinels, and noble metals, can be utilized, and the electrolyte is kept in a matrix (often asbestos). With the exception of hydrogen, the fuel supply is restricted to non-reactive components. Because CO is poisonous, CO_2 will combine with KOH to generate K_2CO_3, which will change the electrolyte. Alkaline batteries must take into account even very modest amounts of CO_2 in the air. Originally created by NASA for use in space missions, the alkaline fuel cell is currently being used in hydrogen-powered cars [26–28].

1.2.4. Phosphoric Acid Fuel Cells (PAFC)

In this type of fuel cell, which runs at 150 to 220 °C, phosphoric acid is employed as the electrolyte and is 100% concentrated. Because phosphoric acid has weak ionic conductivity at low temperatures, the Pt electrocatalyst in the anode suffers from severe CO poisoning. The PAFC is able to operate at the high end of the acid temperature range (100 to 220 °C) because concentrated phosphoric acid has a high relative stability compared to other common acids. Additionally, using concentrated acid reduces the water vapor pressure, making it easier to regulate the water in the cell. In a PAFC, the phosphoric acid electrolyte is held in a silicon carbide matrix, and the anode and cathode are formed of finely distributed platinum catalyst on carbon paper. This form of fuel cell has been used in hotels, hospitals, and office buildings the longest and is the most commercially developed. Large vehicles like buses can also use the phosphoric acid fuel cell [29, 30].

1.2.5. Molten Carbonate Fuel Cell (MCFC)

A molten carbonate salt solution serves as the electrolyte in a molten carbonate fuel cell. Alkali carbonates are often used as the electrolyte and are typically kept in a ceramic $LiAlO_2$ matrix. At 600 to 700 °C, the alkali carbonates melt to produce a highly conductive molten salt, with carbonate ions supplying the ionic conduction necessary for the fuel cell to function. The nickel (anode) and nickel oxide (cathode) are sufficient to induce reaction at the high operating temperatures of MCFCs. No need for noble metals. Instead of using pure hydrogen, it could run on fuel gases generated from coal or natural gas [28], [31, 32].

Table 1.1. List of the top six qualities shared by the five most popular fuel cell types, the alkaline FC, the direct methanol FC, the polymer electrolyte membrane FC, phosphoric acid FC, molten carbonate FC and solid oxide FC.

Fuel Cell	**AFC**	**DMFC**	**PEMFC**	**PAFC**	**MCFC**	**SOFC**
Charge carrier	OH^-	H^+	H^+	H^+	CO_3^{2-}	O^{2-}
Electrolyte	KOH	Polymer	Polymer	H_3PO_4	Li_2CO_3 + K_2CO_3	$Zr_2 + Y_2O_3$
$T_{oper.}$ [°C]	100	60-90	80	200	650	600-1000
Fuels	Pure H_2	Methanol	Pure H_2	CO free H_2	H_2, CO, CH_4	H_2, CO, CH_4

The chemical properties of the electrolyte utilized as the cell's ionic conductor serve as the main criterion for categorizing fuel cells. This in turn influences the operating temperature, the electrode materials, and potential fuels. Table 1.1. is a list of the most popular fuel cell types. A practical drawback of SOFCs and molten carbonate fuel cells is their high working temperature. Additionally, it reduces the theoretical maximum efficiency.

1.3. Solid Oxide Fuel Cells

SOFC is a fuel cell technology that operates at high temperatures. They are incredibly helpful in huge, high-power applications like major industrial stations and electricity generation facilities. The electrolyte in a SOFC system is typically a solid ceramic, and the system runs at temperatures between 600 °C and 1000 °C [33, 34]. Internal reforming is

made possible by the high working temperature, which also encourages quick electro-catalytic processes involving non-precious metals and generates high quality byproduct heat for co-generation. This kind of fuel cell has efficiency levels that may go as high as 70%. The following elements of SOFC technology have potential benefits and effectiveness. SOFC technology is extremely materially demanding [35, 36]:

i) In terms of producing electricity, it is the most effective fuel cell. Additionally, because SOFCs operate at high temperatures, they generate high-quality heat byproducts that may be used to cogeneration or combined cycle applications. This may boost energy efficiency all around even more [37].

ii) It has a wide range of fuel options, including hydrocarbon fuels like natural gas [38].

iii) Expensive noble metals, which may pose concerns with resource availability and cost, are not required for SOFCs [33].

iv) Because of the high working temperature, any carbon monoxide that is created is converted to carbon dioxide, resulting in very little emissions of exhaust gases from SOFCs [39].

All of the materials used in SOFCs are in solid-state. Additionally, the cell design is not fundamentally constrained by the solid-state nature of any SOFC components. Cells can be built in a variety of ways, including planar button, flat plate, and tubular cells, or rolled tubes [40–43].

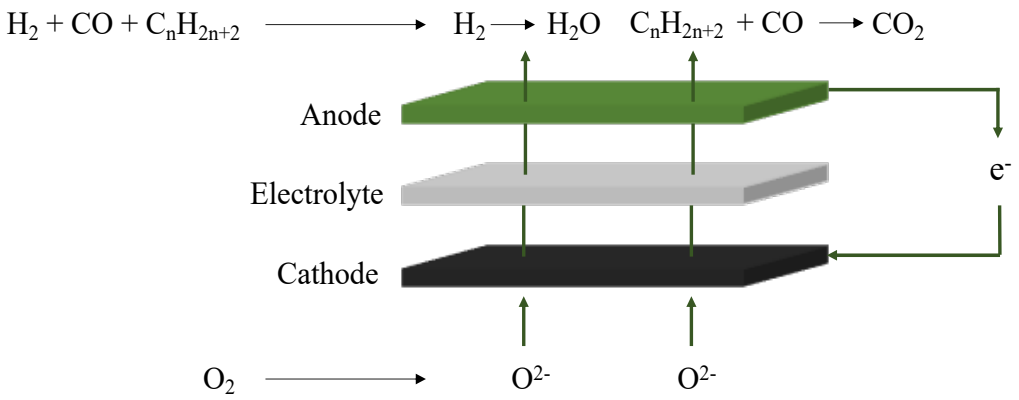


Figure 1.1. Illustration of the principle of a Solid Oxide Fuel Cell (SOFC).

Figure 1.1. shows the basic layout of a SOFC, which consists of two electrodes sandwiched over a hard ceramic zirconia electrolyte. At the cathode, oxygen is reduced to

generate oxide ions. The difference in oxygen potential across the cell drives the movement of the oxide ions through the electrolyte to maintain the overall charge balance. At the anode compartment, the fuel (H_2 or CO) is oxidized, where it interacts with oxygen to produce water or carbon dioxide. The generated electrons must be delivered back to the cathode in order for the redox reactions to be completed. Since the electrolyte is electrically insulating, the transport of electrons takes place across an external circuit, which is where the electrical power is obtained [44]. Each SOFC component performs multiple tasks, so each one has to meet to a number of specifications, including proper stability (chemical, phase, morphological, and dimensional), sufficient conductivity, chemical compatibility with other components, having similar thermal expansion coefficient to prevent cracking during cell operation, dense electrolyte layer to prohibit gas mixing, porous electrodes to allow gas transport to the reaction sites, high durability and strength properties, and ease of assembly [45, 46].

1.3.1. Thermodynamics of SOFC

Figure 1.1 shows the basic structure of a SOFC, which consists of two electrodes (the anode and cathode) separated by a solid electrolyte. Fuel is oxidized at the anode while oxidant is reduced at the cathode. The reduction of oxygen at the cathode is given as

$$O_2 + 4e^- \rightleftharpoons 2O^{2-} . \tag{1.1}$$

Fuels such as CH_4, CO, and H_2 can directly engage in the electrochemical processes, however it is more practical simply to use H_2 as a fuel [47]. Consequently, the following equation can be used to express the entire cell reaction (which creates the cell voltage together with high grade heat regarding the high operating temperature) as

$$2H_2 + 2O^{2-} \overset{K_{eq}}{\leftrightarrow} 2H_2O + 4e^-. \tag{1.2}$$

Voltage is the primary and most often seen signal when evaluating the electrochemical performance of fuel cell. The Nernst potential is the maximum potential that can be produced by a single cell under open circuit voltage, determined for a certain operating temperature and gas composition [48]. The following equation, also known as the Nernst equation, is expressed as the open-circuit voltage (the electromotive force (emf) or reversible (thermodynamic) voltage, *Er*), where *F* is the Faraday constant (96485 C/mol), *R* is the

universal gas constant (8.314 J/K.mol), T is the temperature in Kelvin, and P is the gas pressure in atm. The performance of the fuel cell when it is operating is characterized by cell voltage [49]. It is less than the theoretical or reversible thermodynamic cell voltage (1.23 V), which is determined by the Nernst Equation and can be seen at Figure 1.2 as

$$OCV = E_{H_2/O_2}^{OCV} = E_{H_2/O_2}^{0} - \frac{RT}{nF} ln \frac{P_{H_2O}}{P_{H_2}\sqrt{P_{O_2}}}, \quad (1.3)$$

where E_{H_2/O_2}^{0} is defined so the Nernst Potential (1.23 V for H_2 as fuel) at the standard state and equation is expressed as follows

$$E^0 = \frac{RT}{nF} lnK_{eq} . \quad (1.4)$$

The following equation is calculated for any fuel since E_r is equal to E^0 at the standard state

$$E^0 = -\frac{\Delta G^0}{nF} = -\frac{\Delta H^0 - T\Delta S^0}{nF}, \quad (1.5)$$

where n is the number of electrons involved in the process to convert a single fuel molecule, ΔH^0 is the standard enthalpy change, ΔS^0 is the standard entropy change, and ΔG^0 is the standard Gibbs free energy change of the combustion reaction of the fuel. Both electrical and thermal energy can be generated by the overall processes. For a fuel cell, maximum work from a fuel source is linked to the free energy of the reaction. ΔG is the largest amount of electrical energy accessible, while ΔH is the total amount of heat energy. A reversible fuel cell produces TΔS quantity of heat. Heat is generated by a fuel cell with a negative entropy change [32].

1.3.2. Kinetics

Even though a lot of research on SOFC electrodes has been published, the precise nature of the kinetics of reaction remains unknown. The following equations describe a straightforward kinetic model for both fuel oxidation at the anode and oxygen reduction at the cathode. Ionic conductivity is produced by the diffusion of oxide ions through the electrolyte as oxygen molecules reduced to oxide ions at the cathode. The reaction can be modelled as follows

$$O_2 + 4e^- \rightleftharpoons 2O^{2-}, \quad (1.6)$$

$$\frac{1}{2}O_2 + 2e^- + V_O^{\cdot\cdot} \rightleftharpoons O_O^x, \quad (1.7)$$

where $V_O^{\cdot\cdot}$ is a vacant oxide site and O_O^x is an oxide ion occupying a vacancy in sublattice.

The presence of oxygen and electrons, and oxide ion diffusion from the reaction site (cathode) to the electrolyte are the three fundamental prerequisites for the oxygen reduction reaction as shown by the equations above. In order to complete the circuit and preserve charge neutrality, the solid electrolyte material must have high ionic conductivity while the electrode must have high electrical conductivity. Additionally, the electrode material needs to be porous to allow air or fuel to pass through and out of the reaction sites. As a result, the reaction occurs at the triple phase boundary (TPB) where a gas, electrode and electrolyte materials meet [50, 51]. The oxide ions migrate through the electrolyte, emerge at the anode, and then interact with the fuel (H_2 or CO) as follows in below equations

$$H_2(g) \rightleftharpoons 2H_{ad,Ni}\,, \tag{1.8}$$

$$H_{ad,Ni} \rightleftharpoons H^+_{ad,Ni} + e^-\,, \tag{1.9}$$

$$H^+_{ad,Ni} + O^{2-}_{YSZ} \rightleftharpoons OH^-_{YSZ}\,, \tag{1.10}$$

$$H_{ad,Ni} + OH^-_{YSZ} \rightleftharpoons H_2O + e^-\,. \tag{1.11}$$

1.3.3. Overall Efficiency

The electrochemical efficiency (ε_E) and the heating efficiency (ε_H) are combined to form the SOFC's overall efficiency (ε_{FC}) [52]. The electrochemical efficiency is a result of the fuel cell's Faradaic or current efficiency (ε_J), voltage efficiency (ε_V), and thermodynamic efficiency (ε_T) as calculated at below equation as

$$\varepsilon_{FC} = \varepsilon_E\varepsilon_H = \varepsilon_T\varepsilon_V\varepsilon_J\varepsilon_H\,. \tag{1.12}$$

When the fuel is composed of electrochemically active species in addition to inert gases, impurities, and other combustibles, the heating efficiency must be taken into account. The definition of the heating efficiency, ε_H, is shown below equation as

$$\varepsilon_H = \frac{\Delta H^o}{\Delta H_{com}}\,, \tag{1.13}$$

where ΔH_{com} denotes the total enthalpy of all combustible species found in the fuel gases supplied to the cell, and ΔH^o represents the total amount of enthalpy of fuel species found in the fuel cell to create energy. The amount of energy released during the reaction of a fuel and

an oxidant is known as the thermal efficiency for an energy conversion system. So, the efficiency can be defined as

$$\varepsilon = \frac{useful\ output\ energy}{\Delta H}. \tag{1.14}$$

At normal temperature, hydrogen and oxygen may coexist as fuel and oxidant, but if they are heated up to 500 ˚C and under high pressure, they aggressively combust. In the existence of a flame, like in a heat engine, it is possible to induce the combustion reaction at temperatures lower than 500 ˚C. In a fuel cell, a catalyst can accelerate the rate of hydrogen and oxygen reaction with the presence of an electrolyte at temperatures below than 500 ˚C. Because the fuel and oxidant are properly separated in high temperature fuel cells, a non-combustible reaction can take place at temperatures above 500 ˚C. While the reaction in a fuel cell is electrochemical, that occurring in a heat engine is thermal. The basis for efficiency comparisons of these two systems is the difference between these two energy conversion processes. The free enthalpy changes of the cell, ΔG, can completely be transformed to electrical energy in a fuel cell [53]. If a fuel cell were to operate irreversibly, its optimal thermodynamic efficiency would be defined as

$$\varepsilon_T = \frac{\Delta G}{\Delta H} = 1 - \frac{T\Delta S}{\Delta H}. \tag{1.15}$$

Fuel cell efficiency is most frequently defined as the change in the standard free energy described in below equations as

$$H_2 + \frac{1}{2}O_2 \rightleftharpoons H_2O, \tag{1.16}$$

$$\Delta G^{\circ} = G^{\circ}_{H_2O} - G^{\circ}_{H_2} - \frac{1}{2}G^{\circ}_{O_2}. \tag{1.17}$$

When the water is in liquid form, the Hydrogen/Oxygen reaction has a chemical energy of 285.8 kJ/mol under standard conditions, and it has a free energy of 237.1 kJ/mol. As a result, an ideal fuel cell would have the following thermal efficiency as

$$\varepsilon = \frac{237.1}{285.8} = 0.83. \tag{1.18}$$

The ratio of the operating cell voltage under load to the equilibrium cell voltage is known as the voltage efficiency. The cell potential in a functioning SOFC is never greater than the reversible voltage. Due to a variety of losses, the cell voltage decreases as the fuel

cell current flows out. In addition to current density, other variables like as temperature, pressure, gas flow rate, combustion of gases, and cell material all affect the drop in cell voltage under current load [54]. The thermal efficiency of fuel cell can therefore be expressed in terms of cell voltage as

$$\varepsilon = \frac{useful\ output\ energy}{\Delta H} = \frac{useful\ output\ power}{\left(\frac{\Delta G}{0.83}\right)} = \frac{V_{cell} \cdot I}{\left(\frac{V_{ideal} \cdot I}{0.83}\right)} = \frac{V_{cell} \cdot 0.83}{V_{ideal}} . \quad (1.19)$$

Under normal circumstances, the ideal voltage for a reversible hydrogen and oxygen fuel cell is 1.229 V. As a result, the thermal efficiency of a cell operating at a voltage of V_{cell} is given by

$$\varepsilon = \frac{0.83 \cdot V_{cell}}{V_{ideal}} = \frac{0.83 \cdot V_{cell}}{1.229} = 0.675 \cdot V_{cell} . \quad (1.20)$$

Different current densities can be used to operate a fuel cell; the efficiency of the fuel cell is then determined by the matching cell voltage. The efficiency of a fuel cell is increased by raising cell voltage while decreasing current density. In reality, to get the optimum amount of power, the active cell area must be increased while the current density is lowered.

1.3.4. Voltage Losses (Polarization) in SOFCs

When a fuel cell is attached to a load in a closed circuit, electrochemical processes generate current, and internal non-reversible voltage losses lower the cell potential. The polarization or overpotential, represented as η, is the difference between the operating cell voltage and the estimated reversible voltage. The three forms of polarization that compose up a cell total polarization are charge transfer or activation polarization (η_{act}), diffusion or concentration polarization (η_{conc}), and resistance or ohmic polarization (η_{Ω}) [55]. The total overpotential is then defined as below equation

$$\eta = \eta_{act} + \eta_{conc} + \eta_{\Omega} . \quad (1.21)$$

The activation loss, which is prominent in the low current area, is the first of these main polarizations [56]. Reacting species must overcome an energy barrier during electrochemical reactions in the desired forward direction, such as reduction of oxygen gas at the cathode and oxidation of hydrogen at the anode. The activation energy barrier causes charge transfer polarization, or activation (η_{act}), as seen in Figure 1.2.

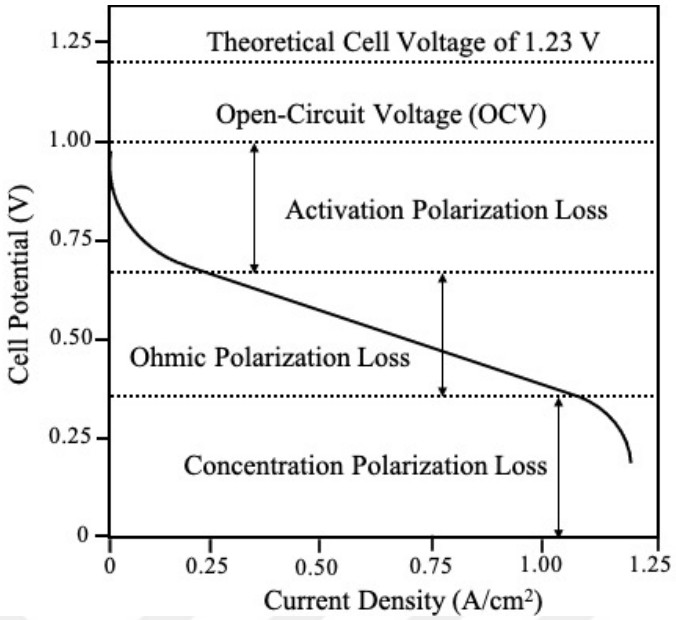


Figure 1.2. Cell potential as function of current density of a fuel cell.

The increase in current flow has a direct correlation with the activation loss. The following equation relates activation polarization loss to current density, *i*,

$$\eta_{act} = \frac{RT}{\alpha nF} ln\left(\frac{i}{i_0}\right), \tag{1.22}$$

where R is the ideal gas constant, T the temperature in Kelvin, η_{act} the activation polarization, α the charge transfer coefficient, n the number of electrons involved, F is the Faraday constant, i is the current density, and i_0 the exchange current density. At equilibrium, the exchange current density is linked to the forward and reverse electrode reaction rates. A powerful fuel cell performance is expected in the presence of a high exchange current density since this indicates high electrochemical reaction rate [57]. Ohmic loss arises due to contact resistances between cell parts as well as resistances to conducting ions through the electrolyte, electrons via the electrodes and current collectors [58]. The ohmic polarization, expressed as

$$\eta_{\Omega} = iR_i\ , \tag{1.23}$$

where R_i is the total ohmic cell resistance, which includes the ionic and electronic resistances.

Since the reactant gas is consumed via the electrochemical reaction, there will be a voltage decrease because of the reduction in the primary concentration of the reactant. As a result, a concentration gradient occurs. The concentration polarization, η_{conc}, is formed by

a number of cases. These include diffusion of reactants and products from the reaction sites and slow diffusion of the gas phase through the electrode pores.

Practically, the electrode reaction is slowed down by mass transport effects, that is, when the supply of reactant and/or the removal of reaction products from the electrode by diffusion is slower than that corresponding to the charging/discharging current (i), diffusion or concentration polarization (η_{conc}) becomes crucial [59]. The limiting current, i_L, is obtained when diffusion totally determines the electrode process. Diffusion or concentration polarization for an electrode process without any activation polarization can be represented as

$$\eta_{conc} = \frac{RT}{zF} ln\left(1 - \frac{i}{i_L}\right). \quad (1.24)$$

By subtracting these overpotentials from the Nernst potential, [49] the cell voltage can be calculated as

$$E_{cell} = E^0 - \eta_{act} - \eta_{conc} - \eta_{\Omega}. \quad (1.25)$$

The fuel cell electrical power output is determined by below equation as

$$W = E_{cell} \cdot i. \quad (1.26)$$

Although polarization cannot be completely prevented, it can be reduced by material selection and cell design. Cell polarization is naturally influenced by temperature, pressure, electrolyte and electrode materials, also the microstructure and design of electrodes. Also most critically, it is clear from the polarization curve that the cathode activation polarization causes the largest voltage loss in a SOFC. Due to the slow kinetics of the oxygen reduction reaction (ORR), the cathode experiences the biggest losses [56]. Therefore, to enhance the system's overall performance, it is essential to comprehend the cathode operations and its catalytic characteristics.

1.3.5. Current and Voltage Characteristics

Several thermodynamic and electrochemical factors, including temperature, pressure, gas concentration, reactant handling, and current density have an impact on fuel cell performance. These factors also directly affect the cell potential and voltage losses. The performance of the fuel cell and other system components can be positively or negatively affected by altering the operating settings. A change in operating circumstances may result

in a decrease in the cost of the cell while an increase in the cost of the supporting components [60]. To accommodate the desired application, the operational characteristics are typically compromised.

By running at optimum operating conditions, it is feasible to gain minimum system cost and accomplish a reasonable cell life. By identifying precise system requirements, such as power level, voltage, and current need, operating conditions are maximized. The power, voltage, and current requirements of the fuel cell stack and individual cells are calculated using this information as well as from life cycles. It is necessary to adjust an ideal cell operating conditions, as indicated in Figure 1.3, up until the system requirements are met.

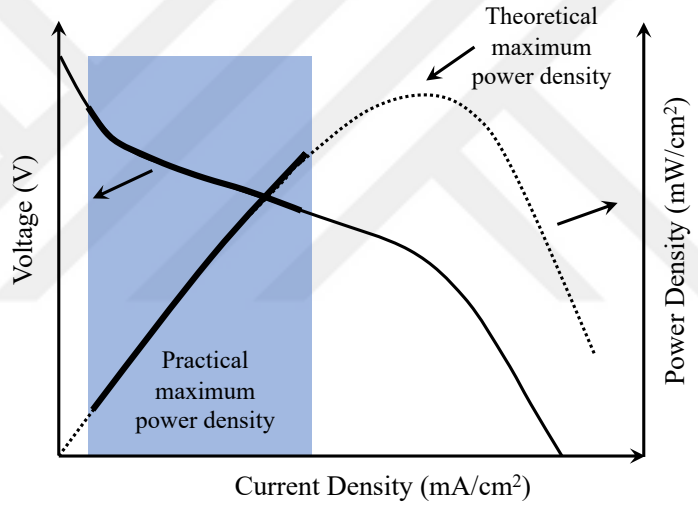


Figure 1.3. The Voltage - Current density and Power density relations for a fuel cell.

Figure 1.3 illustrates the relationship between power density output - current density as well as between voltage - current density. It is particularly interesting to develop fuel cells with greater operating current densities. Stationary power plant operations can benefit more from running at a lower current density but higher voltage. Designing a cell to function at its maximum power density, which peaks at a greater current density, is conventional. Higher power densities, however, will require lower cell voltages resulting in decreased cell efficiency. It is standard procedure to run the cell at a voltage range that produces an equilibrium between low functional lost, which is often close to the left side of the power density peak.

1.4. Experimental and Preparative Techniques

There are two primary groups of methods that are employed to identify an inorganic substance, depending on whether the material is molecular or non-molecular. Usually, a combination of chemical analysis and spectroscopic techniques is used to characterize the material, whether it would be in solid, liquid, or gaseous state [61]. Accordingly, mass spectroscopy provides details about the formula weight of the molecules and that of the subsequent molecular fragments. The functional groups that are present in the molecule—carboxylic acids, ketones, and alcohols—are revealed by IR spectroscopy. It is often feasible to determine how the molecules are pieced together through NMR spectroscopy.

Spectroscopy, microscopy, and diffraction are the three primary categories for the characterization of a crystalline solid material [62, 63]. When a material is crystalline and non-molecular, identification is often done using powder X-ray diffraction, or XRD, and, if necessary, chemical analysis. Every crystalline solid has a unique XRD pattern that can be used as a fingerprint to identify it [64]. A variety of methodologies are required to characterize the solids since the structure of materials on many different levels are interested in. For a solid to be properly identified, one must be aware of some criteria such as unit cell-based crystal structure, crystallographic defects, the structure of the material surface, structural variations between the surface and the bulk. A solid cannot be completely characterized by a single approach. Instead, a number of strategies are combined.

1.4.1. X-Ray Diffraction (XRD)

For more than a century, crystalline material structures have been determined using X-ray diffraction [65]. The electromagnetic radiation known as X-rays has a wavelength of ~1 Å (10^{-10} m). In Figure 1.4, simple black dots are used to illustrate an arranged set of atoms. Assume that the three waves of incident radiation are in phase (angle of incidence = θ) and an atom in the first lattice plane reflects one wave while another one in the second plane reflects the other. The two waves will be in phase only if the further distance travelled by the second wave is a multiple of the wavelength, $n\lambda$. By using straightforward trigonometry, equation can be determined as

$$2d\sin\theta = n\boldsymbol{\lambda}\ . \tag{1.27}$$

The Bragg's equation describes the correlation between the crystal's lattice spacings, *d*, and the wavelength, λ, of incoming X-ray radiation. The dimensions and form of the unit cell, as well as the quantity and arrangement of atoms within the cell, are the two primary elements that affect XRD patterns. Therefore, although having the same crystal structure, two materials will almost probably have different powder patterns. The d-spacing of the lines and intensities are consequently the two distinguishing characteristics of a powder XRD pattern. The d-spacing is the more practical and accurate measurement among of these two. The specifics of the crystal structure and the nature of the atoms determine the diffraction's intensity. An atom's number of electrons and position in the unit cell both affect how strongly it scatters X-rays [66].

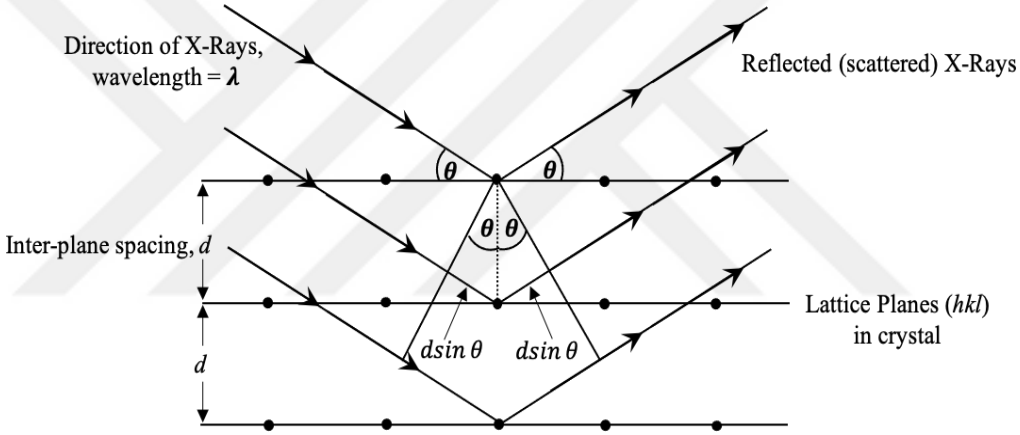


Figure 1.4. Schematic of XRD diffraction.

1.4.2. X-Ray Photoelectron Spectroscopy (XPS)

X-Ray Photoelectron Spectroscopy (XPS) is a surface sensitive spectroscopic technique for analyzing sample [67–70]. A sample is exposed to X-ray radiation in order to extract photoelectrons from inner-shell orbitals [71, 72]. Kinetic energy of these core-level electrons, E_k, is defined as the work function, ϕ, the electron binding energy, E_B, and the energy of the monochromatic X-rays, *hv*, as

$$E_B = hv - E_{kin} - \phi \,. \tag{1.28}$$

In an XPS experiment, a spectrum of emission intensity vs electron binding energy is formed. The method can distinguish between different elements on the surface because each have a distinct set of binding energies. The chemical composition of the surface and the

oxidation state o each element may also be quantitatively analyzed using XPS [73]. The peak area of a binding energy is proportional to the total number of atoms in a specified element [74–76].

1.4.3. Extended X-Ray Absorption Fine Structure (EXAFS)

To better comprehend metal oxides role as electrocatalysts in chemical processes, advanced strategies are needed. In order to investigate the geometric and local structures of materials, including ordered, disordered, and amorphous, X-Ray Absorption Spectroscopy (XAS) is a potential choice [77–80].

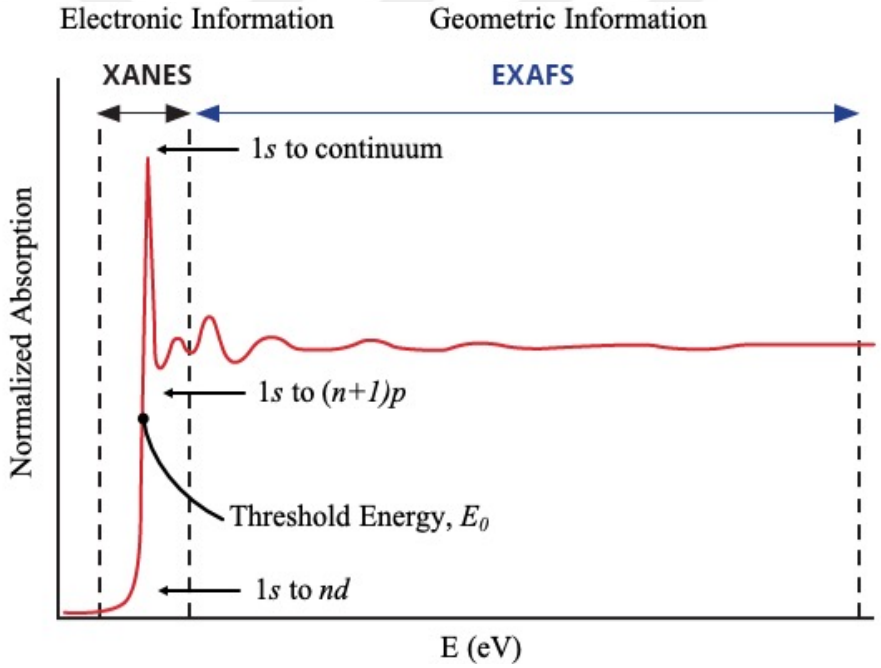


Figure 1.5. Schematic representation of the X-Ray absorption spectrum.

Figure 1.5 provides a schematic representation of the X-ray absorption spectrum. During XAS analysis, an electron is excited from a core level to an unoccupied valence and/or continuum state. The spectra are recorded as two distinct characteristics, XANES and EXAFS, depending on the energy of the incoming X-rays. According to the local geometry and vacant valence states, XANES is generated by the excitation of electrons from the core to empty valence states. By regulating the photon energies and relative intensities of XANES spectra, respectively, it is possible to investigate the oxidation states and local coordination surroundings of atoms in materials [81, 82]. The structural characteristics of materials, such

as the distance between nearby atoms and the environments of local coordination, are clearly displayed in EXAFS spectra [83].

1.4.4. Electrochemical Impedance Spectroscopy (EIS)

The kinetics and mechanics of electrochemical systems can be investigated using electrochemical impedance spectroscopy (EIS) [84]. The voltage is applied, and the system's current flow is recorded. A circuit element's capacity to limit the flow of electrical current is known as resistance. Resistance is defined by Ohm's law as the ratio of voltage V to current I (for an ideal resistor)

$$R = {}^{V}/_{I} . \tag{1.9}$$

In practice, circuit components behave in a far more complicated manner. Impedance becomes useful as a result. Impedance is a measurement of a circuit's capacity to inhibit the flow of electrical current, much like resistance. The Impedance is not restricted by the ideal resistance's simplification, such as the voltage and current in phase and frequency independence. AC impedance is a broader definition of resistance. The frequency influences both its modulus and phase [85]. Typically, an electrochemical cell is given an AC potential (sinusoidal) and the current flowing through the cell is monitored to determine the electrochemical impedance. The answer to this signal is an alternating current signal that contains the excitation frequency and its harmonics. The excitation signal is represented as a function of time so

$$V(t) = V_0 \cos(\omega t) , \tag{1.30}$$

where V_0 is the signal's amplitude, $V(t)$ represents the potential at time t, and ω is the radial frequency [86]. Radial frequency, ω (rad.s^{-1}) and frequency f (Hz) have the following relation

$$\omega = 2\pi f , \tag{1.31}$$

and the response signal, $I(t)$, in a linear system, is phase-shifted (ϕ), and its amplitude, I_o, differs in below equation

$$I(t) = I_0 \cos(\omega t - \phi), \tag{1.32}$$

subsequent expression to use Ohm's Law to determine impedance given in Figure 1.6 as

$$Z(\omega) = \frac{V(t)}{I(t)} = \frac{V_0 \cos(\omega t)}{I_0 \cos(\omega t - \phi)} = Z_0 = \frac{\cos(\omega t)}{\cos(\omega t - \phi)} . \tag{1.33}$$

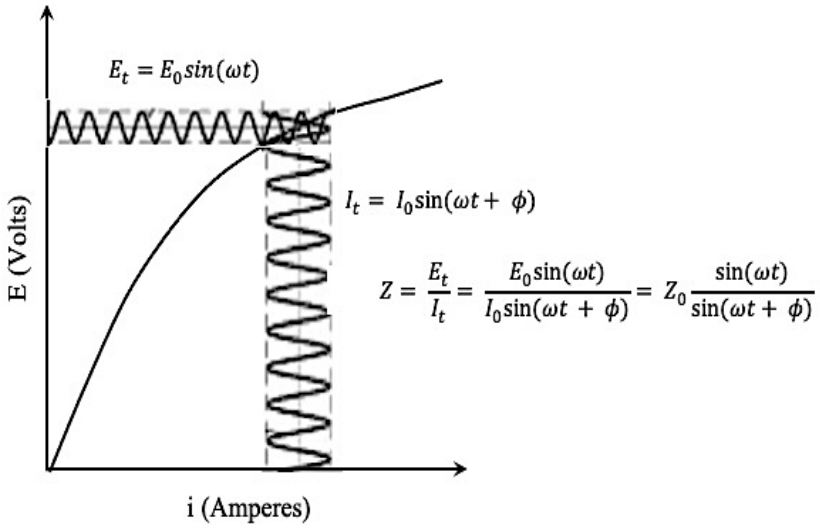


Figure 1.6. AC impedance of a SOFC unit under small amplitude perturbations.

The impedance could be expressed as a complex function using Euler's relationship as below equation

$$exp\,(j\phi) = cos\,\phi + j\,sin\,\phi\,, \tag{1.34}$$

and both following equations are used to explain the potential and the current response

$$V(t) = V_0 exp(j\omega t)\,, \tag{1.35}$$

$$I(t) = I_0 exp(j\omega t - j\phi), \tag{1.36}$$

besides the resulting expression, the impedance is thus represented as a complex number and describes the real and imaginary parts of the formula for *Z(ω)* [57]

$$Z(\omega) = {}^{V(t)}\!/_{I(t)} = Z_0 exp(j\phi) = Z_0(cos\,\phi + j\,sin\,\phi) = Z_0(Z_{real}(\omega) + jZ_{imag}(\omega)). \tag{1.37}$$

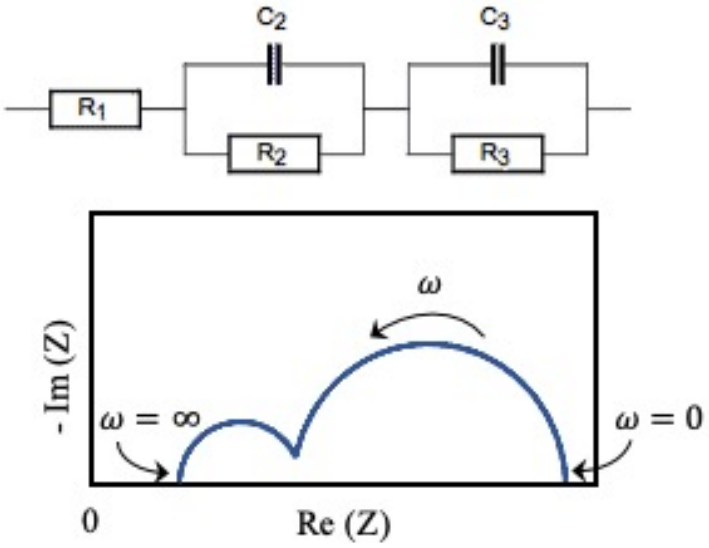


Figure 1.7. Nyquist diagram of impedance Z and related equivalent circuit.

A Nyquist Plot, as in Figure 1.7, is generated by plotting the real component on the X-axis and the imaginary part on the Y-axis. Bode Plot is another representation. Log frequency on the X-axis, absolute impedance, $Z(\omega)$, and phase-shift on the Y-axis are used to illustrate the impedance. Potential and current are the output and input of an electrochemical cell connected to a potentiostat, respectively. In a typical EIS, the cell receives a small AC signal between 1 to 50mV [84].

1.4.4.1. Equivalent Circuit Elements. EIS is an effective technique and instrument for analyzing electrochemical system's performance and for examining the overpotential – polarization – processes in SOFCs [87]. Due to the fact that the frequency responses of the polarization losses differ, this information is used to explain electrochemical mechanisms and characterize the various electrode materials' performances as well as their ion conducting capabilities. The EIS response is produced when a sinusoidal AC voltage or current is applied over a DC bias for various frequency ranges. The sizes and forms of the plots that were produced indicate important details about the operating parameters, the microstructure of the materials used, and its compositions. To fully understand the collected impedance data, suitable modelling illustrations of the systems are designed [88]. Once the spectra have been fitted by the developed equivalent circuit model, the parameters of the impedance can be determined. These models show the system's properties in terms of their physical or chemical meaning, which is helpful in providing an overview on the system. The ideal impedance spectra have an arc for each process. However, because of their capacitive nature allows very little time to relax during a shift in boundary conditions, overlapping arcs are generated in the EIS spectra. The EIS generally exhibits inductive or capacitive impedance at high and low frequencies [87].

EIS data can be analyzed in detail by model fitting to an equivalent circuit including a set of components such as resistors, capacitors and inductors [89]. This method of modelling offers good comparisons of overall performance, however typically lacks accurate explanation of the reasons for the polarization losses because of the overlapping of the arcs. The elements used in the equivalent circuits are given in Table 1.2.

Resistance consists of only real part in the impedance spectra and it is not dependent on the frequency. Several electrochemical reactions employ resistance in two different

forms. Initially, the ohmic resistance is the difference in potential between the reference and working electrodes. The conductivity of the electrolyte material and the electrode's shape affect the ohmic resistance. The ohmic resistance, R_{Ω}, is determined by the point where the real axis and the impedance arc intersects at the high frequency end on the Nyquist plot [1]. Furthermore, when the voltage difference is greater than the open circuit potential, the electrode becomes polarized. Due to surface reactions, the polarized electrode generates a current flow. The reaction kinetics and reactant diffusion both toward and away directions from the electrode regulate the amount of current.

Table 1.2. Equivalent Circuit Elements Used in Modelling.

Equivalent Element	Admittance	Impedance
R	$1/R$	R
L	$1/j\omega L$	$j\omega L$
C	$j\omega C$	$1/j\omega C$
Q (CPE)	$Y_0(j\omega)^{\alpha}$	$1/Y_0(j\omega)^{\alpha}$
W (Warburg)	$Y_0\sqrt{j\omega}$	$1/Y_0\sqrt{j\omega}$
G (Gerischer)	$1/Y_0\sqrt{(k\ +\ j\omega)}$	$Y_0\sqrt{(k\ +\ j\omega)}$

Capacitance, *C*, has an imaginary component and depends on the frequency. Its impedance and frequency have an inversely proportional relationship. Current and voltage are 90 degrees out of phase. On the interface between an electrode and the electrolyte, an electrical double layer exists [90]. This double layer is developed as ions attached to the electrode surface. The charged ions are separated from the charged electrode. This separation is often only a few angstroms. These separated charges form a capacitor. Numerous factors affect the double layer capacitance, including temperature, concentration and types of ions, electrode voltage and roughness, adsorption of impurities. Modeling with an ideal capacitor makes a wrong assumption that the electrode surface is homogeneous. The constant phase element, CPE, is represented by *Q* that models this lack of homogeneity, CPE = $1/[Y_0(j\omega)^n]$,

where Y_0 represents admission of the ideal capacitance and n represents an empirical constant (0-1). Additionally, CPE behaves as a pure capacitor when n value is equal to 1 and as a pure resistor when $n = 0$ [91]. Due to the adsorption of reactants on the surface of the cell, the impedance of an electrochemical cell can appear to be inductive, and this phenomenon is described as an inductance. This behavior can also result from inductance in cell cables, uneven distribution of current and weak response of reference electrode [92].

Electrochemical systems frequently exhibit ion diffusion at interfaces, which represented using the Warburg element. $Z_w = 1/[Y_0(j\omega)^{0.5}]$ is the impedance for a semi-infinite-diffusion layer, where Y_0 is the diffusion admittance. 45° phase angle is produced by Warburg element, which can be described as having equal imaginary and real inputs [92]. The circuit's Gerischer element was originated from the chemical processes occurring in the bulk. It appears to be an element of thin layer diffusion one the Nyquist plot [93].

1.4.4.2. Analysis of the EIS Using the Distribution of Relaxation Times (DRT). For the measurement of polarization resistances in electrochemical devices such as fuel cells and batteries, electrochemical impedance spectroscopy (EIS) is frequently utilized. Also, it is currently the best in-situ approach for evaluating and determining performance barriers for the cell under testing. Usually, a sinusoidal signal is applied across a certain range of frequencies to measure the system response. Since each single electrochemical process has a unique kinetics, this enables them to categorize in certain frequency domain, and their identification is made easier by the use of equivalent circuit model fitting.

A single set of impedance spectra data might be effectively suited to many equivalent circuit models, leading to the provision of unique physical significance. However, the process of developing an equivalent circuit model for fitting the impedance spectra is frequently subjective and is dependent on one's opinion and careful reasoning. Since numerous equivalent circuit models (ECM) can fit the same impedance data and each ECM contains some prior assumptions, a conventional investigation of EIS using ECM fitting may be ineffective and yield no helpful results.

The distribution of relaxation times (DRT) can be used as an option in this situation [94]. DRT is a valuable technique for deconvoluting different relaxation processes of an

electrochemical system with great precision, and it helps identify certain elementary processes according to different time constants [95]. Therefore, after examining the numerous electrochemical processes taking place in the system, the performance or rate-limiting steps can be successfully identified and properly repaired. In addition, a clear description of several fundamental electrochemical processes could help in the logical development of a proper fitting model to quantify the important parameters.

For the polarization resistance, the DRT analysis recommends a number of resistance-capacitance (RC) components as well as suitable resistance (R) and time constant (t) values. Total impedance (Z(ω)) is regarded for the DRT analysis as an equivalent circuit made up of ohmic and polarization resistances with a limitless number of RC components in the series as demonstrated in Figure 1.8 [96].

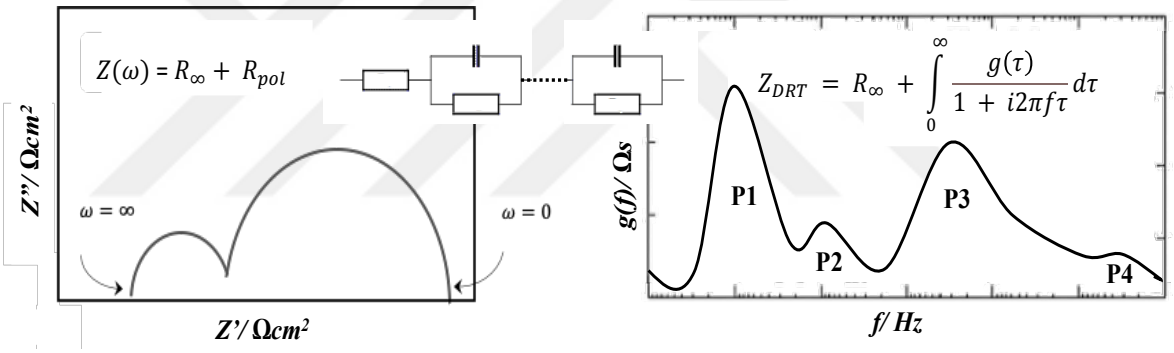


Figure 1.8. Impedance spectra and the corresponding DRT plot.

Finding the usual distribution of EIS frequencies is the primary objective of DRT. To achieve that, a model that is derived from the below equation is fitted against experimental data taken at certain frequencies

$$Z_{DRT} = R_\infty + \int_0^\infty \frac{g(\tau)}{1 + i2\pi f\tau} d\tau \,. \tag{1.38}$$

The $g(\tau)$ is an appropriate function that defines the time-dependent relaxation properties of the investigated electrochemical system, and R_∞ is the ohmic resistance. An equivalent RC circuit can be thought of as the formula in above equation. In other words, an endless sequence of parallel resistors and capacitors are added to an Ohmic resistance to provide the DRT model's impedance.

1.4.5. Tape Casting

For manufacturing of thin, flat layers of SOFC components with thicknesses ranging from 10 to 500 μm, tape casting offers an affordable, reliable, straightforward and quick structuring technique [53]. If it is desired to co-sinter the multilayers in a single step, green layers can be simply superimposed. The preparation of the slurry from the powder, which has been previously synthesized, calcined, and ultimately sieved to achieve the proper phase composition, morphology and grain size distribution, is the first and most crucial stage in the entire process [97]. To create the slurry, organic and/or inorganic ingredients are mixed with the powder. The slurry is then combined and primarily ball-milled to assure homogeneity and agglomeration removal. Afterward, the solution is de-aired under a primary vacuum based on the desired amount of porosity or density. The green tape's thickness is determined by the height of the doctor blade, and the slurry is then prepared for casting.

The tape casting process necessities careful consideration at every stage. Each step must be properly carried out in order to avoid deformation, any fracture, delamination or mechanical problem. Preparing tape casting slurry for the co-sintering step is the first phase in the procedure. The components of the slurry include ceramic powder, binder (Polyvinyl butyral), plasticizer (Polyethylene glycol and Benzyl Butyl Phthalate), and solvent (ethanol and toluene) [98]. The composition, dispersion and homogeneity of the starting powders in the slurry determines the sintering behavior of green tapes and therefore their ultimate microstructure. As a general rule, the higher the solid/liquid ratio, the denser the green tape will be, and as a result, the denser the sintered tape will be. After drying, the green tape still contains all of the organic ingredients. They produce pores during the sintering process because they are eliminated when heated to high temperatures in air between 300 to 700 ^{o}C. In order to customize the final microstructure and density, the ratio of powder to the organics, and therefore the final slurry formulation, must be fine-tuned. The ratio of powder to organic phases can regulate the control of a 1-2 μm size in porosity, which can be quite helpful for improving the number of triple phase boundaries [99].

1.5. Solid Oxide Fuel Cell Materials

1.5.1. Anode

The role of anode or fuel is to make it easier for the fuel to be oxidized and for electrons to be transported from the reaction area to the current collector. When choosing a material for the anode material, some qualities such as electrical, structural and electrochemical must be taken into account. Anode material choice is severely constrained by the high temperature and reducing environment, that is must function in, and it has unique difficulties with respect to chemical stability and material deterioration [100]. The following basic specifications for anode materials should be met in order to reduce the polarization losses of the oxidation reaction: high electrocatalytic activity for fuel gas oxidation, high electrical conductivity, chemical compatibility with other cell compartments and thermal expansion coefficient, porous structure to enable quick transport of fuel gas and reaction byproducts, flexible fuel, simple manufacture, affordable, and lastly high resistance to sulfur poisoning and carbon deposition when utilizing hydrocarbons [101–103].

Traditionally, metals such as Pt, Fe, and Ni were employed as the anode and cathode materials. Ni had been utilized as an anode material for many years due to its affordable cost, chemical stability, and great catalytic activity to fuel oxidation. However, pure Ni has a significant thermal expansion coefficient mismatch with frequently used electrolyte material, YSZ, which weakens the contact between the two materials. Metal oxides and cermets, or ceramic-metallic composites, such as Ni-YSZ, have been developed and they have the additional benefit of larger triple phase boundaries. Because most of the fundamental criteria for SOFC anodes were met, the discovery of Ni-YSZ anodes represented a significant advancement. Additionally, Ni-YSZ improves SOFC efficiency overall due to its strong electrical conductivity, good ionic conductivity, and effective fuel oxidation catalytic activity [104].

1.5.2. Electrolyte

An electrolyte in SOFC unit, which transports oxide ions from the cathode to the anode where they combine with fuel, completes the whole electrochemical reaction. Oxygen

vacancy hopping is a thermally triggered mechanism that allows for oxide ion conductivity. The most popular SOFC electrolyte material right now is YSZ (Yttria-stabilized zirconia). In both reducing and oxidizing environments, YSZ is an electrically insulating material. It has lattice imperfections known as oxygen vacancies. Oxygen vacancies allow oxide ions to diffuse through the electrolyte, leading to a comparatively high oxide ion conductivity [105, 106]. An alternate oxide ionic conductor that has received considerable attention in the field of SOFC is Ceria doped with gadolinium (GDC). Although this material has a significantly greater ionic conductivity than YSZ, it exhibits an electrical conductivity in reducing atmospheres at working temperatures, which results in short cut [107]. For an electrolyte to function effectively, the following conditions must be met: low electrical conductivity, chemical and thermodynamically stable, and sufficient oxide ion conductivity [108].

1.5.3. Cathode

The word electrocatalysis is a combination of two significant physical chemistry subdisciplines, namely electrochemistry and catalysis. In order for a charge transfer to take place in electrochemistry, electrons and charged chemical species must pass over a certain electrochemical potential barrier [109]. Catalysis is the process whereby the involvement of a second material known as a catalyst causes a reaction to proceed more quickly. A catalyst, in contrast to other reagents in the chemical process, is not consumed by the reaction. An electrode material that interacts with certain species during a Faradaic reaction while remaining unmodified is called an electrocatalyst. Due to the heterogeneity of electrode reactions, electrocatalysts are typically heterogeneous catalysts as well [110]. As a result, an electrocatalytic reaction is typically a multistep reaction that includes numerous reactants (both charged and uncharged), as well as a variety of reaction phases (such as gas and solid phase). Usually, it involves many steps, including a charge transfer reaction, surface (or bulk) diffusion, and a series of adsorption reactions [65]. If both the gas and the solid phase participate, the gas phase reactants must first adsorb on the solid surface, followed by an electron transfer reaction or other dissociation process. On the surface, this will produce some neutral or charged intermediate species. These intermediates might subsequently be carried to the reactive sites either on the solid surface or by entering the bulk lattice. In any case, they will eventually reach certain active sites where the crucial phase of the entire reaction—for instance, the charge transfer reaction—would occur. Depending on the kind of

material and the type of reactions taking place, these active sites may be found at the intersection of three phases [111]. Therefore, before investigating a particular electrocatalytic process, the materials must be specified.

The following capabilities of the cathode are necessary for the SOFC to operate effectively: High electrical conductivity ideally more than 100 S/cm in an oxidizing environment; minimum difference between the cathode's thermal expansion coefficient values and those of the cell's materials like electrolyte; good chemical compatibility between the cell compartments; high oxide ion conductivity; enough porosity to enable fast migration of O_2 gas from cathode to electrolyte interface; good stability under an oxidizing environment; oxygen reduction reaction with high catalytic activity. Recognizing the oxygen transport mechanisms in different cathode samples; developing new compositions and microstructures; examining structure and performance relations; analyzing the effect of temperature, cycle, polarization, testing conditions and impurities; generating sophisticated manufacturing processes are the most crucial issues in the field of cathode catalyst research [112–114].

1.5.3.1. Oxygen Reduction Reaction. The molecular oxygen flows and is adsorbed onto the porous cathode surface, where it is reduced to oxide ions by accepting electrons from current collector. Oxygen reduction reactions can take place either on the electrode – gas interface or somewhere close to the electrode – electrolyte – gas contact, depending on the characteristics of the cathode material [115]. Following that, the totally or partially reduced oxide ions or atomic species are transferred by bulk or surface channels to the electrolyte/electrode/gas contact, where the entire reduction takes place.

The fuel is oxidized as a result of subsequent passage of oxide ions to the anode (through diffusion via a dense electrolyte) described as

$$O_2\,(gas) + 4e^-(cathode) \rightleftharpoons 2O^{2-}\,(electrolyte), \tag{1.39}$$

however, on a more fundamental level, this reaction is extremely complex and includes several simple processes including diffusion, adsorption, dissociation, ionization, and eventually the integration of oxygen into the electrolyte crystal lattice. The overall steps in oxygen reduction reaction are shown in below equations, which includes six distinct stages

$$O_{2,gas} \rightleftharpoons O_{2,ads}\,, \tag{1.40}$$

$$O_{2,ads} \rightleftharpoons 2O_{ads}\,, \tag{1.41}$$

$$O_{ads} + e^- \rightleftharpoons O_{ads}^-\,, \tag{1.42}$$

$$O_{ads}^- + e^- \rightleftharpoons O_{ads}^{2-}\,, \tag{1.43}$$

$$O_{ads}^{2-} + V_{\ddot{O}} \rightleftharpoons O_O^X\,, \tag{1.44}$$

$$O_{O,cathode}^X \rightleftharpoons O_{O,electrolyte}^X\,. \tag{1.45}$$

The first step is the adsorption of oxygen gas on the cathode surface. The second one is a representation of the dissociation of oxygen molecules. The reduction of oxygen atoms by taking an electron is the third process. The fourth step is carried out by the partly reduced oxygen atoms having another electron. The fifth step is denoted by the formula $O_{ads}^{2-} + V_{\ddot{O}} \rightleftharpoons O_O^X$,which combines adsorbed oxide ions with the lattice oxygen vacancies. The sixth step shows the movement of oxide ions across the electrolyte-electrode contact. In general, not all of the aforementioned processes—some of which are too quick to be observable—will be the rate-determining steps. The unique frequency of each sub-reaction varies, but it may also be close, which causes the peaks to occasionally overlap [50]. The surface path and the bulk path are the two main types of reaction processes. When O_2 molecules from the gas phase follow the surface path, they adsorb on the surface and diffuse to a location known as the "three phase boundary" (TPB), which brings the electrode, electrolyte, and gas phase into contact. At these electrochemically active locations, oxygen passes through as O^{2-} ions into electrolyte vacancies. When using a pure electronic conductor as the electrode material, such as platinum, the surface route is the only option. An alternate reaction route is however made feasible if the electrode material is an oxide ion conductor.

In this instance, oxygen incorporation is not limited to the TPB regions and can take place throughout the whole electrode surface. The integrated O^{2-} ions subsequently permeate through the bulk of the electrode in the direction of the electrode/electrolyte interface, where they undergo ion transfer. If the electrode material has high ionic conductivity, the surface path may be insignificant but is obviously not eliminated for mixed conducting electrode materials [116, 117].

1.5.3.2. State-of-the-art Cathode Materials. The LSM ($La_{1-x}Sr_xMnO_{3-\partial}$)/YSZ cathode has established itself as a dependable, long-lasting, and technologically compatible component

of SOFCs. It is still effective enough at temperatures higher than 850 ºC. The operating temperature must be lowered to enable the use of less expensive interconnect materials and to lessen degradation issues in order for SOFC to be economically feasible. As a result, there is a demand for efficient novel materials that exhibit low polarization resistance, or R_P, at low temperatures. LSC ($La_{1-x}Sr_xCoO_{3-\partial}$), a member of the group of oxides known as mixed ionic and electronic conductors (MIECs), is one of the most promising candidates [118–120].

It has been demonstrated that this substance has excellent electrocatalytic activity for oxygen reduction. Due to the apparent low activation energy of R_P, the electro-catalytic capabilities appear promising and are also maintained at low T. The high mixed conducting qualities are one factor in the high activity because they allow the reaction zone to extend beyond the triple phase boundary regions and activate a greater portion of the accessible surface area. Other issues with this material include a high thermal expansion coefficient, strong reactivity to YSZ, and thermal instability. Cobalt has been partially replaced with iron in $La_{0.6}Sr_{0.4}Co_{0.2}Fe_{0.8}O_{3-\partial}$ (LSCF) to prevent a TEC mismatch with the other cell compartments [121]. In general, LSCF is thought to be the best material for the next low temperature SOFCs. The perovskite BSCF ($Ba_{0.5}Sr_{0.5}Co_{0.8}Fe_{0.2}O_{3-\partial}$) has demonstrated to have even superior cathode performance, but it has also been shown that this material is rather unstable [122].

1.5.3.3. Perovskite Materials. Perovskite oxides have attracted significant interest over the last few decades and even up to this point due to their catalytic, ionic, combined ionic-electronic, and ionic transport capabilities [123, 124]. The term "perovskite" refers to mixed oxides that have the idealized ABO_3 crystal structure formula seen in Fig. 1.9, where the total positive valence of the A and B cations is equal to 6 (the total negative charge of the oxide ions), which is represented by $A^{2+}B^{4+}O_3$ or $A^{1+}B^{5+}O_3$ or $A^{3+}B^{3+}O_3$. Perovskite often appears as $ABO_{3-\partial}$, where ∂ represents the oxygen anion deficit or excess depending on the total amount of valence of the A and B-site cations. The actual charge of the oxide ions in transition metal oxides is shown to be different from the formal "2-" charge. The perovskite crystals are often stated with a stoichiometric formula of $ABO_{3-\delta}$ for oxide electro-neutrality and charge compensation. Because each type of element has a distinct requirement for the ionic radius, various types of elements are present in the A and B-sites of the crystal. The

size of the A-site cation is typically bigger (~1.10 Å), whereas the size of the B-site cation is around 0.621 Å, with 12 oxygen anions surrounding the A-site cation and 6 oxygen anions surrounding the B-site cation, respectively [125].

While the B-site is mostly made up of smaller transition metal ions in a six-fold coordination with oxygen, the A-site cation is often comprised of alkaline earth, alkaline, and lanthanide ions in a twelve-fold coordination. The molecular orbital diagram for ABO_3 crystal structure with no π bonding was displayed in Figure 1.10. Molecular orbital (MO) diagram is employed to express energy levels of atomic and molecular orbitals. By developing MO diagram for perovskite structure, many different chemical and physical properties of materials such as reactivity, electrical/ionic conductivity, catalytic activity, optical and magnetic characteristics. In Figure 1.10, the energy levels of orbitals of six oxygen atoms in the center and A, Co on the left, and B, La on the right, cations are displayed. Interactions as 12-fold coordination between La and oxygen, and 6-fold coordination between Co and oxygen are built with overlapping of symmetrically appropriate atomic orbitals. When all the electrons in the system are placed on MO diagram, highest occupied molecular orbital (HOMO) level is assigned to t_{2g} energy level of Co, B-site metal. This elaborates the catalytic activity in ORR, due to occupied HOMO level with electrons. Also, the electrical/ionic conductivity of perovskite structure is related to this energy levels in MO diagram, since lowest unoccupied molecular orbital (LUMO) can be on both A and B site metal orbital overlapping with oxygen. Most likely LUMO resides on Co in this structure due to low ionization energy of 3d orbital as e_g*.

The goal of this thesis is to provide an overview on our knowledge of the processes on the surface/bulk interactions and ORR kinetics, as well as methods for adjusting the bulk and surface of the cathode to maximize cathode stability and efficiency. Perovskites have quite different compositions in their bulk/surface; the distortion of the perovskite structure in a particular direction is thought to be the cause of the improvement of crystal properties. Besides, surface atoms on perovskites often have greater free energies and lower coordination numbers than bulk atoms. This causes surface atoms to be reorganized and separated certain cations from the bulk to the surface (Figure 1.9b). Also, it is well known that perovskites exhibit great flexibility when doped with different cations at either the A or B-sites. The mismatch in ionic sizes of the dopants (Sr^{2+}, ionic radius 1.44 Å), and hosts

(La^{3+}, 1.36 Å) can cause an increase in lattice elastic energy and serve as the thermodynamic driving force for mobility of oxygen ions. The oxygen ions must pass through a trigonal planar phase formed by two A-site and one B-site ion, while the large space around an A_2B triangle phase facilitates easy oxygen-ion migration. "Saddle point" is one way to describe this surrounding area.

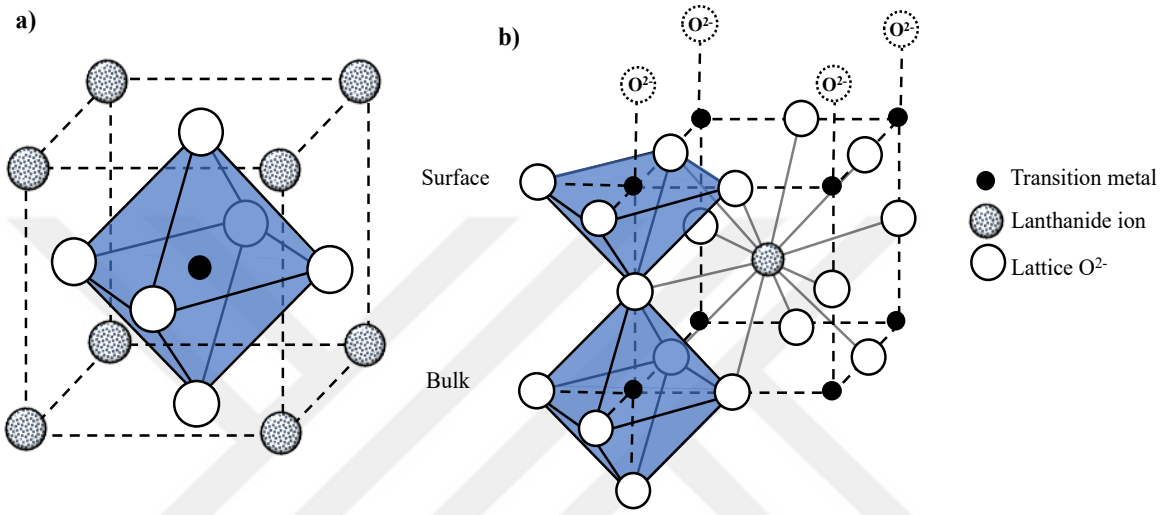


Figure 1.9. (a) Perovskite unit cell (b) the anions on the edges, the B-cations in the corners, and the A-cation in the center.

Furthermore, the majority of A-site cations are redox inactive and do not directly contribute to ORR, in which these cations are crucial for defining the long-term stability and cathode performance. For instance, due to large ionic size, A-site cations can alter the overall oxidation state of B-site cations by influencing the lattice spacing for B-site cations, which often reside within voids generated by A-site cations. In fact, it can be possible to improve cathode catalytic activity and stability by rationally modifying perovskite oxide properties by A-site doping. In this study, both V and Gd doping for A-site in perovskite structure are analyzed for SOFC cathode material for ORR catalytic activity and mixed electrical/ionic conductivity. The perfect simple perovskite crystal can be thought of as a cubic close-packed structure with layers of oxygen and A-cations placed closely together along the cubic direction. B-site cations are present in some of the resultant octahedral holes. Perovskite may alternatively be seen as a framework similar to ReO_3 with cubic $Pm\bar{3}m$ space group, made up of corner-sharing BO_6 octahedra with A-site ions positioned in twelve-coordinate interstices [124]. The most crucial need for a stable cubic perovskite phase structure was discovered to be the presence of a stable BO_3 skeleton [126]. When the B-site ion radius is

greater than 0.51 Å, stable octahedral coordination inside the perovskite crystals is effective structurally. Additionally, eight BO_6 octahedral positions at which large A-site cations are coordinated can further stabilize the BO_3 structural sub-lattice.

The BO_6 crystalline sub-lattice may deviate from the ideal cubic illustration in the existence of small or large A-cations. The A-site cation radius typically has a lower limit of 0.9 Å. If this distortion is excessive, different crystal geometries like orthorhombic or rhombohedral are preferred. The tolerance factor defines the maximum A and B-site cation size that may be allowed to preserve a certain structure as follows

$$t = \frac{(r_A + r_O)}{\sqrt{2}\,(r_B + r_O)}, \tag{1.46}$$

where the radii of the A-site, B-site cations, and the oxygen anion are denoted by r_A, r_B and r_O, respectively. In perovskite oxides, t equal 1 indicates the ideal cubic structure, but its variation from 1 denotes an imbalance between the equilibrium A-O and B-O bond lengths [127]. In practice, the perovskite structure can exist over a fairly large tolerance range with t values between 0.75 and 1. The orthorhombic distortion occurs when the tolerance factor is greater than 0.75 but less than 0.9. The A-cations in this instance are shifted along pseudo-cubic directions. If the crystal lattice has a tolerance factor, t between 0.9 and 1.0, a slight deformation from cubic to rhombohedral symmetry may occur. The cubic structure building is estimated using the Goldschmidt tolerance factor. The A-site cation contacts the B-site cation and vice versa in a perfect packing, which is the basis for the calculation of the Goldschmidt factor [128].

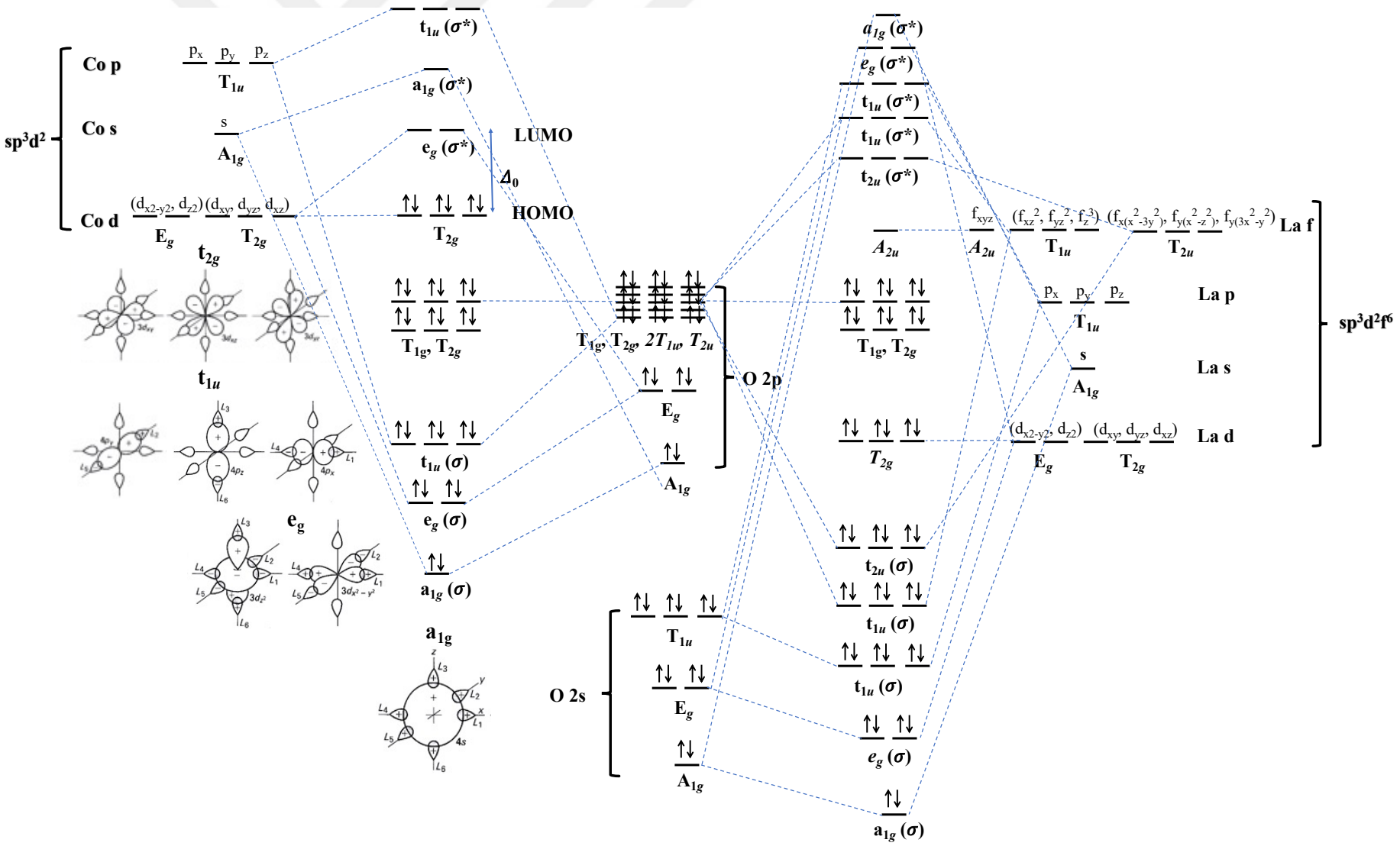


Figure 1.10. Molecular orbital diagram for an ABO_3 perovskite crystal structure.

The electrical neutrality, that is the sum of valences of A and B-site cations must be equal to the total charge of oxygen anions, is another need that must be satisfied for the perovskite in addition to the radius of the cations. Therefore, doping the perovskite structure with various cations of different ionic radius and valence makes it feasible to partially substitute A and B-site cations. Non-stoichiometry phenomenon in perovskite is now quite prevalent and can result from cation deficiency due to the tolerance of the structure to changes in its compositional elements [129].

Oxygen vacancies are more prevalent in perovskite with cation deficiencies. With regard to oxygen ionic conduction, oxygen vacancies are especially crucial. At the high and low oxygen pressure sides, oxygen gas is introduced into and expelled from the lattice. If there is an imbalance in the oxygen composition, the oxygen anions are allowed to be moved arbitrarily inside the crystal through a hopping mechanism as demonstrated in Figure 1.11. This is only possible when the oxygen anions have enough thermal energy to get over the activation needed to go from one lattice site to another, which is satisfied at high temperatures [125].

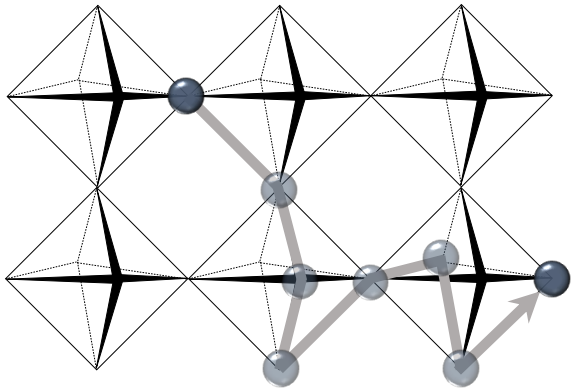


Figure 1.11. Bulk oxygen transport process.

By replacing ions with comparable size but differing valence, the oxygen vacancy concentration can be changed. For instance, the partial replacement of certain A^{3+} ions by Sr^{2+} in $A_{1-x}Sr_xBO_{3-\partial}$ can result in the formation of oxygen vacancies in the crystal structure. Charge neutrality is preserved when the B-cations choose a mixed-valence state due to the development of oxygen vacancies as well as a shift in the valence state of the B-site cations. Due to their high oxygen vacancy concentration and aliovalent state, oxide crystals can exhibit high electrical and ionic conductivity [130]. By doping a multivalent metal for B-

site, such as Fe or Mn, the oxygen vacancy concentration can also be raised. Electrical neutrality is only preserved by the formation of oxygen vacancies if the B-site valence state is kept stable. The perovskite oxides may exhibit ionic conductivity to a greater extent in this situation [131].

The following expression demonstrates how the electrical conductivity in the structure is achieved by B-site metal ions through overlapping B-O-B bonds

$$B^{m+} - O^{2-} - B^{(m+1)+} \rightarrow B^{(m+1)+} - O^{-} - B^{(m+1)+} \rightarrow B^{(m+1)+} - O^{2-} - B^{m+} . \quad (1.47)$$

Oxygen vacancies are known to facilitate oxygen adsorption, dissociation, and diffusion. High oxygen vacancy concentration, however, could have a suppressive impact on the electron polaron hopping mechanism in the perovskite. In this view, a loss in electrical conductivity is frequently seen along with a growth in oxygen non-stoichiometry. A significant charge-transfer resistance may also be caused by poor electrical conductivity [132, 133].

2. SCOPE OF THE THESIS

As already noted, a successful commercialization of the SOFC technology depends on a number of conditions being met with regard to the cathode material. Numerous studies are being conducted in an effort to identify a material that meets all parameters but none have emerged yet. Furthermore, there is still a lack of fundamental understanding about the electrochemical processes occurring inside the air electrode, and there are several contradictions in the literature. Therefore, it is crucial to continue the study of SOFC cathodes. The purpose of this thesis is to study the internal structure of a conventional SOFC cathode and using the information provided, propose recommendations which could enhance the cell performance. This PhD thesis is composed of four parts, each leading toward the aim of improved cathode materials and use in the cell design.

Some of the most advanced cathodes for SOFCs are the LSM, LSC and LSF oxides, which all have some disadvantages, such as having poor ionic conductivity, and chemical compatibility, etc. There are some solutions for this problem and one way is the development of single-phase materials with mixed ionic-electrical conductivity. For instance, by doping the A-site of perovskite crystal with different oxidation state of metal, concentration of oxygen vacancies can be increased due to the charge neutrality, hence improved oxide ion conductivity. In the first and second chapters, the incorporation of Vanadium and Gadolinium metal doped LSC as cathode materials in intermediate temperature solid oxide fuel cells, as well as the explanation of the associated electrode reaction mechanism, are the main goals of these two chapters. In Chapter 3, the analysis on doping of multivalent Vanadium metal into LSF oxide crystal was carried out and experimental comparison is made on the reaction processes with other three developed cathode samples. At the last chapter, Lanthanum replacement with Vanadium metal in LSM oxide was researched as if the cathode material has higher electrical and ionic conductivity, and adaptable composition. Lastly, as a result of the existence of an aliovalent element in the oxide crystal, however, these materials essentially ran into a number of problems, which were concentrated in detail.

In this thesis, $La_{0.595}V_{0.005}Sr_{0.4}CoO_{3-\partial}$ (LV05SC), $La_{0.5}Gd_{0.10}Sr_{0.4}CoO_{3-\partial}$ (LG10SC), $La_{0.57}V_{0.03}Sr_{0.4}FeO_{3-\partial}$ (LV3SF), and $La_{0.595}V_{0.005}Sr_{0.4}MnO_{3-\partial}$ (LV05SM) perovskite oxides

were synthesized by sol-gel method and evaluated as cathode materials for IT-SOFC. The synthesized powders demonstrated perovskite structure as single-phase crystal with a rhombohedral lattice structure and space group of R-3cH. Also, they revealed a good chemical stability with the GDC electrolyte sample. The XPS analysis showed the presence of V^{4+}/V^{5+} and Gd^{3+}. The partial substitution of Vanadium or Gadolinium into A-site seemed to be compensated by B-cations. The shared electron pairs enabled continuous electron flow between A and B-site and better performance of cathode. The diffusion processes of oxide ions (O^{2-}) were found to be the limiting step for ORR by the EIS analysis and DRT calculations. These findings suggested that the compounds are promising cathode materials for IT-SOFCs. Advances in diffusion processes of ions in the materials promotes the performance of fuel cells.

3. SYNTHESIS, CHARACTERIZATION AND PERFORMANCE ANALYSIS OF $La_{0.595}V_{0.005}Sr_{0.4}CoO_{3-\partial}$ (LV05SC) CATHODE SAMPLE

This section is partially published as: Kisa, A.E., and O. Demircan, "Synthesis and characterization of $La_{0.595}V_{0.005}Sr_{0.4}CoO_{3-\delta}$ as a novel cathode material for solid oxide fuel cells (SOFC)", *Journal of Sol-Gel Science and Technology*, Vol. 82, pp. 352–362, 2017 [134, 135]. Kisa, A.E., and O. Demircan, "Transition Metal Doped Solid Oxide Fuel Cell Cathodes", *Journal of the Turkish Chemical Society Section A: Chemistry*, Vol. 5, pp. 1153-1168, 2018 [136].

3.1. Introduction

Low pollutant emissions and harmless byproducts improve fuel cells as one of the highly efficient and environmentally friendly energy conversion devices. Solid oxide fuel cells (SOFCs) are accepted as an electrochemical energy conversion technology that directly transforms the chemical energy into electrical energy. Because of its high efficiency, adaptability to a variety of fuels, and environmental sensitivity, SOFCs have received a lot of research interest [97]. Decreasing fabrication costs and improving system stability, which are the key barriers to commercialization for fuel cells, are the primary objectives of development of contemporary SOFC for researchers. The materials used in both electrodes supported SOFCs, which operate in the temperature range of 800-1000 ^{o}C, should be less costly and provide fewer material compatibility issues [33]. One of the efficient ways to address the design and durability difficulties is to lower the operating temperatures to the intermediate range (IT, 600-800 ^{o}C). However, as the conventional cathode $La_{0.6}Sr_{0.4}CoO_{3-\partial}$ (LSC) exhibits weak catalytic activity for the oxygen reduction reaction (ORR) at low temperatures, the significant increase in cathode polarization resistance has emerged as a major problem limiting the electrochemical performance of IT-SOFCs [50].

The ORR which is supposed to take place at TPBs, is fundamentally an electrochemical process involving charge transfer. Since Pt electrodes were the only SOFC

cathode material utilized until 1965, significant studies on those electrodes have led to the realization by increasing the size of the active zone on the electrode/electrolyte interface, it is possible to enhance the ORR kinetics at lower temperatures [137]. This inspires scientists to explore and develop the possible use of the transition metal oxides, or perovskites, as SOFC cathodes [138]. Perovskites display strong ORR catalytic capabilities, chemical and thermal durability, as well as noticeable mixed electrical and ionic conductivity [139]. They are also comparatively less expensive than Pt metal.

The large activation energy and slow ORR processes are responsible for the substantial cathodic polarization losses. Polarization losses at the cathode caused by ORR generate the majority of the total losses in such SOFCs with thin film electrolytes. Additionally, the migration of oxide ions inside the porous cathode is a vital factor for the cell performance [50]. In practice, there are two main methods to reduce cathode polarization losses: either by selecting a cathode material composition that is optimally matching to the triple phase boundary (TPB, including ion conducting layer, electron conducting layer, and the gas phase) to improve oxide ion exchange and diffusion kinetics or by modifying the cathode/electrolyte interface microstructure to increase the TPB dimensions [140]. The surface and/or active area is another essential element for better performance for ORR, according to electrochemical studies on dense, porous, and porous/dense double layered cathode materials based on LSC and LSM ($La_{1-x}Sr_xCoO_3$ and $La_{1-x}Sr_xMnO_3$, respectively) [121], [141–147].

Mixed ionic-electronic conductors (MIECs) are designed to expand the ORR active range from the TPB to the whole air electrode surface so that the electrode reaction kinetics can be improved in order to address this problem [148]. For this purpose, perovskite cathodes, particularly based on Co and Fe, are the most promising preferences among MIECs because of their superior electrocatalytic activity at the IT region for the ORR [149]. By employing the incoming electrons from the anode current collector, the flowing molecular oxygen is converted to oxide ions by catalytic conversion onto the surface of the porous cathode. The location of the ORR might be close to the electrode/gas interface or on the electrode/electrolyte/gas interface, depending on the characteristics of the cathode material [150]. The oxide ions or oxygen atomic species, which are entirely or partially reduced, are subsequently transferred by bulk or surface routes to the electrolyte/electrode/gas contact,

where the complete ORR takes place [151]. The fuel is oxidized as a result of the oxide ions' subsequent passage to the anode (through diffusion via a dense electrolyte). By selecting the optimal composition of the constituent materials and adjusting the sintering and processing conditions to produce grains of different sizes, modification of the cathode microstructure ultimately determines the performance of the cathode [122], [152, 153].

As a possible electrode material, perovskite oxides ABO_3 exhibit a variety of advantageous properties, such as improvement in oxygen ion mobility and higher stability of the mixed valence states of Ti, V, Nb, Mo and other elements in the crystal structure [154–157]. By using atomic substitution/doping or non-stoichiometry on either cation or anion sub-lattices, the composition of ABO_3 may be greatly enhanced. Such modifications trigger the improvements on electrical and ionic conductivities, sintering behavior and catalytic performance. The perovskite structure offers an a priori choice of the active site crucial to catalysis when an inactive A-site ion (like La^{3+} or Sr^{3+}) is combined with active B-site ion (like Co^{3+}, Mn^{3+} or Ti^{3+}). Additionally, the selection of the A ion can change the characteristics of the B ion and its nearby oxygen ions [158]. By doping Vanadium metal to the A site, the oxide electro-neutrality and charge compensation mechanism suggests that the negative charge defect caused by Sr^{2+} replacing La^{3+} at the A-site is compensated by aliovalent V ions. V^{4+} and V^{5+} are the two key oxidation states which are proved by XPS analysis. So, the continuous conduction of electrons through B-O-B and V-O-V saddle points is made possible by shared electron pairs of B^{3+}/B^{4+} and V^{4+}/V^{5+}.

In this chapter, the effects of changes in the oxidation states of doped transition metals such as Vanadium were investigated to understand ORR mechanism in the operation of SOFC on intermediate temperature range by employing the tape casting and co-firing procedures to produce the single cells with anode-supported thin electrolytes to enhance the electrical characteristics of perovskite materials. Both electrical and ionic conductivities, and the performance of perovskite materials have been measured for a variety of temperatures by employing EIS and DRT calculations. As a results of these analysis, adsorption, dissociation, and diffusion processes were found to be the ORR's limiting steps. These findings suggest that this V-doped perovskite structure, LV05SC, is a promising cathode material for IT-SOFCs.

3.2. Material Synthesis

Utilizing the sol-gel method, $La_{0.6-x}V_xSr_{0.4}CoO_{3-\partial}$ (LVxSC, x = 0.005) powders were produced. Reagents included La, Sr, and Co nitrates as well as V acetate (purity > 99.9%, Aldrich Chemicals, USA). Separately, each reagent was dissolved in distilled water at the proper stoichiometric ratio. To produce a homogenous solution, all of the solutions were afterwards combined and agitated. As complexation and polymerization agents, ethylene glycol and citric acid, in varying amounts, were added after they had completely dissolved.

The citric acid to total metal ions ratio was maintained at approximately 1:2. The solution was allowed to evaporate on a hotplate upon prolonged heating, the gel spontaneously burned, transforming into a light and delicate ash. Following a gentle heating-induced gelation, the resulting gel was placed in a drying oven at 500 °C for 2 hours to eliminate organic components. Subsequently, it was subjected to sintering at 900 °C for 3 hours to yield perovskite compounds possessing satisfactory crystalline structure, as confirmed through X-ray diffraction analysis.

3.3. Characterization, Electrochemical Measurements and Fabrication Procedures

The phase identifications of $La_{0.595}V_{0.005}Sr_{0.4}Co_{3-\partial}$ (LV05SC) cathode sample were obtained by X-ray diffraction (XRD) employing a Rigaku D/MAX-Ultima+/PC Diffractometer with Cu-Kα radiation (λ = 1.54056 Å). The diffraction patterns were recorded in the range of $20^o<2\theta<80^o$ with 0.01 steps and step-counting time of 8s/step. The phases were identified with JCPDS Database. The VESTA program was used to build the crystal structure of LV05SC using expected values from XRD data. All X-ray Absorption Fine Structure (XAFS) studies were completed in Photon (Nakhon Ratschasima/Thailand) Laboratories by using BL8:XAS beamline. Analysis and calculations were accomplished by using the dispersion fitting for a cluster with the size of 10 Å with 379 atoms (La, Sr, V, Co, and O) via FEFF 8.2 code ($f_{eff}(k,r)$ an effective scattering amplitude). An Al K-Alpha anode ($h\nu$ = 1486.6 eV, with spot size of 400 μm)-equipped Thermo Scientific K-Alpha Surface Analysis instrument was used to conduct X-ray photoelectron spectroscopy. The energy step size was set as 0.100 eV and the charge effect was calibrated using the binding energy of

C1s (284.5eV). XPS Peak 4.1 software was used to collect and analyze survey spectra at a pass energy of 50 eV and high-resolution spectra at a pass energy of 20 eV for quantification purposes. SEM-FEG, Philips XL 30 at an accelerating potential of 10 kV was used to study the surface and cross-section morphology of the sintered cells.

Performance and electrochemical impedance spectra (EIS) were measured from 500 to 800°C utilizing a self-made test setup contained of numerous gas mass flowmeters, a furnace (Figure 3.1). The sintered cells were attached to a zirconia tube with a ceramic paste. The electrodes' current collectors were made of Au paste and wires connected the electrodes to the testing instrument. The current-voltage (I -V) characterization was conducted with the Gamry Ref 3000 Potentiostat (Gamry Instruments, Warminster, PA, USA) using H_2 as the fuel and oxygen as the oxidant. The AC impedance data were collected with an AC signal of 10 mV in the frequency range of 1 MHz - 0.1 Hz.

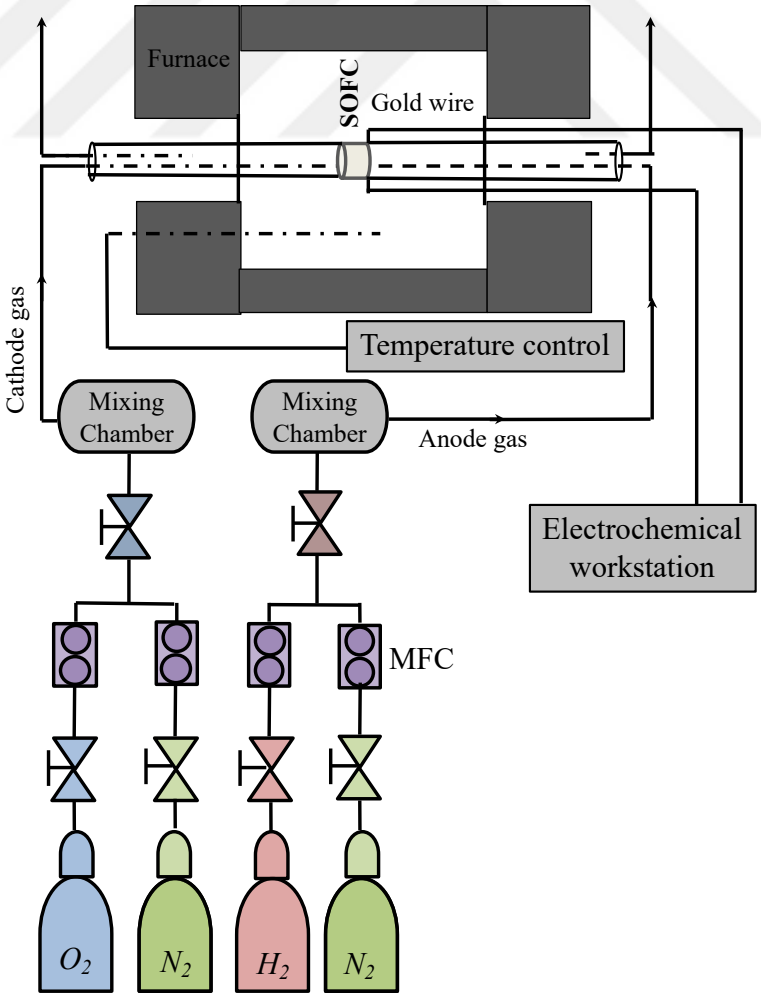


Figure 3.1. A schematic representation of the experimental SOFC setup.

Commercial YSZ (Yttria-Stabilized Zirconia (8% Y) – Tape Cast Grade Powder, Fuel Cell Materials Ltd., USA) and GDC (Gadolinium Doped Ceria (20% Gd) – Tape Cast Grade Powder, Fuel Cell Materials Ltd., USA) powders were used to prepare the electrolyte layers. The anode slurry was obtained by mixing YSZ or GDC and fine grade NiO powder (Fuel Cell Materials Ltd., USA). A two-step ball milling procedure was used to produce the slurries for tape casting. In the first step, polyvinyl butyral (PVB) was used as the binder and ethanol/toluene as the solvent to homogeneously disperse all the particles. Secondly, in order to give an ideal viscosity, the required amounts of plasticizers polyethylene glycol (PEG) and benzyl-butyl-phthalate (BBP) were added to the slurry and ball-milled again for 24 hours.

There were two processes in the tape casting process as well. The de-aired electrolyte and anode slurries were initially cast at a blade height of app. 10, 20 and 200 μm, respectively. The green tapes were cut into disks with a 13mm diameter after drying for 24 hours. One sheet of YSZ and/or GDC electrolytes and two layers of anode green tapes were stacked in order to produce anode-supported cells. The layers were assembled in random directions for relaxation of the residual internal stress and uniaxially laminated for 5 mins. The laminates were subsequently co-sintered at 1250 ^{o}C in air for 3h after burn-out of the organic components. Following co-sintering, the cathode paste was produced using LV05SC powder and electrolyte material with a weight ratio of 50:50, and brush coated onto electrolyte with an active area of 0.5 cm^2. The cathode layer was then sintered at 1100 ^{0}C for 5 h.

3.4. Results and Discussion

3.4.1. Phase Compositions and Structure

A common method for determining the composition and crystal structure of materials is X-ray diffraction (XRD). Because it enables researchers to ascertain the crystal structure and phase composition of the material, two crucial elements that might affect the electrochemical performance of the cathode, it is very helpful for studying SOFC cathode materials [142], [159]. $LaCoO_3$ or $La_{0.6}Sr_{0.4}CoO_3$ are two common perovskite-type oxides used in SOFC cathodes [160]. These materials have complicated crystal structures, and XRD

can be used to identify the many crystal phases that are present in the material as well as to pinpoint its specific details of crystal structures including atomic positions and lattice constants [143].

In Figure 3.2, the XRD pattern is shown for the cathode sample synthesized by sol-gel reaction after calcination at 900 ^{o}C for 3 h. A rhombohedrally distorted structure (space group R-3c:167) is formed with minor secondary phases. Phase, crystallite size and lattice parameters are calculated and also found matching with software crystallography open database (COD). XRD pattern reveals that synthesized cathode material has single phase with lattice parameters of *a,b*= 5.426 Å, *c*= 13.240 Å α, β= 90.00^{o} γ= 120.00^{o} and volume of 337.53 Å^{3}. All peaks in the XRD pattern are relatively sharp, indicating good incorporation into the lattice of the metal oxides used in the powder synthesis. These results further prove that the prepared catalysts have formed well $ABO_{3-\partial}$ perovskite structure.

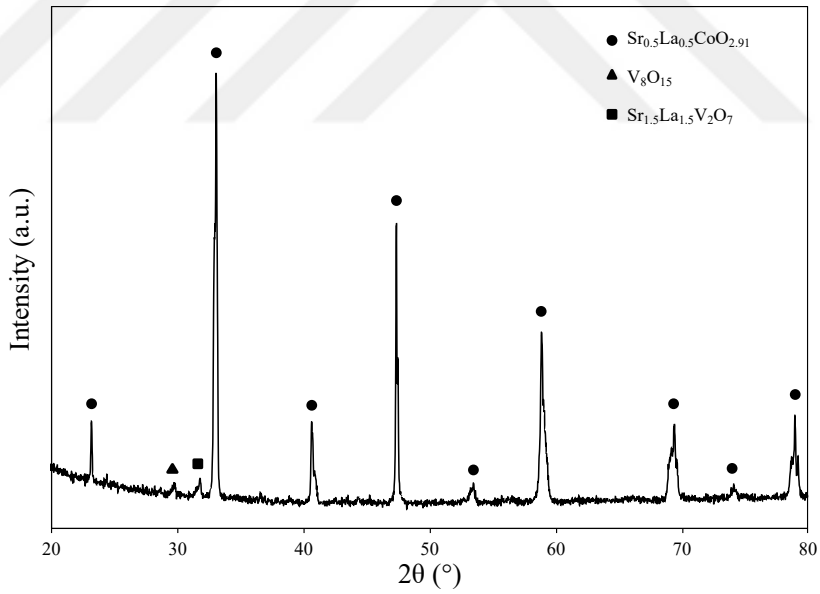


Figure 3.2. XRD data of $La_{0.595}V_{0.005}Sr_{0.4}Co_{3-\partial}$ cathode powder.

3.4.2. EXAFS Analysis

Recent research has concentrated mainly on employing X-ray absorption spectroscopy (XAS) analysis to understand the processes of electrocatalysts [161]. In terms of experimental measurements, it has been recommended that XAS is used to examine the geometric local structures and electron configurations of the electrocatalysts [78-80].

Recently, perovskite oxides have become interesting candidates for bifunctional electrocatalysts, due to their higher catalytic activity and great structural and chemical stability during the ORR and OER (oxygen evolution reaction) [162]. Cho and colleagues used ex-situ X-ray absorption near-edge structure (XANES) and extended X-ray absorption fine structure (EXAFS) analysis to demonstrate how the concentration of oxygen vacancies and the valence state of B-site cations strongly influence the catalytic activity of perovskite oxides [163]. To better comprehend roles of metal oxides as electrocatalysts in chemical processes, advanced techniques are needed. For investigating the geometric and local structures of materials, including ordered, disordered, and amorphous ones, XAS is a potential choice. In the XAS analysis, an electron is stimulated from a core level to an unoccupied valence and/or continuum state [81].

Measured and calculated absorption coefficients of the LV05SC at the Co K-edge XAS spectra are shown in Figure 3.3a. The k-space range from 0 to 10 $Å^{-1}$ was used to conduct the Fourier transform. Two peaks between 7700–7730 eV are generated by 1s–4p transitions of Co [164–166]. La peaks observed between 7800–7750 eV. The normalized, back-ground subtracted, and k^3-weighted Radial distribution function (RDF) analysis of XAFS data is given in Figure 3.3b for which the Co atom is accepted as the zero point in the space model. Atomic distances of Co–O, Co–La, Co–Sr, Co–Co are calculated by RDF analysis. The first one, appearing at 1.49, is attributed to the octahedrally coordinated Co - O shell at 1.92 in Figure 3.3b, and the second one, peaking at 3.17, is caused by the simultaneous scattering of Co-La, Co-V, Co–Sr, and Co-Co shells and the multiple scattering of Co-O-Co/Co-O-Co-O shells. These distances are matching when compared to perovskite structure and also confirmed by XRD analysis.

The FEFF parameters used to fit the XAS $k^3X(k)$ Fourier transform seen in Figure 3.3c are reported in Table 3.1 along with the study of Hass and colleagues [167, 168]. VESTA software was used to create the crystal structure of LV05SC using predicted parameters from XRD measurements, and the interatomic distances measured are presented in Table 3.1. The measured lattice parameters and interatomic distances correlated well with the literature and crystallographic data. The radial distribution or structural functions of the sample are very similar to that of pure $LaCoO_3$, suggesting the formation of ABO_3 perovskite, which is consistent with the XRD analysis [169].

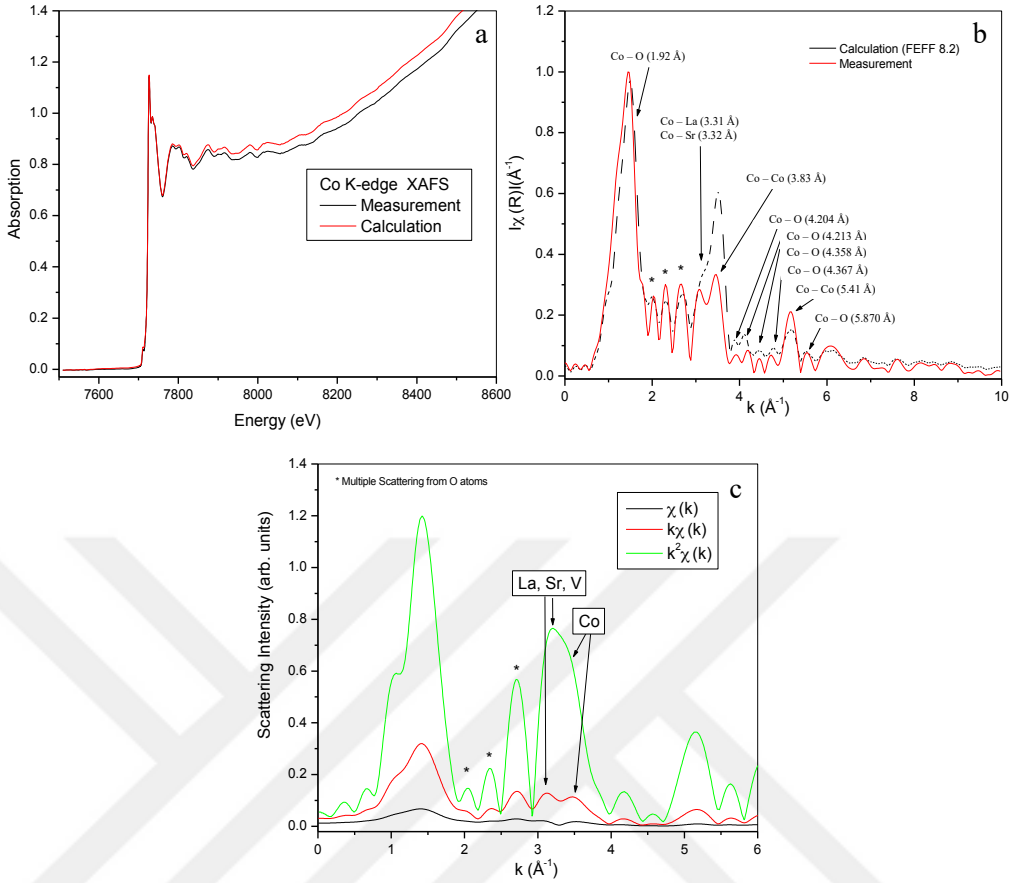


Figure 3.3. (a) Raw and calculated Co K-edge X-ray absorption spectrum of LV05SC perovskite, (b) Normalized, back-ground subtracted, and k^3-weighted Co-EXAFS spectrum, (c) Radial structure function obtained by Fourier Transform of $k^3X(k)$.

Multiplications of XAFS data of the Co K-edge of the LV05SC and the k (wavenumber, $Å^{-1}$) values displayed in Figure 3.3c. These two significant coordination peaks in Figure 3.3c provide information about the environment of the central metal ions. These multiplications are expected to respond proportionally with respect to atomic number, mass and type of metal ions located on the same site in perovskite crystal structure. Data in Co atom region (around 3.5 $Å^{-1}$) show the conservation of environmental symmetry and the consistent increase with respect to atomic number, mass and number of Co ions. On the other hand, very small shift and very weak increase, which are much weaker than expected for La atom with the atomic number of 57, are detected in the La atom region (around 3.2 $Å^{-1}$). These trends in XAFS data verify the stability in Co atom region, and the uncertainty in La atom region in perovskite structure. Therefore, XAFS data prove that the smaller atoms such as Sr and/or V engage the crystal sites originally occupied by La atoms. By replacing La atoms with V atoms some of the characteristic properties such as ionic conductivity, and

catalytic activity of the LV05SC material would be modified as expected. Hence, the performance of the cathode material enhances due to multiple stable oxidation states of V atoms such as +4 and +5.

Table 3.1. Structural parameters of $La_{0.595}V_{0.05}Sr_{0.4}CoO_{3-\partial}$ sample derived from Co - XAS analysis.

Fitting Results	**Coordination Numbers**	**Space Group: R – 3c:H**		
Path	**CN**	**R (Å) (XAS)**	**R (Å) (XRD)**	**R (Å) [169]**
Co - O	6	1.920	1.924	1.925
Co - La	6	3.310	3.284	3.316
Co - Sr	6	3.320	3.320	3.327
Co - Co	6	3.830	3.823	3.826

3.4.3. XPS Analysis

For analyzing the chemical composition of the surface of SOFC cathode layers within the first few nanometers, XPS is a well-known and often used surface-sensitive spectroscopic method [170, 171]. The surface properties of LV05SC sample examined by XPS, all elements, such as La3d, V2p, Sr3d, Co2p, and O1s have obviously existed in the crystal which is approved from the full scan survey spectra shown in Figure 3.4a. The XPS spectrum of La3d is shown in Figure 3.4b. It has two wide peaks with a splitting of 16.7 eV, one at lower binding energy at 833.01 eV and another at higher binding energy at 849.71 eV, which correspond to the La3d5/2 and La3d3/2 spectra, respectively. The relative intensity ratio for La3d5/2 and La3d3/2 is around 1.38; these values are closely related to those found in the literature [172]. The difference between the La3d5/2 doublet splitting, which is about 3.6 eV, confirms the existence of lanthanum hydroxides [173, 174]. As a result, the La3d is in +3 oxidation states, as shown by the distinct separation of these spin-orbit splitting. Also, the substitution of La ions by Sr and V ions did not result in any observable shift in the position of these peaks in XRD, EXAFS and XPS spectra.

The high resolution XPS spectra of V2p, which can be seen in Figure 3.4c, can be deconvoluted into four peaks at 515.6, 516.4, 522.4, and 523.7 eV, which indicates the

oxidation states of vanadium in this sample are +5 and +4 [175–177]. The area ratio between the V2p3/2 and V2p1/2 energy levels, arising from the orbital splitting of the V2p energy level, was set to 1.5:1, and the energy separation between the two levels was set at 7.7 eV. These results are in good agreement with the results from other studies [178, 179].

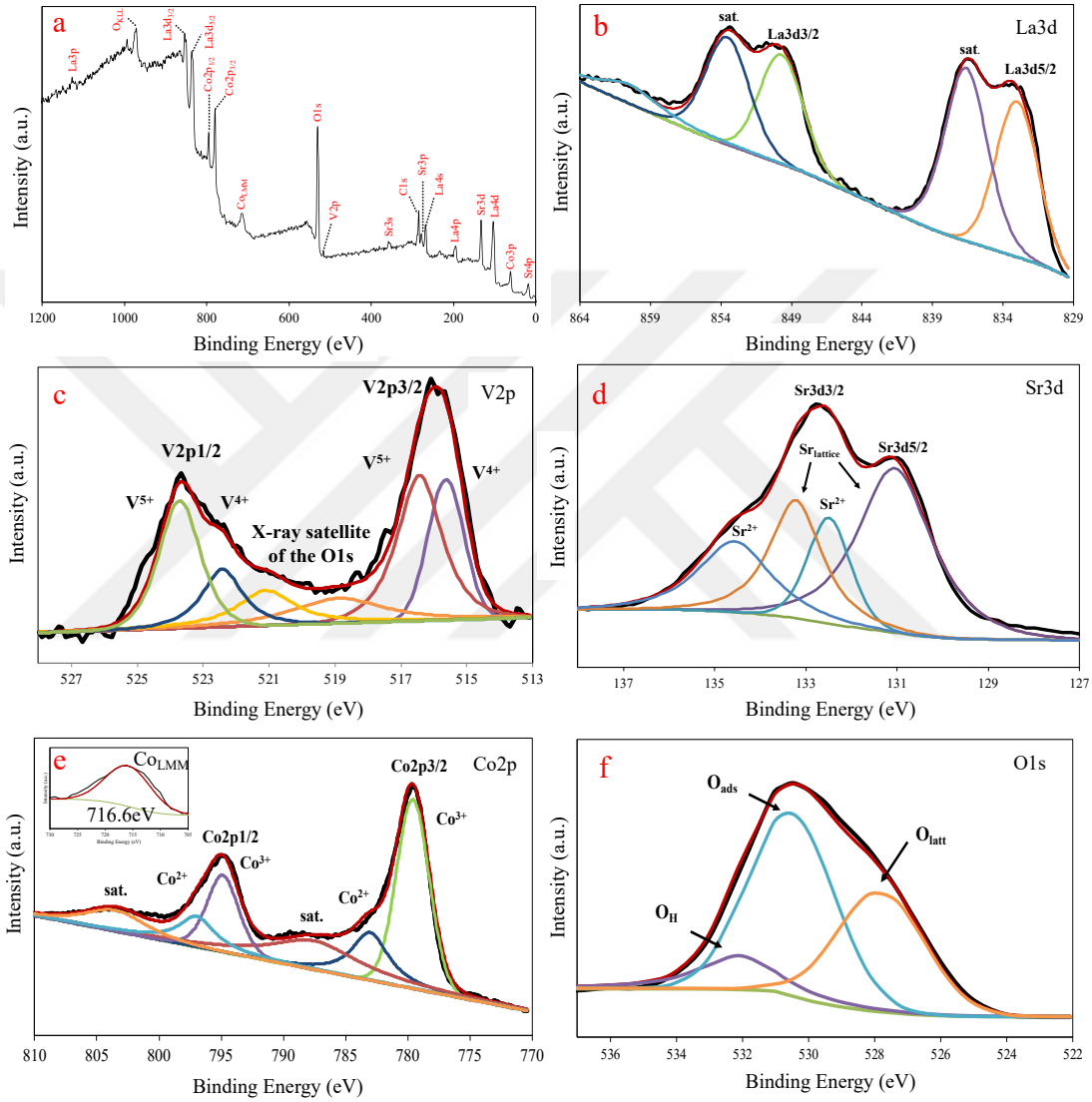


Figure 3.4. XPS survey spectra of (a) LV05SC perovskite, (b) La3d3/2 and La3d5/2, (c) V2p1/2 and V2p3/2, (d) Sr3d3/2 and Sr3d5/2, (e) Co2p1/2 and Co2p3/2, (f) O1s.

Additionally, the X-ray satellite of the O1s core level is responsible for the appearance of two peaks at 518.9 and 521.1 eV [180, 181]. The three peaks at 527.8, 530.5, and 532.1 eV in the core-level O 1s spectra (Figure 3.4f) can be attributed to the V-O bonding, adsorbed hydroxyl groups, and molecular water, respectively [175], [182]. According to the oxide electro neutrality and charge compensation mechanism, the negative charge defect caused

by Sr^{2+} and V^{4+}/V^{5+} replacing La^{3+} at the A site appears to be compensated for by Co^{3+}. The shared electron pairs Co^{2+}/Co^{3+} and V^{4+}/V^{5+} allow for continuous electron transfer across Co-O-Co and V-O-V.

The Sr3d core-level spectra were particularly helpful for determining the bulk and surface contributions in the spectra since the Sr3d levels had a distinct surface core-level shift [183]. The performance loss of the cathode samples in SOFC is widely known to be caused by Sr segregation, which has been confirmed by earlier studies [184, 185]. Shown in Figure 3.4d, the Sr3d spectra were well matched using two sets of spin-orbit doublets with an energy separation of 2 eV and an area ratio of ~2. The significant peaks of the Sr3d5/2 and Sr3d3/2 components were seen in the spectra of the LV05SC sample at 131.0 and 133.2 eV, respectively. The contributions to the Sr3d photoelectron spectrum were discovered to be due to perovskite lattice-bound Sr ($Sr_{lattice}$). The Sr atoms in Sr-OH, Sr-CO_3, Sr-Sr, and Sr-O bonds near the surface of the cathode sample ($Sr_{surface}$), which do not have perovskite structures, are responsible for the two additional minor peaks at 132.5 and 134.5 eV [186–190]. Because no obvious peaks assigned to carbonates could be seen in the X-ray diffraction patterns (Figure 3.2), the effect caused by carbonate compounds is negligible. Furthermore, the binding energies of Sr in the Sr-O structure ($Sr_{surface}$) and Sr in the lattice ($Sr_{lattice}$) are very similar, even beyond the resolution limit of this experiment configuration. The $Sr_{surface}$ therefore most likely results from the formation of the $Sr(OH)_2$ phase from SrO or from the development of a $Sr(OH)_2$-like binding environment such as SrOH on the Sr of the perovskite lattice or on the Sr of a separated SrO phase. Even though it is clear that the $Sr_{surface}$ associated with $Sr(OH)_2$ species is mostly on perovskite lattice. For the LV05SC sample, the $Sr_{lattice}/Sr_{surface}$ ratio of 2 indicates that the $Sr_{lattice}$ component of the Sr3d occurs to a greater extent. A Sr-OH signature peak is present in the bonding environment in all three cases (Figure 3.4f shows O1s spectra that demonstrates its presence). These results are expected for a perovskite structure.

The Co2p spectrum is divided into two distinct peaks and two weak satellites, as shown by the XPS data in Figure 3.4e. Co2p3/2 and Co2p1/2 might be the two spin orbit doublets identified as cobalt oxides at 779.3 and 794.8 eV, respectively. Two peaks at 779.5 and 783.0 eV, corresponding to the Co^{3+} and Co^{2+} configurations, can be seen in the spin orbit doublet of Co2p(3/2). The Co2p(1/2) spin orbit doublet can also be divided into two different peaks

that are attributed to Co^{3+} and Co^{2+}, respectively, and are located at binding energies of 794.8 and 796.9 eV. The Co_3O_4 cubic phase can be identified by the Co2p(3/2) and Co2p(1/2) splitting energy difference of 15.5 eV.

The appearance of the two satellite peaks at binding energies of 787.5 and 803.5 eV near the two spin orbit doublets provides additional evidence for the presence of cobalt oxides. This suggest that most Cobalt ions are present as trivalent cations with Co^{3+}/Co^{2+} ratio of 2.28 [191, 192]. Since the valence of Co ions mostly form with higher oxidation state such as Co^{3+} to Co^{2+}, the oxygen vacancies are formed in the crystal structure so that the electrical neutrality of the perovskite can be maintained. A higher Co^{3+} to Co^{2+} ratio enhances the catalytic capacity of sample surface to absorb oxygen, strengthening the Co-O bond and enhancing ORR performance. To adjust the electrocatalytic activity, Malkhandi carried out a comprehensive study on the perovskites. It was concluded that the catalytic activity is determined by the relative strength of the Co-O bonding [193].

The position of the Co_{LMM} Auger line (Figure 3.4e, inset) further supports the existence of both cobalt valence states. The peak at 716.6 eV of binding energy (E_B) is equivalent to kinetic energy of 770 eV by the below equation. The equation below can be used to calculate the modified Auger parameter, α

$$\alpha = 1486.6\ eV + KE\ (Co_{LMM}) - KE\left(Co2p_{3/2}\right) = 1551.0\ eV\ , \qquad (3.1)$$

where KE is kinetic energy [194]. This value of α indicates the coexistence of Co^{2+} and Co^{3+} since it is between the given values for CoO (α = 1549.8 eV) and Co_3O_4 (α = 1552.9 eV).

The XPS spectrum of O1s shown in Figure 3.4f exhibits two peaks, one at 530.5 eV due to adsorbed oxygen (O_{ads}) in the form of highly oxidative O^-/O_2^{2-} species, and one at 527.8 eV assigned to lattice oxygen (O_{latt}, O^{2-}) within perovskite. The extra peak at 532.1 eV, which is not always visible in O1s spectra, is caused by the physical and chemical adsorption of molecular water or hydroxyl groups on the surface of defects (O_H) [195–197]. The content of oxygen vacancy in materials can be determined by analyzing the ratio of O_{ads}/O_{lat}. The value for LV05SC cathode is 1.49. This ratio suggests that V doping can be an effective way to raise the oxygen vacancy concentration in electrode materials, provide more active sites and higher oxygen ion conduction in the reaction process.

Because lanthanum oxide has a hygroscopic characteristic when exposed to air, the highest binding energy of O1s (532.15 eV) is thought to be due to a water molecule associated with the surface lanthanum oxide. It should be noted that molecular water and surface-adsorbed oxygen in the form of hydroxyl or oxygen groups could be easily removed by heating to generate oxygen vacancies. But, removing highly oxidative oxygen species (O^- /O_2^{2-}) requires a significantly higher temperature.

In most cases, the oxygen vacancies caused by the oxygen-deficient perovskite oxides can result in different oxidation states of the transition metal ions and hence increase the catalytic activity of the perovskite [198]. Also, the total amount of oxygen adsorbed in perovskite oxides corresponds to the amount of oxygen vacancies. The catalytic activity of a catalyst increases with the amount of oxygen vacancies present on its surface [199].

3.4.4. Fabrication of Anode-Supported Electrolyte via Tape casting/Lamination/Co-firing

For producing thin, thick, flat, and large-area ceramic tapes with the thickness range of 10-1000 μm, tape casting is a respectable manufacturing technique. This method is employed to create a range of electrical devices, including multi-layer ceramic capacitors, low-temperature co-firing ceramics, and other devices and is quite straightforward compared to other common methods for fabricating ceramic layers. Making SOFC components by this method is particularly appealing since it may be more affordable to produce in large quantities. In order to manufacture planar electrode-supporting SOFCs, tape casting method has been extensively used. However, due to the challenges that come with fabricating a thin ceramic layer with no gas permeability, tape casting technology has not been successful in the fabrication of electrolytes with thicknesses below 10 μm. Co-firing of the electrode and electrolyte layers is another low-cost manufacturing method, and effective application of this technique would improve the productivity while consuming less energy. However, minimizing the deformation of the structure owing to mismatches in the thermo-mechanical and physical characteristics of the different layers was necessary for a successful co-firing of the multi-layer structure. There have been a few research efforts on fabricating the flat-type SOFCs.

The attempt to lower the operating temperature from 800 to 600 ºC or below is one of the primary research goals in this area. The benefits of SOFCs operating at lower temperatures include a larger selection of materials, improved long-term performance, system compactness and perhaps lower fuel cell costs [200, 201]. To address these concerns there have been many research efforts including reducing the thickness of the YSZ layer and using substitute electrolyte materials having better ionic conductivity than YSZ at low and intermediate temperatures, such as gadolinium doped ceria (GDC - $Gd_{0.2}Ce_{0.8}O_{1.95}$) and doped $LaGaO_3$ [202–206]. Despite the reports of effective operation at low and intermediate temperatures, the best materials and methods for low-cost process producing stable and consistently high SOFC performance have not yet been fully addressed.

To achieve adequate energy conversion rates and provide a suitable power output, a SOFC with a thin electrolyte sheet is preferred [207]. In this thesis, thin YSZ/GDC electrolytes and NiOYSZ/NiOGDC anode layers were prepared via tape-casting (Figure 3.5). They were used to produce YSZ-NiOYSZ, GDC-NiOGDC, and YSZ-GDC-NiOGDC anode-supported fuel cells with different thicknesses.

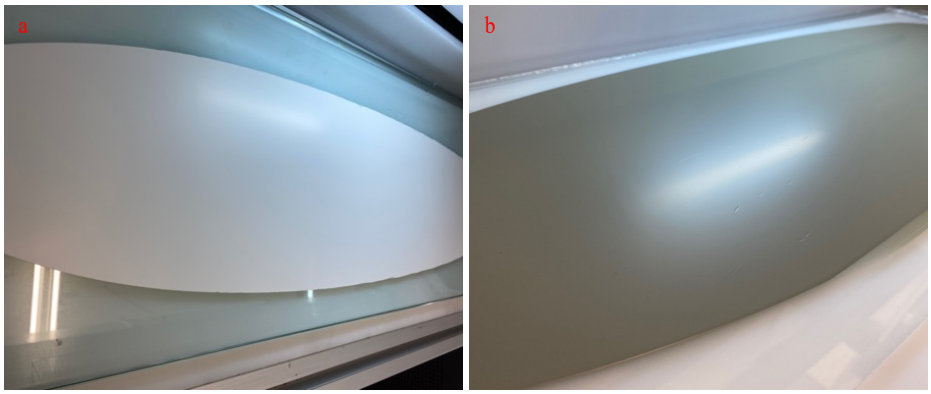


Figure 3.5. Pictures of the green tapes of (a) YSZ electrolyte, (b) NiOYSZ anode layers.

3.4.5. Surface Morphology Analysis of the Cell

Figure 3.6 - 9 display cross-sectional SEM micrographs of YSZ-NiOYSZ, GDC-NiOGDC, and GDC-YSZ-NiOYSZ half-cells. The thickness of YSZ and GDC electrolyte layers were 17.67 and 73.33 µm, respectively. In order to observe the effect of double-layer electrolyte in cell performance, YSZ and GDC tapes in different thicknesses were attached together, as demonstrated in Figure 3.8 and 3.9. In those combinations, YSZ electrolyte layer

has a thickness of ~ 21.70 µm, and GDC layers have 35.84 and 4.23 µm. It is evident that the porous anode layers were tightly attached to the electrolyte layers, which were quite dense and crack-free. Also, there were no cracks or delamination found between the layers, demonstrating a strong interfacial adhesion.

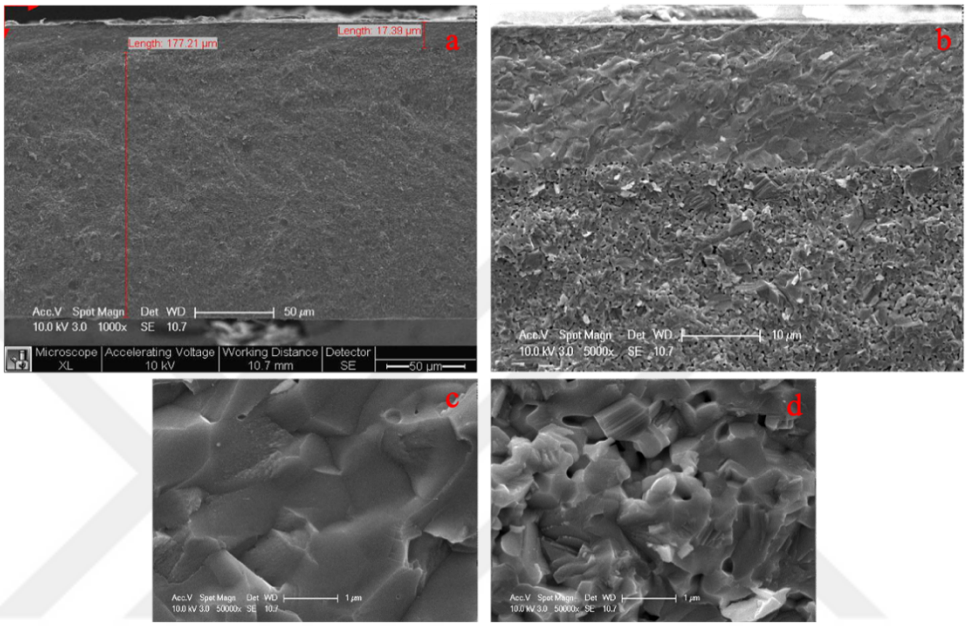


Figure 3.6. SEM images of (a)YSZ-NiOYSZ half-cell cross section, (b) closer look to interfaces, (c) YSZ electrolyte, and (d) NiOYSZ anode.

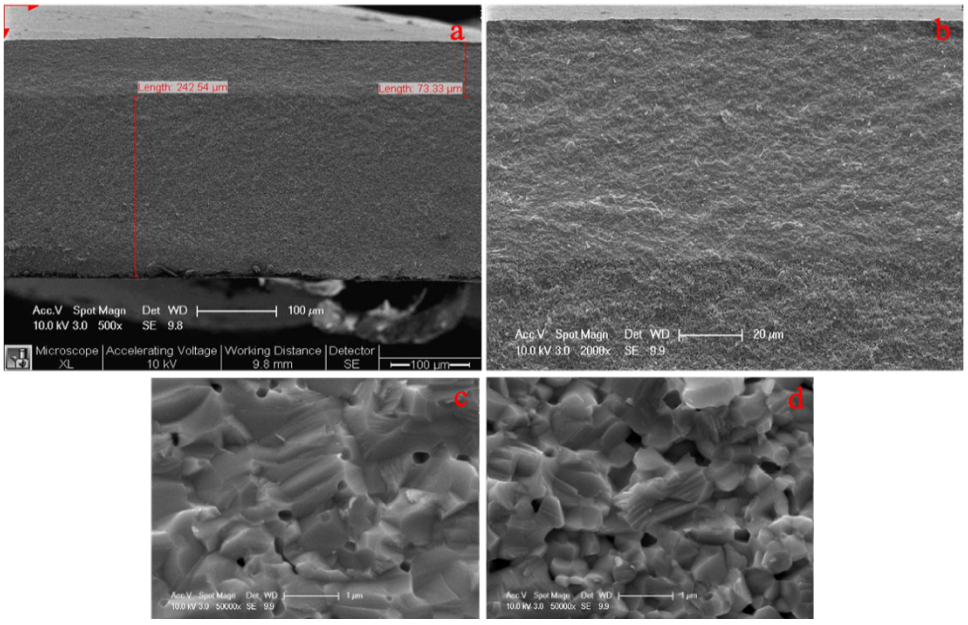


Figure 3.7. SEM images of (a) GDC-NiOGDC half-cell cross section, (b) closer look to interfaces, (c) GDC electrolyte, and (d) NiOGDC anode.

After fabrication and co-firing steps of green layers, LV05SC cathode powder was mixed with electrolyte material with a weight ratio of 50:50, and paint-brushed on electrolyte layer with an active area of 0.5 cm^2. Those prepared anode-supported cells were followed a final sintering procedure at 1100 ^{0}C for 5 h.

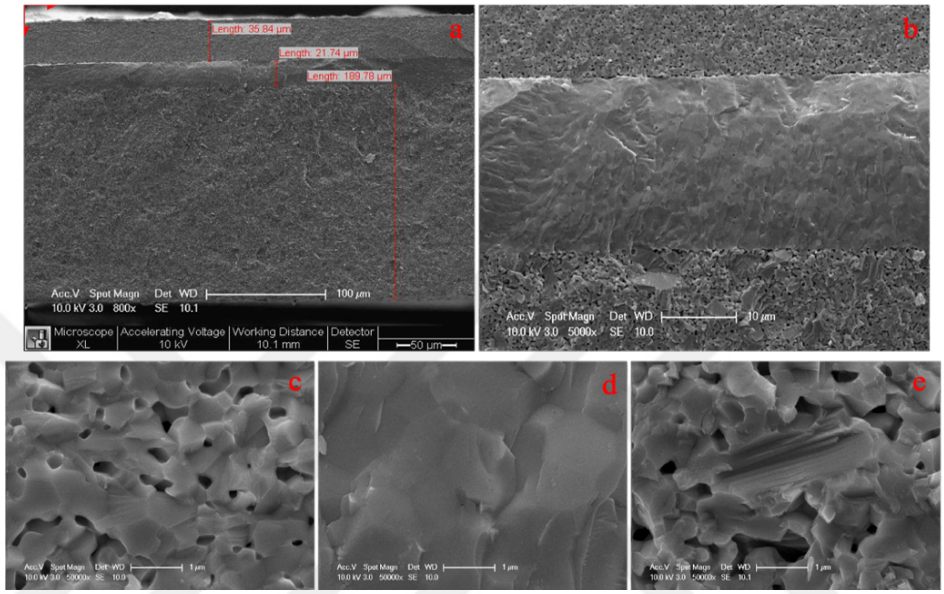


Figure 3.8. SEM images of (a) GDC (35 µm)-YSZ-NiOYSZ half-cell cross section, (b) closer look to interfaces, (c) GDC electrolyte, (d) YSZ electrolyte, and (e) NiOYSZ anode.

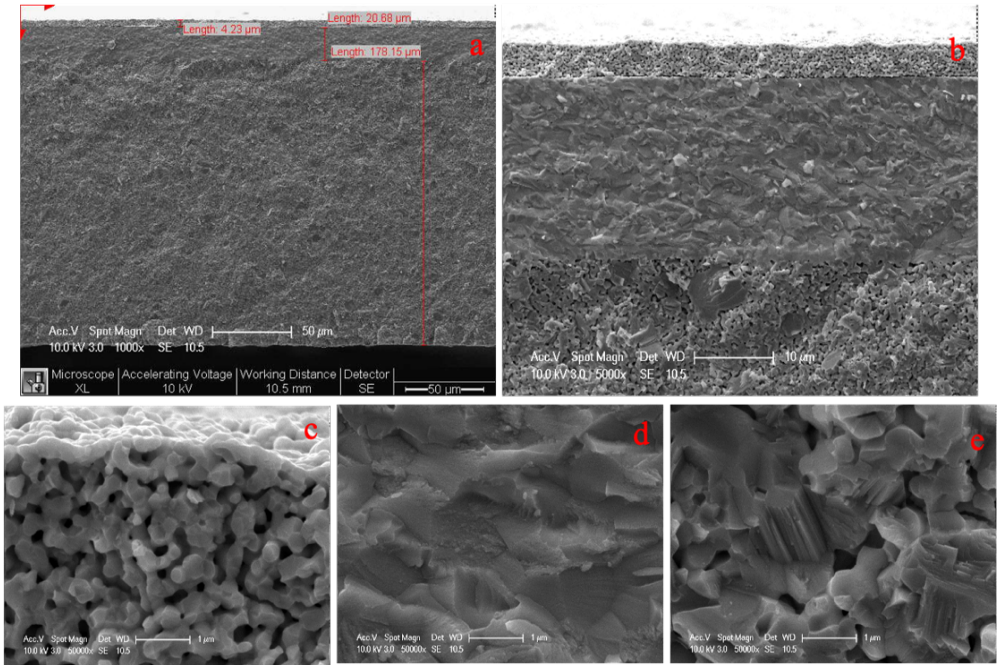


Figure 3.9. SEM images of (a) GDC (5 µm)-YSZ-NiOYSZ half-cell cross section, (b) closer look to interfaces, (c) GDC electrolyte, (d) YSZ electrolyte, and (e) NiOYSZ anode.

In order to determine the best preparation and sintering temperature steps, XRD analysis were carried out. Figure 3.10 illustrates the XRD patterns of the co-sintered half cells. All diffraction peaks can be indexed to pure cubic fluorite phase of YSZ at Figure 3.10a. And no other impurities were detected in the patterns at Figure 3.10b – d, indicating that high cubic phase purity GDC layers could be prepared by regulated steps.

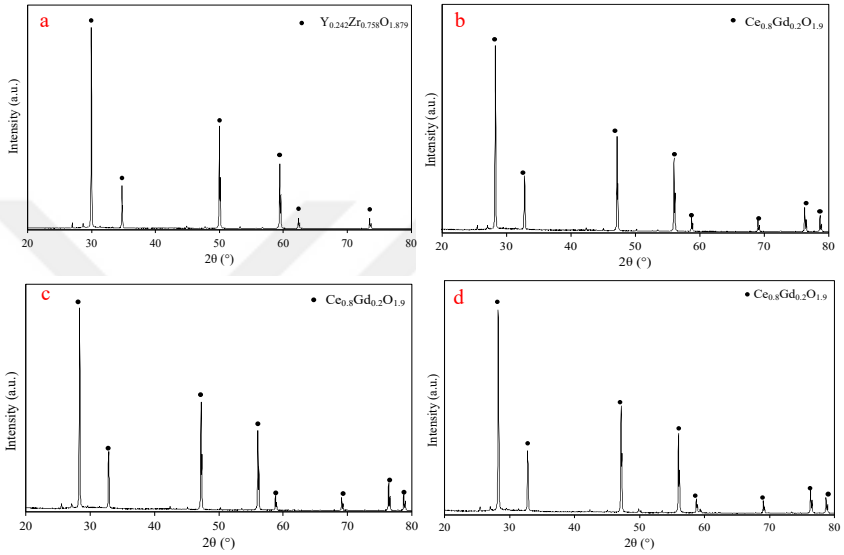


Figure 3.10. XRD analysis from electrolyte layer of (a) YSZ-NiOYSZ, (b) GDC-NiOGDC, (c) GDC (35 µm)-YSZ-NiOYSZ, and (d) GDC (5 µm)-YSZ-NiOYSZ half-cells.

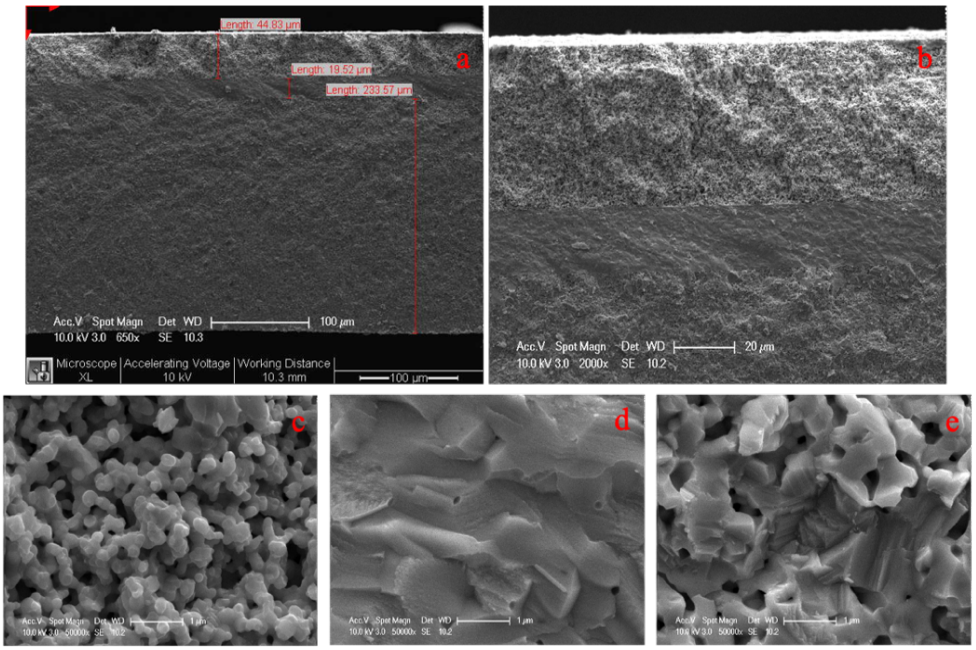


Figure 3.11. SEM images of LV05SC-YSZ-NiOYSZ fuel cell, (a) cross section, (b) closer look to interfaces, (c) LV05SC cathode, (d) YSZ electrolyte, and (e) NiOYSZ anode.

In Figure 3.11 - 14, LV05SC composite cathode layers can be clearly measured as 44.83, 8.68, 9.87 and 21.74 µm. Figure 3.11c – 14c illustrates the cathode layers have nice porous structure, which is a keystone for high cell performance. This is one of the desired properties for the cathode that having high catalytic surface area for ORR, beside this controlling the physical support. It is also observed that gas-tight non porous electrolyte layers were achieved with high density (Figure 3.11d – 14d). In addition, homogeneous contacts that formed along interfaces between electrode and electrolyte layers are obvious.

Two primary functions of a good electrode/electrolyte interface in SOFCs are to firstly enable oxide ions transfer from cathode to anode, and minimize or prevent reactivity between cell components during operation. However, reactivity between electrode and electrolyte is common because of harsh working conditions of SOFCs. Using zirconia electrolytes, Backhaus examines several cathodes in a recent study applied to SOFC materials [208, 209]. It is discovered that the cathode/electrolyte interphase diffusion, segregation and structure changes all had an unfavorable effect on the oxygen exchange rate and the overall performance of the cell. When Grosjean and colleagues examined the behavior of $La_{0.8}Sr_{0.2}MnO_3$ on YSZ electrolytes, they discovered a rapid degradation following a prolonged treatment at 850 ºC and an order-of-magnitude drop in electrical performance [210].

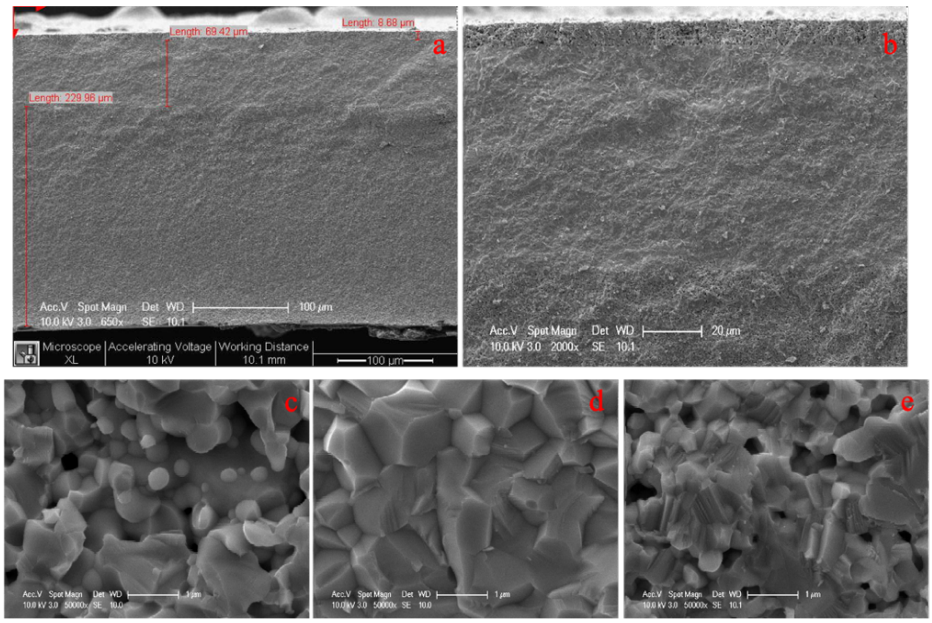


Figure 3.12. SEM images of LV05SC-GDC-NiOGDC fuel cell, (a) cross section, (b) closer look to interfaces, (c) LV05SC cathode, (d) GDC electrolyte, and (e) NiOGDC anode.

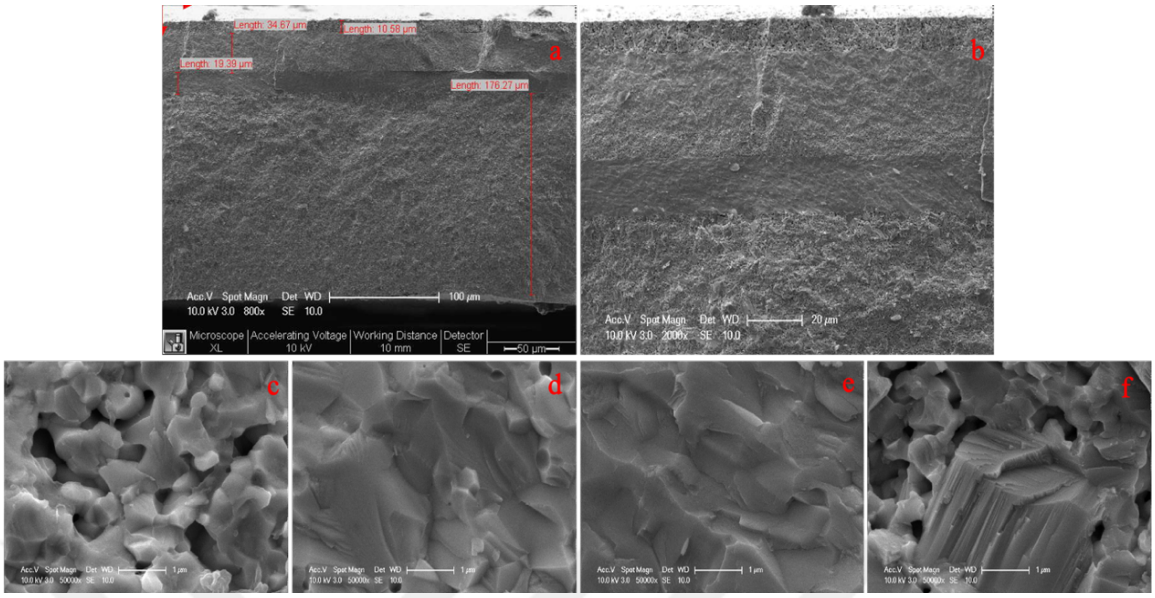


Figure 3.13. SEM images of LV05SC-GDC (35 µm)-YSZ-NiOYSZ fuel cell, (a) cross section, (b) closer look to interfaces, (c) LV05SC cathode, (d) GDC electrolyte, (e) YSZ electrolyte, and (f) NiOYSZ anode.

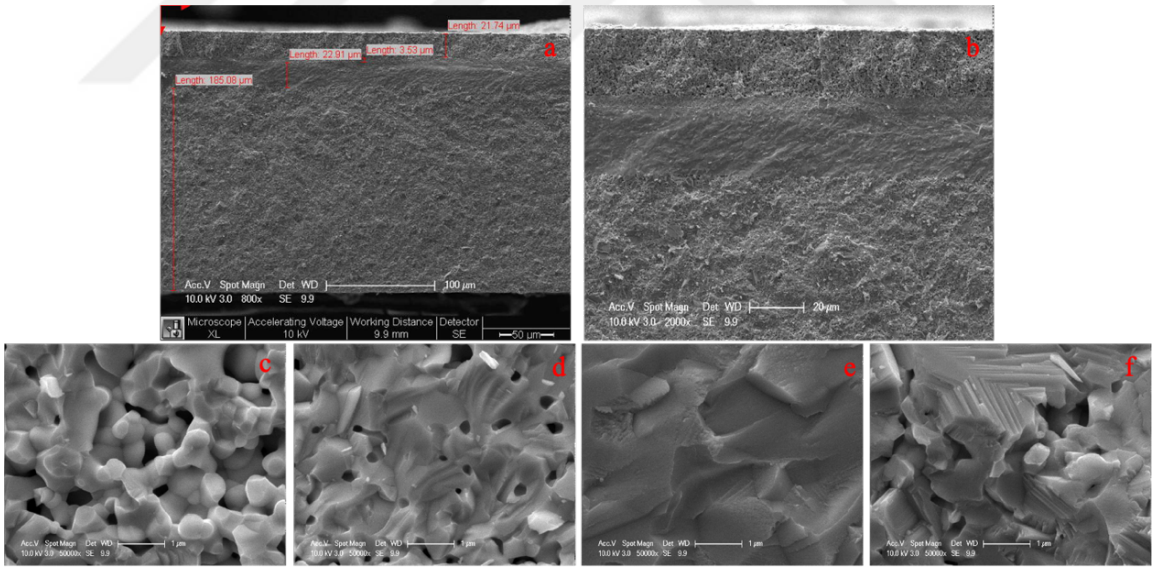


Figure 3.14. SEM images of LV05SC-GDC (5 µm)-YSZ-NiOYSZ fuel cell, (a) cross section, (b) closer look to interfaces, (c) LV05SC cathode, (d) GDC electrolyte, (e) YSZ electrolyte, and (f) NiOYSZ anode.

The resistive $La_2Zr_2O_7$ phase was shown to be associated with the efficiency decrease [211, 212]. The ionic conductivity decreases as a result of these impurity formations, which lowers cell performance. In order to eliminate interface reactions between cathode and YSZ electrolyte, GDC layer were casted on YSZ as a buffer layer. The thickness of GDC

interlayer for segregation against Zr from YSZ electrolyte is measured as 35 and 4 µm (Figure 3.13 and 14). Figure 3.15 demonstrates the XRD patterns of LV05SC cathode layers of fuel cells with double layer electrolytes. It is clear that there was no impurity or shift in the crystal structure of LV05SC cathode and GDC electrolytes.

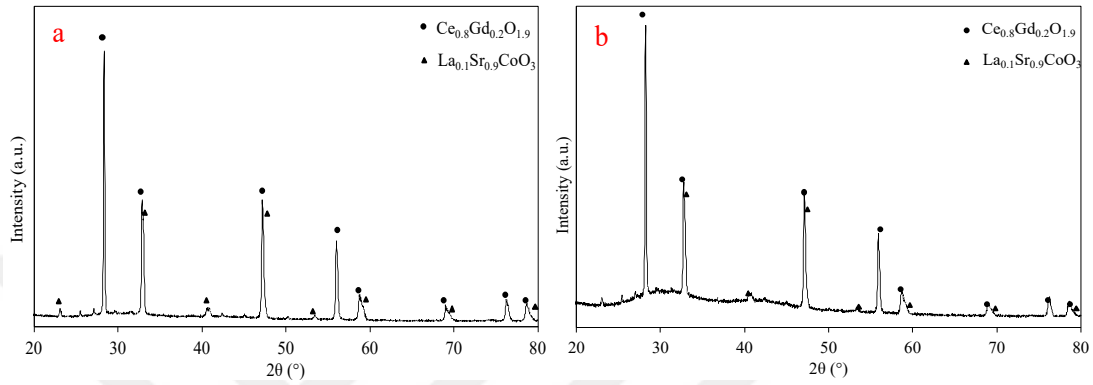


Figure 3.15. XRD analysis from cathode side of (a) LV05SC-GDC (35 µm)-YSZ-NiOYSZ, (b) LV05SC-GDC (5 µm)-YSZ-NiOYSZ fuel cells.

3.4.6. Single Cell Performances

The current-voltage characteristics of the SOFC with YSZ electrolyte are plotted in Figure 3.16. With hydrogen as a fuel and oxygen/nitrogen gas blend as an oxidant, the measured open circuit voltages are 0.73, 0.80, 0.76, and 1.12 V at 500, 600, 700 and 800 °C, respectively, to a certain degree those values were lower than those calculated by the Nernst equation [213, 214]. The lower OCV readings could be the result of short circuit that originated from the thin electrolyte layer, gas leakage as well as poor sealing. The maximum power densities of the single cell were 0.028, 0.13, 0.45, and 5 mW/cm^2 at 500, 600, 700 and 800 °C, respectively. The higher cell performance could be succeeded by further optimization.

Figure 3.17a displays the impedance spectra of the cell measured under open circuit potential at between 500-800 °C. The asymmetrical shape of impedance plots suggests that there are several mechanisms under selected frequency of 0.1 – 10^6 Hz. The equivalent circuit used to model the experimental data is displayed in Figure 3.17 inset. L_b, C, Q and R in the circuit stand for inductance, capacitance, constant phase element (CPE) like pseudo capacitance, and resistance, respectively.

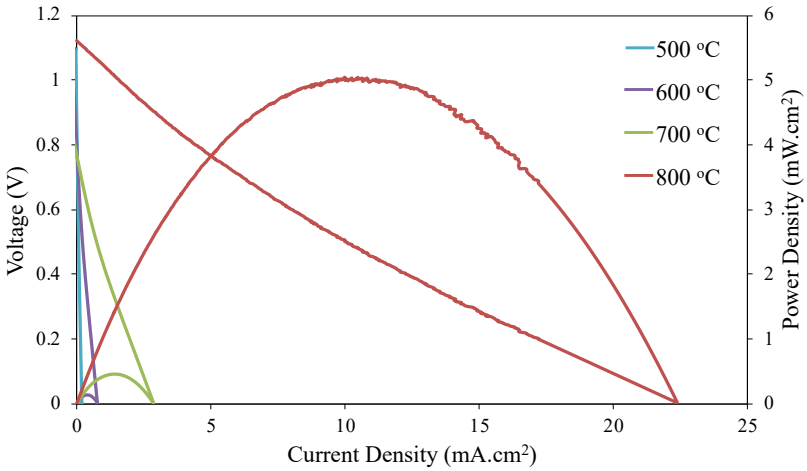


Figure 3.16. I-V curves and output power density of single cell with LV05SC-YSZ-NiYSZ at different temperatures.

The circuit is a suitable representation for this experimental system and allows for the evaluation of EIS data. These data could be explained as oxygen reduction at mixed ionic-electronic conducting cathode film essentially follows the bulk path way, in which oxygen is first adsorbed on the electrode's surface then incorporated as oxide ion into the bulk and transported to the electrode/electrolyte phase boundary, where it eventually reaches the crystal structure of the electrolyte layer.

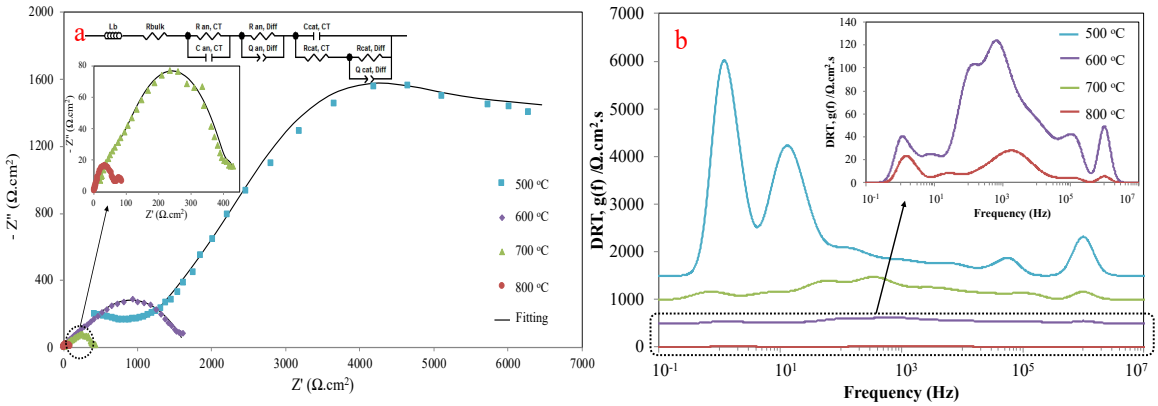


Figure 3.17. (a) Nyquist plots of LV05SC-YSZ-NiYSZ cell at OCV conditions, inset: Equivalent circuit model, (b) DRT curve of impedance spectra as a function of operating temperature at 500 - 800 °C.

Within the bulk pathway, the major resistive process $R_{cat,diff}$ is the electrochemical resistance associated with oxygen exchange at the cathode surface. At low frequencies, the matching semicircle in the spectra is observed, submitting a capacitive like behavior. This

behavior, designated as $Q_{cat,diff}$, is called constant phase element linked to variations in the oxygen stoichiometry in the electrode bulk. As a result, information about the electrode's surface ($R_{cat,diff}$) and bulk ($Q_{cat,diff}$) can be found in the dominant low-frequency arc. The transfer of oxide ions across the electrode/electrolyte interface corresponds to the resistive component of medium-frequency ($R_{cat,CT}$). An interfacial capacitance connected to the same boundary is the mid-frequency capacitance ($C_{cat,CT}$). The ohmic resistance (R_{bulk}) of the electrolyte and non-zero electrical contact resistance of gold wires are responsible for the high-frequency intercept of the impedance spectra [215, 216].

At high frequencies, there may be just one arc visible due to the grain boundary resistance becoming insignificant as the temperature increases. The increased electrochemical activity can be attributed to the increasing electrical conductivity and vacancy concentration with temperature, which improves the charge transfer and oxygen surface exchange in the cathode sample and thus improves the ORR that occurs at the cathode/electrolyte interface. Furthermore, low-frequency arc exhibited greater values than high-frequency semi-circle in all temperature range. Additionally, the low-frequency arc contribution on total resistance in the investigated temperature range was considerable, showing that the oxygen adsorption, dissociation and diffusion process in the cathode sample is the ORR's limiting step [146], [217]. The electrochemical circuit parameters obtained from the impedance spectra fittings are summarized in the Table 3.2.

Regardless of its difficulty in data analysis, electrochemical setups have been studied using impedance spectroscopy. This method is the most appropriate procedure available for evaluating and determining the performance obstacles for the operating cell. The process of measuring the response usually involves applying a sinusoidal signal within a predetermined frequency range. They can be classified into various time domains by the kinetics of each individual electrochemical process and detecting each step can be easier with an equivalent circuit model. Even yet, designing a model to fit the impedance data is frequently subjective and dependent on personal judgement. As a consequence, a single set of data can be effectively fitted to many models. A standard examination of EIS by model fitting could not proceed and yield relevant information since each model has certain assumptions and several model could fit with the same impedance data. In this situation, the Distribution Relaxation Times (DRT) method could be helpful. As a result, the rate limiting steps can be successfully

recognized and effectively resolved after examining electrochemical processes in the system. Simultaneously, a brief explanation of basic electrochemical steps could help in the logical development of a suitable model to evaluate the relevant parameters. In this study, impedance spectroscopy together with DRT and equivalent circuit model analysis were performed to thoroughly characterize the cell. With a regularization value (λ) of 10^{-3}, the impedance data were subjected to DRT analysis. To research the EIS and DRT dependence over working temperatures, the cell was studied in the temperature range of 500 to 800 °C (Figure 3.17b). With the values in Table 3.2, the impedance spectra were measured at various potentials at 800 °C as well (Figure 3.18a).

Table 3.2. EIS Fitting values of LV05SC-YSZ-NiYSZ fuel cell at 500-800°C.

	500 °C	600 °C	700 °C	800 °C	Unit
Ran, Diff	435.9	59.4	28.005	12.55	ohm.cm^2
Lb	1.52E-07	3.51E-11	1.23E-12	3.87E-07	H
Rbulk	252	32.24	17.615	3.1855	ohm.cm^2
Rcat, Diff	9490	1475	346.2	61.55	ohm.cm^2
Rcat,CT	275.05	64	30.37	2.8725	ohm.cm^2
Ccat, CT	1.54E-10	5.72E-09	3.93E-08	5.19E-08	F
Qcat, Diff	3.43E-05	1.4E-05	2.94E-05	4.88E-05	S*s^a
a2	0.3609	0.4575	0.511	0.6022	
Qan, Diff	3.52E-07	2.7E-08	1.11E-07	0.00618	S*s^a
a1	0.6042	0.7905	0.8049	0.7151	
Ran, CT	1002.5	33.41	17.26	9.99	ohm.cm^2
Can, CT	2.79E-05	1.94E-07	0.01523	0.018025	F

Each peak in the DRT represents a specific electrode procedure. The term “integral peak area” denotes to electrode polarization resistance. In Figure 3.18b, it is evident that the high frequency response has a relatively minor impact when compared to the low frequency response. It is suggested that in these oxide materials, the low frequency contribution originates from the flux of the reactants or mass transport process (gas diffusion), whereas the high frequency peaks are caused by the oxide ions charge transfer in electrodes [91], [153], [218, 219]. The modest contributions that could not be detected and would require more experimental study, such as impedance analysis under different gas concentrations.

However, it is essential and suggests the significance of using different and bi-layer electrolyte materials in order to reduce the total polarization resistance contribution of interfacial resistance.

In the developed equivalent circuit model in Figure 3.18a, each parameter has unique representation in DRT. In order to clarify the contribution of each reaction step in the cell, each reaction step can be labeled as P, that is composed of capacitor and resistance to denote the adsorption, diffusion and reaction processes, respectively. In the Figure 3.18b, over the analyzed frequency range of 1 MHz - 0.1 Hz, six deconvoluted peaks designated as P1 - P6 from high to low frequency appeared to be evident signifying six different electrochemical processes. In this model, P2 and P6 symbolize two anode processes, whereas P1, P3, P4, and P5 symbolize four cathode processes. The hydrogen charge transfer is symbolized by P2 [220, 221], and the gas diffusion in the anode is symbolized by P6 [96], [222, 223]. P1 stands for the transfer of oxide ions across cathode/electrolyte interface and via the electrolyte network in the cathode [224]. P3 is labeled for oxygen species (O^-/O_2^{2-}) diffusion to the TPBs, P4 is for ORR at TPB regions, and finally P5 represents oxygen gas diffusion in cathode [221–223]. The resistance of each process is associated with the activation energy of the corresponding step. A larger activation energy corresponds with increased resistance.

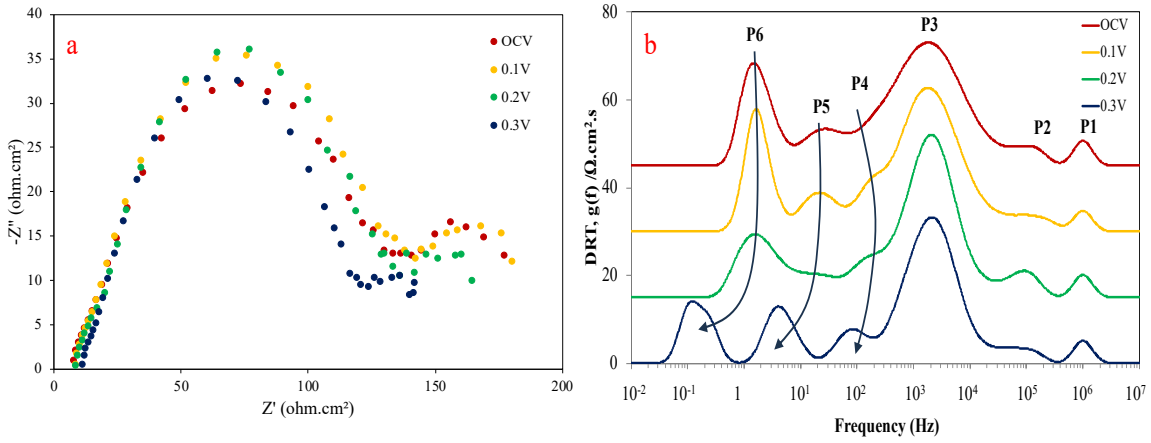


Figure 3.18. (a) Nyquist plots of LV05SC-YSZ-NiYSZ cell, (b) DRT patterns under different applied voltages at 800 °C.

The frequency (*f*) is related to the reaction rate and can be expressed as $f = 1/(2\pi RC)$. Faster response rates are associated with higher values of *f*. From the Figure 3.18b, the overlapped processes as well as the resistances at the low frequency region started to separate

with applied voltages. As mentioned above, deconvoluted peaks at low frequencies are related with the diffusion and exchange of oxygen species (O^-/O_2^{2-}) at the TPBs and mass transfer of reactants in the cathode, it is easy to clarify $R_{cat,diff}$ is the rate limiting step. The detailed equivalent circuit fitting values in Table 3.2 also proved this phenomenon.

The DRT finding in the Figure 3.18b was derived from impedance data taken under different voltages, shown in Figure 3.18a. The significance of each peak corresponds to a particular sub-step. As seen in Figure 3.18b, the shifts in P4, P5 and P6 are more obvious with increasing applied voltages. Furthermore, as the applied potentials increase, P1, P2 and P3 remain unaffected and P4, P5, and P6 move to lower frequencies. Therefore, P1 – P3 are associated with the oxide species transfer via electrolyte or across the interface, whereas P4 – P6 are related with the surface electrode kinetics that respond discretely at applied potentials [225–227].

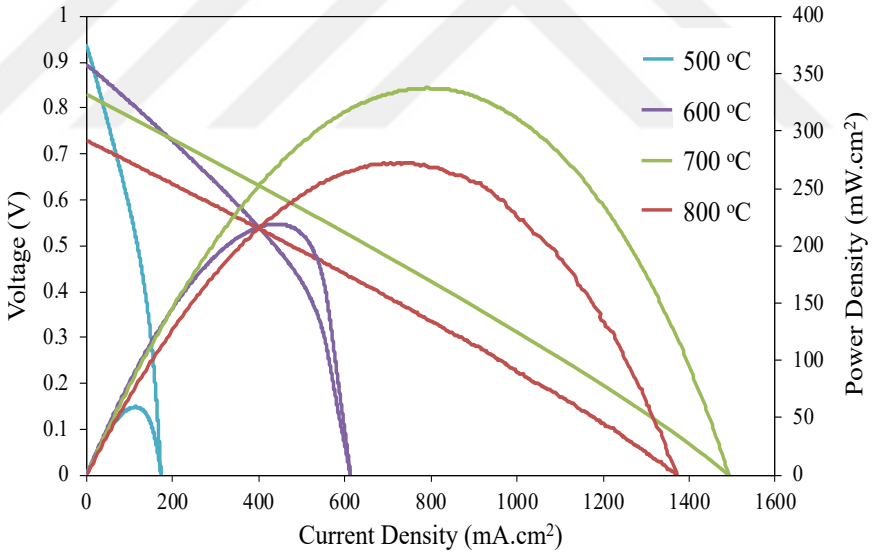


Figure 3.19. I-V curves and output power density of single cell with LV05SC-GDC-NiGDC at different temperatures.

To confirm the suggested methodology in this thesis, the performance of fuel cells constructed using different electrolyte materials were tested. Figure 3.19 displays the I-V and I-P curves of the LV05SC-GDC-NiGDC cell. The highest power density was achieved at 700 °C with 338 mW/cm^2. This shows that, although operating at a lower temperature of 100 °C, the cell with LV05SC-GDC composite cathode can provide results with higher power and current densities. OCV values obtained were 0.94, 0.9, 0.83, and 0.73 V for 500,

600, 700 and 800 ºC, respectively. Also, those values decrease from 0.94 to 0.73 V with the temperature increase and close to 0.98 V of theoretical value at 600 ºC [228, 229].

Partial reduction of Ce^{4+} to Ce^{3+} restricts the usage of the GDC as single-layer electrolyte. Multivalency of Ce atom gives the material electrical conductivity, which lowers the OCV values and power density as a result [230]. Consequently, intermediate temperature solid oxide fuel cells are mostly prepared using the single-layer GDC electrolyte, whose characteristics are studied at temperatures not higher than 650 ºC [231–236]. However, some studies considered that since the electrochemical reaction area expands, a small degree of electrolyte electrical conductivity can be advantageous for enhancing processes on electrodes.

Moreover, as GDC electrolyte has higher ionic conductivity than conventional YSZ electrolyte. This enhanced ionic conductivity causes as increase in the oxide transport at the interface between electrode/electrolyte, which minimizes the charge transfer polarization resistance. Therefore, the SOFC total polarization resistance could be decreased and permits further improvement in cell performance [237, 238].

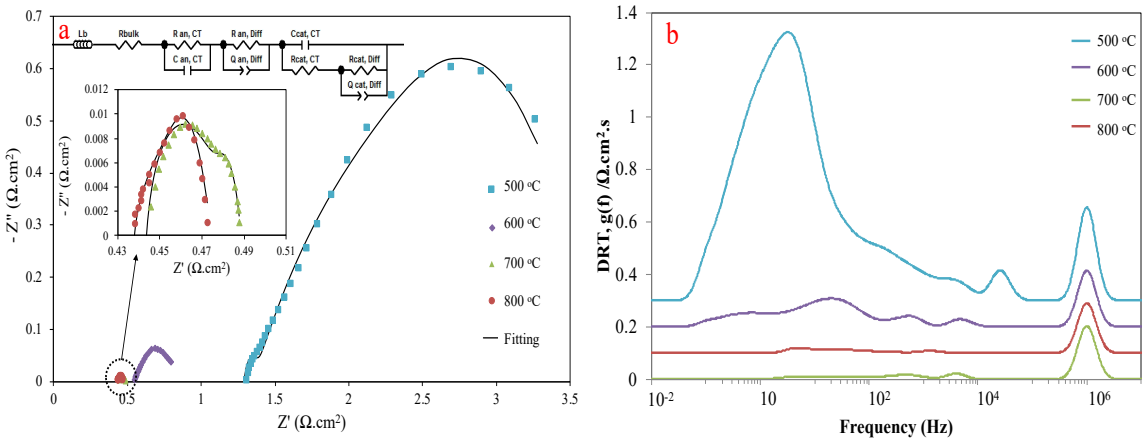


Figure 3.20. (a) Nyquist plots of LV05SC-GDC-NiGDC cell at OCV conditions, inset: Equivalent circuit model, (b) DRT curve of impedance spectra as a function of operating temperature at 500 - 800 ºC.

The Nyquist data shown in Figure 3.20a displays the impedance of the cell with GDC electrolyte studied at 500 - 800 ºC. It is common to see a semi-circle arc in impedance spectra. The ohmic and polarization resistance could be measured by the intercepts on the x-

axis. Total resistance decreases as the working temperature increases. This is because, as the temperature decreases, the total resistance of the cell increases and the high-frequency arc intensity also increases and moves into the lower frequency area. This trend indicates that the reaction steps in the cell could be signified as physicochemical processes. Lower than 700 ^{o}C, the low frequency arc intensity increases, suggesting a temperature independent behavior [239]. The same behavior also can be observed in Figure 3.20a that the cell has lower total resistance at 700 ^{o}C.

Table 3.3. EIS Fitting values of LV05SC-GDC-NiGDC fuel cell at 500-800°C.

	500 ^{o}C	600 ^{o}C	700 ^{o}C	800 ^{o}C	Unit
Ran, Diff	0.46265	0.545	0.000443	0.062	ohm.cm^2
Lb	3.89E-07	3.62E-07	3.58E-07	3.54E-07	H
Rbulk	0.5075	1.64E-05	1.68E-06	9.58E-05	ohm.cm^2
Rcat, Diff	1.984	0.255	0.044225	0.0727	ohm.cm^2
Rcat,CT	0.7655	0.012515	0.4378	0.3692	ohm.cm^2
Ccat, CT	3.87E-08	0.0011	7.2E-08	8.78E-08	F
Qcat, Diff	0.0588	0.212	0.236	5.65	S*s^a
a2	0.5	0.5528	0.5	0.1876	
Qan, Diff	0.30105	1.18E-07	255.8	1.24E-06	S*s^a
a1	1	0.9432	1	0.7054	
Ran, CT	0.0834	0.018795	0.00625	0.01286	ohm.cm^2
Can, CT	7.69E-05	15.395	4.851	0.8775	F

To deepen the reaction mechanism, the corresponding equivalent circuit model is represented in the inset of Figure 3.20a and the fitting parameters were given in Table 3.3. The DRT spectra calculated from the impedance of the cell was shown in Figure 3.20b and Figure 3.21b. In Figure 3.20b, the intensity as well as the polarization of the peaks at lower frequency diminish as temperature increases. However, the peak at high frequency range which is related to charge transfer process is less temperature-dependent. As the integral peak area denotes to electrode polarization resistance, the peaks at 700 ^{o}C have the lowest values. In Figure 3.21b, DRT analysis of the impedance data under different applied potentials derived from the impedance data at Figure 3.21a were presented.

In Figure 3.21b, five DRT peaks were spotted and each peak has its own electrode reaction process. Two or three DRT peaks at high frequency were attributed to the charge transfer and oxide ion transfer processes. At mid-frequency region, peaks are related to diffusion and exchange of oxygen species at the TPBs. The oxygen nonstoichiometric variations were patterned below 1 Hz. However, some corresponding peaks were overlapped for each cell reaction. As seen from the DRT analysis in Figure 3.21b, P2-P5 became more recognizable and shifts to lower frequency region with increasing applied voltages. Although P1 peak was not affected by voltage differences, this difference avails the P4 peak intensity became more exquisite at 10 Hz, which is labelled as oxygen gas diffusion in cathode.

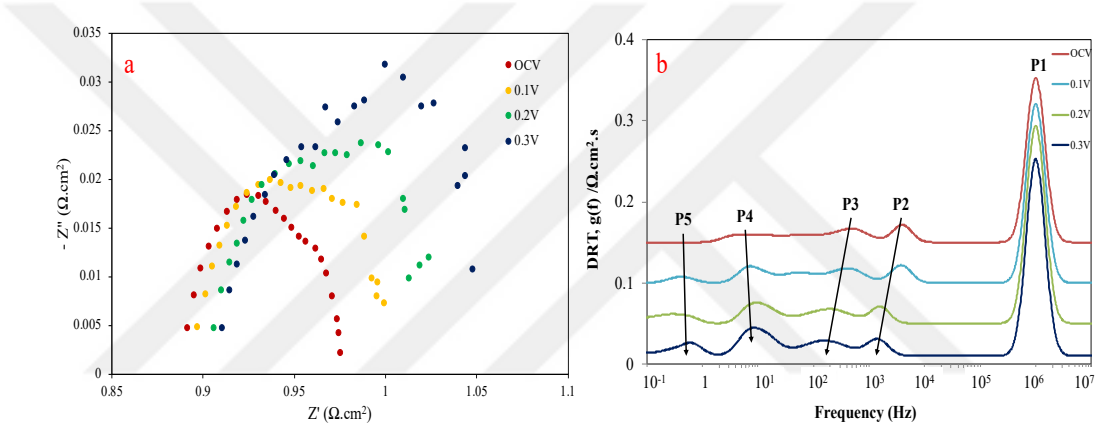


Figure 3.21. (a) Nyquist plots of LV05SC-GDC-NiGDC cell, (b) DRT patterns under different applied voltages at 700 °C.

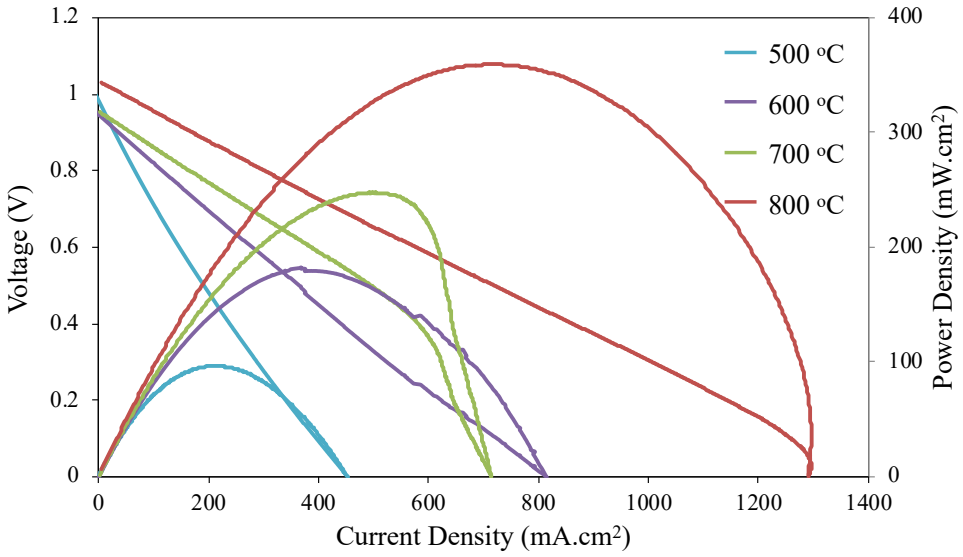


Figure 3.22. I-V curves and output power density of single cell with LV05SC- GDC (35 µm)-YSZ-NiYSZ at different temperatures.

The developed cathode material was then combined with double-layer electrolyte anode supported half-cell. Figure 3.22 shows the I-V and I-P polarization curves of the LV05SC- GDC (35 µm)-YSZ-NiYSZ cell at various temperatures between 500 – 800 °C. At 800 °C, peak power density of 360 mW/cm^2 was reached with 1.03 V open circuit potential. The ohmic and concentration polarization under high current density were the rate-determining processes of this cell, according to the IV characteristics and impedance data. The improved cell should operate even better at lower temperatures if the microstructures of electrodes especially cathode compartment and also electrolyte thickness are optimized.

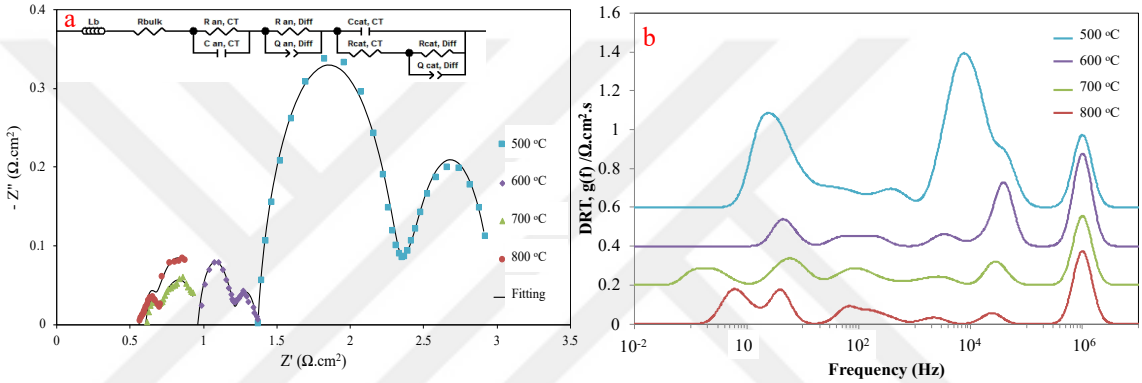


Figure 3.23. (a) Nyquist plots of LV05SC-GDC (35 µm)-YSZ-NiYSZ cell at OCV conditions, inset: Equivalent circuit model, (b) DRT curve of impedance spectra as a function of operating temperature at 500 - 800 °C.

However, the cell potentials and measured polarization curves only show the overall performance loss; precise information on losses and fluctuations caused by polarization and ohmic resistances during cell operation was not provided. Therefore, in order to determine which sub-reaction is in charge of the cell deterioration, EIS method and equivalent model fitting were performed and the resultant values were given at Table 3.4. The relevant measured spectra were displayed in Figure 3.23a. From the Nyquist spectra two arcs can be prominent at high and low frequencies. It is apparent that the ohmic resistance – the high frequency contact with the x-axis – has decreased as working temperature increases. The high-frequency arcs in EIS spectra, on the other hand, are comparable and only slightly alter in size over time. However, there are noticeable variations in the low-frequency arc. In anode-supported cells, the anode mostly affects the high frequency area (above 200 Hz), while the cathode effects the mid-frequency zone (1-400 Hz) and diffusion affects the impedance spectrum below 10 Hz [221], [240-244]. While the greatest variation in the

spectrum is mostly seen at low frequencies, both cathode and anode influences could be seen in the imaginary part (y-axis) of the spectrum. But compared to the frequency zone corresponding to cathode reaction processes, zone allocated to anode reactions changed comparatively negligible, suggesting that the anode was only slightly influenced, leading to a minor rise in the polarization – activation and concentration – resistances. Given that reactions related changes in the cathode are responsible for the detected behaviors of the impedance spectra, this indicates that cathode deterioration was the primary factor contributing to the degradation performance of the cell [244, 245]. Several cell sub-reaction pathways have been examined by using the DRT analysis. The impedance elements were distinguished by this method based on the distinctive timeframes of each one. The DRT findings of LV05SC-GDC (35 μm)-YSZ-NiYSZ cell at 500, 600, 700 and 800 °C are displayed in Figure 3.23b. Charge transfer between the electrode and electrolyte is often responsible for high frequency region. Surface processes are represented by the intermediate frequency and gas diffusion by the low frequency region [246–248].

Table 3.4. EIS Fitting values of LV05SC-GDC (35 μm)-YSZ-NiYSZ cell at 500-800°C.

	500 °C	600 °C	700 °C	800 °C	Unit
Ran, Diff	0.592	0.15455	0.625	0.34645	ohm.cm^2
Lb	3.74E-07	3.91E-07	3.77E-07	3.83E-07	H
Rbulk	0.9245	0.20805	0.1393	1.75E-05	ohm.cm^2
Rcat, Diff	1.024	0.30775	0.2258	0.0961	ohm.cm^2
Rcat,CT	0.40995	0.028865	0.4013	0.044845	ohm.cm^2
Ccat, CT	9.53E-08	9.54E-07	1.03E-07	2.36E-05	F
Qcat, Diff	0.000318	0.000685	1462	2.2805	S*s^a
a2	0.7277	0.6514	0.9762	0.8782	
Qan, Diff	0.16165	0.36785	0.36265	0.3819	S*s^a
a1	0.771	0.6095	0.2146	0.3195	
Ran, CT	0.033765	0.6675	0.04564	0.5075	ohm.cm^2
Can, CT	0.1105	4.89E-08	6.18E-05	7.2E-08	F

In Figure 3.23b, the highest intensity peaks are seen in the surface exchange domain, indicating that those sub-reactions account for the majority of impedance losses at 500 - 600 °C. However, with increase in temperature they diminished and the peak at high frequency stays unaffected by the temperature difference. In contrast to the impedance curve in Figure

3.24a; which exhibits overlap between the polarization reactions, the computed DRT peaks distinctly demonstrates at least seven separate reactions in Figure 3.24b. It is evident that the process P1 which charge transfer reactions was inactive both thermally and under applied potentials. Processes P2 -P7 perform, by contrast, thermal activation and specific voltage dependencies. All peaks except charger transfer shifts to lower frequency region and superimposed each other with increase of applied voltage. This shows that except P1, P7 identified as mass transport sub-step remained resistive under different temperature and voltages.

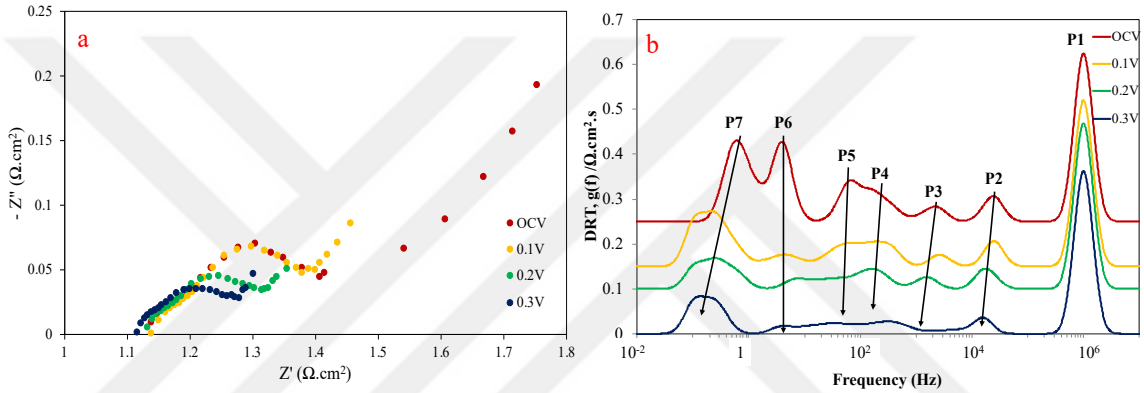


Figure 3.24. (a) Nyquist plots of LV05SC-GDC (35 µm)-YSZ-NiYSZ cell, (b) DRT patterns under different applied voltages at 800 ºC.

Figure 3.25 shows cell potential and current-power density curves of the cell with 5 µm GDC barrier layer at 500 – 800 ºC in H_2 fuel. The OCV values of the cell were app. 1V, which is a little lower than the theoretically expected value. Imperfect sealing and a small short circuit resulting from the thin GDC/YSZ double-layer electrolyte might be the cause of the lower OCV values. Also, partial reduction of Ce^{4+} to Ce^{3+} in GDC material reduces the open circuit potential. The maximum power density was 90 mW/cm^2, which is 75% lower than the cell with 35µm GDC/YSZ bi-layer electrolyte. Performance measurements could show some valuable information about the cell structure, however analyzing in detail the cell reactions via impedance spectroscopy and DRT analysis should be continued. Electrochemical Impedance spectroscopy (EIS) measurements at open-circuit potential for LV05SC/GDC (5 µm)/YSZ/NiYSZ cell were recorded at the temperature range of 500 – 800 ºC. In the experiments, various electrochemical reaction steps, such as charge transfer, gas diffusion or adsorption, were analyzed. The Nyquist plots as a function of temperature are displayed at Figure 3.26a. As predicted, the resistance values which were derived from the

diameters of the impedance arcs have dropped as temperature increases. Many processes overlapped with each other, hence only two semi-circle arcs were visible.

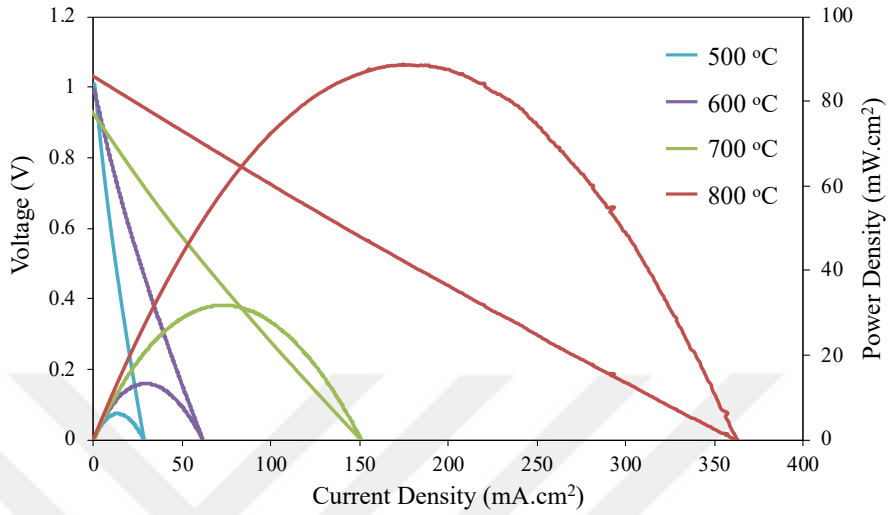


Figure 3.25. I-V curves and output power density of single cell with LV05SC- GDC (5 µm)-YSZ-NiYSZ at different temperatures.

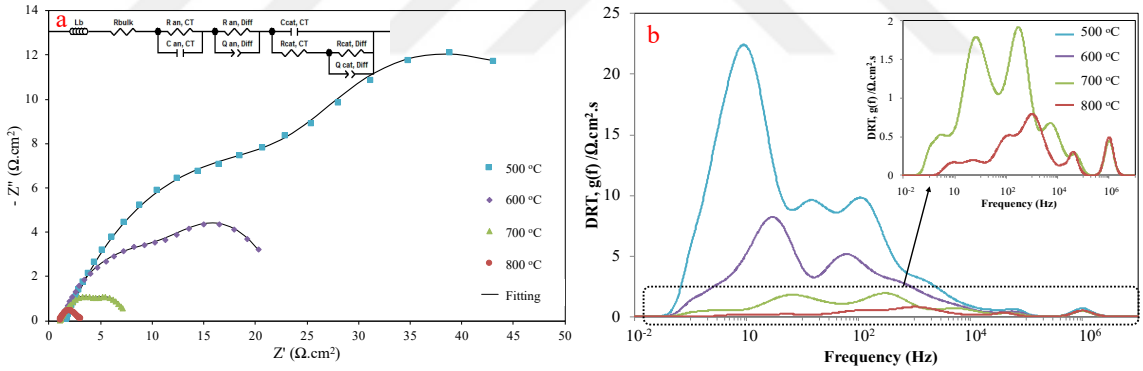


Figure 3.26. (a) Nyquist plots of LV05SC-GDC (5 µm)-YSZ-NiYSZ cell at OCV conditions, inset: Equivalent circuit model, (b) DRT curve of impedance spectra as a function of operating temperature at 500 - 800 °C.

Figure 3.26a inset shows the equivalent circuit model and the fitting results were given in Table 3.5. As clearly seen that $R_{cat,diff}$ has the highest polarization resistance among other cell resistances. However, fitting an impedance data is a judgmental issue. So, by computing the distribution of relaxation times, the overlapping impedance arcs were deconvoluted in order to examine the electrode processes in more detail. Figure 3.26b represents the findings. In Figure 3.26b, comparison between different temperatures were studied and it revealed that low frequency processes were more resistive in lower temperatures. As the working

temperature increases, those processes became less dominant, indicating that mass transfer reactions were no longer resistive steps. Also, the mid-frequency reactions which are surface exchange processes developed at 800 °C, proving that oxygen gas diffusion at cathode shows largest resistance as revealed at impedance data.

Table 3.5. EIS Fitting values of LV05SC-GDC (5 µm)-YSZ-NiYSZ fuel at 500-800°C.

	500 °C	600 °C	700 °C	800 °C	Unit
Ran, Diff	31.29	10.605	2.215	0.8105	ohm.cm^2
Lb	3.8E-07	3.84E-07	4.12E-07	3.9E-07	H
Rbulk	1.063	0.5235	0.010745	0.41255	ohm.cm^2
Rcat, Diff	25.265	10.825	4	1.2235	ohm.cm^2
Rcat,CT	0.572	0.5745	0.9635	0.577	ohm.cm^2
Ccat, CT	6.13E-08	4.76E-08	2.43E-08	6.59E-08	F
Qcat, Diff	0.001127	0.00178	0.020115	0.00527	S*s^a
a2	0.5419	0.538	0.5465	0.6	
Qan, Diff	0.014345	0.01471	0.003324	0.019	S*s^a
a1	0.6513	0.6469	0.5124	0.4	
Ran, CT	5.365	1.1525	0.615	0.1323	ohm.cm^2
Can, CT	0.026515	0.08635	0.001407	0.9175	F

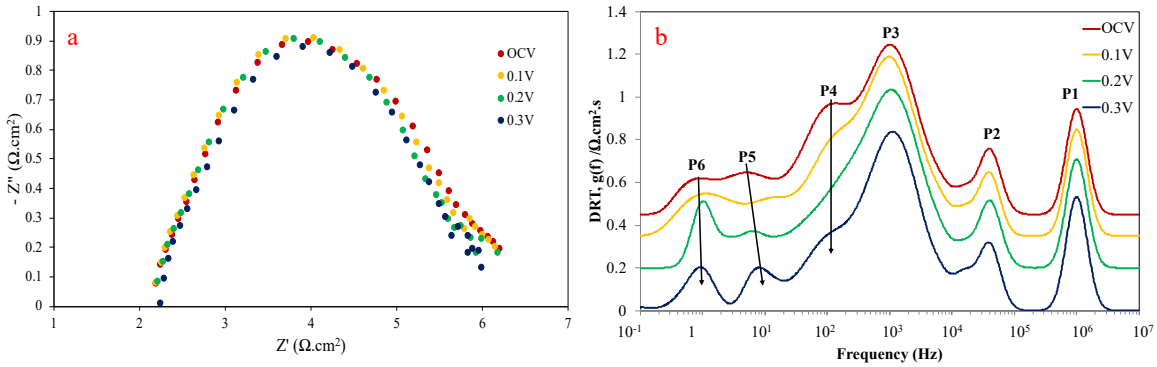


Figure 3.27. (a) Nyquist plots of LV05SC-GDC (5 µm)-YSZ-NiYSZ cell, (b) DRT patterns under different applied voltages at 800 °C.

Six DRT peaks derived from Figure 3.27a were found over the investigated time scale with several applied potentials in Figure 3.27b. Every peak denotes a rate-limiting electrode reaction, and the resistance of the corresponding process is indicated by the peak's area. P1

and P2 were attributed to bulk resistance as well as the oxide ion incorporation at the electrode/electrolyte interface and fuel charge transfer at anode, respectively.

Also, they were unresponsive to voltage differences. P3 peak at mid-frequency which denoted to the diffusion of oxygen species to the TPBs, remained invariant as well. However, when voltage was varied, P4 showed slight decrease which means that increasing given potential to the system ease the oxygen surface exchange and reduction reaction. At low frequency region, P5 and P6 peaks behaved in opposite way, showing the properties of diffusion related reactions. Hence, those DRT findings were in good agreement with the earlier indicated EIS and model fitting results.

3.5. Conclusion

As a conclusion to this chapter, single cells with YSZ, GDC and bi-layer electrolytes were produced and their performance, impedance and DRT behaviors under different temperature and voltages were reviewed. It was concluded that the cells with GDC (35μm)/YSZ double layer electrolyte exhibited highest power density with 360 mW/cm^2. In EIS plots, two separate arcs were visible showing highest polarization resistance contribution from mid and low frequency regions. Also, from the circuit model fitting results at Table 3.2 – 3.5, it could be reviewed that $R_{cat,diff}$ sub-reaction has the highest influence on total resistance with the values of 11373, 2.35, 1.6 and 41.32 Ω/cm^2 for single cells with YSZ, GDC, GDC (35 μm)/YSZ and GDC (5μm)/YSZ electrolyte combinations, respectively. From the DRT findings, charge transfer resistance contribution was neglected, because this peak is mostly labelled for transport of oxide ions through electrolyte network which is called as R_{bulk}. For single cell with YSZ electrolyte has performed largest resistance at diffusion and exchange of oxygen species (O^-/O_2^{2-}) at the TPBs and mass transfer of reactants in the cathode processes, and also the cell showed dependency on applied voltages at low frequency. The mass transfer reactions such as oxygen and hydrogen gas diffusion in the electrodes have become more visible. In the cell with only single layer GDC electrolyte, minor contributions from each cell process, except charge transfer in electrolyte, were bserved. With increasing applied voltage, peaks separated from each other and P4 which signifies ORR at cathode has the highest peak intensity.

In order to compare bi-layer electrolyte influence in the cell performance, GDC layers were attached with different thicknesses on conventional YSZ electrolyte. In the first situation, GDC layer with 35 μm thickness were tape casted and laminated, and the performance, EIS and DRT results were studied. It has the highest power density among the other combinations and the lowest $R_{cat,diff}$ value in equivalent circuit fitting results. This estimation was also approved by DRT findings. Low frequency peaks have the major effect on total cell resistance. With applied potentials, mass transfer related processes were affected and have shifted towards lower frequencies showing contribution originates from the flux of the reactants.

At the final case, a thin GDC layer were laminated with YSZ electrolyte and the cell was undertaken various experiments. The cell has exhibited similar behavior with the first cell prepared with YSZ electrolyte. Cathode surface exchange reactions has been determined as the rate limiting steps same as the case in the first cell. Moreover, with applied potentials gas diffusion processes developed higher resistances.

After all sets of analysis, modelling and calculations with different electrode and electrolyte material combinations, and their micro and 3D structures; the materials and interfaces could be manipulated and tailored on different length scales. Difficulties at the electrochemical interface can be identified by connected chemical, structural, and electrochemical characteristics in combination with comprehensive characterization approaches.

4. SYNTHESIS, CHARACTERIZATION AND PERFORMANCE ANALYSIS OF $La_{0.50}Gd_{0.10}Sr_{0.4}CoO_{3-\partial}$ (LG10SC) CATHODE SAMPLE

4.1. Introduction

One of the main objectives for solid oxide fuel cell global commercialization is to bring down the cost and improve stability by lowering working temperature to 400 – 700 ^{o}C [249]. Numerous oxide materials including Mn, Fe, Co and Ni have been investigated for use as cathode materials at intermediate temperatures [250–252]. The oxygen ion diffusion coefficient, oxygen surface exchange rate, and electrical conductivity are the three basic properties that electrode formulations have been created to calculate in terms of cathode performance. There is a substantial amount of data that demonstrates the higher activation rates of cobalt-containing perovskites and establishes these parameters. Since Cobalt can adopt 2+, 3+, and 4+ oxidation states, compounds containing Cobalt have usually been the subject of much research due to their unusual electrical and magnetic characteristics [50].

The perovskite oxides $LnBaCo_2O_{5+\partial}$ (LnBCO; Ln = La, Pr, Nd, Sm, Gd and Y) have been studied as intermediate temperature SOFC cathodes in recent years due to their high electrical conductivity, fast oxygen diffusion and surface exchange kinetics, which result in excellent electrochemical performance [253–259]. By doping or non-stoichiometry on either cation or anion sub-lattices, the composition of ABO_3 may be greatly enhanced. Such modifications trigger the improvements on electrical and ionic conductivities, sintering behavior and catalytic performance. The perovskite structure offers an a priori choice of the active site crucial to catalysis when an inactive A-site ion (like La^{3+} or Sr^{3+}) is combined with active B-site ion (like Co^{3+}, Mn^{3+} or Ti^{3+}). Additionally, the selection of the A ion can change the characteristics of the B ion and its nearby oxygen ions [158]. By doping Gadolinium metal to the A site, the oxide electro-neutrality and charge compensation mechanism suggests that the negative charge defect caused by Sr^{2+} replacing La^{3+} at the A-site is compensated by Gd ions. Gd^{3+} is the two key oxidation state which is proved by XPS analysis.

The development of anode supported cells has been inhibited to this day in part by our lack of a thorough knowledge of the physical causes and contributions of the many polarization processes that affect the performance of the cell. One of the most promising techniques for deconstructing intricate electrochemical systems, like SOFCs, is electrochemical impedance spectroscopy (EIS). The resultant impedance spectra are frequently examined using an equivalent circuit approximation of a model function. Without knowing the precise amount of polarization processes that really contribute to the cell's overall voltage loss, the equivalent circuit model must be specified already in this situation. This frequently results in the accepted model having quite a lot of uncertainty. In this study, an alternate method for assessing impedance spectra is employed to address that drawback. The distribution function of relaxation times (DRT) associated with the impedance response is analyzed in order to pre-identify the causes for voltage losses. The information gathered in this method was utilized to evaluate potential cathode compositions in terms of surface exchange kinetics and oxide ion diffusion, allowing the rate limiting parameters to be found.

In this chapter, it was studied certain perovskite oxides with substitution of Gd^{3+} arranged A-cations to understand ORR mechanism in the operation of SOFC on intermediate temperature range by employing the tape casting and co-firing procedures to generate the single cells with anode-supported thin electrolytes to enhance the electrical characteristics of perovskite materials. Both electrical and ionic conductivities, and the performances of perovskite materials have been measured for a variety of temperatures by employing EIS and DRT calculations. As a results of these analysis, adsorption, dissociation, and diffusion processes were found to be the ORR's limiting steps. These findings suggest that this Gd-doped perovskite structure, LG10SC, is a promising cathode material for IT-SOFCs.

4.2. Material Synthesis

Applying the sol-gel method, $La_{0.6-x}Gd_xSr_{0.4}CoO_{3-\partial}$ (LGxSC, x = 0.10) powders were produced. Reagents included La, Gd, Sr, and Co nitrates as (purity > 99.9%, Aldrich Chemicals, USA). Separately, each reagent was dissolved in distilled water at the proper stoichiometric ratio. To produce a homogenous solution, all of the solutions were afterwards combined and agitated. As complexation and polymerization agents, ethylene glycol and citric acid, in varying amounts, were added after they had completely dissolved.

The citric acid to total metal ions ratio was maintained at approximately 1:2. The solution was allowed to evaporate on a hotplate upon prolonged heating, the gel spontaneously burned, transforming into a light and delicate ash. Following a gentle heating-induced gelation, the resulting gel was placed in a drying oven at 500 °C for 2 hours to eliminate organic components. Subsequently, it was subjected to sintering at 900 °C for 3 hours to yield perovskite compounds possessing satisfactory crystalline structure, as confirmed through X-ray diffraction analysis.

4.3. Characterization, Electrochemical Measurements and Fabrication Procedures

The phase identifications of $La_{0.5}Gd_{0.1}Sr_{0.4}CoO_{3-\partial}$ (LG10SC) cathode sample were obtained by X-ray diffraction (XRD) employing a Rigaku D/MAX-Ultima+/PC Diffractometer with Cu-Kα radiation (λ = 1.54056 Å). The diffraction patterns were recorded in the range of $20^o<2\theta<80^o$ with 0.01 steps and step-counting time of 8s/step. The phases were identified with JCPDS Database. Thermo Scientific's Kα Surface Analysis instrument was used for the XPS analysis. The surface properties of the powdered materials were captured using an Al-Kα X-Ray source (hv = 1486.6 eV) at room temperature and a 10^{-7} Pa vacuum) with a spot size of 400 μm, and the constant pass energy values were set at 150 eV. The charge effect was calibrated using the binding energy of C1s (284.5 eV), and the energy step size was adjusted at 0.100 eV. XPS Peak 4.1 software was used to collect and analyze survey spectra at a pass energy of 50 eV and high-resolution spectra at a pass energy of 20 eV for quantification purposes. SEM-FEG, Philips XL 30 at an accelerating potential of 10 kV was used to study the surface and cross-section morphology of the sintered cells. Performance and electrochemical impedance spectra (EIS) were measured from 500 to 800°C utilizing a self-made test setup contained of numerous gas mass flowmeters, a furnace (Figure 3.1). The sintered cells were attached to a zirconia tube with a ceramic paste. The electrodes' current collectors were made of Au paste and wires connected the electrodes to the testing instrument. The current-voltage (I -V) characterization was conducted with the Gamry Ref 3000 Potentiostat (Gamry Instruments, Warminster, PA, USA) using H_2 as the fuel and oxygen as the oxidant. The AC impedance data were collected with an AC signal of 10 mV in the frequency range of 1 MHz - 0.1 Hz.

Commercial YSZ (Yttria-Stabilized Zirconia (8% Y) – Tape Cast Grade Powder, Fuel Cell Materials Ltd., USA) and GDC (Gadolinium Doped Ceria (20% Gd) – Tape Cast Grade Powder, Fuel Cell Materials Ltd., USA) powders were used to prepare the electrolyte layers. The anode slurry was obtained by mixing YSZ or GDC and fine grade NiO powder (Fuel Cell Materials Ltd., USA). A two-step ball milling procedure was used to produce the slurries for tape casting. In the first step, polyvinyl butyral (PVB) was used as the binder and ethanol/toluene as the solvent to homogeneously disperse all the particles. Secondly, in order to give an ideal viscosity, the required amounts of plasticizers polyethylene glycol (PEG) and benzyl-butyl-phthalate (BBP) were added to the slurry and ball-milled again for 24 hours. There were two processes in the tape casting process as well. The de-aired electrolyte and anode slurries were initially cast at a blade height of app. 10, 20 and 200 μm, respectively.

The green tapes were cut into disks with a 13mm diameter after drying for 24 hours. One sheet of YSZ and/or GDC electrolytes and two layers of anode green tapes were stacked in order to produce anode-supported cells. The layers were assembled in random directions for relaxation of the residual internal stress and uniaxially laminated for 5 mins. The laminates were subsequently co-sintered at 1250 ^{o}C in air for 3h after burn-out of the organic components. Following co-sintering, the cathode paste was produced using LV05SC powder and electrolyte material with a weight ratio of 50:50, and brush coated onto electrolyte with an active area of 0.5 cm^2. The cathode layer was then sintered at 1100 ^{0}C for 5 h.

4.4. Results and Discussion

4.4.1. Phase Composition and Structure

The crystal structure and composition of perovskite can be studied using XRD analysis of cathode materials, which can aid in improving the SOFC cathode's performance by examining the effects of various processing conditions. The phase, purity, and crystallinity of the $La_{0.5}Gd_{0.1}Sr_{0.4}CoO_{3-\partial}$ (LG10SC) perovskite cathode material were determined using the X-ray diffraction method. The XRD for the cathode sample produced by the sol-gel procedure is displayed in Figure 4.1 following a three-hour calcination at 900 ^{o}C. With small

secondary phases, a deformed rhombohedral structure (space group R-3c:167) is generated. The lattice parameters, phase, and crystallite size were computed and compared to the software crystallographic open database (COD).

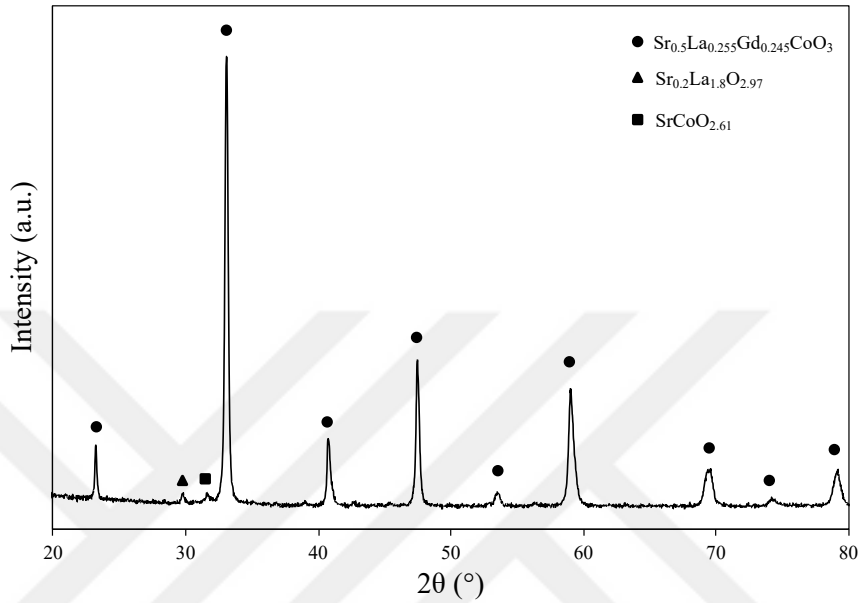


Figure 4.1. XRD data of $La_{0.5}Gd_{0.1}Sr_{0.4}Co_{3-\partial}$ cathode powder.

A single phase with lattice parameters of *a, b* = 5.408 Å, *c* = 13.198 Å α, β = 90.00° γ = 120.00°, and volume of 334.27 $Å^3$ is shown by the XRD pattern of the produced cathode material. The rather strong peaks in the XRD pattern show that the metal oxides utilized in the powder syntheses have been well incorporated into their lattice. These findings demonstrate that the prepared catalysts have effectively produced $ABO_{3-\partial}$ perovskite structures.

4.4.2. XPS Analysis

The surface properties of LG10SC sample examined by XPS, all elements, such as La3d, Gd4d, Sr3d, Co2p, and O1s have obviously existed in the crystal which is approved from the full scan survey spectra shown in Figure 4.2a. The XPS spectrum of La3d is shown in Figure 4.2b. It has two wide peaks with a splitting of 16.7 eV, one at lower binding energy at 833.01 eV and another at higher binding energy at 849.71 eV, which correspond to the La3d5/2 and La3d3/2 spectra, respectively. The relative intensity ratio for La3d5/2 and La3d3/2 is around 1.38; these values are closely related to those found in the literature [172].

The difference between the La3d5/2 doublet splitting, which is about 3.6 eV, confirms the existence of lanthanum hydroxides [173, 174]. As a result, the La3d is in +3 oxidation states, as shown by the distinct separation of these spin-orbit splitting. Also, the substitution of La ions by Sr and Gd ions did not result in any observable shift in the position of these peaks in XRD and XPS spectra.

Figure 4.2c show the high-resolution XPS peaks of Gd at the 4d core level. The Gd4d5/2 and Gd4d3/2 oxidation states are responsible for the peaks at binding energy 141.26 and 146.33 eV, confirming the presence of Gd^{3+} valence in the Gd-O-Gd bond in Gd_2O_3. The effective synthesis of Gd-doped LSC cathode is further confirmed by the XPS spectrum [260–263].

The Sr3d core-level spectra were particularly helpful for determining the bulk and surface contributions in the spectra since the Sr3d levels had a distinct surface core-level shift [183]. The performance loss of the cathode samples in SOFC is widely known to be caused by Sr segregation, which has been confirmed by earlier studies [184, 185]. Shown in Figure 4.2d, the Sr3d spectra were well matched using two sets of spin-orbit doublets with an energy separation of 2 eV and an area ratio of ~2. The significant peaks of the Sr3d5/2 and Sr3d3/2 components were seen in the spectra of the LG10SC sample at 131.0 and 133.2 eV, respectively. The contributions to the Sr3d photoelectron spectrum were discovered to be due to perovskite lattice-bound Sr ($Sr_{lattice}$). The Sr atoms in Sr-OH, Sr-CO_3, Sr-Sr, and Sr-O bonds near the surface of the cathode sample ($Sr_{surface}$), which do not have perovskite structures, are responsible for the two additional minor peaks at 132.5 and 134.5 eV [186–190]. Because no obvious peaks assigned to carbonates could be seen in the X-ray diffraction patterns (Figure 4.1), the effect caused by carbonate compounds is negligible. Furthermore, the binding energies of Sr in the Sr-O structure ($Sr_{surface}$) and Sr in the lattice ($Sr_{lattice}$) are very similar, even beyond the resolution limit of this experiment configuration. The $Sr_{surface}$ therefore most likely results from the formation of the $Sr(OH)_2$ phase from SrO or from the development of a $Sr(OH)_2$-like binding environment such as SrOH on the Sr of the perovskite lattice or on the Sr of a separated SrO phase. Even though it is clear that the $Sr_{surface}$ associated with $Sr(OH)_2$ species is mostly on perovskite lattice. For the LG10SC sample, the $Sr_{lattice}/Sr_{surface}$ ratio of 2 indicates that the $Sr_{lattice}$ component of the Sr3d occurs to a greater extent. A Sr-OH signature peak is present in the bonding environment in all three

cases (Figure 4.2f shows O1s spectra that demonstrates its presence). These results are as expected for a perovskite structure.

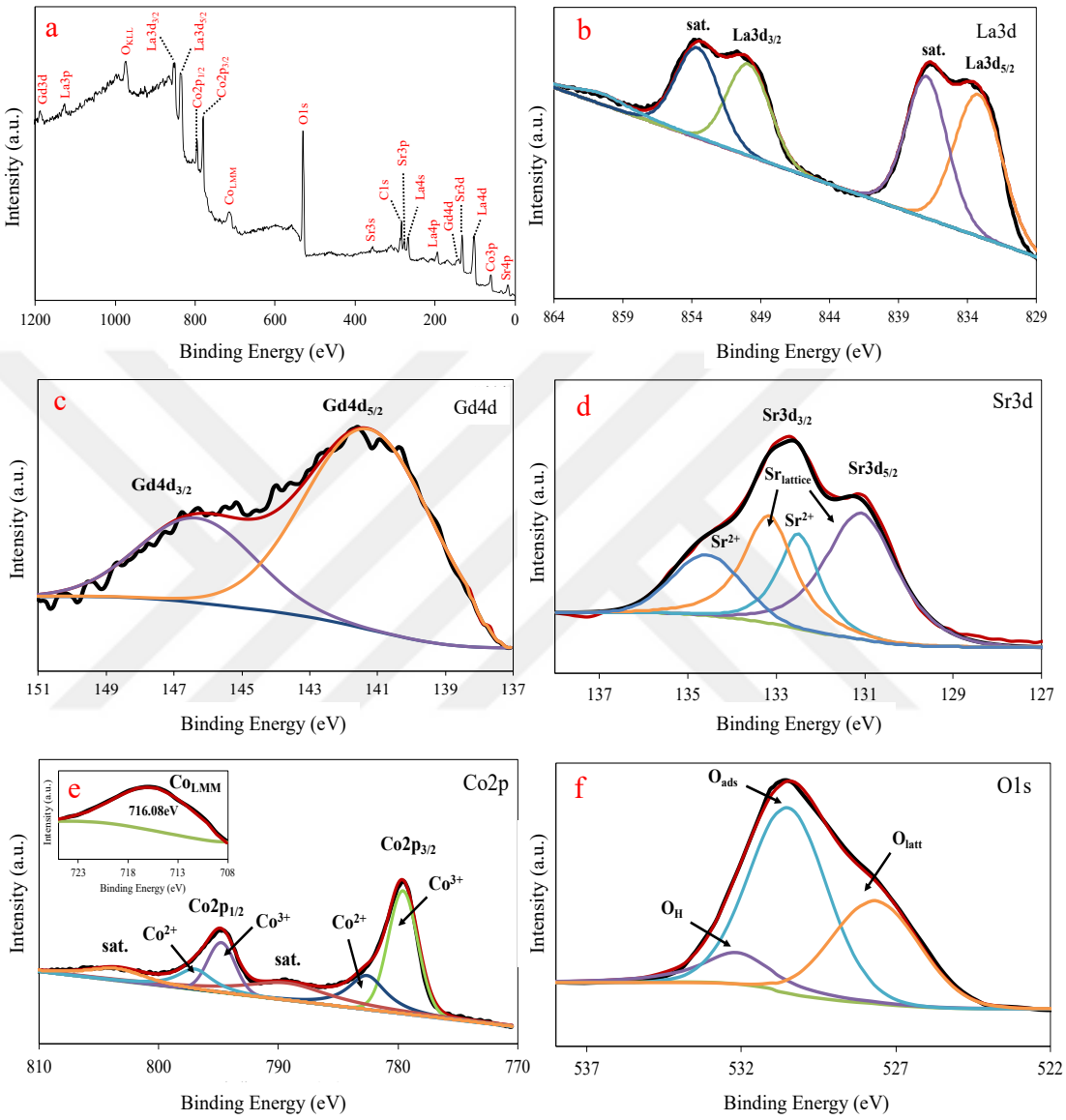


Figure 4.2. XPS survey spectra of (a) LG10SC perovskite, (b) La3d3/2 and La3d5/2, (c) Gd4d3/2 and Gd4d5/2, (d) Sr3d3/2 and Sr3d5/2, (e) Co2p1/2 and Co2p3/2, (f) O1s.

The Co2p spectrum is divided into two distinct peaks and two weak satellites, as shown by the XPS data in Figure 4.2e. Co2p3/2 and Co2p1/2 might be the two spin orbit doublets identified as cobalt oxides at 779.3 and 794.8 eV, respectively. Two peaks at 779.5 and 783.0 eV, corresponding to the Co^{3+} and Co^{2+} configurations, can be seen in the spin orbit doublet of Co2p(3/2). The Co2p(1/2) spin orbit doublet can also be divided into two different peaks that are attributed to Co^{3+} and Co^{2+}, respectively, and are located at binding energies of 794.8

and 796.9 eV. The Co_3O_4 cubic phase can be identified by the Co2p(3/2) and Co2p(1/2) splitting energy difference of 15.5 eV.

The appearance of the two satellite peaks at binding energies of 787.5 and 803.5 eV near the two spin orbit doublets provides additional evidence for the presence of cobalt oxides. This suggest that most Cobalt ions are present as trivalent cations with Co^{3+}/Co^{2+} ratio of 2.10 [191, 192]. Since the valence of Co ions mostly form with higher oxidation state such as Co^{3+} to Co^{2+}, the oxygen vacancies are formed in the crystal structure so that the electrical neutrality of the perovskite can be maintained. A higher Co^{3+} to Co^{2+} ratio enhances the catalytic capacity of sample surface to absorb oxygen, strengthening the Co-O bond and enhancing ORR performance. To adjust the electrocatalytic activity, Malkhandi carried out a comprehensive study on the perovskites. It was concluded that the catalytic activity is determined by the relative strength of the Co-O bonding [193]. The position of the Co_{LMM} Auger line (Figure 4.2e, inset) further supports the existence of both Cobalt valence states at Co^{2+} and Co^{3+}. The detailed explanation was given by Equation 3.1.

The XPS spectrum of O1s shown in Figure 4.2f exhibits two peaks, one at 530.5 eV due to adsorbed oxygen (O_{ads}) in the form of highly oxidative O^-/O_2^{2-} species, and one at 527.8 eV assigned to lattice oxygen (O_{latt}, O^{2-}) within perovskite. The extra peak at 532.1 eV, which is not always visible in O1s spectra, is caused by the physical and chemical adsorption of molecular water or hydroxyl groups on the surface of defects (O_H) [195–197]. In general, the oxygen vacancies that arise from the oxygen-deficient perovskite oxides can cause unique oxidation states of the transition metal ions, which in turn increases the catalytic activity of the perovskite catalysts [198]. Mostly, the pool of Oads is correlated with the amount of oxygen vacancy concentration. Accordingly, there may be a decrease in the lattice oxygen concentration when partial replacement of La and Sr by other cations leads to a formation of oxygen vacancies. The O_{ads}/O_{latt} ratio with the value of 1.63, LG10SC was greater than other synthesized cathode materials, because more vacancies were generated.

Since lanthanum oxide has a hygroscopic characteristic when exposed to air, the highest binding energy of O1s (532.15 eV) is thought to be due to a water molecule associated with the surface lanthanum oxide. It should be noted that molecular water and surface-adsorbed oxygen in the form of hydroxyl or oxygen groups could be easily removed

by heating to generate oxygen vacancies. But, removing highly oxidative oxygen species (O^- /O_2^{2-}) requires a significantly higher temperature.

4.4.3. Fabrication of Anode-Supported Electrolyte via Tape casting/Lamination/ Co-firing

5.

For producing thin, thick, flat, and large-area ceramic tapes with the thickness range of 10-1000 μm, tape casting is a respectable manufacturing technique. This method is employed to create a range of electrical devices, including multi-layer ceramic capacitors, low-temperature co-firing ceramics, and other devices and is quite straightforward compared to other common methods for fabricating ceramic layers. Making SOFC components by this method is particularly appealing since it may be more affordable to produce in large quantities. In order to manufacture planar electrode-supporting SOFCs, tape casting method has been extensively used. However, due to the challenges that come with fabricating a thin ceramic layer with no gas permeability, tape casting technology has not been successful in the fabrication of electrolytes with thicknesses below 10 μm. Co-firing of the electrode and electrolyte layers is another low-cost manufacturing method, and effective application of this technique would improve the productivity while consuming less energy. However, minimizing the deformation of the structure owing to mismatches in the thermo-mechanical and physical characteristics of the different layers was necessary for a successful co-firing of the multi-layer structure. There have been a few research efforts on fabricating the flat-type SOFCs.

The attempt to lower the operating temperature from 800 to 600 ºC or below is one of the primary research goals in this area. The benefits of SOFCs operating at lower temperatures include a larger selection of materials, improved long-term performance, system compactness and perhaps lower fuel cell costs [200, 201]. To address these concerns there have been many research efforts including reducing the thickness of the YSZ layer and using substitute electrolyte materials having better ionic conductivity than YSZ at low and intermediate temperatures, such as gadolinium doped ceria (GDC - $Gd_{0.2}Ce_{0.8}O_{1.95}$) and doped $LaGaO_3$ [202–206]. Despite the reports of effective operation at low and intermediate temperatures, the best materials and methods for low-cost process producing stable and consistently high SOFC performance have not yet been fully addressed. To achieve adequate

energy conversion rates and provide a suitable power output, a SOFC with a thin electrolyte sheet is preferred [207]. In this thesis, , thin YSZ/GDC electrolytes and NiOYSZ/NiOGDC anode layers were prepared via tape-casting (Figure 4.3). They were used to produce YSZ-NiOYSZ, GDC-NiOGDC, and YSZ-GDC-NiOGDC anode-supported fuel cells with different thicknesses.

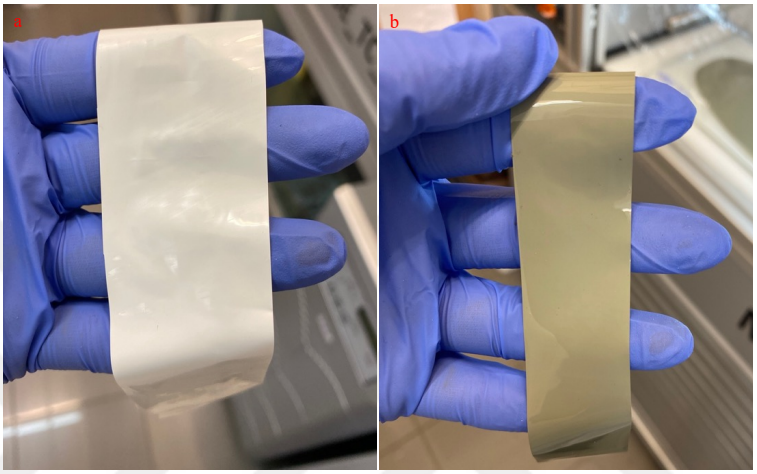


Figure 4.3. Pictures of the green tapes of (a) GDC electrolyte, (b) NiOGDC anode layers.

5.1.1. Surface Morphology Analysis of the Cell

Cross-sectional SEM micrographs of constructed fuel cells with an LG10SC cathode sample are shown in Figures 4.4–8. The electrolyte layers of YSZ and GDC have thicknesses of 19.39 and 50.53 µm, respectively. As seen in Figures 4.7 and 4.8, YSZ and GDC tapes of varying thicknesses were adhered together to examine the impact of double-layer electrolyte on cell performance. The YSZ electrolyte layer in certain combinations has a thickness of 14.69 µm, whereas the GDC layers have 37.02 and 5.29 µm.

Figure 4.6 illustrates how the microstructure looks like a sponge after nickel oxide is reduced by hydrogen. This is because the ultra-fine holes in the GDC and Ni particles are distributed uniformly and are mostly created during NiO reduction. It is clear that the thick, crack-free electrolyte layers were securely attached to the porous anode layers. More importantly, the first need for proper cell functioning was met since all of the cell's components were permanently attached together flawlessly and did not have a tendency to peel apart.

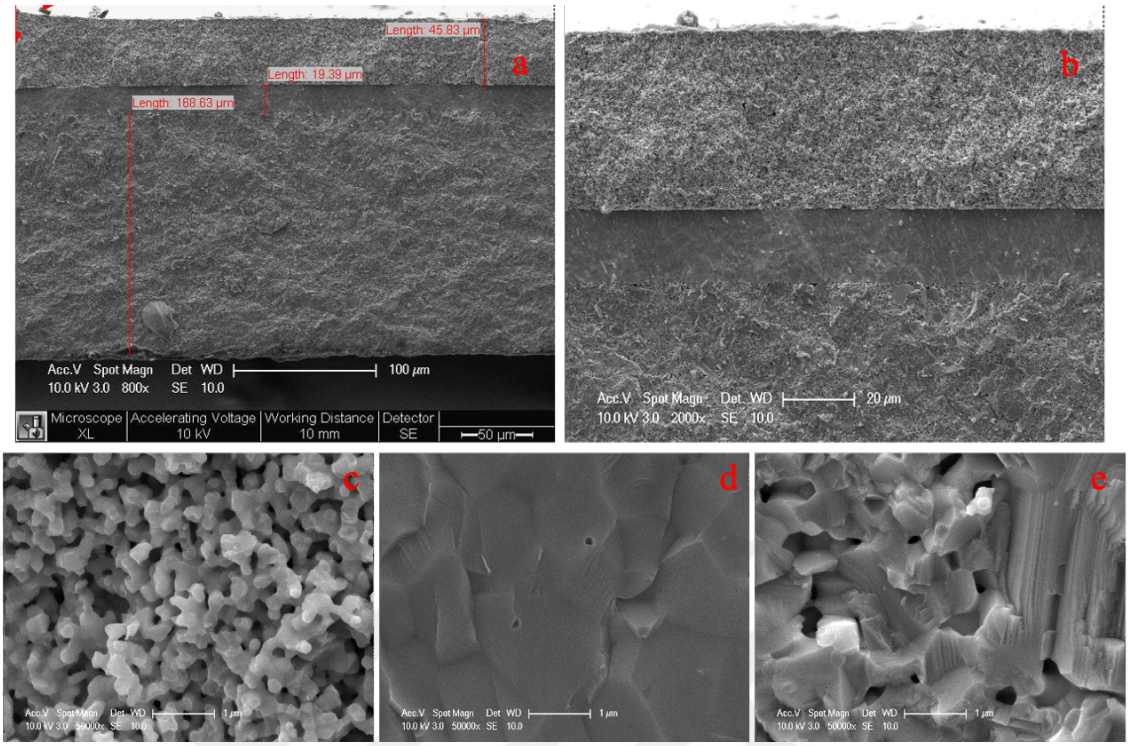


Figure 4.4. SEM images of LG10SC-YSZ-NiOYSZ fuel cell, (a) cross section, (b) closer look to interfaces, (c) LG10SC cathode, (d) YSZ electrolyte, and (e) NiOYSZ anode.

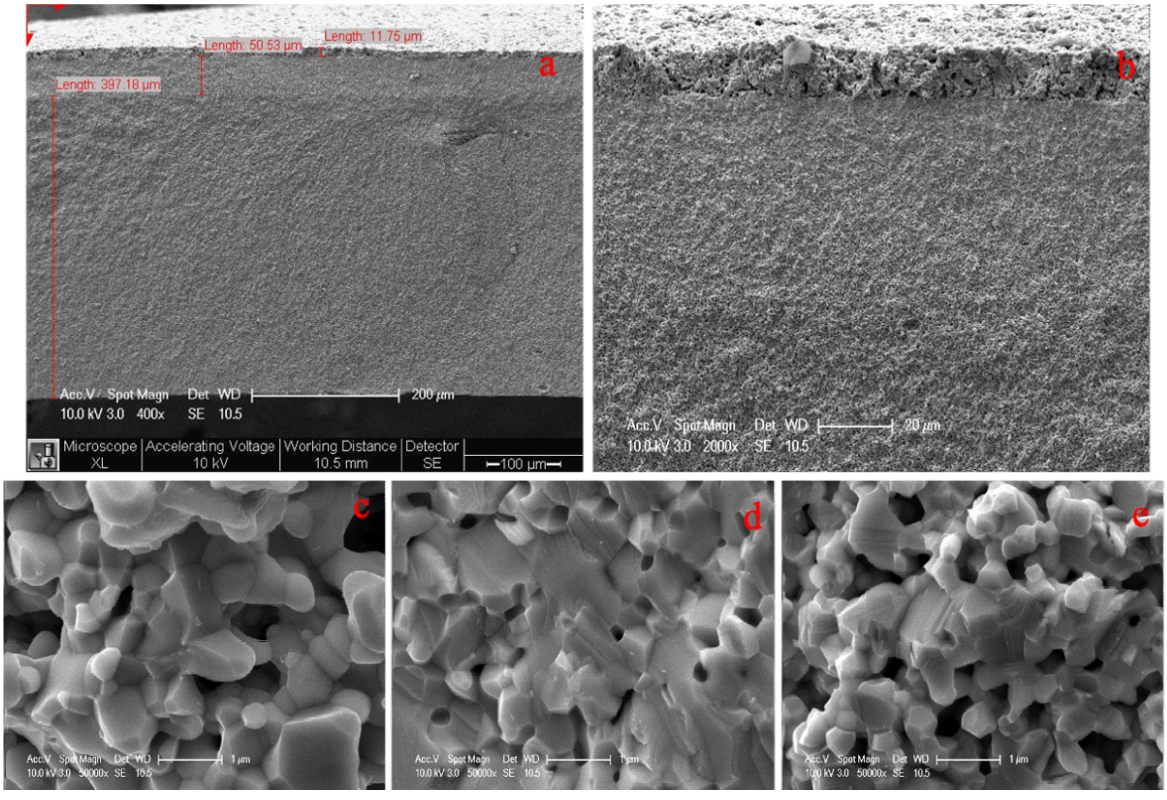


Figure 4.5. SEM images of LG10SC-GDC-NiOGDC fuel cell, (a) cross section, (b) closer look to interfaces, (c) LG10SC cathode, (d) GDC electrolyte, and (e) NiOGDC anode.

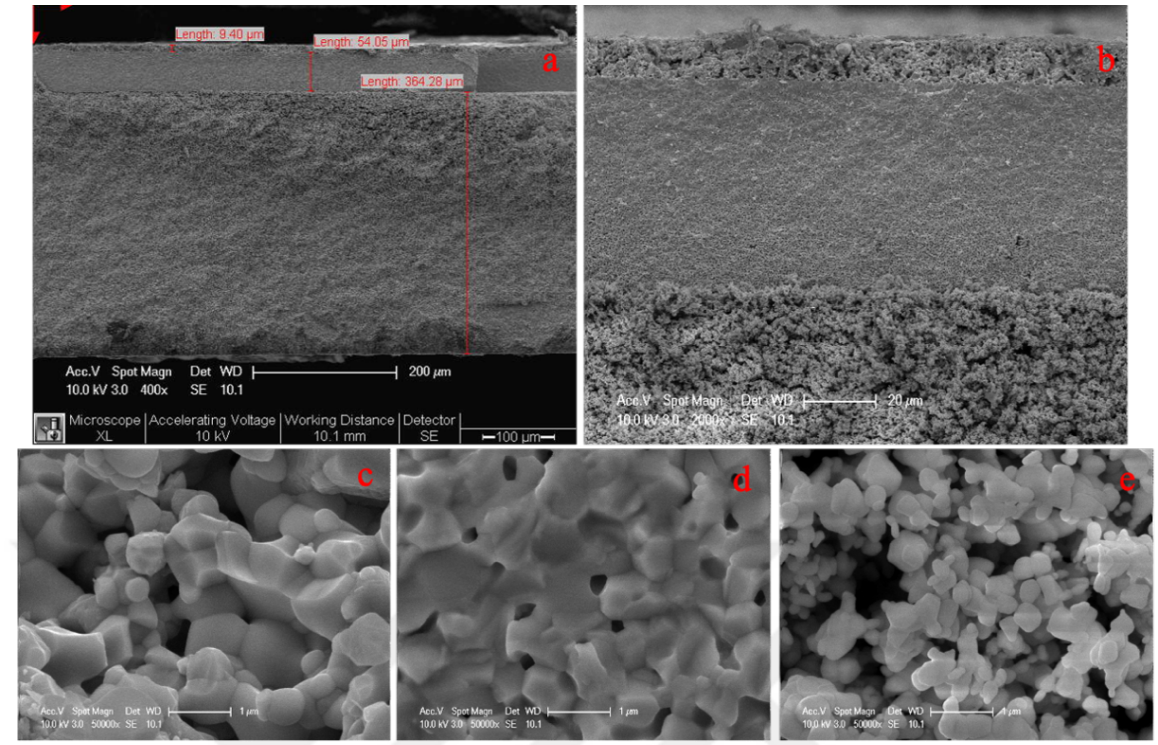


Figure 4.6. SEM images of LG10SC-GDC-NiGDC fuel cell after reduction by H_2, (a) cross section, (b) closer look to interfaces, (c) LG10SC cathode, (d) GDC electrolyte, and (e) NiGDC anode.

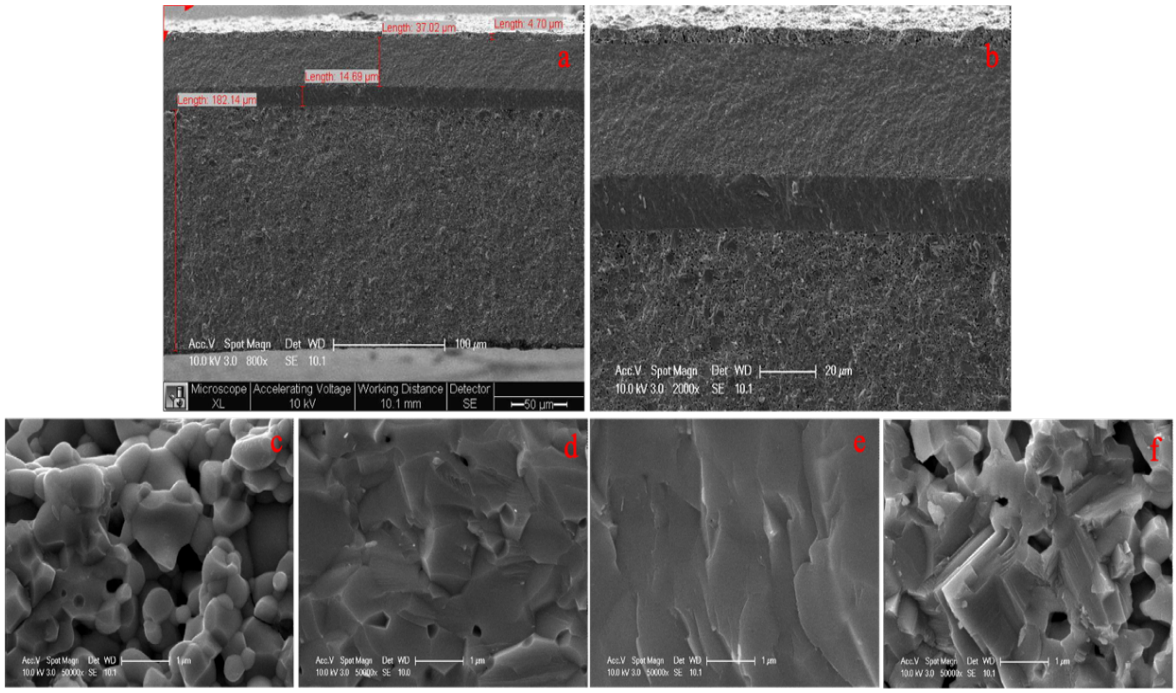


Figure 4.7. SEM images of LG10SC-GDC (35 µm)-YSZ-NiOYSZ fuel cell, (a) cross section, (b) closer look to interfaces, (c) LG10SC cathode, (d) GDC electrolyte, (e) YSZ electrolyte, and (f) NiOYSZ anode.

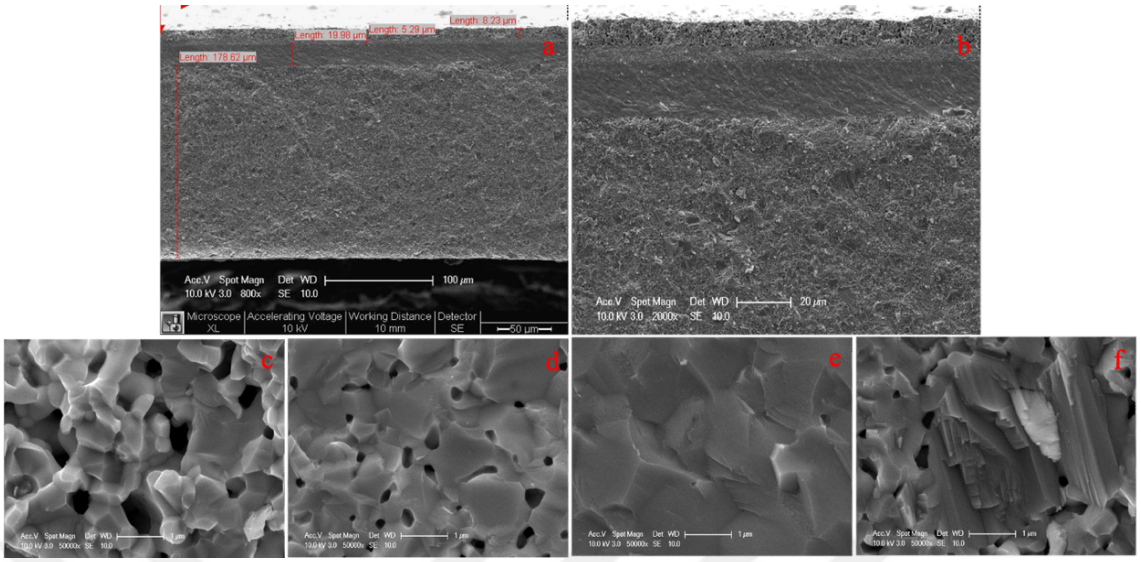


Figure 4.8. SEM images of LG10SC-GDC (5 µm)-YSZ-NiOYSZ fuel cell, (a) cross section, (b) closer look to interface, (c) LG10SC cathode, (d) GDC electrolyte, (e) YSZ electrolyte, and (f) NiOYSZ anode.

Following the stages of green layer production and cofiring, 50:50 weight ratio of LG10SC cathode powder and electrolyte material was mixed together and the mixture was paint-brushed onto the electrolyte layer, covering 0.5 cm^2 of active area. The final sintering step for those constructed anode-supported cells was carried out for five hours at 1100 ºC. The measurements of the LV05SC composite cathode layers in Figures 4.4–8 are clearly 45.83, 11.75, 9.40, and 4.70 µm. A crucial element for achieving optimal cell performance is the cathode layers' nice porous structure, as seen in Figures 4.4c–4.8c. Aside from managing the physical support, this is one of the preferred characteristics of the cathode with a large catalytic surface area for ORR. Additionally, it is noted that high density, gas-tight, non-porous electrolyte layers were produced (Figure 4.4 – 4.8d and e). Furthermore, uniform connections that developed at the interfaces between the layers of electrolyte and electrode are clearly visible.

In SOFCs, an effective electrode/electrolyte interface serves two main purposes: it facilitates the passage of oxide ions from the cathode to the anode and reduces or eliminates reactivity between the cell's constituent parts while it's operating. However, because of the challenging operating circumstances of SOFCs, reactivity between the electrode and electrolyte is frequent. In a recent work applied to SOFC materials, Backhaus investigates multiple cathodes using zirconia electrolytes [208, 209]. It is found that the oxygen exchange

rate and the overall performance of the cell were adversely affected by the cathode/electrolyte interphase diffusion, segregation, and structural alterations. An order-of-magnitude decrease in electrical performance and a quick deterioration after an extended treatment at 850 °C were observed by Grosjean and colleagues when they studied the behavior of $La_{0.8}Sr_{0.2}MnO_3$ on YSZ electrolytes [210]. The efficiency drop was shown to be related to the resistive $La_2Zr_2O_7$ phase [211, 212]. These impurity deposits lead to a reduction in ionic conductivity, which in turn reduces cell function.

In this purpose, GDC layer was cast on YSZ as a buffer layer to remove interface reactions between cathode and YSZ electrolyte. As shown in Figures 4.7 and 4.8, the GDC interlayer thickness for segregation against Zr from YSZ electrolyte is measured to be 35 and 5 µm.

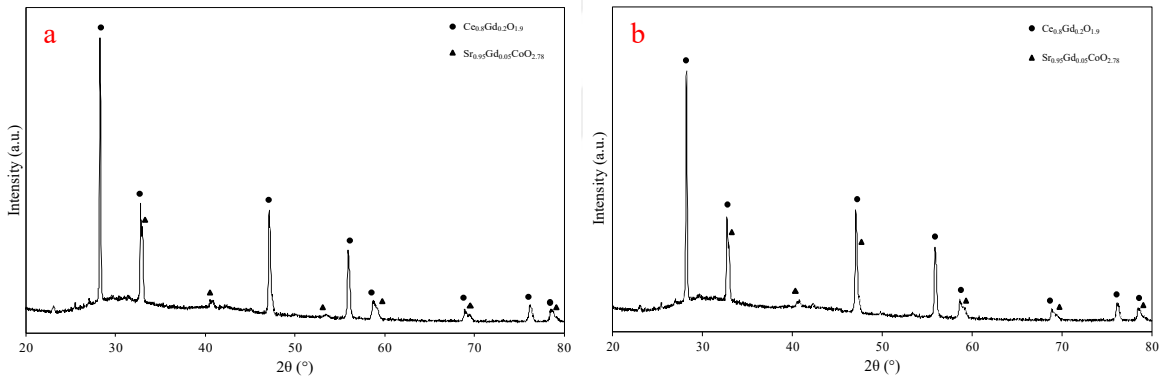


Figure 4.9. XRD analysis from cathode side of (a) LG10SC-GDC (35 µm)-YSZ-NiOYSZ, (b) LG10SC-GDC (5 µm)-YSZ-NiOYSZ fuel cells.

The XRD patterns of the LG10SC cathode layers in fuel cells with double layer electrolytes are shown in Figure 4.9. It is evident that the crystal structures of the GDC electrolytes and the LG10SC cathode did not change or contain any impurities.

5.1.2. Single Cell Performances

Figure 4.10 shows the current-voltage characteristics of the SOFC using YSZ electrolyte. The observed open circuit voltages at 500, 600, 700, and 800 °C, respectively, with hydrogen as the fuel and an oxygen/nitrogen gas blend acting as the oxidant, are 0.99, 0.92, 0.73, and 0.72 V. These values were, to some extent, lower than those determined by

the Nernst equation [213, 214]. The thin electrolyte layer-induced short circuit, gas leakage, and inadequate sealing might be the cause of the lower OCV values. The highest power densities of single cell at 500, 600, 700, and 800 °C were 0.51, 1.62, 2.30, and 6.50 mW/cm^2, respectively. Nevertheless, the cell's electrode resistance is too high for a useful SOFC. Among the elements affecting cell performance are the pore distribution, microstructure, triple phase boundary area, and contact between the electrodes and electrolyte layer. These parameters regulate the activation and concentration resistances of the electrodes as well as the ohmic resistance of the electrode/electrolyte interface. Additional improving might lead to even better cell performance.

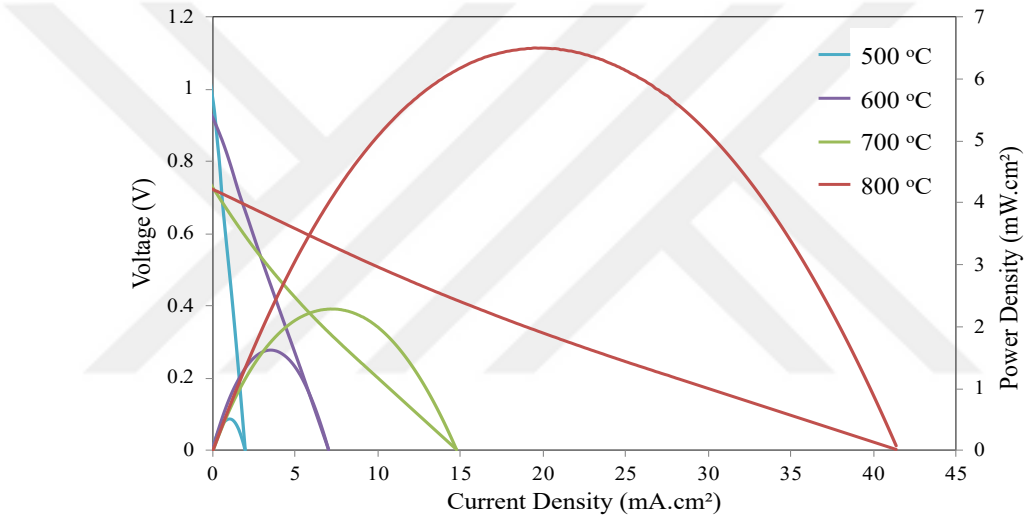


Figure 4.10. I-V curves and output power density of single cell with LG10SC-YSZ-NiYSZ at different temperatures.

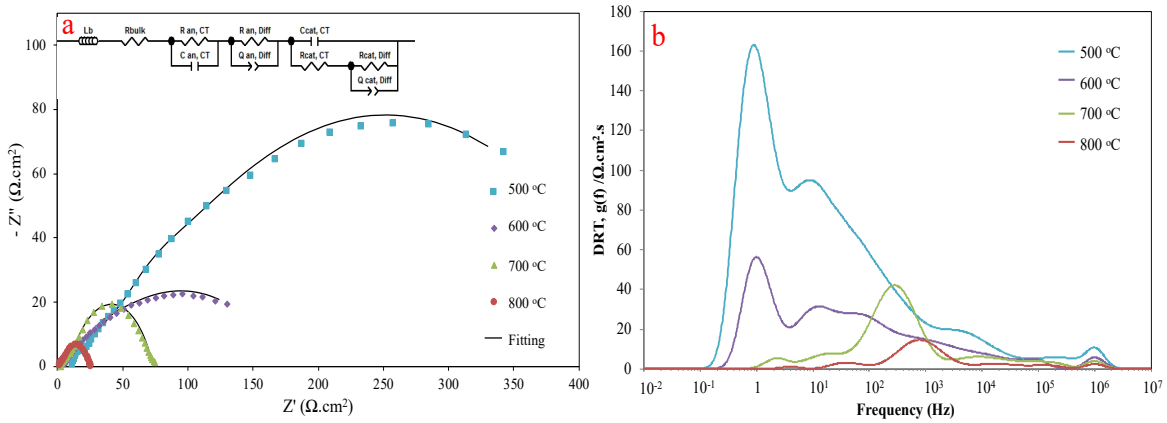


Figure 4.11. (a) Nyquist plots of LG10SC-YSZ-NiYSZ cell at OCV conditions, inset: Equivalent circuit model, (b) DRT curve of impedance spectra as a function of operating temperature at 500 - 800 °C.

The impedance spectrum of the cell, recorded at 500–800 ^{o}C under open circuit potential, is shown in Figure 4.11a. The asymmetrical form of impedance graphs indicates the existence of many processes operating within the chosen frequency range of 0.1 – 10^6 Hz. Figure 4.11a inset shows the corresponding circuit that was utilized to simulate the experimental results. In the circuit, inductance, capacitance, resistance, and constant phase element (CPE) such as pseudo capacitance are represented by the letters Lb, C, Q, and R, respectively.

The circuit enables the interpretation of EIS data and serves as an appropriate representation for this experimental system. These data could be explained by the fact that oxygen reduction at mixed ionic-electronic conducting cathode film basically follows the bulk path way. Oxygen is transported to the electrode/electrolyte phase boundary, where it eventually reaches the electrolyte layer's crystal structure, after first being adsorbed on the electrode's surface and then incorporated as an oxide ion into the bulk.

The main resistive process $R_{cat,diff}$ in the bulk route is the electrochemical resistance related to the cathode surface oxygen exchange. The corresponding semicircle in the spectrum is seen at low frequencies, suggesting a capacitive-like characteristic. This behavior, denoted as $Q_{cat,diff}$, is referred to as a constant phase element that is associated with changes in the bulk electrode oxygen stoichiometry. Consequently, the dominating low-frequency arc contains information on the bulk ($Q_{cat,diff}$) and surface ($R_{cat,diff}$) of the electrode. The resistive component of medium-frequency ($R_{cat,CT}$) relates to the transport of oxide ions across the electrode/electrolyte interface. The mid-frequency capacitance ($C_{cat,CT}$) is an interfacial capacitance coupled to the same boundary. The high-frequency intercept of the impedance spectra is caused by the ohmic resistance (Rbulk) of electrolyte and the non-zero electrical contact resistance of gold conducting wires. Because the resistance at the grain boundary becomes negligible with increasing temperature, there could only be one visible arc at high frequencies. Increased electrical conductivity and vacancy concentration with temperature are responsible for the enhanced electrochemical activity. These factors also enhance charge transfer and oxygen surface exchange in the cathode sample, which in turn enhances ORR at the cathode/electrolyte interface. Additionally, in every temperature range, the low-frequency arc showed higher values than the high-frequency semi-circle. The oxygen adsorption, dissociation, and diffusion process in the cathode sample is the limiting

stages of ORR, as evidenced by the significant high-frequency arc contribution to total resistance in the temperature range under investigation [146], [217]. Table 4.1 provides a summary of the electrochemical circuit characteristics that were determined by the fitting of impedance spectra.

Table 4.1. EIS Fitting values of LG10SC-YSZ-NiYSZ fuel cell at 500-800°C.

	500 °C	600 °C	700 °C	800 °C	Unit
Ran, Diff	16.09	7.265	3.894	1.5815	ohm.cm^2
Lb	4.34E-08	4.13E-07	3.95E-07	3.77E-07	H
Rbulk	11.765	2.569	1.824	1.0595	ohm.cm^2
Rcat, Diff	415.8	165.5	63.05	20.37	ohm.cm^2
Rcat,CT	7.005	0.265	0.9725	2.3175	ohm.cm^2
Ccat, CT	4.23E-08	8.67E-07	6.66E-08	1.01E-06	F
Qcat, Diff	0.000373	0.000917	8.8E-05	0.000124	S*s^a
a2	0.4567	0.3495	0.694	0.6887	
Qan, Diff	3.41E-05	4.67E-05	2.28E-06	1.57E-06	S*s^a
a1	0.7001	0.4842	0.818	0.8247	
Ran, CT	10.175	2.627	3.2955	0.5605	ohm.cm^2
Can, CT	0.000103	0.000324	2.74E-06	0.041155	F

To fully characterize the cell, equivalent circuit model analysis, DRT, and impedance spectroscopy were used. DRT analysis was performed on the impedance data with a regularization value (λ) of 10^{-3}. The cell was investigated in the 500–800 °C temperature range in order to investigate the EIS and DRT dependency across operating temperatures (Figure 4.11b). The impedance spectra were also measured at different potentials at 800 °C using the values listed in Table 4.1 (Figure 4.12a). As can be seen in Figure 4.11b, the high frequency response is not as significant as the low frequency response. It has been proposed that in these oxide materials, the high frequency peaks are generated by the charge transfer of oxide ions in electrodes, whereas the low frequency contribution comes from reactant flow or mass transport (gas diffusion) [91], [153], [218, 219]. The mid-frequency processes were more noticeable when the working temperature was raised to 700 °C, indicating that the rate-limiting stages at higher temperatures were diffusion and exchange of oxygen species at the TPBs. The minor contributions that were undetectable and would need further

experimental research, including impedance measurements at various gas concentrations. Nonetheless, it is crucial and emphasizes the need of employing distinct, bi-layer electrolyte materials to lessen the interfacial resistance's overall polarization resistance contribution.

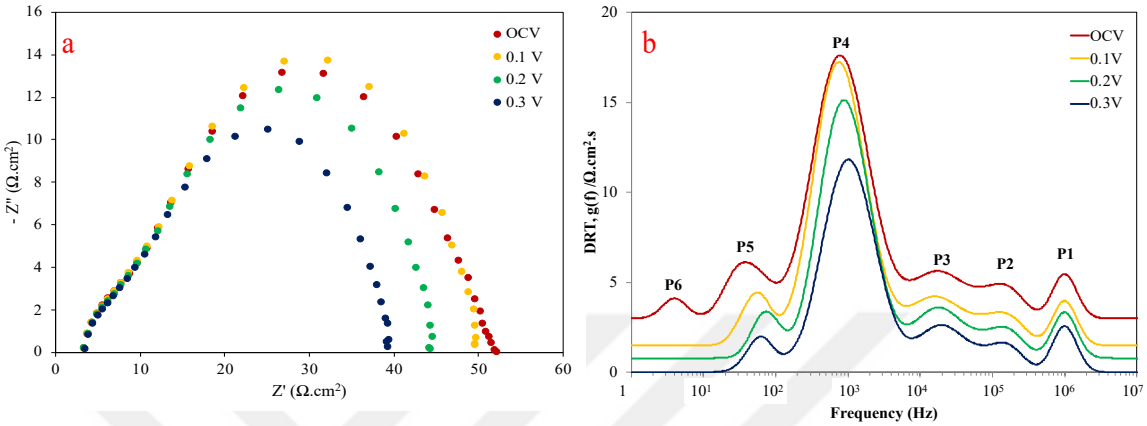


Figure 4.12. (a) Nyquist plots of LG10SC-YSZ-NiYSZ cell, (b) DRT patterns under different applied voltages at 800 ºC.

Every parameter in the established equivalent circuit model shown in Figure 4.12a has a distinct DRT representation. Each reaction stage in the cell can be designated with the letter P, which stands for resistance and capacitor to represent the adsorption, diffusion, and reaction processes, respectively, to make the contributions of each step easier to understand. Six deconvoluted peaks, identified as P1 through P6, from high to low frequency seemed to be visible in Figure 4.12b covering the examined frequency range of 1 MHz - 0.1 Hz, indicating six distinct electrochemical processes. P1, P3, P4, and P5 represent the four cathode processes in this model, whereas P2 and P6 represent the two anode processes. P2 represents the hydrogen charge transfer, while P6 represents the gas diffusion in the anode [96], [220-223]. P1 denotes the passage of oxide ions through the cathode's electrolyte network and across the cathode/electrolyte contact [224]. P4 indicates ORR at TPB areas, P5 shows oxygen gas diffusion in the cathode, and P3 is labeled for oxygen species (O^-/O_2^{2-}) diffusion to the TPBs [221–223]. The resistance of each process is linked to the activation energy of accompanying step. More resistance is correlated with a higher activation energy. The formula for the frequency (f), which is proportional to the response rate, is $f = 1/(2\pi RC)$. Higher levels of f are correlated with faster reaction rates. Figure 4.12a displays the impedance data collected at various voltages, from which the DRT result in Figure 4.12b was obtained. Every peak's significance is associated with a certain sub-step. The changes

in P5 and P6 become more noticeable as applied voltage increases, as seen in Figure 4.12b. Moreover, P1–P4 stay same when the applied potentials rise, P5 shifts to higher frequencies, and P6 peak vanishes. Voltage changes therefore have little effect on high and mid frequency activities, which are related to surface exchange reactions and charge transfer. On the other hand, the gas diffusion steps-correlated low frequency peaks P5 and P6 overlap and move to higher frequencies. It is clear that $R_{cat,diff}$ is the rate-limiting step. As was previously indicated, deconvoluted peaks at low frequencies are due to the diffusion and exchange of oxygen species (O^-/O_2^{2-}) at the TPBs and mass transfer of reactants in the cathode. This phenomenon was further confirmed by the comprehensive equivalent circuit fitting values in Table 4.1.

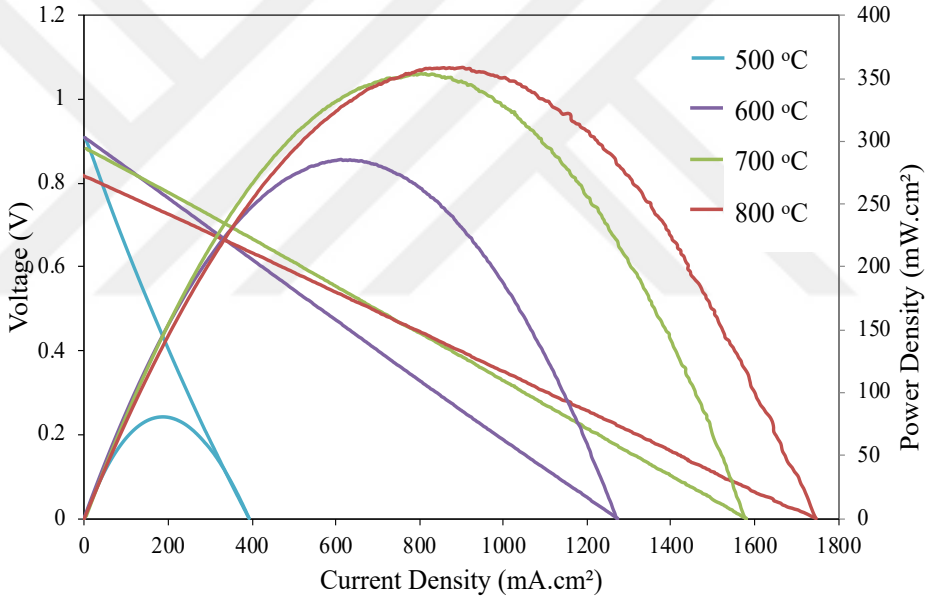


Figure 4.13. I-V curves and output power density of single cell with LG10SC-GDC-NiGDC at different temperatures.

Tests were conducted on the performance of fuel cells built with various electrolyte materials in order to validate the approach proposed in this thesis. The I-V and I-P curves of LG10SC-GDC-NiGDC cell are shown in Figure 4.13. The power densities at 500, 600, 700, and 800 °C were 80.83, 285.20, 353.58, and 360 mW/cm^2, respectively. The OCV values at 500, 600, 700, and 800 °C were found to be 0.92, 0.90, 0.88, and 0.82 V. Additionally, when the temperature increases, those values drop from 0.92 to 0.82 V and, at 600 °C, approach the predicted value of 0.98 V [228, 229]. The use of GDC as a single-layer electrolyte is limited by the partial conversion of Ce^{4+} to Ce^{3+}. The material's electrical conductivity,

which is caused by the multivalency of the Ce atom, reduces the OCV values and power density [230]. As a result, the single-layer GDC electrolyte, whose properties are investigated at temperatures no more than 650 °C, is typically used for developing intermediate temperature solid oxide fuel cells [231–236]. Nonetheless, certain research has suggested that a slight degree of electrolyte electrical conductivity may be helpful for improving processes on electrodes as the electrochemical reaction area grows. Furthermore, compared to traditional YSZ electrolyte, GDC electrolyte has a better ionic conductivity. By increasing oxide transport at the electrode/electrolyte interface as a result of the increased ionic conductivity, the charge transfer polarization resistance is reduced. Consequently, it can be possible to reduce the SOFC total polarization resistance, which would allow for even greater cell performance improvement [237, 238].

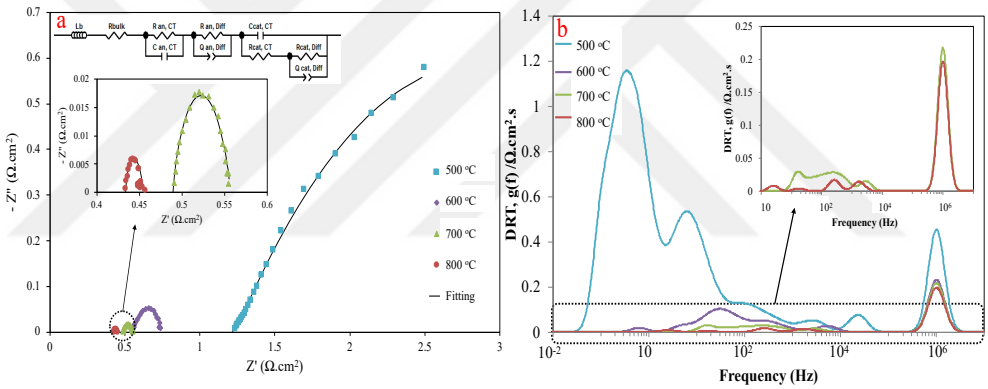


Figure 4.14. (a) Nyquist plots of LG10SC-GDC-NiGDC cell at OCV conditions, inset: Equivalent circuit model, (b) DRT curve of impedance spectra as a function of operating temperature at 500 - 800 °C.

Figure 4.14a displays the impedance of the cell with GDC electrolyte evaluated at 500 - 800 °C. Semi-circle arcs are frequently observed in impedance spectra. The intercepts on the x-axis might be used to assess the polarization and ohmic resistance. With an increase in working temperature, total resistance reduces. This is because the high-frequency arc intensity rises and shifts into the lower frequency region as the temperature drops, increasing the overall resistance of the cell. This pattern suggests that the reaction steps of the cell may be referred to as physicochemical reactions. The low frequency arc intensity rises below 700 °C, indicating a behavior that is independent of temperature [239]. The related equivalent circuit model is shown in the inset of Figure 4.14a to further clarify the response process, and Table 4.2 provides the fitting values.

Table 4.2. EIS Fitting values of LG10SC-GDC-NiGDC fuel cell at 500-800°C.

	500 °C	600 °C	700 °C	800 °C	Unit
Ran, Diff	0.26535	0.031835	1.04E-08	0.4218	ohm.cm^2
Lb	3.5E-07	3.56E-07	3.65E-07	3.09E-07	H
Rbulk	0.8725	0.1831	7.88E-07	0.002356	ohm.cm^2
Rcat, Diff	3.0545	0.17365	0.07045	0.02367	ohm.cm^2
Rcat,CT	0.30865	0.35645	0.48435	0.00726	ohm.cm^2
Ccat, CT	2.08E-07	1.08E-07	6.48E-08	7.41E-05	F
Qcat, Diff	0.15945	0.12265	0.2154	0.271	S*s^a
a2	0.4197	0.6576	0.5773	0.6	
Qan, Diff	1.6665	0.26225	10055	2.31E-07	S*s^a
a1	0.6098	0.422	0.4	0.4	
Ran, CT	0.05685	0.002776	0.002504	2.496	ohm.cm^2
Can, CT	3.15E-05	0.01106	0.00372	4108.5	F

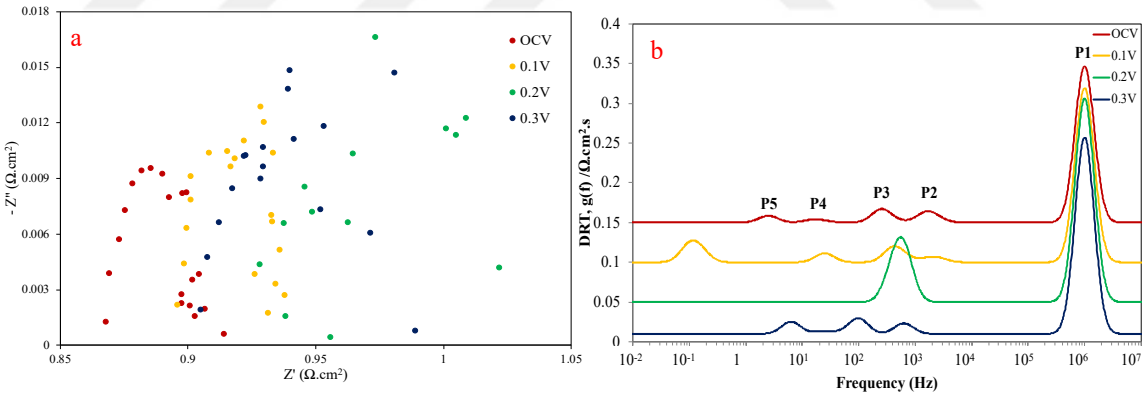


Figure 4.15. (a) Nyquist plots of LG10SC-GDC-NiGDC cell, (b) DRT patterns under different applied voltages at 800 °C.

The DRT spectra that were determined using the impedance data were displayed in Figures 4.14b and 4.15b. As temperature rises, both the polarization and strength of the lower frequency peaks in Figure 4.14b decrease. The charge transfer process-related peak at high frequencies, however, is less temperature-dependent. The DRT analysis of the impedance data under various applied potentials, which were obtained from the impedance data in Figure 4.15a, was displayed in Figure 4.15b. Five peaks were identified in Figure 4.15b, and each peak has its unique electrode reaction pathway. High frequency peak P1 was associated

with the processes of charge transfer and oxide ion transfer. A determination was challenging since both the DRT calculations and the EIS spectra were ambiguous in the mid- and low-frequency regions.

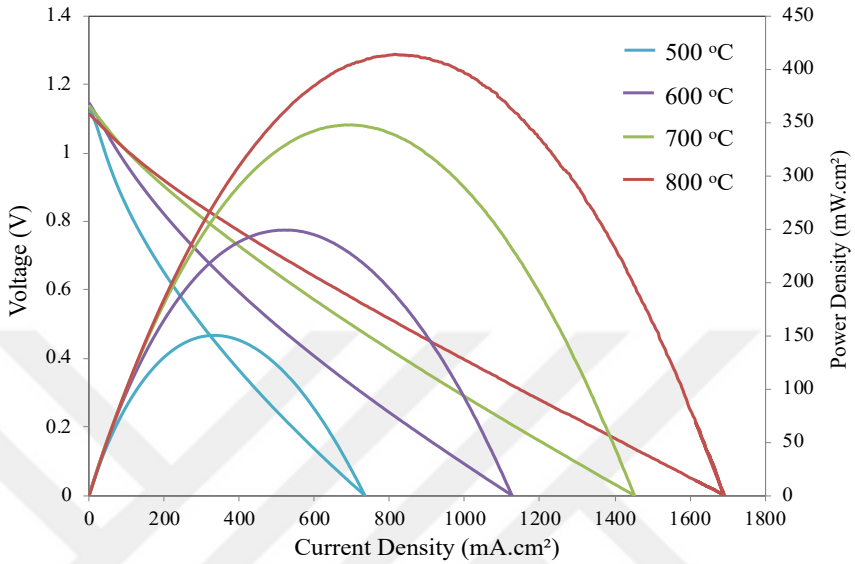


Figure 4.16. I-V curves and output power density of single cell with LG10SC-GDC (35 µm)-YSZ-NiYSZ at different temperatures.

A double-layer electrolyte anode supported half-cell was paired with the produced cathode material. The I-V and I-P polarization curves of the LG10SC- GDC (35 µm)-YSZ-NiYSZ cell at different temperatures ranging from 500 to 800 °C are displayed in Figure 4.16. With an open circuit potential of 1.12 V, a peak power density of 415 mW/cm^2 was achieved at 800 °C. Based on the IV characteristics and impedance data, the rate-determining mechanisms of this cell were the ohmic and concentration polarization under high current density. If the microstructures of the electrodes, particularly the cathode compartment and the electrolyte thickness, are tuned, the enhanced cell should perform even better at lower temperatures.

The observed polarization curves and cell potentials, however, only display the overall performance loss; exact details on the losses and fluctuations brought on by ohmic resistances and polarization during cell operation were not given. Thus, the EIS approach and equivalent model fitting were carried out in order to identify which sub-reaction is responsible for the cell degeneration, and the resulting values were shown in Table 4.3. Figure 4.17a presented the relevant measured spectra. At both high and low frequencies, two

distinct arcs could be seen in the Nyquist spectra. It is evident that as operating temperature increases, the ohmic resistance—the high frequency contact with the x-axis—has reduced. In contrast, the high-frequency arcs in EIS spectra are similar and show very minor size changes over time. That being said, there are discernible differences in the low-frequency arc. In anode-supported cells, the cathode influences the mid-frequency zone (1-400 Hz), whereas diffusion impacts the impedance spectrum below 10 Hz [221], [240-244]. The anode mostly affects the high frequency area at above 200 Hz.

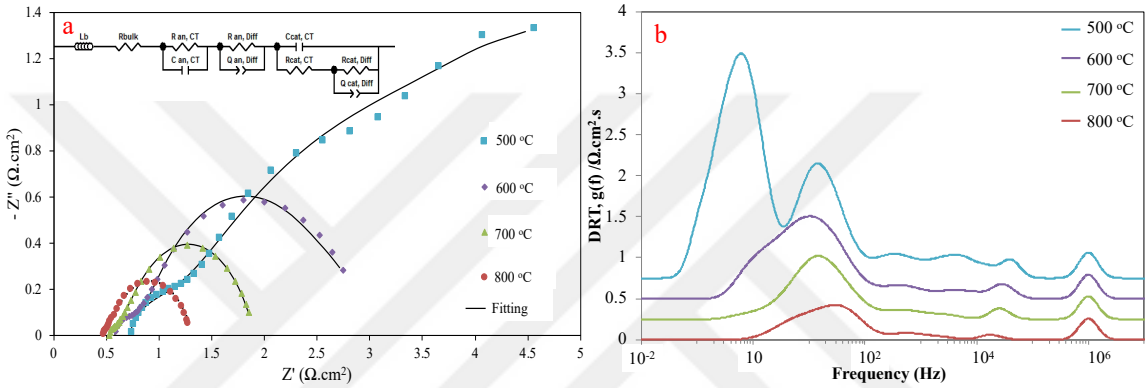


Figure 4.17. (a) Nyquist plots of LG10SC-GDC (35 µm)-YSZ-NiYSZ cell at OCV conditions, inset: Equivalent circuit model, (b) DRT curve of impedance spectra as a function of operating temperature at 500 - 800 °C.

The imaginary section of the spectrum, or y-axis, shows evidence of both cathode and anode impacts, even though the largest change in the spectrum is mostly observed at low frequencies. However, the frequency zone corresponding to anode reaction processes altered rather negligibly when compared to the cathode reaction zone. This suggests that the anode was only marginally affected, resulting in a tiny increase in the polarization, activation, and concentration resistances. The observed behaviors of the impedance spectra are caused by changes in the cathode that are connected to reactions, which suggests that cathode deterioration was the main factor influencing the cell's degrading performance [244, 245].

Using the DRT technique, a number of cell sub-reaction pathways have been investigated. This strategy allowed the impedance components to be identified by their unique timings. Figure 4.17b shows the DRT results of the LG10SC-GDC (35 µm)-YSZ-NiYSZ cell at 500, 600, 700, and 800 °C. For high frequency regions, charge transfer between the electrode and electrolyte is frequently responsible. The middle frequency

represents surface processes, whereas the low frequency region represents gas diffusion [246–248].

Table 4.3. EIS Fitting values of LG10SC-GDC (35 µm)-YSZ-NiYSZ fuel cell at 500-800°C.

	500 °C	600 °C	700 °C	800 °C	Unit
Ran, Diff	0.6585	0.3516	0.1993	0.126	ohm.cm^2
Lb	3.918	1.857	1.2265	0.7605	H
Rbulk	3.25E-07	3.48E-07	3.42E-07	3.44E-07	ohm.cm^2
Rcat, Diff	0.617	0.29375	0.31465	0.25645	ohm.cm^2
Rcat,CT	0.010025	0.007985	0.019875	0.18465	ohm.cm^2
Ccat, CT	0.4237	0.5065	0.4361	0.3005	F
Qcat, Diff	3.17	0.1888	0.01132	0.002675	S*s^a
a2	1.3385	0.23565	0.1557	0.17985	
Qan, Diff	0.4487	1.96E-07	3.71E-07	3.17E-07	S*s^a
a1	0.035285	0.02532	0.028645	0.040795	
Ran, CT	0.5284	0.7159	0.7204	0.6822	ohm.cm^2
Can, CT	2.111	2.004	0.04256	26.765	F

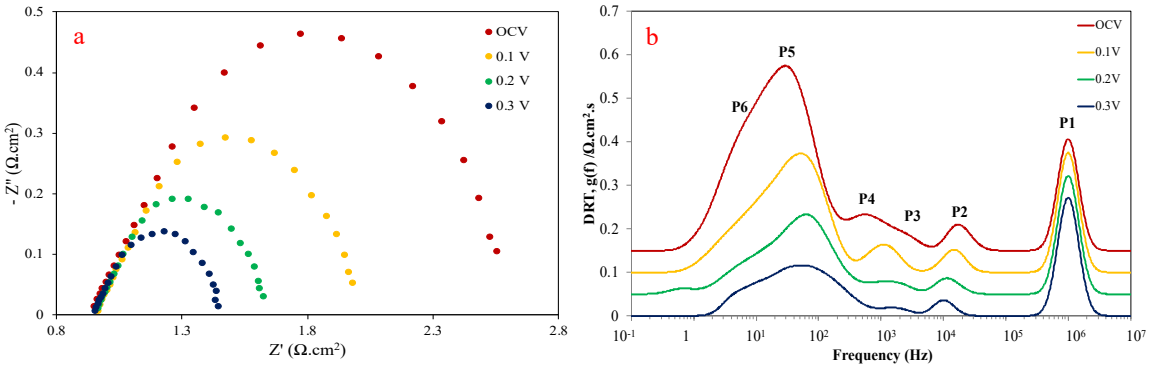


Figure 4.18. (a) Nyquist plots of LG105SC-GDC (35 µm)-YSZ-NiYSZ cell, (b) DRT patterns under different applied voltages at 800 °C.

The surface exchange region exhibits the largest intensity peaks in Figure 4.17b, suggesting that such sub-reactions are primarily responsible for impedance losses at 500–600 °C. But when the temperature increased, they reduced, and the temperature difference had no effect on the high frequency peak. The estimated DRT peaks in Figure 4.18b clearly

show at least six independent reactions, in contrast to the impedance curve in Figure 4.18a, which shows overlap between the polarization processes. It is clear that under applied potentials as well as at high temperatures, process P1, which involves charge transfer processes, was dormant. In contrast, some voltage dependence and heat activation are carried out by processes P2 through P6. With the exception of charger transfer, all peaks move into a lower frequency range and overlap when the applied voltage increases. This indicates that P6, which was designated as the mass transport sub-step, remained resistive at various voltages and temperatures, with the exception of P1. Cell potential and current-power density curves of the cell with a 5 µm GDC barrier layer at 500–800 °C in H_2 fuel are displayed in Figure 4.19. The cell's OCV readings were around 1 V, which is a bit less than the value that would be predicted theoretically. The lower OCV readings might be the consequence of a minor short circuit caused by the thin GDC/YSZ double-layer electrolyte and imperfect sealing. Additionally, the open circuit potential in GDC material is decreased by partial reduction of Ce^{4+} to Ce^{3+}. At 700 °C, the highest power density was 170 mW/cm^2, which is 60% less than the cell with a 35µm GDC/YSZ bi-layer electrolyte. This demonstrates that the cell with the LG10SC-GDC composite cathode may provide results with greater power and current densities even while running at a lower temperature of 100 °C. Performance measures may provide useful insights into the structure of the cell, but more work has to be done to thoroughly examine the cell processes using DRT and impedance spectroscopy.

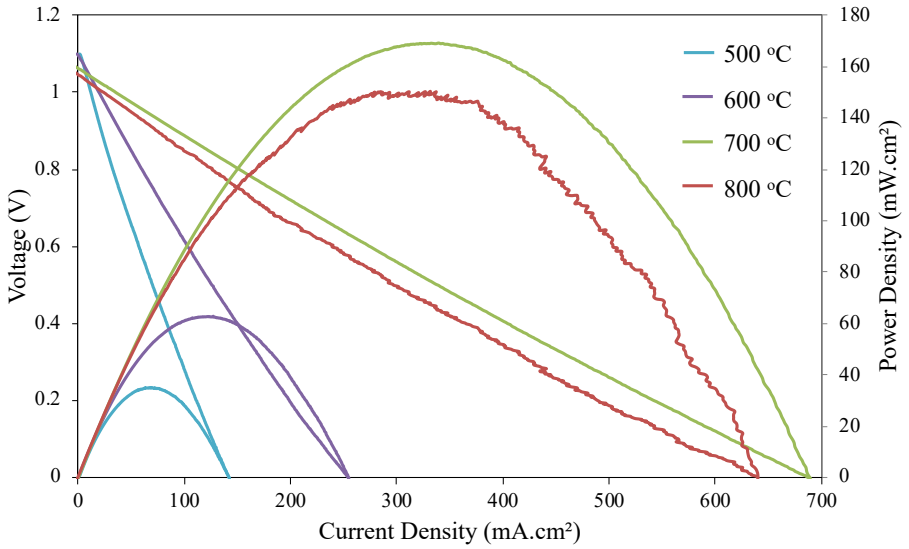


Figure 4.19. I-V curves and output power density of single cell with LG10SC-GDC (5 µm)-YSZ-NiYSZ at different temperatures.

At a temperature range of 500 to 800 ºC, electrochemical impedance spectroscopy (EIS) measurements were collected for the LG10SC/GDC (5 µm)/YSZ/NiYSZ cell. Different electrochemical reaction processes, including charge transfer, gas diffusion, and adsorption, were examined in the studies. Figure 4.20a shows the Nyquist plots as a function of temperature. Due to several processes overlapping, only two semi-circle arcs could be seen. The cell has a reduced overall resistance at 700 ºC, but as expected, the resistance values that were obtained from the diameters of the impedance arcs have decreased as temperature rises. The related equivalent circuit model was shown in the inset of Figure 4.20a to examine the response process, and Table 4.4 provided the fitting values.

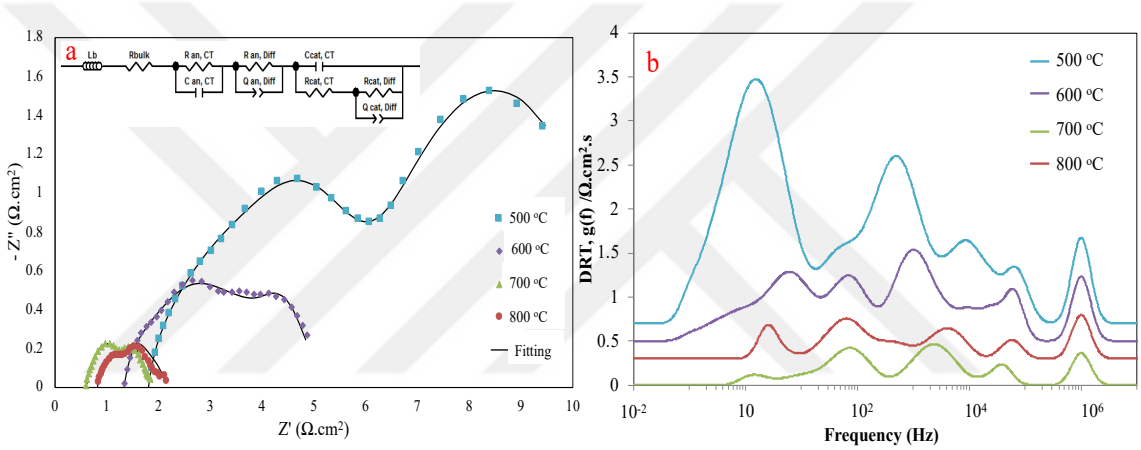


Figure 4.20. (a) Nyquist plots of LG10SC-GDC (5 µm)-YSZ-NiYSZ cell at OCV conditions, inset: Equivalent circuit model, (b) DRT curve of impedance spectra as a function of operating temperature at 500 - 800 ºC.

It is evident from Table 4.4 that $R_{cat,diff}$ has the highest polarization resistance of all the cell resistances. Fitting an impedance data, however, is a subjective problem. Therefore, in order to gain a deeper understanding of the electrode processes, the overlapping impedance arcs were deconvoluted by calculating the distribution of relaxation times. Figure 4.20b illustrates the results. A comparison of various temperatures is shown in Figure 4.20b, which indicates that low frequency processes were more resistant to temperature drops. These processes were less prominent as the working temperature increase, suggesting that mass transfer reactions were no longer resistive stages. Additionally, it can be seen from the impedance data that the mid-frequency reactions, which are surface exchange processes, evolved at 700 ºC and demonstrate that oxygen gas diffusion at the cathode exhibits the strongest resistance.

Table 4.4. EIS Fitting values of LG10SC-GDC (5 µm)-YSZ-NiYSZ fuel cell at 500-800°C.

	500 °C	600 °C	700 °C	800 °C	Unit
Ran, Diff	4.1555	3.8455	1.038	0.47135	ohm.cm^2
Lb	4.15E-07	3.94E-07	3.9E-07	3.98E-07	H
Rbulk	0.929	0.705	0.21105	0.33025	ohm.cm^2
Rcat, Diff	4.727	0.573	0.25975	0.8395	ohm.cm^2
Rcat,CT	0.6685	0.3384	0.2707	0.4022	ohm.cm^2
Ccat, CT	4.18E-08	1.33E-07	1.45E-07	9.89E-08	F
Qcat, Diff	0.00306	4.643	0.001297	0.01328	S*s^a
a2	0.4142	0.7084	0.8387	0.4038	
Qan, Diff	0.04887	0.008895	0.037205	0.1562	S*s^a
a1	0.7346	0.3341	0.312	0.4865	
Ran, CT	0.4823	0.3066	0.16595	0.1225	ohm.cm^2
Can, CT	0.001415	0.20365	0.02712	0.028165	F

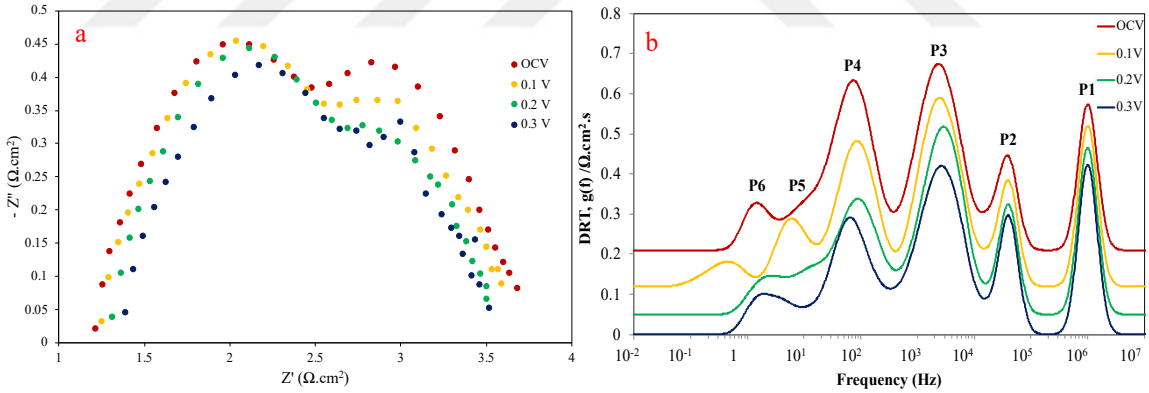


Figure 4.21. (a) Nyquist plots of LG10SC-GDC (5 µm)-YSZ-NiYSZ cell, (b) DRT patterns under different applied voltages at 700 °C.

5.2. Conclusion

As conclusion, single cells with YSZ, GDC and bi-layer electrolytes were produced and their performance, impedance and DRT behaviors under different temperature and voltages were reviewed. It was concluded that the cells with GDC (35µm)/YSZ double layer electrolyte exhibited highest power density with 415 mW/cm^2. In EIS plots, two separate arcs were visible showing highest polarization resistance contribution from mid and low

frequency regions. Also, from the circuit model fitting results at Table 4.1 – 4.4, it could be reviewed that $R_{cat,diff}$ sub-reaction has the highest influence on total resistance with the values of 664.12, 3.32, 1.48 and 6.40 Ω/cm^2 for single cells with YSZ, GDC, GDC (35 μm)/YSZ and GDC (5μm)/YSZ electrolyte combinations, respectively.

From the DRT findings, charge transfer resistance contribution was neglected, because this peak is mostly labelled for transport of oxide ions through electrolyte network which is called as R_{bulk}. For single cell with YSZ electrolyte has performed largest resistance at diffusion and exchange of oxygen species (O^-/O_2^{2-}) at the TPBs and mass transfer of reactants in the cathode processes, and also the cell showed dependency on applied voltages at low frequency. The mass transfer reactions such as oxygen and hydrogen gas diffusion in the electrodes have become more visible. In the cell with only single layer GDC electrolyte, minor contributions from each cell process, except charge transfer in electrolyte, were observed. In the applied voltage case, both EIS and DRT calculations were inconclusive, hence making a judgement on cell processes were challenging.

In order to compare bi-layer electrolyte influence in the cell performance, GDC layers were attached with different thicknesses on conventional YSZ electrolyte. In the first scenario, GDC layer with 35 μm thickness were tape casted and laminated, and the performance, EIS and DRT results were studied. It has highest power density among other combinations and lowest $R_{cat,diff}$ value in equivalent circuit fitting results. This estimation was also approved by DRT findings. Low frequency peaks have the major effect on total cell resistance. With applied potentials, mass transfer related processes were disturbed and have shifted towards higher frequencies showing contribution originates from the flux of the reactants.

At the final case, a thin GDC layer with 5μm thickness were laminated with YSZ electrolyte and the cell was undertaken various experiments. In DRT calculations, it was concluded that with temperature variations each cell processes have similar contribution to total resistance. Also, with applied potentials the cell showed no dependency at high and mid-frequency regions, but the processes at lower frequencies accelerated simultaneously so, these two mass transport peaks overlapped.

6. SYNTHESIS, CHARACTERIZATION AND PERFORMANCE ANALYSIS OF $La_{0.57}V_{0.03}Sr_{0.4}FeO_{3-\partial}$ (LV3SF) CATHODE SAMPLE

This section is partially published as: Kisa, A.E., and O. Demircan, "Transition Metal Doped Solid Oxide Fuel Cell Cathodes", *Journal of the Turkish Chemical Society Section A: Chemistry*, Vol. 5, pp. 1153-1168, 2018 [136].

6.1. Introduction

Lanthanum Ferrite based oxides have become more significant due to their special properties. $La_{1-x}Sr_xFeO_{3-\partial}$ (LSF) perovskite materials exhibit strong electrical and ionic conductivity at high temperatures; hence they could be employed in applications as air electrodes in solid oxide fuel cells, gas sensors, and oxygen-permeable membranes [264–270]. A significant obstacle to the implementation of these applications is mechanical damage during operating or material manufacturing. Mechanical stresses could be result from a number of factors, including mismatches in the thermal expansion coefficients of the components, and changes caused brought on by variations in valence state of Fe in LSF (distortion in crystal structure). Stresses brought on by these occurrences might cause the equipment to malfunction. Design-related considerations thus need a detailed grasp of the phase development and thermal characteristics as a function of composition, temperature, and oxygen stoichiometry. The partial replacement of Sr^{2+} for La^{3+} in $LaFeO_3$ can result in oxygen vacancies and significantly change its electrical and ionic conductivities, also the maximum electrical conductivity is achieved in $La_{0.5}Sr_{0.5}FeO_{3-\partial}$ [271]. Solid-state chemistry and catalytic activity of $La_{0.5}Sr_{0.5}FeO_{3-\partial}$ can be further enhanced by doping at the A-site [272, 273]. Given that $LaVO_3$-based oxides exhibit high catalytic activity and good electrical conductivity on par with metals [274, 275]. This contribution modifies the oxygen vacancies and electrical structure of LSF by partial substituting the A-cation with V.

In this chapter, the effects of changes in the oxidation states of doped transition metals such as Vanadium were investigated to understand ORR mechanism in the operation of

SOFC on intermediate temperature range by employing the tape casting and co-firing procedures to produce the single cells with anode-supported thin electrolytes to enhance the electrical characteristics of perovskite materials. Both electrical and ionic conductivities, and the performance of perovskite materials have been measured for a variety of temperatures by employing EIS and DRT calculations. As a results of these analysis, adsorption, dissociation, and diffusion processes were found to be the ORR's limiting steps. These findings suggest that this V-doped perovskite structure, LV3SF, is a promising cathode material for IT-SOFCs.

6.2. Material Synthesis

Utilizing the sol-gel method, $La_{0.6-x}V_xSr_{0.4}FeO_{3-\partial}$ (LVxSF, x = 0.03) powders were produced. Reagents included La, Sr, and Fe nitrates as well as V acetate (purity > 99.9%, Aldrich Chemicals, USA). Separately, each reagent was dissolved in distilled water at the proper stoichiometric ratio. To produce a homogenous solution, all of the solutions were afterwards combined and agitated. As complexation and polymerization agents, ethylene glycol and citric acid, in varying amounts, were added after they had completely dissolved. The citric acid to total metal ions ratio was maintained at approximately 1:2. The solution was allowed to evaporate on a hotplate upon prolonged heating, the gel spontaneously burned, transforming into a light and delicate ash. Following a gentle heating-induced gelation, the resulting gel was placed in a drying oven at 500 °C for 2 hours to eliminate organic components. Subsequently, it was subjected to sintering at 900 °C for 3 hours to yield perovskite compounds possessing satisfactory crystalline structure, as confirmed through X-ray diffraction analysis.

6.3. Characterization, Electrochemical Measurements and Fabrication Procedures

The phase identifications of $La_{0.57}V_{0.03}Sr_{0.4}FeO_{3-\partial}$ (LV3SF) cathode sample were obtained by X-ray diffraction (XRD) employing a Rigaku D/MAX-Ultima+/PC Diffractometer with Cu-Kα radiation (λ = 1.54056 Å). The diffraction patterns were recorded in the range of $20^o<2\theta<80^o$ with 0.01 steps and step-counting time of 8s/step. The phases were identified with JCPDS Database. An Al K-Alpha anode ($h\nu$ = 1486.6 eV, with spot size

of 400 μm)-equipped Thermo Scientific K-Alpha Surface Analysis instrument was used to conduct X-ray photoelectron spectroscopy. The energy step size was set as 0.100 eV and the charge effect was calibrated using the binding energy of C1s (284.5eV). XPS Peak 4.1 software was used to analyze and deconvolute survey spectra at a pass energy of 50 eV and high-resolution spectra at a pass energy of 20 eV for quantification purposes. SEM-FEG, Philips XL 30 at an accelerating potential of 10 kV was used to study the surface and cross-section morphology of the sintered cells. Performance and electrochemical impedance spectra (EIS) were measured from 500 to 800°C utilizing a self-made test setup contained of numerous gas mass flowmeters, a furnace (Figure 3.1). The sintered cells were attached to a zirconia tube with a ceramic paste. The electrodes' current collectors were made of Au paste and wires connected the electrodes to the testing instrument. The current-voltage (I - V) characterization was conducted with the Gamry Ref 3000 Potentiostat (Gamry Instruments, Warminster, PA, USA) using H_2 as the fuel and oxygen as the oxidant. The AC impedance data were collected with an AC signal of 10 mV in the frequency range of 1 MHz - 0.1 Hz.

Commercial YSZ (Yttria-Stabilized Zirconia (8% Y) – Tape Cast Grade Powder, Fuel Cell Materials Ltd., USA) and GDC (Gadolinium Doped Ceria (20% Gd) – Tape Cast Grade Powder, Fuel Cell Materials Ltd., USA) powders were used to prepare the electrolyte layers. The anode slurry was obtained by mixing YSZ or GDC and fine grade NiO powder (Fuel Cell Materials Ltd., USA). A two-step ball milling procedure was used to produce the slurries for tape casting. In the first step, polyvinyl butyral (PVB) was used as the binder and ethanol/toluene as the solvent to homogeneously disperse all the particles. Secondly, in order to give an ideal viscosity, the required amounts of plasticizers polyethylene glycol (PEG) and benzyl-butyl-phthalate (BBP) were added to the slurry and ball-milled again for 24 hours. There were two processes in the tape casting process as well. The de-aired electrolyte and anode slurries were initially cast at a blade height of app. 10, 20 and 200 μm, respectively. The green tapes were cut into disks with a 13mm diameter after drying for 24 hours. One sheet of YSZ and/or GDC electrolytes and two layers of anode green tapes were stacked in order to produce anode-supported cells. The layers were assembled in random directions for relaxation of the residual internal stress and uniaxially laminated for 5 mins. The laminates were subsequently co-sintered at 1250 ^{o}C in air for 3h after burn-out of the organic components. Following co-sintering, the cathode paste was produced using LV05SC

powder and electrolyte material with a weight ratio of 50:50, and brush coated onto electrolyte with an active area of 0.5 cm^2. The cathode layer was then sintered at 1100 ^0C for 5 h.

6.4. Results and Discussion

6.4.1. Phase Composition and Structure

To determine the phase, purity, and crystallinity of the $La_{0.57}V_{0.03}Sr_{0.4}FeO_{3-\partial}$ (LV3SF) perovskite cathode material, X-ray diffraction method was utilized. The XRD is displayed in Figure 5.1 for the cathode sample that was created using a sol-gel process and calcined for three hours at 900 ^oC. With small secondary phases, a deformed rhombohedral structure (space group R-3c:167) is generated. The lattice parameters, phase, and crystallite size are computed and compared to the software crystallographic open database (COD). A single phase with lattice parameters of *a, b* = 5.517 Å, *c* = 13.446 Å, α, β= 90.00^o γ= 120.00^o and volume of 354.44 $Å^3$ is shown by the XRD pattern of the produced cathode material. The rather strong peaks in the XRD pattern show that the metal oxides utilized in the powder syntheses have been well incorporated into their lattice. These findings provide additional evidence that the prepared catalysts successfully generated the $ABO^{3-\partial}$ perovskite structure.

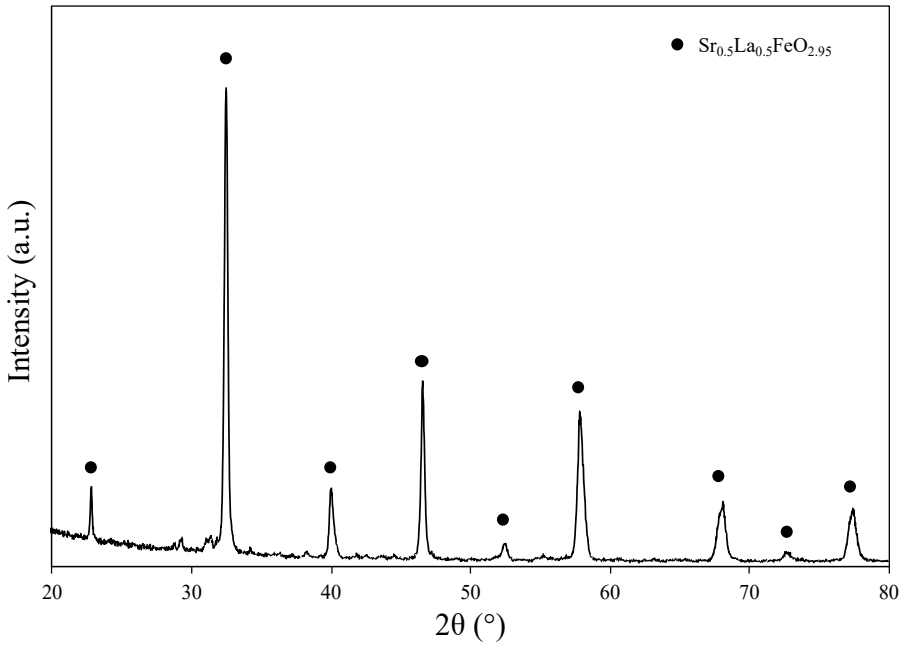


Figure 6.1. XRD data of $La_{0.57}V_{0.03}Sr_{0.4}FeO_{3-\partial}$ cathode powder.

6.4.2. XPS Analysis

The surface properties of LV3SF sample examined by XPS, all elements, such as La3d, V2p, Sr3d, Fe2p, and O1s have obviously existed in the crystal which is approved from the full scan survey spectra shown in Figure 5.2a. The XPS spectrum of La3d is shown in Figure 5.2b. It has two wide peaks with a splitting of 16.7 eV, one at lower binding energy at 833.01 eV and another at higher binding energy at 849.71 eV, which correspond to the La3d5/2 and La3d3/2 spectra, respectively. The relative intensity ratio for La3d5/2 and La3d3/2 is around 1.38; these values are closely related to those found in the literature [172]. The difference between the La3d5/2 doublet splitting, which is about 3.6 eV, confirms the existence of lanthanum hydroxides [173, 174]. As a result, the La3d is in +3 oxidation states, as shown by the distinct separation of these spin-orbit splitting. Also, the substitution of La ions by Sr and V ions did not result in any observable shift in the position of these peaks in XRD and XPS spectra. The high resolution XPS spectra of V2p, which can be seen in Figure 5.2c, can be deconvoluted into four peaks at 515.6, 516.4, 522.4, and 523.7 eV, which indicates the oxidation states of vanadium in this sample are +5 and +4 [175–177]. The area ratio between the V2p3/2 and V2p1/2 energy levels, arising from the orbital splitting of the V2p energy level, was set to 1.5:1, and the energy separation between the two levels was set at 7.7 eV. These results are in good agreement with the results from other studies [178, 179].

It is known that the binding energies found by XPS for an atom's core electrons depend on its chemical state, the electrostatic potential caused by the charge distribution on the atoms at the ionized site, effects of the final state; and work functions. In general, increasing the number of electronegative elements like oxygen on the metal atom A causes an increase in core electron binding energies. Figure 5.2f displays the whole range of corresponding binding energies measured for O1s peak. The three peaks at 527.8, 530.5, and 532.1 eV in the core-level O 1s spectra can be attributed to the V-O bonding, adsorbed hydroxyl groups, and molecular water, respectively [175], [182]. According to the oxide electro neutrality and charge compensation mechanism, the negative charge defect caused by Sr^{2+} and V^{4+}/V^{5+} replacing La^{3+} at the A site appears to be compensated for by Fe^{2+}/Fe^{3+}. The shared electron pairs Fe^{2+}/Fe^{3+} and V^{4+}/V^{5+} allow for continuous electron transfer across Fe-O-Fe and V-O-V.

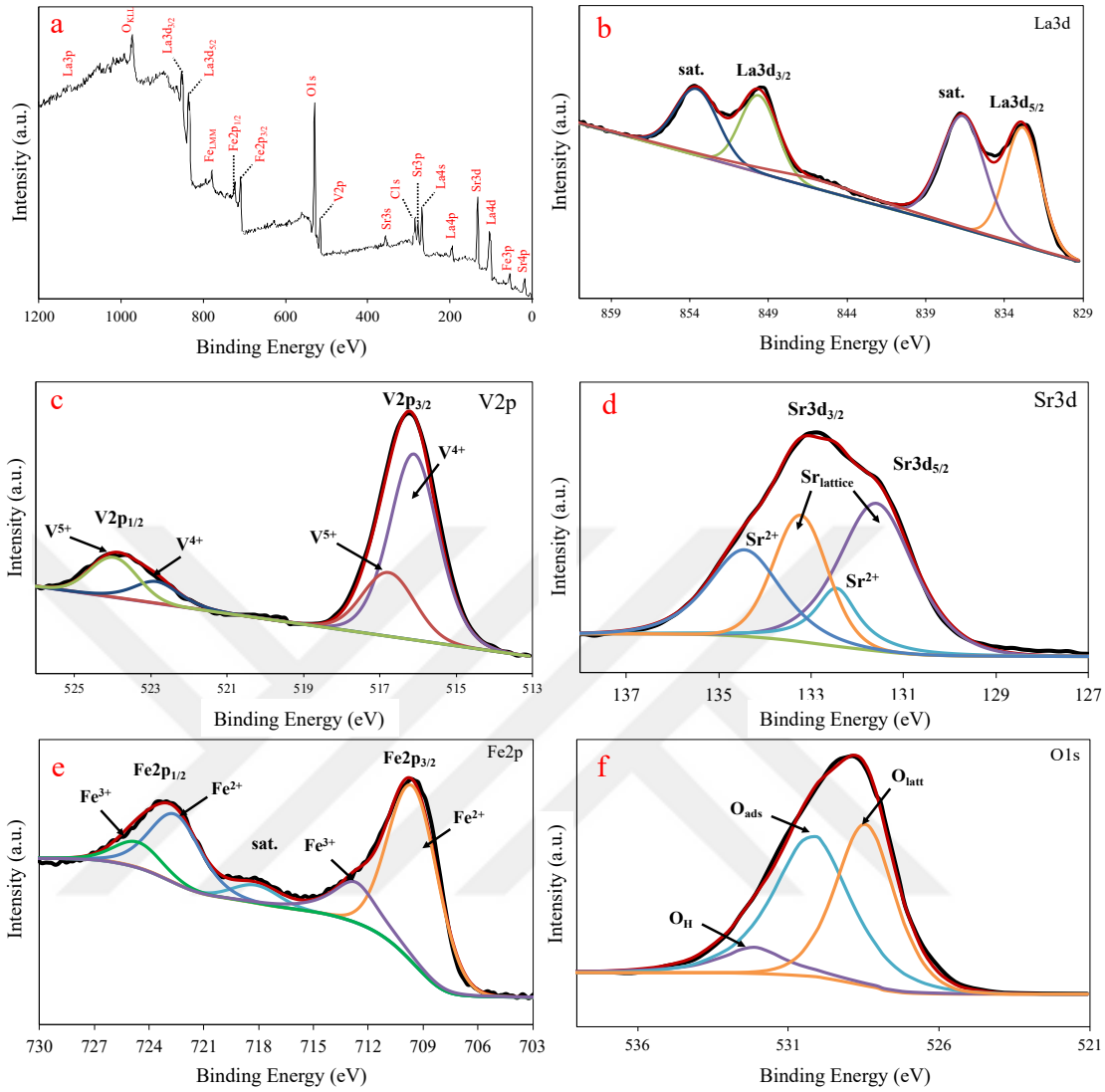


Figure 6.2. XPS survey spectra of (a) LV3SF perovskite, (b) La3d3/2 and La3d5/2, (c) V2p1/2 and V2p3/2, (d) Sr3d3/2 and Sr3d5/2, (e) Fe2p1/2 and Fe2p3/2, (f) O1s.

The Sr3d core-level spectra were particularly helpful for determining the bulk and surface contributions in the spectra since the Sr3d levels had a distinct surface core-level shift [183]. The performance loss of the cathode samples in SOFC is widely known to be caused by Sr segregation, which has been confirmed by earlier studies [184, 185]. Shown in Figure 5.2d, the Sr3d spectra were well matched using two sets of spin-orbit doublets with an energy separation of 2 eV and an area ratio of ~2. The significant peaks of the Sr3d5/2 and Sr3d3/2 components were seen in the spectra of the LV05SC sample at 131.0 and 133.2 eV, respectively. The contributions to the Sr3d photoelectron spectrum were discovered to be due to perovskite lattice-bound Sr ($Sr_{lattice}$). The Sr atoms in Sr-OH, Sr-CO_3, Sr-Sr, and Sr-O bonds near the surface of the cathode sample ($Sr_{surface}$), which do not have perovskite

structures, are responsible for the two additional minor peaks at 132.5 and 134.5 eV [186–190]. Because no obvious peaks assigned to carbonates could be seen in the X-ray diffraction patterns (Figure 5.1), the effect caused by carbonate compounds is negligible. Furthermore, the binding energies of Sr in the Sr-O structure ($Sr_{surface}$) and Sr in the lattice ($Sr_{lattice}$) are very similar, even beyond the resolution limit of this experiment configuration. The $Sr_{surface}$ therefore most likely results from the formation of the $Sr(OH)_2$ phase from SrO or from the development of a $Sr(OH)_2$-like binding environment such as SrOH on the Sr of the perovskite lattice or on the Sr of a separated SrO phase. Even though it is clear that the $Sr_{surface}$ associated with $Sr(OH)_2$ species is mostly on perovskite lattice. For the LV3SF sample, the $Sr_{lattice}/Sr_{surface}$ ratio of 2 indicates that the $Sr_{lattice}$ component of the Sr3d occurs to a greater extent. A Sr-OH signature peak is present in the bonding environment in all three cases (Figure 5.2f shows O1s spectra that demonstrates its presence). These results are expected for a perovskite structure.

Fe2p3/2 and Fe2p1/2 peaks of LV3SF cathode sample was observed in the range of 709.53 – 712.70 eV and 722.55 – 724.62, accordingly seen in Figure 5.2e. These two peaks are separated by approximately 13.5 eV. For every sample in XPS, the Fe2p3/2 peak deconvolutes into two sub-peaks. Regarding the peak at around 718.20 eV, it was attributed to the satellite peak of Fe2p3/2. The fitted peaks at binding energy of 709.53 and 722.55 eV in the spectra observed in Figure 5.2e were assigned to octahedral Fe^{2+}. The second smaller peaks at binding energy of 712.70 and 724.62 eV corresponds to Fe^{3+}. The ratio between the Fe2+ and Fe3+ fittings further demonstrate that Fe^{2+}-O provides the majority of the Fe-O bonding contribution [276]. Continuous electron-hopping routes can be provided by the presence of Fe^{2+}/Fe^{3+} and V^{4+}/V^{5+} pairs such as Fe^{2+} - O^{2-} - $Fe^{3+} \rightarrow$ Fe3+ - O^{-} - Fe3+ $\rightarrow$ Fe^{3+} - O^{2-} - Fe^{2+} and V^{4+} - O^{2-} - $V^{5+} \rightarrow V^{5+}$ - O^{-} - $V^{5+} \rightarrow V^{5+}$ - O^{2-} - V^{4+} [277, 278]. Based on the calculated fitting areas of every oxidation state, the atomic ratios of V^{4+}/V^{5+} and Fe^{2+}/Fe^{3+} showed that there is forward reaction $Fe^{2+} + V^{5+} \rightarrow Fe^{3+} + V^{4+}$ in order to preserve the electroneutrality in the LV3SF sample.

The XPS spectrum of O1s shown in Figure 5.2f exhibits two peaks, one at 530.5 eV due to adsorbed oxygen (O_{ads}) in the form of highly oxidative O^{-}/O_2^{2-} species, and one at 527.8 eV assigned to lattice oxygen (O_{latt}, O^{2-}) within perovskite. The extra peak at 532.1 eV, which is not always visible in O1s spectra, is caused by the physical and chemical

adsorption of molecular water or hydroxyl groups on the surface of defects (O_H) [195–197]. Oxygen vacancies are expressed as a percentage of adsorbed oxygen in perovskite oxides. The catalytic activity increases with the concentration of oxygen vacancies on the catalyst surface. Hence, the molar ratio of O_{ads}/O_{latt} is correlated to the performance of the cathode material. The ratio value of LV3SF was 1.20.

As lanthanum oxide has a hygroscopic characteristic when exposed to air, the highest binding energy of O1s (532.15 eV) is thought to be due to a water molecule associated with the surface lanthanum oxide. It should be noted that molecular water and surface-adsorbed oxygen in the form of hydroxyl or oxygen groups could be easily removed by heating to generate oxygen vacancies. But, removing highly oxidative oxygen species (O^-/O_2^{2-}) requires a significantly higher temperature.

6.4.3. Fabrication of Anode-Supported Electrolyte via Tape casting/Lamination/ Co-firing

For producing thin, thick, flat, and large-area ceramic tapes with the thickness range of 10-1000 μm, tape casting is a respectable manufacturing technique. This method is employed to create a range of electrical devices, including multi-layer ceramic capacitors, low-temperature co-firing ceramics, and other devices and is quite straightforward compared to other common methods for fabricating ceramic layers. Making SOFC components by this method is particularly appealing since it may be more affordable to produce in large quantities. In order to manufacture planar electrode-supporting SOFCs, tape casting method has been extensively used. However, due to the challenges that come with fabricating a thin ceramic layer with no gas permeability, tape casting technology has not been successful in the fabrication of electrolytes with thicknesses below 10 μm. Co-firing of the electrode and electrolyte layers is another low-cost manufacturing method, and effective application of this technique would improve the productivity while consuming less energy. However, minimizing the deformation of the structure owing to mismatches in the thermo-mechanical and physical characteristics of the different layers was necessary for a successful co-firing of the multi-layer structure. There have been a few research efforts on fabricating the flat-type SOFCs.

The attempt to lower the operating temperature from 800 to 600 ºC or below is one of the primary research goals in this area. The benefits of SOFCs operating at lower temperatures include a larger selection of materials, improved long-term performance, system compactness and perhaps lower fuel cell costs [200, 201]. To address these concerns there have been many research efforts including reducing the thickness of the YSZ layer and using substitute electrolyte materials having better ionic conductivity than YSZ at low and intermediate temperatures, such as gadolinium doped ceria (GDC - $Gd_{0.2}Ce_{0.8}O_{1.95}$) and doped $LaGaO_3$ [202–206]. Despite the reports of effective operation at low and intermediate temperatures, the best materials and methods for low-cost process producing stable and consistently high SOFC performance have not yet been fully addressed.

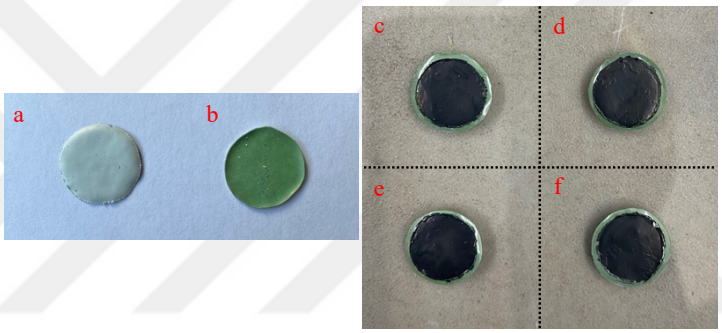


Figure 6.3. Pictures of the YSZ/NiOYSZ half cells from (a) top and (b) bottom, fuel cells after cathode sample brush-painted on electrolyte layer (c) LV3SF-YSZ-NiOYSZ, (d) LV3SF-GDC-NiOGDC, (e) LV3SF-GDC (35 µm)-YSZ-NiOYSZ, and (f) LV3SF-GDC (5µm)-YSZ-NiOYSZ.

To achieve adequate energy conversion rates and provide a suitable power output, a SOFC with a thin electrolyte sheet is preferred [207]. In this thesis, thin YSZ/GDC electrolytes and NiOYSZ/NiOGDC anode layers were prepared via tape-casting. They were used to produce YSZ-NiOYSZ, GDC-NiOGDC, and YSZ-GDC-NiOGDC anode-supported fuel cells with different thicknesses. Figure 5.3 shows the images YSZ/NiOYSZ half-cell and fuel cells prepared with LV3SF cathode sample onto different electrolyte combinations.

6.4.4. Surface Morphology Analysis of the Cell

Cross-sectional SEM micrographs of constructed fuel cells with an LV3SF cathode sample are shown in Figures 5.4–7. The electrolyte layers of YSZ and GDC have thicknesses

of 18.80 and 72.86 µm, respectively. YSZ and GDC tapes of varying thicknesses were adhered to one another in order to study the impact of double-layer electrolyte on cell performance, as shown in Figures 5.6 and 5.7. In certain combinations, the GDC layers have a thickness of 35.84 and 6.46 µm, while the YSZ electrolyte layer has about 20 µm. It is clear that the thick, crack-free electrolyte layers were securely bonded to the porous anode layers. More importantly, the first need for proper cell functioning was met since all of the cell's components had been attached together flawlessly and did not have a tendency to peel apart.

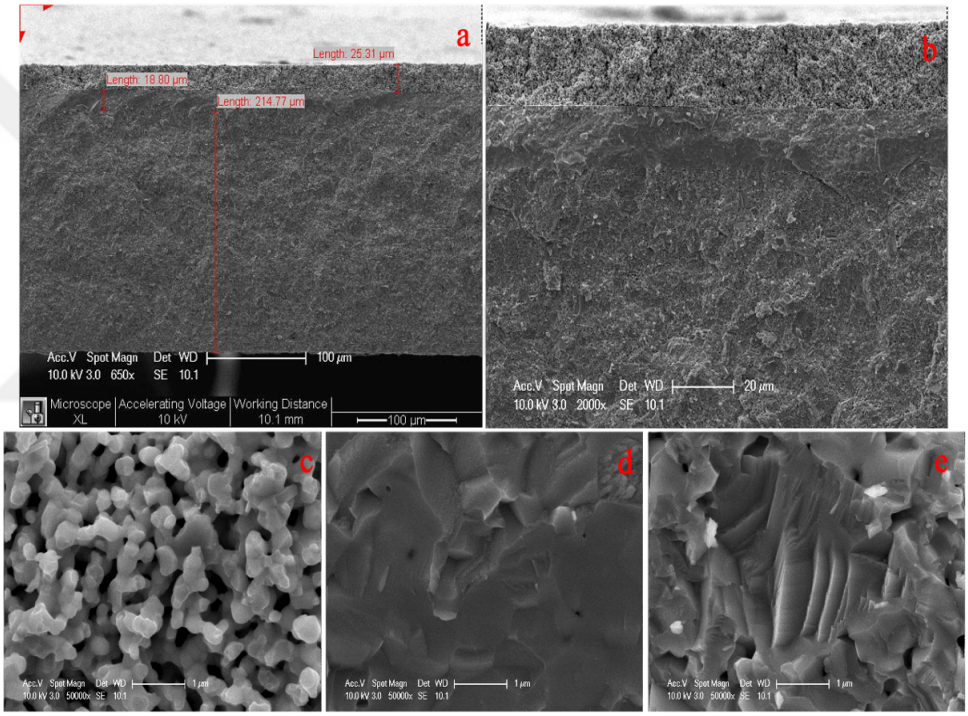


Figure 6.4. SEM images of LV3SF-YSZ-NiOYSZ fuel cell, (a) cross section, (b) closer look to interfaces, (c) LV3SF cathode, (d) YSZ electrolyte, and (e) NiOYSZ anode.

Following the procedures of green layer fabrication and cofiring, LV3SF cathode powder was paint-brushed onto the electrolyte layer with an active area of 0.5 cm^2 after being combined with electrolyte material in a weight ratio of 50:50. The final sintering step for those constructed anode-supported cells was carried out for five hours at 1100 °C. The measured values of the LV3SF composite cathode layers in Figures 5.4–7 are 25.31, 32.90, 10.58, and 33.49 µm. High cell performance is largely dependent on the porous structure of cathode layer, as seen in Figures 5.4c–7c. Controlling the physical support is only one of the required qualities of a cathode with a large catalytic surface area for ORR. Additionally, it is

noted that large densities of gas-tight, non-porous electrolyte layers were attained (Figure 5.4 – 5.7d and e). Furthermore, uniform connections that developed at the interfaces between the layers of electrolyte and electrode are clearly visible.

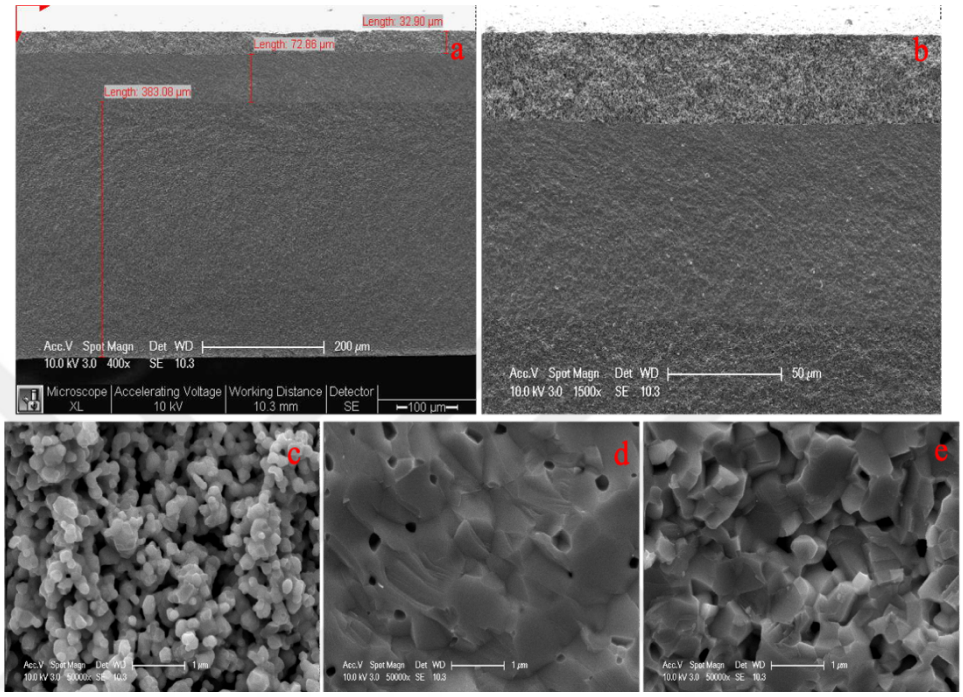


Figure 6.5. SEM images of LV3SF-GDC-NiOGDC fuel cell, (a) cross section, (b) closer look to interfaces, (c) LV3SF cathode, (d) GDC electrolyte, and (e) NiOGDC anode.

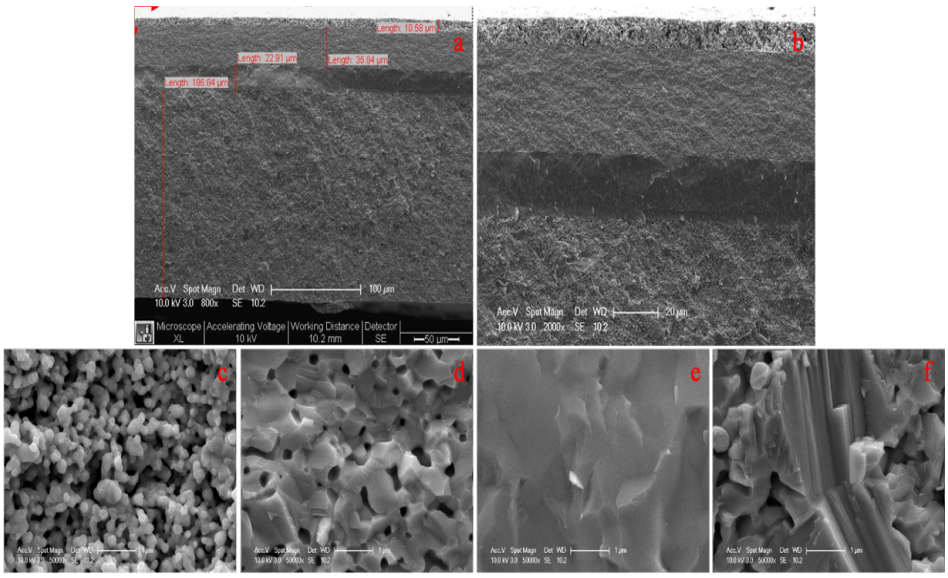


Figure 6.6. SEM images of LV3SF-GDC (35 µm)-YSZ-NiOYSZ fuel cell, (a) cross section, (b) closer look to interfaces, (c) LV3SF cathode, (d) GDC electrolyte, (e) YSZ electrolyte, and (f) NiOYSZ anode.

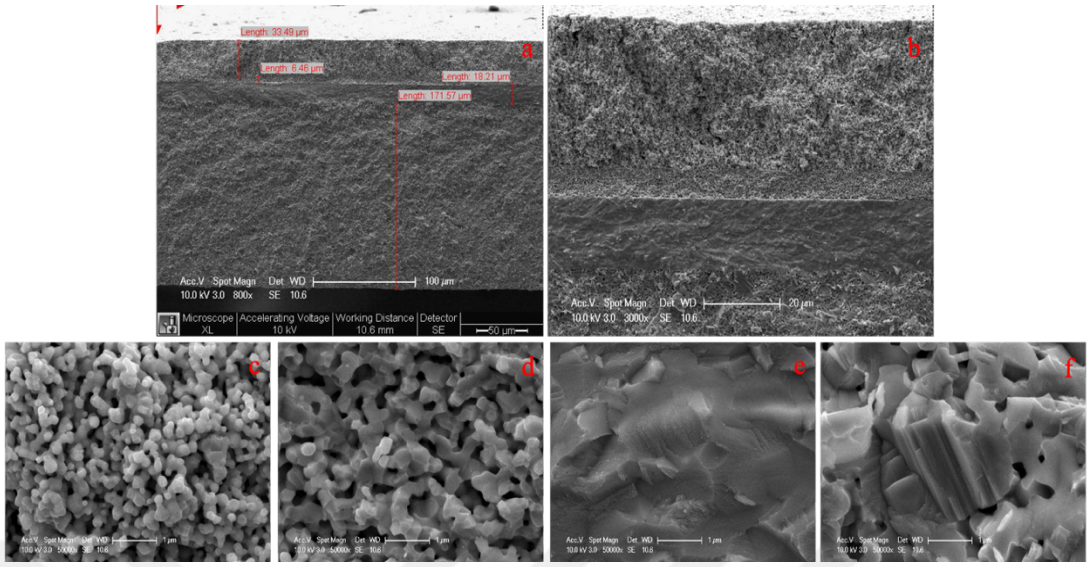


Figure 6.7. SEM images of LV3SF-GDC (5 µm)-YSZ-NiOYSZ fuel cell, (a) cross section, (b) closer look to interfaces, (c) LV3SF cathode, (d) GDC electrolyte, (e) YSZ electrolyte, and (f) NiOYSZ anode.

Enabling oxide ion transport from cathode to anode and reducing or eliminating reactivity between cell components during operation are the two main purposes of an effective electrode/electrolyte interface in SOFCs. However, because of the difficult operating circumstances of SOFCs, reactivity between the electrode and electrolyte is prevalent. Backhaus has recently studied several cathodes used to SOFC materials using zirconia electrolytes [208, 209]. It is found that the oxygen exchange rate and the overall performance of the cell were adversely affected by the cathode/electrolyte interphase diffusion, segregation, and structural alterations. Upon studying the behavior of $La_{0.8}Sr_{0.2}MnO_3$ on YSZ electrolytes, Grosjean and his colleagues observed an order-of-magnitude decrease in electrical performance and a fast deterioration after an extended treatment at 850 ºC [210]. The efficiency loss was demonstrated to be related to the resistive La2Zr2O7 phase [211, 212]. These forms of impurities lead to a reduction in ionic conductivity, which in turn reduces cell function.

Casting a GDC layer on top of YSZ electrolyte served as a buffer layer to eliminate interface reactions between the cathode and electrolyte. As shown in Figures 5.6 and 5.7, the GDC interlayer thickness for segregation against Zr from YSZ electrolyte is measured to be 35 and 5 µm. Following the half-cell lamination and co-firing processes, X-ray diffraction studies were performed to see if any impurities had developed during the sintering process.

The electrolyte layers' phase composition and crystallinity are shown in Figure 5.8. It is evident that the LV3SF cathode and GDC electrolytes' crystal structures were free of impurities and shifts.

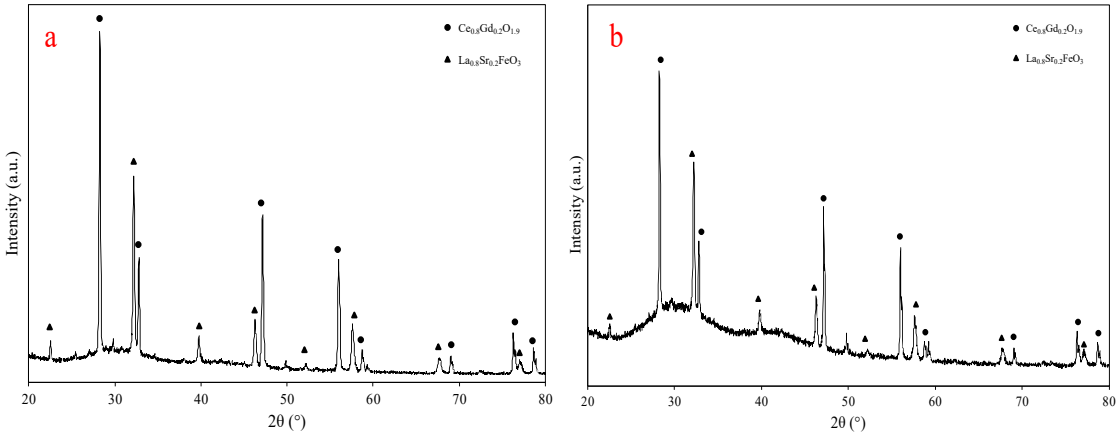


Figure 6.8. XRD analysis from cathode side of (a) LV3SF-GDC (35 µm)-YSZ-NiOYSZ fuel cell, (b) LV3SF-GDC (5 µm)-YSZ-NiOYSZ fuel cell.

6.4.5. Single Cell Performances

Figure 5.9 shows the current-voltage characteristics of the SOFC using YSZ electrolyte. At 500, 600, 700, and 800 ºC, respectively, the observed open circuit voltages with hydrogen as the fuel and an oxygen/nitrogen gas blend as the oxidant are 0.91, 0.92, 1.03, and 1.04 V. These values were, to some extent, lower than those determined using the Nernst equation [213, 214]. Poor sealing, gas leakage, and short circuits originating from the thin electrolyte layer might all be the cause of the lower OCV readings. At 500, 600, 700, and 800 ºC, the single cell's highest power densities were 0.18, 1.19, 7.18, and 13.10 mW/cm^2, respectively. Additional adjusting may be necessary to get the improved cell performance.

The impedance spectrum, measured at 500–800 ºC under open circuit voltage, is shown in Figure 5.10a. There may be many processes operating at the chosen frequency range of 0.1–10^6 Hz, according to the asymmetrical form of impedance graphs. Figure 5.10 inset shows the equivalent circuit that was utilized to simulate the experiment results. In the circuit, the values of Lb, C, Q, and R correspond to inductance, capacitance, resistance, and constant phase element (CPE) such as pseudo capacitance.

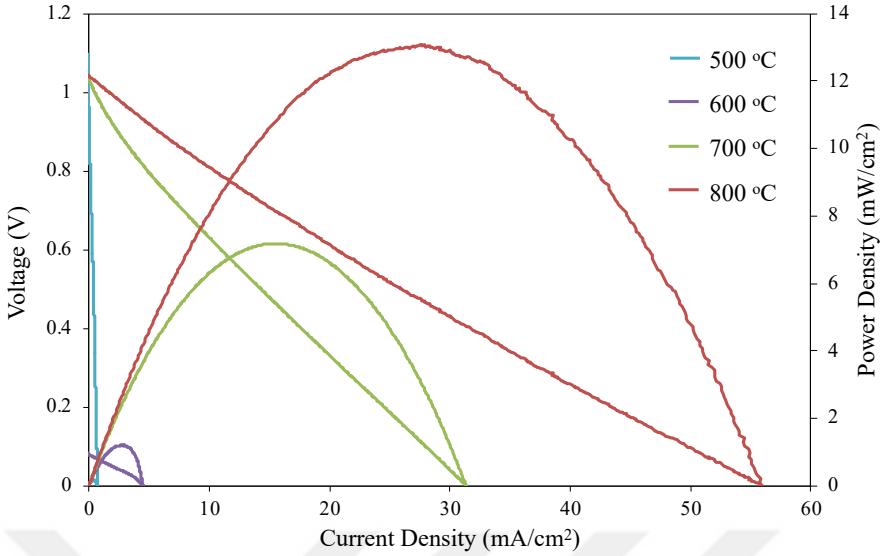


Figure 6.9. I-V curves and output power density of single cell with LV3SF-YSZ-NiYSZ at different temperatures.

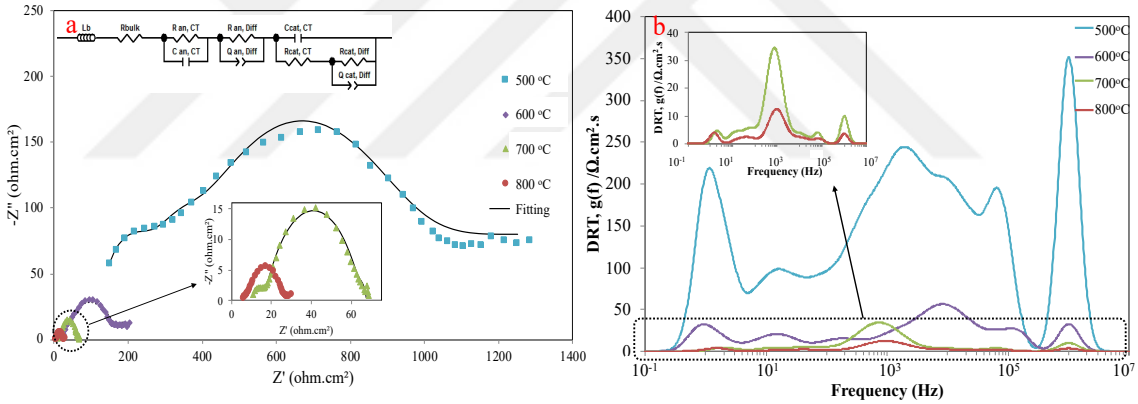


Figure 6.10. (a) Nyquist plots of LV3SF-YSZ-NiYSZ cell at OCV conditions, inset: Equivalent circuit model, (b) DRT curve of impedance spectra as a function of operating temperature at 500 - 800 °C.

For this experimental system, the circuit serves as an appropriate representation, and it permits the assessment of EIS data. These data could be explained by the fact that oxygen reduction at mixed ionic-electronic conducting cathode film basically follows the bulk path way. Oxygen is transported to the electrode/electrolyte phase boundary, where it eventually reaches the electrolyte layer's crystal structure, after first being adsorbed on the electrode's surface and then incorporated as an oxide ion into the bulk. The main resistive process $R_{cat,diff}$ in the bulk route is the electrochemical resistance related to the cathode surface oxygen exchange. The matching semicircle in the spectrum is seen at low frequencies, giving a

capacitive-like characteristic. This behavior, denoted as $Q_{cat,diff}$, is referred to as a constant phase element that is associated with changes in the bulk electrode oxygen stoichiometry. Consequently, the dominating low-frequency arc contains information on the bulk ($Q_{cat,diff}$) and surface ($R_{cat,diff}$) of the electrode. The resistive component of medium-frequency ($R_{cat,CT}$) relates to the transport of oxide ions across the electrode/electrolyte interface. The mid-frequency capacitance ($C_{cat,CT}$) is an interfacial capacitance coupled to the same boundary. The high-frequency intercept of the impedance spectra is caused by the ohmic resistance (R_{bulk}) of the electrolyte and non-zero electrical contact resistance of gold wires.

Table 6.1. EIS Fitting values of LV3SF-YSZ-NiYSZ fuel cell at 500-800°C.

	500 °C	600 °C	700 °C	800 °C	Unit
Ran, Diff	436.8	44.785	6.685	10.26	ohm.cm^2
Lb	3.07E-08	8.62E-13	1.41E-07	2.78E-07	H
Rbulk	116.95	0.4424	8.33	4.5955	ohm.cm^2
Rcat, Diff	1442	149.6	48.095	16.01	ohm.cm^2
Rcat,CT	0.20355	20.49	2.229	0.001165	ohm.cm^2
Ccat, CT	5.34E-10	4.14E-11	5.17E-08	2.03E-08	F
Qcat, Diff	0.000219	2.24E-05	5.86E-05	0.010765	S*s^a
a2	0.1388	0.4686	0.6917	0.1558	
Qan, Diff	3.38E-06	0.004124	2.17E-05	0.000302	S*s^a
a1	0.6138	0.5824	0.5117	0.6286	
Ran, CT	40.745	0.7575	2.569	4.2715	ohm.cm^2
Can, CT	3.37E-08	0.037335	0.01412	6.15E-05	F

Because the resistance at the grain boundary becomes negligible with increasing temperature, there could only be one visible arc at high frequencies. Increased electrical conductivity and vacancy concentration with temperature are responsible for the enhanced electrochemical activity. These factors also enhance charge transfer and oxygen surface exchange in the cathode sample, which in turn enhances ORR at the cathode/electrolyte interface. Additionally, in every temperature range, the low-frequency arc showed higher values than the high-frequency semi-circle. The oxygen adsorption, dissociation, and diffusion process in the cathode sample is the ORR's limiting phase, as evidenced by the significant low-frequency arc contribution to total resistance in the temperature range under

investigation [146], [217]. Table 5.1 provides a summary of the electrochemical circuit characteristics derived from the impedance spectra fits.

As several models may fit the same impedance data and each model includes assumptions, a normal model fitting analysis of the EIS could not proceed and produce relevant data. The Distribution Relaxation Times (DRT) approach may be useful in this case. Examining the electrochemical processes in the system allows for the successful identification and effective resolution of the rate limiting steps. Concurrently, a brief overview of fundamental electrochemical processes can help in the rational construction of an appropriate model to assess particular parameters. Impedance spectroscopy, equivalent circuit model analysis, and DRT were used in this investigation to fully describe the cell. The impedance data were submitted to DRT analysis with a regularization value (λ) of 10^{-3}.

The cell was investigated in the 500–800 ºC temperature range in order to investigate the EIS and DRT dependency across operating temperatures (Figure 5.10b). The impedance spectra were also measured at different potentials at 800 ºC using the values listed in Table 5.1 (Figure 5.11a).

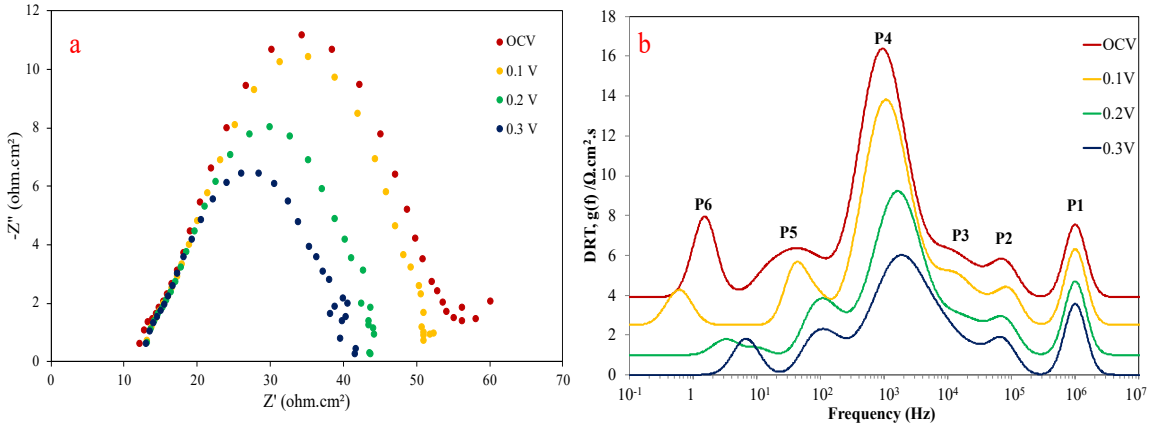


Figure 6.11. (a) Nyquist plots of LV3SF-YSZ-NiYSZ cell, (b) DRT patterns under different applied voltages at 800 ºC.

Every peak in the DRT corresponds to a certain electrode process. The resistance to electrode polarization is indicated by the term "integral peak area." The influence of the high frequency response is very small in comparison to the low frequency response, as seen in Figure 5.10b. It has been proposed that in these oxide materials, the high frequency peaks

are generated by the charge transfer of oxide ions in electrodes, whereas the low frequency contribution comes from reactant flow or mass transport (gas diffusion) [91], [153], [218-219]. Minor contributions that could not be discovered and would necessitate more experimental investigation, such as impedance analysis at varied gas concentrations. Nonetheless, it is crucial and emphasizes the need of employing distinct, bi-layer electrolyte materials to lessen the interfacial resistance's overall polarization resistance contribution.

Every parameter has a distinct representation in DRT in the developed equivalent circuit model shown in Figure 5.10a. Each reaction step in the cell can be designated with the letter P, which stands for resistance and capacitor to represent the adsorption, diffusion, and reaction processes, respectively, to make the contributions of each step easier to understand. Six deconvoluted peaks, identified as P1 - P6, from high to low frequency appeared to be present in Figure 5.11b spanning the investigated frequency range of 1 MHz - 0.1 Hz, indicating six distinct electrochemical processes.

P1, P3, P4, and P5 represent the four cathode processes in this model, whereas P2 and P6 represent the two anode processes. P2 represents the transfer of hydrogen charges, whereas P6 signifies the diffusion of gas in the anode [96], [220-223]. The term P1 denotes the movement of oxide ions through the electrolyte network in the cathode and across the cathode/electrolyte contact [224]. P3 is designated for the diffusion of oxygen species (O^-/O_2^{2-}) to the TPBs, P4 is for the ORR at TPB areas, and P5 is for the diffusion of oxygen gas in the cathode [221–223]. The activation energy of each process's corresponding phase is linked to its resistance. More resistance is correlated with a higher activation energy. Figure 5.11a displays the impedance data collected at various voltages, from which the DRT finding in Figure 5.11b was generated. Every peak's significance is associated with a certain sub-step. The changes in P5 and P6 become more noticeable as applied voltage increases, as seen in Figure 5.11b. Moreover, P1–P4 stay same when the applied potentials rise, P5 shifts to higher frequencies, and P6 peak disappears. Voltage changes therefore have little effect on high and mid frequency activities, which are related to surface exchange reactions and charge transfer. On the other hand, the gas diffusion steps-correlated low frequency peaks P5 and P6 overlap and move to higher frequencies. It is clear that $R_{cat,diff}$ is the rate-limiting step. As was previously indicated, deconvoluted peaks at low frequencies are due to the diffusion and exchange of oxygen species (O^-/O_2^{2-}) at the TPBs and mass transfer of reactants in the

cathode. This phenomenon was further confirmed by the detailed equivalent circuit fitting values in Table 5.1.

The performance of fuel cells made with various electrolyte materials was evaluated in order to validate the methods proposed in this research. The I-V and I-P curves for the LV3SF-GDC-NiGDC cell are shown in Figure 5.12. At 500, 600, 700, and 800 ºC, the power densities were 39.17, 135.72, 170.15, and 182.20 mW/cm^2, respectively. The OCV values at 500, 600, 700, and 800 ºC were 1.10, 0.84, 0.63, and 0.73 V. Use of GDC as a single-layer electrolyte is restricted by partial conversion of Ce^{4+} to Ce^{3+}. The material has electrical conductivity due to the multivalency of the Ce atom, which therefore reduces the OCV values and power density [230]. Consequently, the single-layer GDC electrolyte, whose properties are investigated at temperatures no greater than 650 ºC, is mostly used to produce intermediate temperature solid oxide fuel cells [231–236]. Nonetheless, certain research has suggested that a slight degree of electrolyte electrical conductivity may be helpful for improving processes on electrodes as the electrochemical reaction area grows. Furthermore, GDC electrolyte has a greater ionic conductivity in comparison to traditional YSZ electrolyte. By increasing oxide transport at the electrode/electrolyte interface as a result of the increased ionic conductivity, the charge transfer polarization resistance is reduced. Consequently, it may be possible to reduce the SOFC total polarization resistance, which would allow for even greater cell performance improvement [237, 238].

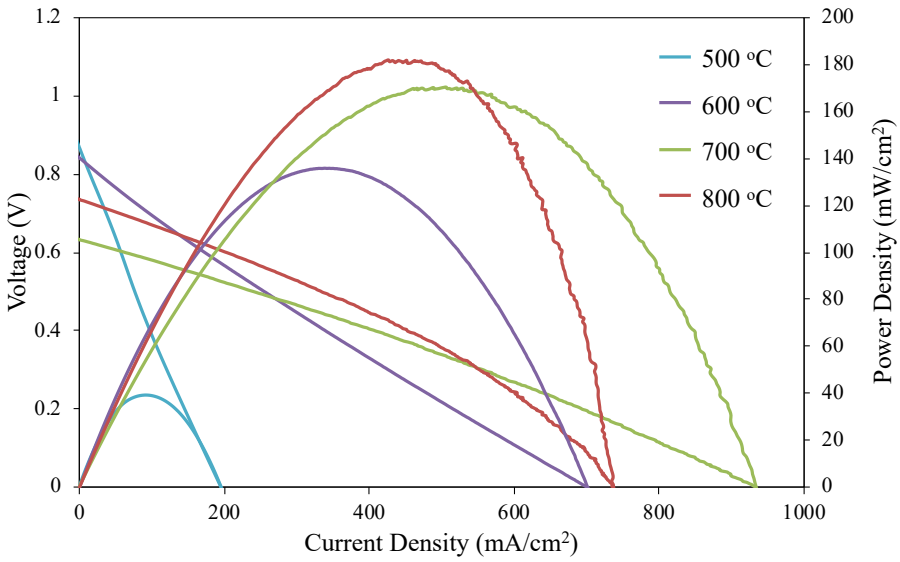


Figure 6.12. I-V curves and output power density of single cell with LV3SF-GDC-NiGDC at different temperatures.

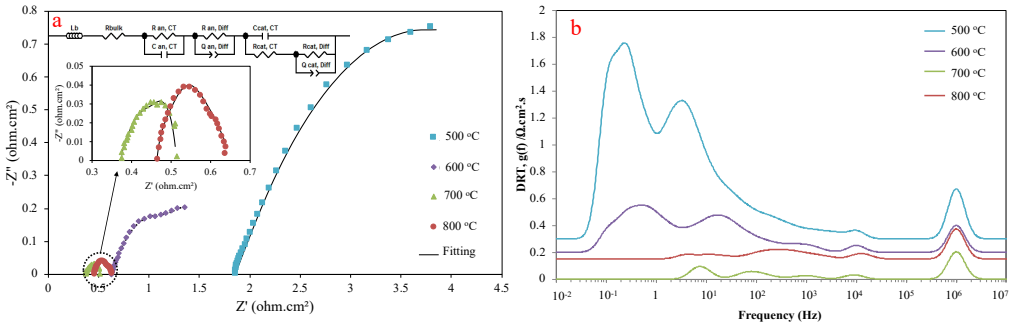


Figure 6.13. (a) Nyquist plots of LV3SF-GDC-NiGDC cell at OCV conditions, inset: Equivalent circuit model, (b) DRT curve of impedance spectra as a function of operating temperature at 500 - 800 °C.

The impedance of the cell with GDC electrolyte investigated at 500–800 °C is revealed by the Nyquist data in Figure 5.13a. Impedance spectra frequently show a semi-circle arc. The intercepts on the x-axis might be used to assess the polarization and ohmic resistance. With an increase in working temperature, total resistance lowers. This is because as the temperature drops, the cell's overall resistance rises and the high-frequency arc's intensity rises as well, moving into the lower frequency region. This pattern suggests that the cell's response stages can be classified as physicochemical processes. The low frequency arc intensity rises below 700 °C, indicating a behavior that is independent of temperature [239].

Table 6.2. EIS Fitting values of LV3SF-GDC-NiGDC fuel cell at 500-800°C.

	500 °C	600 °C	700 °C	800 °C	Unit
Ran, Diff	0.9805	0.77	0.07725	0.17035	ohm.cm^2
Lb	3.59E-07	3.334E-07	3.04E-07	3.5E-07	H
Rbulk	0.876	0.14235	0.306	0.000169	ohm.cm^2
Rcat, Diff	3.773	0.4568	0.10075	0.000482	ohm.cm^2
Rcat,CT	0.019295	0.029375	0.000123	0.44785	ohm.cm^2
Ccat, CT	0.000139	0	5.71E-07	7.42E-08	F
Qcat, Diff	0.0763	0.0000008	0.21515	0.118	S*s^a
a2	0.4777	0.823	0.5527	0.5599	
Qan, Diff	2.16E-07	0.09795	0.015905	0.19065	S*s^a
a1	0.8574	0.5209	0.3691	0.3975	
Ran, CT	0.00446	0.22785	0.03151	0.031945	ohm.cm^2
Can, CT	0.04506	2.2905	1.0465	0.01853	F

The related equivalent circuit model is shown in the inset of Figure 5.13a to further clarify the response process, and Table 5.2 provides the fitting parameters. Figures 5.13b and 5.14b display the DRT spectra that were determined using the impedance. As the temperature rises, both the polarization and intensity of the lower frequency peaks in Figure 5.13b decrease. The charge transfer process-related peak at high frequencies, however, is less temperature-dependent. DRT analysis of the impedance data under various applied potentials, obtained from the impedance data in Figure 5.14a, was shown in Figure 5.14b.

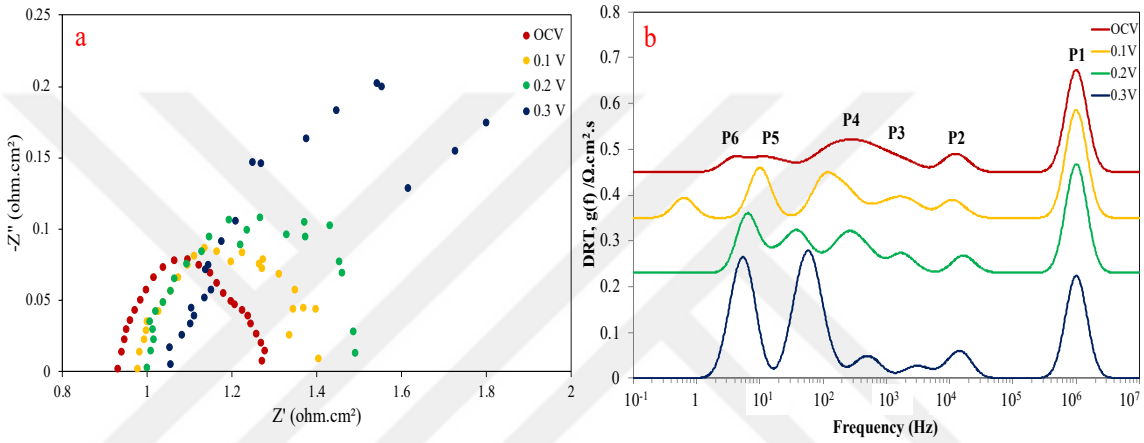


Figure 6.14. (a) Nyquist plots of LV3SF-GDC-NiGDC cell, (b) DRT patterns under different applied voltages at 800 °C.

Six peaks with individual electrode reaction processes were identified in Figure 5.14b. High frequency peak P1 was associated with the processes of charge transfer and oxide ion transfer. Peaks in the mid-frequency range are associated with oxygen species exchange and diffusion at the TPBs. The changes in oxygen nonstoichiometric were structured below 1 Hz. For every cell response, there were a few comparable peaks that overlapped, though. P3-P6 became apparent and shifted to a lower frequency zone with increased applied voltages, as shown by the DRT analysis in Figure 5.14b. Voltage variations had no effect on the P1 or P2 peaks, but they did cause the P5 peak's strength to increase at 10 Hz, which is known as the oxygen gas diffusion in the cathode.

Anode-supported double-layer electrolyte half-cell was then coupled with the developed cathode material. The I-V and I-P polarization curves of the LV3SF- GDC (35 µm)-YSZ-NiYSZ cell at different temperatures ranging from 500 to 800 oC are displayed in Figure 5.15. With an open circuit potential of 1.11 V, a peak power density of 304 mW/cm^2

was achieved at 800 °C. IV characteristics and impedance data indicated that the rate-determining mechanisms of this cell were concentration and ohmic polarization under high current density. If the microstructures of the electrodes, particularly the cathode compartment and the electrolyte thickness, are tuned, the upgraded cell should function even better at lower temperatures.

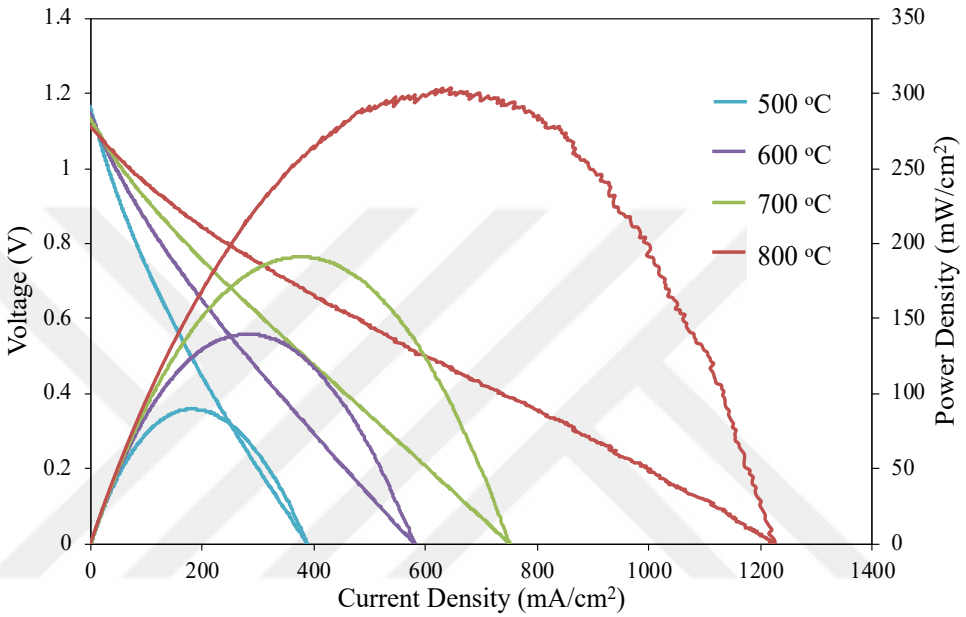


Figure 6.15. I-V curves and output power density of single cell with LV3SF-GDC (35 µm)-YSZ-NiYSZ at different temperatures.

Accurate information on losses and fluctuations resulting from polarization and ohmic resistances during cell operation was not supplied; instead, the cell potentials and observed polarization curves simply display the overall performance loss. Thus, the EIS approach and equivalent model fitting were carried out in order to identify which sub-reaction is responsible for the cell degeneration, and the resulting values were shown in Table 5.3. Figure 5.16a presented the appropriate measured spectra. At both high and low frequencies, two distinct arcs could be seen in the Nyquist spectra. The high frequency contact with the x-axis, or ohmic resistance, is clearly reduced as operating temperature rises. In contrast, the high-frequency arcs in EIS spectra are similar and show very minor size changes over time. On the other hand, the low-frequency arc exhibits discernible fluctuations. The anode mostly influences the high frequency region (above 200 Hz) in anode-supported cells, whereas the cathode impacts the mid-frequency zone (1-400 Hz) and diffusion affects the impedance spectrum below 10 Hz [221], [240-244].

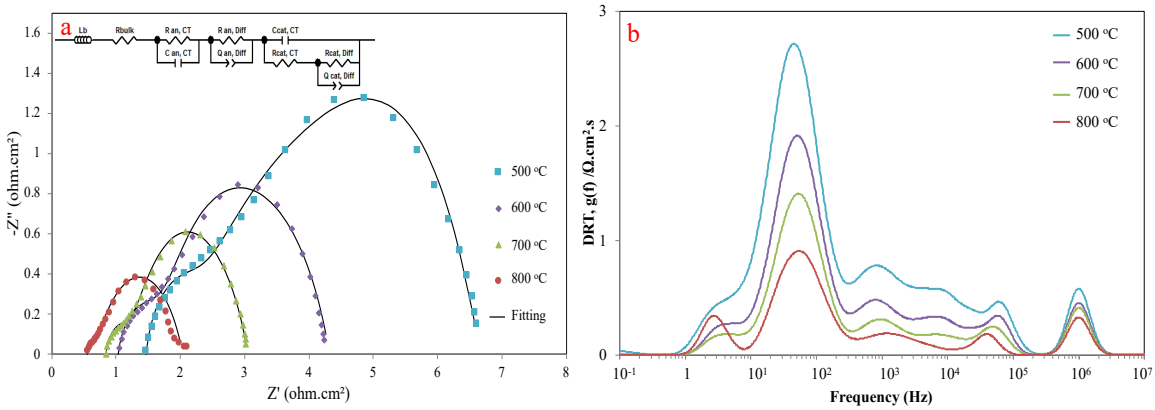


Figure 6.16. (a) Nyquist plots of LV3SFC-GDC (35 µm)-YSZ-NiYSZ cell at OCV conditions, inset: Equivalent circuit model, (b) DRT curve of impedance spectra as a function of operating temperature at 500 - 800 °C.

Table 6.3. EIS Fitting values of LV3SF-GDC (35 µm)-YSZ-NiYSZ fuel cell at 500-800°C.

	500 °C	600 °C	700 °C	800 °C	Unit
Ran, Diff	0.8695	2.3455	1.557	1.292	ohm.cm^2
Lb	3.46E-07	3.28E-07	3.26E-07	3.37E-07	H
Rbulk	0.8315	0.561	0.3837	1.62E-06	ohm.cm^2
Rcat, Diff	3.3665	0.7825	0.4679	0.26535	ohm.cm^2
Rcat,CT	0.576	0.4189	0.40725	0.47675	ohm.cm^2
Ccat, CT	7.09E-08	1.01E-07	1.04E-07	5.79E-08	F
Qcat, Diff	0.004744	0.001203	0.001618	0.01126	S*s^a
a2	0.6	0.6	0.6047	0.4371	
Qan, Diff	0.000286	0.00708	0.009655	0.014325	S*s^a
a1	0.7	0.7	0.7041	0.6646	
Ran, CT	1.038	0.21135	0.23565	2.75E-08	ohm.cm^2
Can, CT	0.00919	0.01071	0.01548	38.38	F

Both cathode and anode effects may be observed in the imaginary section (y-axis) of the spectrum, even though the largest fluctuation in the spectrum is mostly observed at low frequencies. Nevertheless, the frequency zone attributed to anode reactions varied small in comparison to the cathode reaction region, indicating that the anode was only marginally affected and that this resulted in a small rise in the polarization, activation, and concentration resistances. The observed behaviors of the impedance spectra are caused by changes in the

cathode that are connected to reactions, which suggests that cathode deterioration was the main factor influencing the cell's degrading performance [244, 245].

Using the DRT technique, a number of cell sub-reaction pathways have been examined. This approach allowed the impedance sources to be identified by their unique timings. Figure 5.16b shows the DRT results of the LV3SF-GDC (35 µm)-YSZ-NiYSZ cell at 500, 600, 700, and 800 ºC. High frequency region is generally caused by charge transfer between the electrode and electrolyte. The middle frequency represents surface processes, whereas the low frequency zone represents gas diffusion [246–248]. The surface exchange region exhibits the largest intensity peaks in Figure 5.16b, suggesting that such sub-reactions are primarily responsible for impedance losses at 500–600 ºC. But when the temperature increased, they declined, and the temperature difference had no effect on the high frequency peak.

The estimated DRT peaks in Figure 5.17b clearly show at least five independent reactions, in contrast to the impedance curve in Figure 5.17a, which shows overlap between the polarization processes. It is clear that the P1 process, which involves charge transfer processes, was inactive under applied potentials and at high temperatures. In contrast, P2 through P5 processes handle particular voltage dependence and heat activation. With an increase in applied voltage, all peaks—aside from charger transfer—were impacted and overlapped. With the exception of P1, P5—which was identified as the mass transfer sub-step—remains resistive at varying voltages and temperatures, as this indicates.

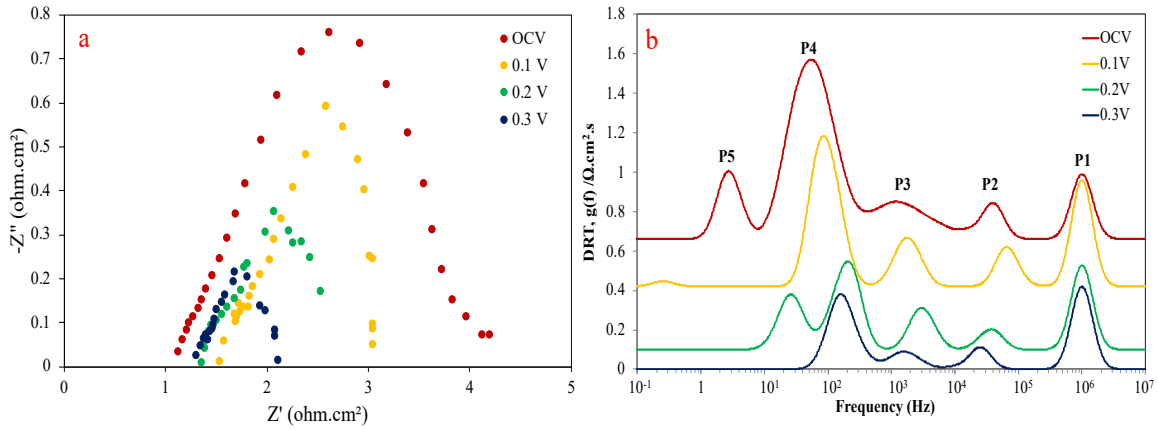


Figure 6.17. (a) Nyquist plots of LV3SF-GDC (35 µm)-YSZ-NiYSZ cell, (b) DRT patterns under different applied voltages at 800 ºC.

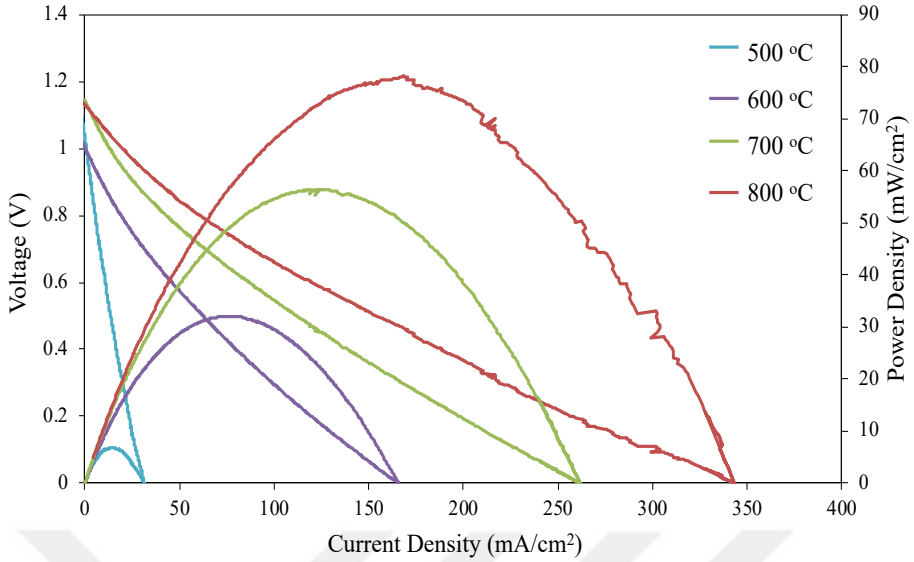


Figure 6.18. I-V curves and output power density of single cell with LV3SF-GDC (5 µm)-YSZ-NiYSZ at different temperatures.

Cell potential and current-power density curves of the cell with a 5 µm GDC barrier layer at 500–800 °C in H_2 fuel are displayed in Figure 5.18. The cell's OCV readings were around 1V, which is slightly lower than the value that would be predicted in theory. The lower OCV readings could be due to inadequate sealing and a slight short circuit caused by the thin GDC/YSZ double-layer electrolyte. Additionally, the open circuit potential in GDC material is decreased by partial reduction of Ce^{4+} to Ce^{3+}. 78 mW/cm^2 was the greatest power density, which is 75% less than the cell that used a 35µm GDC/YSZ bi-layer electrolyte.

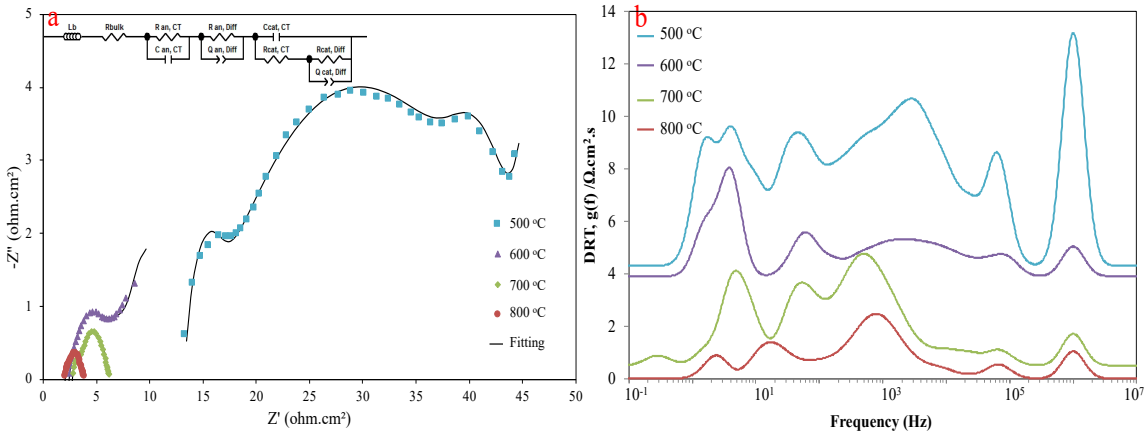


Figure 6.19. (a) Nyquist plots of LV3SF-GDC (5 µm)-YSZ-NiYSZ cell at OCV conditions, inset: Equivalent circuit model, (b) DRT curve of impedance spectra as a function of operating temperature at 500 - 800 °C.

Performance measures may provide useful insights into the structure of the cell, but more work has to be done to thoroughly examine the cell processes using DRT and impedance spectroscopy. In the temperature range of 500 to 800 ºC, electrochemical impedance spectroscopy (EIS) measurements were collected for the LV3SF/GDC (5 µm)/YSZ/NiYSZ cell. Charge transfer, gas diffusion, and adsorption were among the electrochemical reaction stages that were examined in the tests. Figure 5.19a shows the Nyquist plots as a function of temperature. The resistance values that were obtained from the impedance arc diameters have decreased with temperature, as expected. Due to several processes overlapping, only two semi-circle arcs could be seen.

Table 5.4 provides the fitting findings, and Figure 5.19a inset displays the corresponding circuit model. It is evident that, when compared to other cell resistances, $R_{cat,diff}$ has the highest polarization resistance. Fitting impedance data, however, is a matter of opinion. Therefore, in order to gain a deeper understanding of the electrode processes, the overlapping impedance arcs were deconvoluted by calculating the distribution of relaxation times.

Table 6.4. EIS Fitting values of LV3SF-GDC (5 µm)-YSZ-NiYSZ fuel cell at 500-800ºC.

	500 ºC	600 ºC	700 ºC	800 ºC	Unit
Ran, Diff	30.545	1.476	3.254	1.9445	ohm.cm^2
Lb	1.38E-07	3.89E-07	4.13E-07	4.11E-07	H
Rbulk	12.29	1.654	1.653	0.9465	ohm.cm^2
Rcat, Diff	150	8.265	3.2035	0.562	ohm.cm^2
Rcat,CT	3.107	0.3097	1.0165	0.8175	ohm.cm^2
Ccat, CT	4.44E-08	5.33E-08	4.82E-08	4.95E-08	F
Qcat, Diff	0.168	0.01661	0.003978	411.95	S*s^a
a2	0.8413	0.2423	0.4769	0.3676	
Qan, Diff	0.001175	0.000684	914	0.00988	S*s^a
a1	0.3322	0.6404	0.01992	0.319	
Ran, CT	0.8735	2.156	0.37095	0.25995	ohm.cm^2
Can, CT	3.49E-05	0.145	2.53E-06	0.001235	F

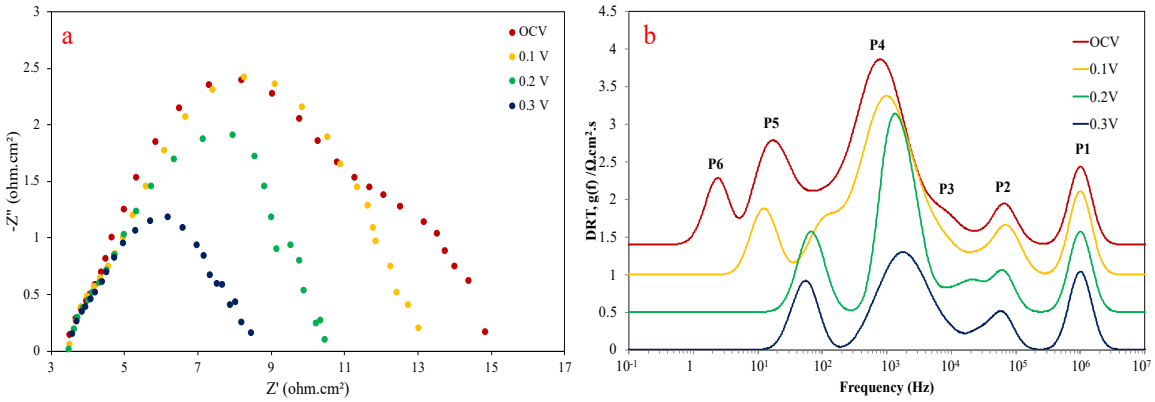


Figure 6.20. (a) Nyquist plots of LV3SF-GDC (5 µm)-YSZ-NiYSZ cell, (b) DRT patterns under different applied voltages at 800 ºC.

Figure 5.19b illustrates the results. Low frequency processes were more resistive at lower temperatures, as seen by the comparison of various temperatures in Figure 5.19b. Mass transfer reactions were no longer resistive steps, as evidenced by the processes becoming less prominent as the working temperature increased. Furthermore, the impedance data indicates that the oxygen gas diffusion at the cathode exhibits the strongest resistance, as demonstrated by the mid-frequency reactions, which are surface exchange processes that evolved at 800 ºC.

Over the examined time scale, six DRT peaks generated from Figure 5.20a were discovered in Figure 5.20b with several applied potentials. Each peak represents a rate-limiting electrode reaction, and the size of the peak indicates the resistance of the associated process. P1 and P2 were ascribed to bulk resistance, fuel charge transfer at the anode, and oxide ion incorporation at the electrode/electrolyte interface, respectively. Furthermore, they showed no reaction to voltage variations. Additionally, the P3 peak at mid-frequency, which indicated the transport of oxygen species to the TPBs, did not change. P4 did, however, slightly drop when the voltage was changed, indicating that a higher potential applied to the system might facilitate the reduction process and oxygen surface exchange. P5 and P6 peaks exhibited opposing behavior at low frequencies, illuminating the characteristics of diffusion-related responses. These two peaks moved to a higher frequency range and overlapped one another. As a consequence, the DRT results agreed well with the model fitting and previously suggested EIS.

6.5. Conclusion

As a conclusion to this chapter, single cells with YSZ, GDC and bi-layer electrolytes were produced and their performance, impedance and DRT behaviors under different temperature and voltages were reviewed. It was concluded that the cells with GDC (35µm)/YSZ double layer electrolyte exhibited highest power density with 304 mW/cm^2. In EIS plots, two separate arcs were visible showing highest polarization resistance contribution from mid and low frequency regions. Also, from the circuit model fitting results at Table 5.1 – 5.4, it could be reviewed that $R_{cat,diff}$ sub-reaction has the highest influence on total resistance with the values of 1655.70, 4.33, 4.88 and 162.03 Ω/cm^2 for single cells with YSZ, GDC, GDC (35 µm)/YSZ and GDC (5µm)/YSZ electrolyte combinations, respectively.

From the DRT findings, charge transfer resistance contribution was neglected, because this peak is mostly labelled for transport of oxide ions through electrolyte network which is called as R_{bulk}. For single cell with YSZ electrolyte has performed largest resistance at diffusion and exchange of oxygen species (O^-/O_2^{2-}) at the TPBs and mass transfer of reactants in the cathode processes, and also the cell showed dependency on applied voltages at low frequency. The mass transfer reactions such as oxygen and hydrogen gas diffusion in the electrodes have become more visible. In the cell with only single layer GDC electrolyte, minor contributions from each cell process, except charge transfer in electrolyte, were observed. With increasing applied voltage, peaks separated from each other and became more visible, also P5-P6 peaks which signifies mass transport processes have the highest peak intensity.

In order to compare bi-layer electrolyte influence in the cell performance, GDC layers were attached with different thicknesses on conventional YSZ electrolyte. In the first scenario, GDC layer with 35 µm thickness were tape casted and laminated, and the performance, EIS and DRT results were studied. It has highest power density among other combinations and lowest $R_{cat,diff}$ value in equivalent circuit fitting results. This estimation was also approved by DRT findings. Low frequency peaks have the major effect on total cell resistance. With applied potentials, mass transfer related processes were disturbed and have shifted towards higher frequencies showing contribution originates from the flux of the

reactants. At the final case, a thin GDC layer were laminated with YSZ electrolyte and the cell was undertaken various experiments. The cell has exhibited similar behavior with the first cell prepared with YSZ electrolyte. Cathode surface exchange reactions has determined as rate limiting steps same as the case in the first cell. Moreover, with applied potentials gas diffusion processes developed higher resistances.

After all sets of analysis, modelling and calculations with different electrode and electrolyte material combinations, and their micro and 3D structures; the materials and interfaces could be manipulated and tailored on different length scales. Difficulties at the electrochemical interface can be identified by connected chemical, structural, and electrochemical characteristics in combination with comprehensive characterization approaches.

7. SYNTHESIS, CHARACTERIZATION AND PERFORMANCE ANALYSIS OF $La_{0.595}V_{0.005}Sr_{0.4}MnO_{3-\partial}$ (LV05SM) CATHODE SAMPLE

This section is partially published as: Kisa, A.E., and O. Demircan, “Transition Metal Doped Solid Oxide Fuel Cell Cathodes”, *Journal of the Turkish Chemical Society Section A: Chemistry*, Vol. 5, pp. 1153-1168, 2018 [136]. Kisa, A.E., and O. Demircan, "Fabrication and electrochemical performance of $La_{0.595}V_{0.005}Sr_{0.4}MnO_{3-\partial}$ (LV05SM) cathode material for solid oxide fuel cells", *Turkish Journal of Chemistry*, Vol. 42, No. 6, pp. 1479-1498, 2018 [279].

7.1. Introduction

Perovskite materials such as $La_{1-x}Sr_xMnO_{3-\delta}$ (LSM) with x between 0.15 and 0.50 are the most commonly used and studied cathode materials for standard SOFCs [280]. These Sr-doped lanthanum perovskites stay stable both in oxygen excess-oxidizing and oxygen deficient-reducing gas atmospheres [281]. Oxygen deficiency leads to oxygen vacancies while oxygen excess results in metal site vacancies, which improves electrode properties due to facilitation of activation of O_2 in the ORR. However, the ionic conductivity of LSM is extremely low due to the low concentration of oxide ion vacancies [282]. This causes practical limitations and restrictions for the application of LSM, especially at low temperatures (<800 °C). As the working temperature of SOFC system decreases below 800 °C, the oxide ion conductivity for the traditional cathode materials like LSM distresses the ORR performance [283]. Therefore, incorporation of a material or doping with another metal with comparable higher oxide ion conductivity may improve the cathode performance.

Vanadium is one of the most abundant and widely allocated metals in the earth’s crust and is found in nearly 150 different minerals [284]. The most widespread use of vanadium is in catalysis, and vanadium oxide-based catalysts are used in the production of important chemicals such as sulfuric acid and phthalic anhydride, and in the reduction of environmental pollution like NOx from vent-gas of power plants [285–287]. Multiple oxidation states for V such as +2, +3, +4, and +5 provide it with extra stability under oxidizing and reducing

conditions [288]. Also, due to their multivalent oxide structures, vanadium oxides are commonly used for selective catalytic reduction reactions.

In this chapter, the effects of changes in the oxidation states of doped transition metals such as Vanadium were investigated to understand ORR mechanism in the operation of SOFC on intermediate temperature range by employing the tape casting and co-firing procedures to produce the single cells with anode-supported thin electrolytes to enhance the electrical characteristics of perovskite materials. Both electrical and ionic conductivities, and the performance of perovskite materials have been measured for a variety of temperatures by employing EIS and DRT calculations. As a results of these analysis, adsorption, dissociation, and diffusion processes were found to be the ORR's limiting steps. These findings suggest that this V-doped perovskite structure, $La_{0.595}V_{0.005}Sr_{0.4}MnO_{3-\partial}$ (LV05SM), is a promising cathode material for IT-SOFCs.

7.2. Material Synthesis

Utilizing the sol-gel method, $La_{0.6-x}V_xSr_{0.4}MnO_{3-\partial}$ (LVxSM, x = 0.005) powders were produced. Reagents included La, Sr, and Mn nitrates as well as V acetate (purity > 99.9%, Aldrich Chemicals, USA). Separately, each reagent was dissolved in distilled water at the proper stoichiometric ratio. To produce a homogenous solution, all of the solutions were afterwards combined and agitated. As complexation and polymerization agents, ethylene glycol and citric acid, in varying amounts, were added after they had completely dissolved.

The citric acid to total metal ions ratio was maintained at approximately 1:2. The solution was allowed to evaporate on a hotplate upon prolonged heating, the gel spontaneously burned, transforming into a light and delicate ash. Following a gentle heating-induced gelation, the resulting gel was placed in a drying oven at 500 °C for 2 hours to eliminate organic components. Subsequently, it was subjected to sintering at 900 °C for 3 hours to yield perovskite compounds possessing satisfactory crystalline structure, as confirmed through X-ray diffraction analysis.

7.3. Characterization, Electrochemical Measurements and Fabrication Procedures

The phase identifications of $La_{0.595}V_{0.005}Sr_{0.4}MnO_{3-\partial}$ (LV05SM) cathode sample were obtained by X-ray diffraction (XRD) employing a Rigaku D/MAX-Ultima+/PC Diffractometer with Cu-Kα radiation (λ = 1.54056 Å). The diffraction patterns were recorded in the range of $20^o<2\theta<80^o$ with 0.01 steps and step-counting time of 8s/step. The phases were identified with JCPDS Database. An Al K-Alpha anode ($h\nu$ = 1486.6 eV, with spot size of 400 μm)-equipped Thermo Scientific K-Alpha Surface Analysis instrument was used to conduct X-ray photoelectron spectroscopy. The energy step size was set as 0.100 eV and the charge effect was calibrated using the binding energy of C1s (284.5eV). XPS Peak 4.1 software was used to collect and analyze survey spectra at a pass energy of 50 eV and high-resolution spectra at a pass energy of 20 eV for quantification purposes. SEM-FEG, Philips XL 30 at an accelerating potential of 10 kV was used to study the surface and cross-section morphology of the sintered cells. Performance and electrochemical impedance spectra (EIS) were measured from 500 to 800°C utilizing a self-made test setup contained of numerous gas mass flowmeters, a furnace (Figure 3.1). The sintered cells were attached to a zirconia tube with a ceramic paste. The electrodes' current collectors were made of Au paste and wires connected the electrodes to the testing instrument.

The current-voltage (I -V) characterization was conducted with the Gamry Ref 3000 Potentiostat (Gamry Instruments, Warminster, PA, USA) using H_2 as the fuel and oxygen as the oxidant. The AC impedance data were collected with an AC signal of 10 mV in the frequency range of 1 MHz - 0.1 Hz. Commercial YSZ (Yttria-Stabilized Zirconia (8% Y) – Tape Cast Grade Powder, Fuel Cell Materials Ltd., USA) and GDC (Gadolinium Doped Ceria (20% Gd) – Tape Cast Grade Powder, Fuel Cell Materials Ltd., USA) powders were used to prepare the electrolyte layers. The anode slurry was obtained by mixing YSZ or GDC and fine grade NiO powder (Fuel Cell Materials Ltd., USA). A two-step ball milling procedure was used to produce the slurries for tape casting. In the first step, polyvinyl butyral (PVB) was used as the binder and ethanol/toluene as the solvent to homogeneously disperse all the particles. Secondly, in order to give an ideal viscosity, the required amounts of plasticizers polyethylene glycol (PEG) and benzyl-butyl-phthalate (BBP) were added to the slurry and ball-milled again for 24 hours.

There were two processes in the tape casting process as well. The de-aired electrolyte and anode slurries were initially cast at a blade height of app. 10, 20 and 200 µm, respectively. The green tapes were cut into disks with a 13mm diameter after drying for 24 hours. One sheet of YSZ and/or GDC electrolytes and two layers of anode green tapes were stacked in order to produce anode-supported cells. The layers were assembled in random directions for relaxation of the residual internal stress and uniaxially laminated for 5 mins. The laminates were subsequently co-sintered at 1250 ºC in air for 3h after burn-out of the organic components. Following co-sintering, the cathode paste was produced using LV05SC powder and electrolyte material with a weight ratio of 50:50, and brush coated onto electrolyte with an active area of 0.5 cm^2. The cathode layer was then sintered at 1100 ^{0}C for 5 h.

7.4. Results and Discussion

7.4.1. Phase Composition and Structure

$La_{0.595}V_{0.005}Sr_{0.4}MnO_{3-\partial}$ (LV05SM) perovskite cathode material was subjected to X-ray diffraction method to determine phase, purity, and crystallinity. The XRD for the cathode sample produced by the sol-gel procedure is displayed in Figure 6.1 following a three-hour calcination at 900 ºC. A small secondary phase forms along with a distorted rhombohedral structure (space group R-3c:167).

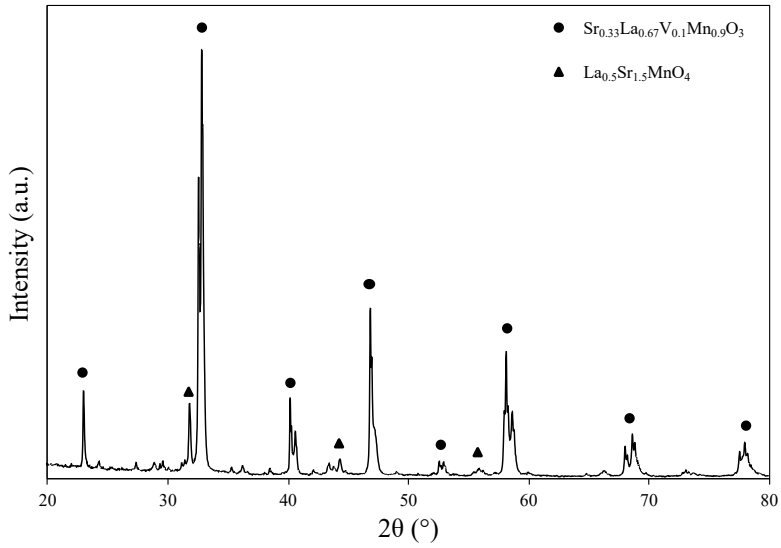


Figure 7.1. XRD data of $La_{0.595}V_{0.005}Sr_{0.4}MnO_{3-\partial}$ cathode powder.

The lattice parameters, phase, and crystallite size are computed and compared to the software crystallographic open database (COD). A single phase with lattice parameters of *a, b* = 5.509 Å, *c* = 13.365 Å**,** α, β= 90.00° γ= 120.00°, and volume of 351.31 Å^3 is shown by the XRD pattern of the produced cathode material. Good integration of the metal oxides utilized in the powder synthesis into the lattice is indicated by the relatively sharp peaks in the XRD pattern. These findings provide more evidence that the prepared catalysts successfully generated the $ABO_{3-\partial}$ perovskite structure.

7.4.2. XPS Analysis

The surface properties of LV05SM sample examined by XPS, all elements, such as La3d, V2p, Sr3d, Mn2p, and O1s have obviously existed in the crystal which is approved from the full scan survey spectra shown in Figure 6.2a. The XPS spectrum of La3d is shown in Figure 6.2b. It has two wide peaks with a splitting of 16.7 eV, one at lower binding energy at 833.01 eV and another at higher binding energy at 849.71 eV, which correspond to the La3d5/2 and La3d3/2 spectra, respectively. The relative intensity ratio for La3d5/2 and La3d3/2 is around 1.38; these values are closely related to those found in the literature [172]. The difference between the La3d5/2 doublet splitting, which is about 3.6 eV, confirms the existence of lanthanum hydroxides [173, 174]. As a result, the La3d is in +3 oxidation states, as shown by the distinct separation of these spin-orbit splitting. Also, the substitution of La ions by Sr and V ions did not result in any observable shift in the position of these peaks in XRD and XPS spectra.

The high resolution XPS spectra of V2p, which can be seen in Figure 6.2c, can be deconvoluted into four peaks at 515.6, 516.4, 522.4, and 523.7 eV, which indicates the oxidation states of vanadium in this sample are +5 and +4 [175–177]. The area ratio between the V2p3/2 and V2p1/2 energy levels, arising from the orbital splitting of the V2p energy level, was set to 1.5:1, and the energy separation between the two levels was set at 7.7 eV. These results are in good agreement with the results from other studies [178, 179].

It is known that the binding energies found by XPS for core electrons of atoms depend on its oxidation state, the electrostatic potential caused by the charge distribution on the atoms at the ionized site, effects of the final state; and work functions. In general, increasing

the number of electronegative elements like oxygen on the metal atom A causes an increase in core electron binding energies. Figure 6.2f displays the whole range of corresponding binding energies measured for O1s peak. The three peaks at 527.8, 530.5, and 532.1 eV in the core-level O 1s spectra can be attributed to the V-O bonding, adsorbed hydroxyl groups, and molecular water, respectively [175], [182]. According to the oxide electro neutrality and charge compensation mechanism, the negative charge defect caused by Sr^{2+} and V^{4+}/V^{5+} replacing La^{3+} at the A site appears to be compensated for by Fe^{2+}/Fe^{3+}. The shared electron pairs Mn^{3+}/Mn^{4+} and V^{4+}/V^{5+} allow for continuous electron transfer across Mn-O-Mn and V-O-V.

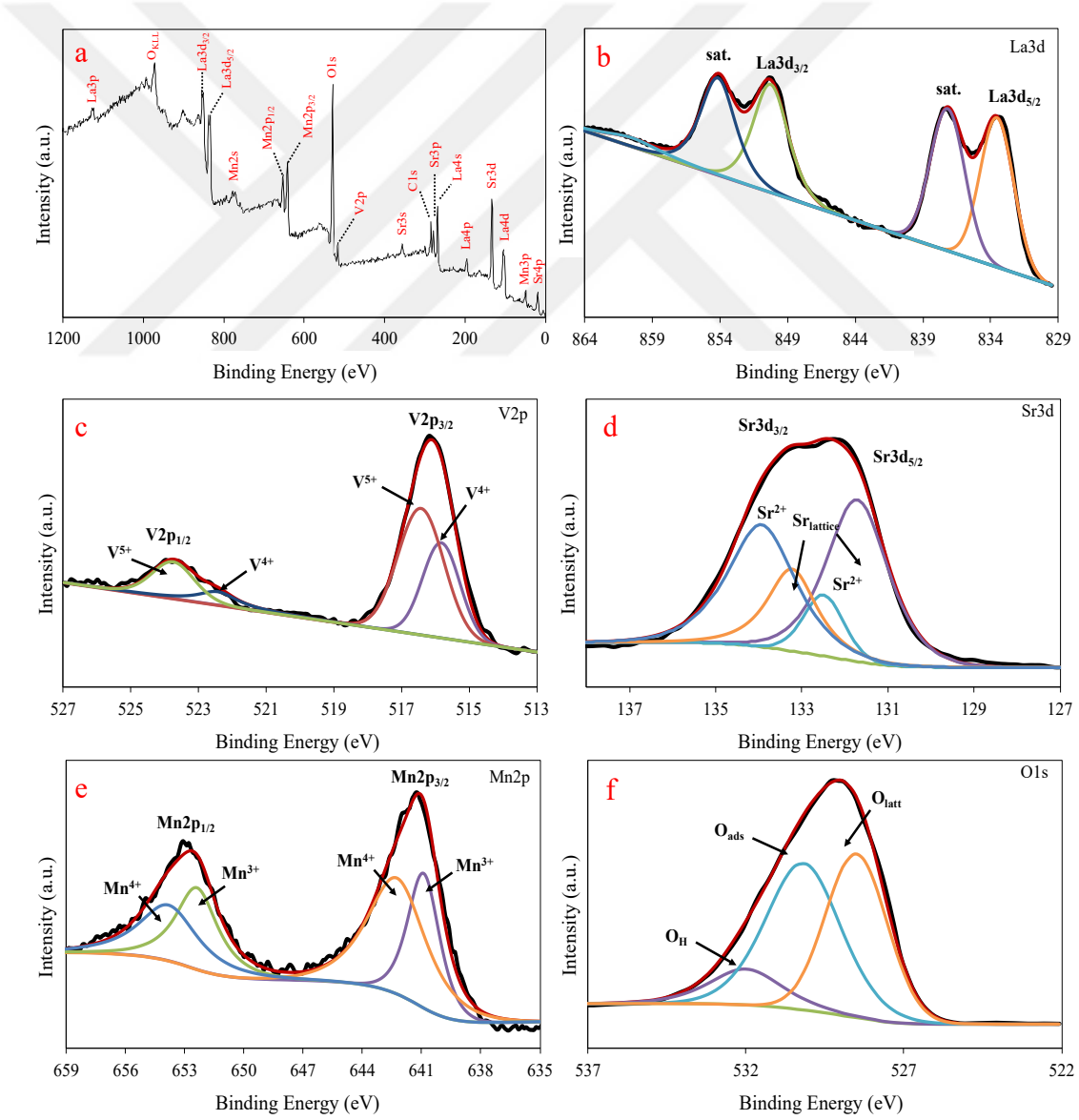


Figure 7.2. XPS survey spectra of (a) LV05SM perovskite, (b) La3d3/2 and La3d5/2, (c) V2p1/2 and V2p3/2, (d) Sr3d3/2 and Sr3d5/2, (e) Mn2p1/2 and Mn2p3/2, (f) O1s.

The Sr3d core-level spectra were particularly helpful for determining the bulk and surface contributions in the spectra since the Sr3d levels had a distinct surface core-level shift [183]. The performance loss of the cathode samples in SOFC is widely known to be caused by Sr segregation, which has been confirmed by earlier studies [184, 185]. Shown in Figure 6.2d, the Sr3d spectra were well matched using two sets of spin-orbit doublets with an energy separation of 2 eV and an area ratio of ~2. The significant peaks of the Sr3d5/2 and Sr3d3/2 components were seen in the spectra of the LV05SC sample at 131.0 and 133.2 eV, respectively. The contributions to the Sr3d photoelectron spectrum were discovered to be due to perovskite lattice-bound Sr ($Sr_{lattice}$). The Sr atoms in Sr-OH, Sr-CO_3, Sr-Sr, and Sr-O bonds near the surface of the cathode sample ($Sr_{surface}$), which do not have perovskite structures, are responsible for the two additional minor peaks at 132.5 and 134.5 eV [186–190]. Because no obvious peaks assigned to carbonates could be seen in the X-ray diffraction patterns (Figure 6.1), the effect caused by carbonate compounds is negligible. Furthermore, the binding energies of Sr in the Sr-O structure ($Sr_{surface}$) and Sr in the lattice ($Sr_{lattice}$) are very similar, even beyond the resolution limit of this experiment configuration. The $Sr_{surface}$ therefore most likely results from the formation of the $Sr(OH)_2$ phase from SrO or from the development of a $Sr(OH)_2$-like binding environment such as SrOH on the Sr of the perovskite lattice or on the Sr of a separated SrO phase. Even though it is clear that the $Sr_{surface}$ associated with $Sr(OH)_2$ species is mostly on perovskite lattice. For the LV3SF sample, the $Sr_{lattice}/Sr_{surface}$ ratio of 2 indicates that the $Sr_{lattice}$ component of the Sr3d occurs to a greater extent. A Sr-OH signature peak is present in the bonding environment in all three cases (Figure 6.2f shows O1s spectra that demonstrates its presence). These results are expected for a perovskite structure.

As displayed in Figure 6.2e, Mn2p demonstrated two peaks with binding energies of 640.98 eV and 652.58 eV. After fitting, the curve was examined in more detail. The fitted data shows that the Mn2p3/2 XPS peak splits into two halves at about 640.90 and 642.26 eV, and Mn2p1/2 has emission peaks at 652.39 and 653.84 eV. These two are attributed to Mn^{3+} and Mn^{4+} surface species, that proves that the coexistence of mixed oxidation states of Mn enhance the both electrical - ionic conductivity, and also ORR activity [289–291].

The XPS spectrum of O1s shown in Figure 6.2f exhibits two peaks, one at 530.5 eV due to adsorbed oxygen (O_{ads}) in the form of highly oxidative O^-/O_2^{2-} species, and one at

527.8 eV assigned to lattice oxygen (O_{latt}, O^{2-}) within perovskite. The extra peak at 532.1 eV, which is not always visible in O1s spectra, is caused by the physical and chemical adsorption of molecular water or hydroxyl groups on the surface of defects (O_H) [195–197]. It is well acknowledged that the redox cycling capacity on Mn ions is closely correlated with the ratio of surface Mn^{3+}/Mn^{4+}. Oxygen vacancies are stated as percentage of adsorbed oxygen on perovskite surface. O_{ads}/O_{latt} ratio of LV05SM cathode was calculated as 1.13. The catalytic activity increases with the quantity of oxygen vacancies on the surface [199]**.** Due to the hygroscopic characteristic of lanthanum oxide when exposed to air, the highest binding energy of O1s (532.15 eV) is thought to be due to a water molecule associated with the surface lanthanum oxide. It should be noted that molecular water and surface-adsorbed oxygen in the form of hydroxyl or oxygen groups could be easily removed by heating to generate oxygen vacancies. But, removing highly oxidative oxygen species (O^-/O_2^{2-}) requires a significantly higher temperature.

7.4.3. Fabrication of Anode-Supported Electrolyte via Tape casting/Lamination/ Co-firing

For producing thin, thick, flat, and large-area ceramic tapes with the thickness range of 10-1000 μm, tape casting is a respectable manufacturing technique. This method is employed to create a range of electrical devices, including multi-layer ceramic capacitors, low-temperature co-firing ceramics, and other devices and is quite straightforward compared to other common methods for fabricating ceramic layers. Making SOFC components by this method is particularly appealing since it may be more affordable to produce in large quantities. In order to manufacture planar electrode-supporting SOFCs, tape casting method has been extensively used. However, due to the challenges that come with fabricating a thin ceramic layer with no gas permeability, tape casting technology has not been successful in the fabrication of electrolytes with thicknesses below 10 μm.

Co-firing of the electrode and electrolyte layers is another low-cost manufacturing method, and effective application of this technique would improve the productivity while consuming less energy. However, minimizing the deformation of the structure owing to mismatches in the thermo-mechanical and physical characteristics of the different layers was necessary for a successful co-firing of the multi-layer structure. There have been a few

research efforts on fabricating the flat-type SOFCs. The attempt to lower the operating temperature from 800 to 600 ºC or below is one of the primary research goals in this area. The benefits of SOFCs operating at lower temperatures include a larger selection of materials, improved long-term performance, system compactness and perhaps lower fuel cell costs [200, 201]. To address these concerns there have been many research efforts including reducing the thickness of the YSZ layer and using substitute electrolyte materials having better ionic conductivity than YSZ at low and intermediate temperatures, such as gadolinium doped ceria (GDC - $Gd_{0.2}Ce_{0.8}O_{1.95}$) and doped $LaGaO_3$ [202–206]. Despite the reports of effective operation at low and intermediate temperatures, the best materials and methods for low-cost process producing stable and consistently high SOFC performance have not yet been fully addressed. To achieve adequate energy conversion rates and provide a suitable power output, a SOFC with a thin electrolyte sheet is preferred [207].

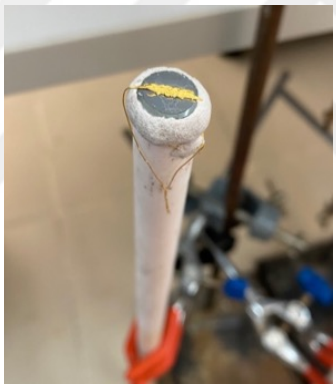


Figure 7.3. Picture of the fuel cell attached to a zirconia tube set-up.

In this chapter, thin YSZ/GDC electrolytes and NiOYSZ/NiOGDC anode layers were prepared via tape-casting. They were used to produce YSZ-NiOYSZ, GDC-NiOGDC, and YSZ-GDC-NiOGDC anode-supported fuel cells with different thicknesses. Figure 6.3 shows the image of a fuel cell prepared with LV05SM cathode sample after all fabrication procedures.

7.4.4. Surface Morphology Analysis of the Cell

Cross-sectional SEM micrographs of constructed fuel cells with an LV05SM cathode sample are shown in Figures 6.4–7. The electrolyte layers of YSZ and GDC have thicknesses of 18.80 and 67.37 µm, respectively. YSZ and GDC tapes of varying thicknesses were

attached to one another in order to observe the impact of double-layer electrolyte on cell performance, as shown in Figures 6.6 and 6.7. The thickness of the YSZ layer is 15.79 µm and the GDC electrolyte layers are 14.46 and 23.14 µm in certain combinations. The electrolyte layers, which were rather dense and crack free, were clearly securely complied to the porous anode layers. The primary requirement for optimal cell functioning was fulfilled since the different parts of the cell were firmly bonded to one another without showing any signs of delamination.

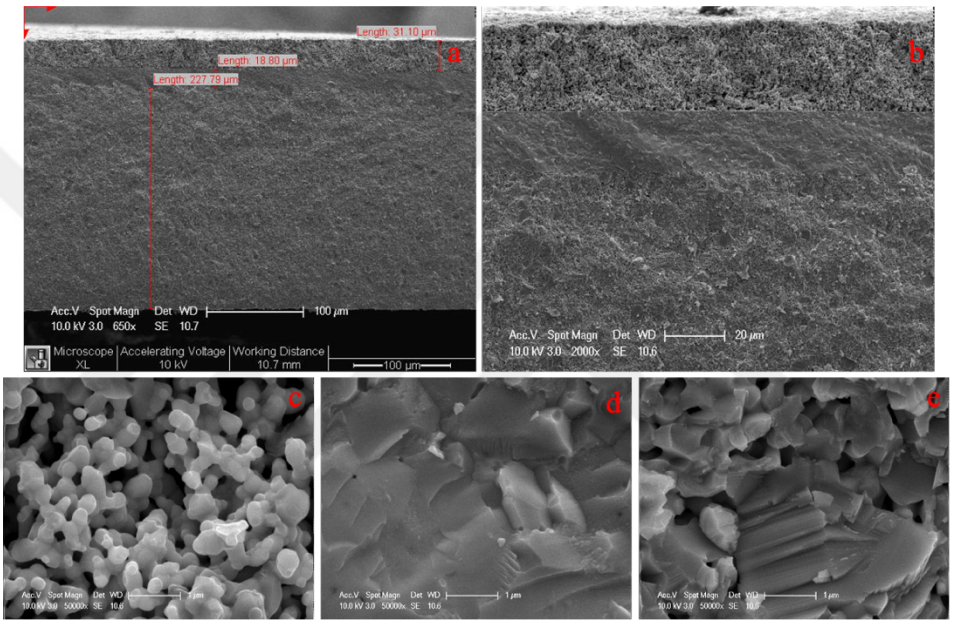


Figure 7.4. SEM images of LV05SM-YSZ-NiOYSZ fuel cell, (a) cross section, (b) closer look to interfaces, (c) LV05SM cathode, (d) YSZ electrolyte, and (e) NiOYSZ anode.

LV05SM cathode powder was mixed with electrolyte material in a 50:50 weight ratio and paint-brushed onto the electrolyte layer with an active area of 0.5 cm^2 following the procedures of green layer fabrication and cofiring. The final sintering step for those constructed anode-supported cells was carried out for five hours at 1100 °C. The measurements of the LV05SM composite cathode layers in Figures 6.4–7 are clearly 31.10, 20.37, 59.30, and 60.02 µm.

A crucial element for achieving optimal cell performance is the porous structure of cathode layer, as seen in Figures 6.4c–7c. Controlling the physical support is only one of the required qualities of a cathode with a large catalytic surface area for ORR. It has also been noted that high density, gas-tight, non-porous electrolyte layers have been obtained (Figure

6.4 – 6.7d and e). Furthermore, it is evident that homogenous connections developed at the interfaces between the layers of electrolyte and electrode.

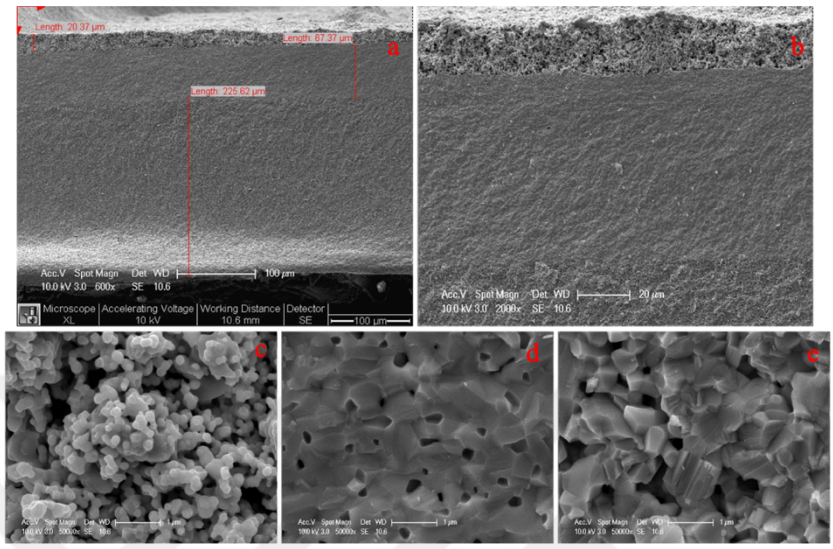


Figure 7.5. SEM images of LV05SM-GDC-NiOGDC fuel cell, (a) cross section, (b) closer look to interfaces, (c) LV05SM cathode, (d) GDC electrolyte, and (e) NiOGDC anode.

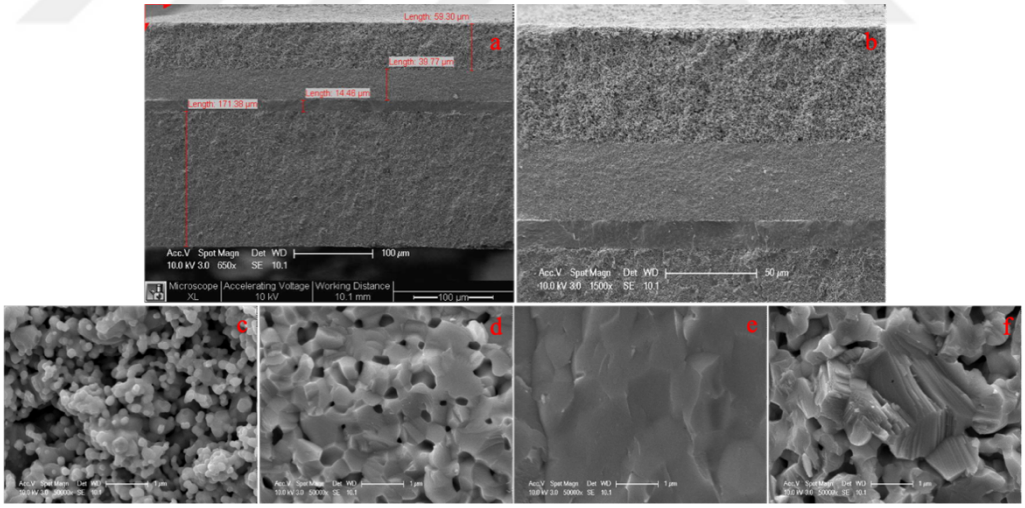


Figure 7.6. SEM images of LV05SM-GDC (35 µm)-YSZ-NiOYSZ fuel cell, (a) cross section, (b) closer look to interfaces, (c) LV05SM cathode, (d) GDC electrolyte, (e) YSZ electrolyte, and (f) NiOYSZ anode.

Enabling oxide ion transport from cathode to anode and reducing or eliminating reactivity between cell components during operation are the two main purposes of an effective electrode/electrolyte interface in SOFCs. The severe operating conditions of SOFCs, however, frequently result in reactivity between the electrode and electrolyte. In a

recent work applied to SOFC materials, Backhaus investigates multiple cathodes using zirconia electrolytes [208, 209]. It is found that the oxygen exchange rate and the overall performance of the cell were adversely affected by the cathode/electrolyte interphase diffusion, segregation, and structural alterations. An order-of-magnitude decrease in electrical performance and a quick deterioration after a protracted treatment at 850 ºC were observed by Grosjean and colleagues when they studied the behavior of $La_{0.8}Sr_{0.2}MnO_3$ on YSZ electrolytes [210].

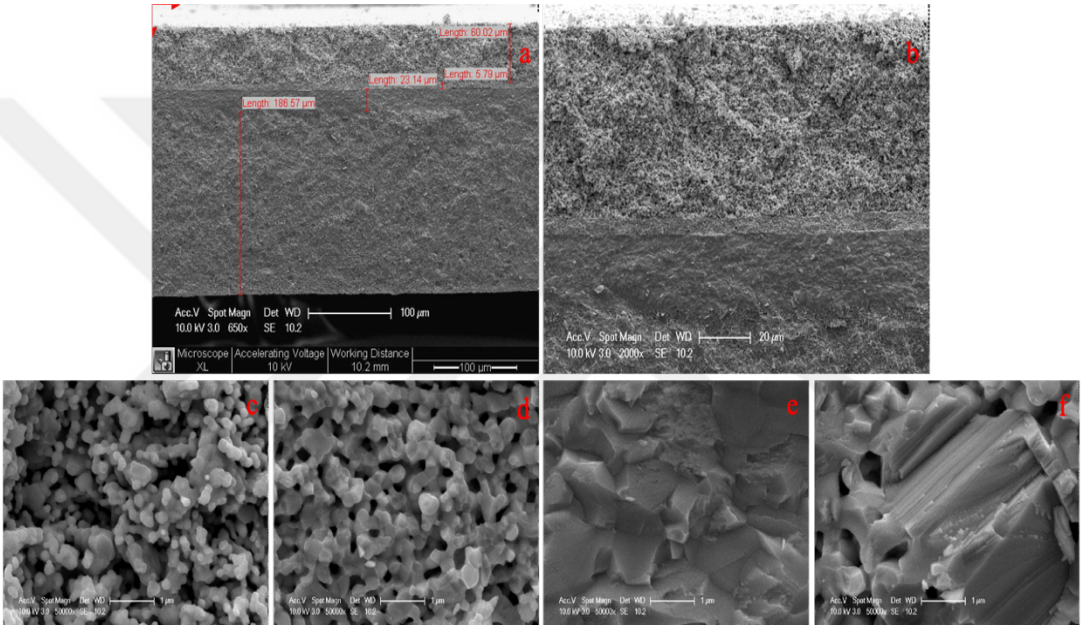


Figure 7.7. SEM images of LV05SM-GDC (5 µm)-YSZ-NiOYSZ fuel cell, (a) cross section, (b) closer look to interfaces, (c) LV05SM cathode, (d) GDC electrolyte, (e) YSZ electrolyte, and (f) NiOYSZ anode.

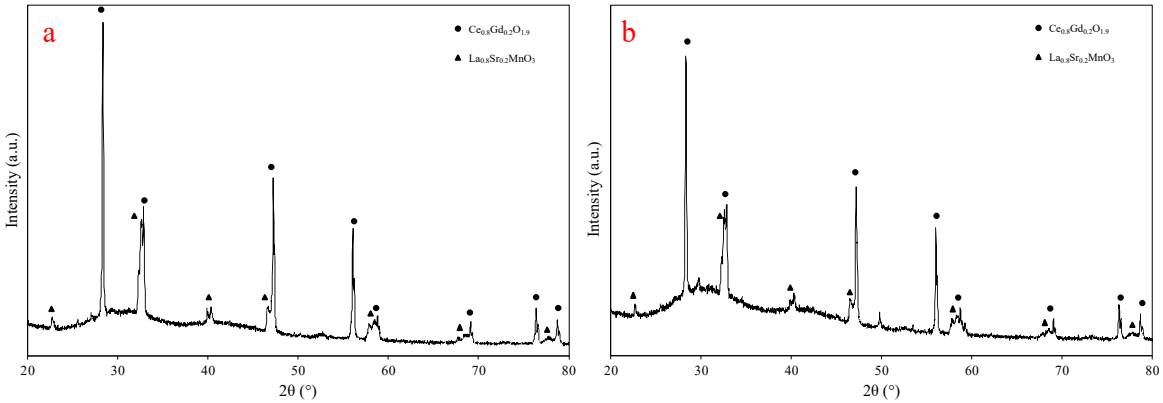


Figure 7.8. XRD analysis from cathode side of (a) LV05SM-GDC (35 µm)-YSZ-NiOYSZ fuel cell, (b) LV05SM-GDC (5 µm)-YSZ-NiOYSZ fuel cell.

The resistive $La_2Zr_2O_7$ phase is one of the microstructural/chemical alterations that has been linked to the decline in efficiency [211, 212]. These impurity deposits lead to a reduction in ionic conductivity, which in turn reduces cell function. GDC layer was cast on YSZ as a buffer layer in order to prevent interface interactions between the cathode and YSZ electrolyte, cathode degradation to generate certain metal oxide forms, and cathode/YSZ interface cracking. For segregation against Zr from YSZ electrolyte, the GDC interlayer's thickness is measured to be 35 and 5 µm (Figure 6.6 and 6.7). Following the half-cell lamination and co-firing processes, X-ray diffraction studies were performed to see if any impurities had developed during the sintering process. The crystallinity and phase composition of the electrolyte layers are shown in Figure 6.8. It is evident that the crystal structures of LV3SF cathode and GDC electrolytes were free of impurities and shifts.

7.4.5. Single Cell Performances

Figure 6.9 shows the plotted current-voltage characteristics of the SOFC using YSZ electrolyte. The recorded open circuit voltages at 500, 600, 700, and 800 °C, respectively, are 1.16, 1.17, 1.16, and 1.14 V with hydrogen as the fuel and an oxygen/nitrogen gas mixture as the oxidant. The single cell's highest power densities at 500, 600, 700, and 800 °C were 15.52, 33.03, 61.51, and 95.32 mW/cm^2, respectively. Additional adjustment might lead to even greater cell performance.

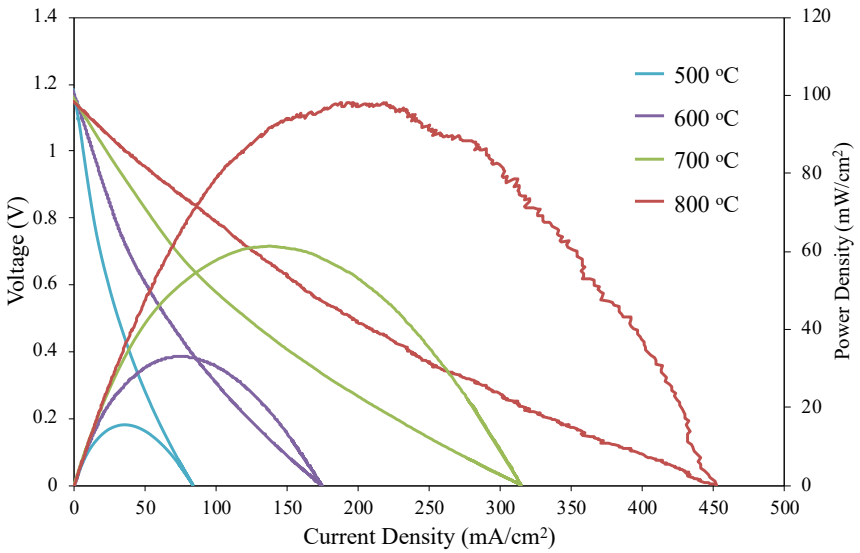


Figure 7.9. I-V curves and output power density of single cell with LV05SM-YSZ-NiYSZ at different temperatures.

The impedance spectrum of the cell, recorded at 500–800 °C under open circuit potential, is shown in Figure 6.10a. The asymmetrical form of impedance graphs indicates the existence of many processes operating within the chosen frequency range of 0.1 – 10^6 Hz. Figure 6.10 inset shows the corresponding circuit that was utilized to mimic the experimental results. In the circuit, inductance, capacitance, resistance, and constant phase element (CPE) such as pseudo capacitance are represented by the letters Lb, C, Q, and R, respectively.

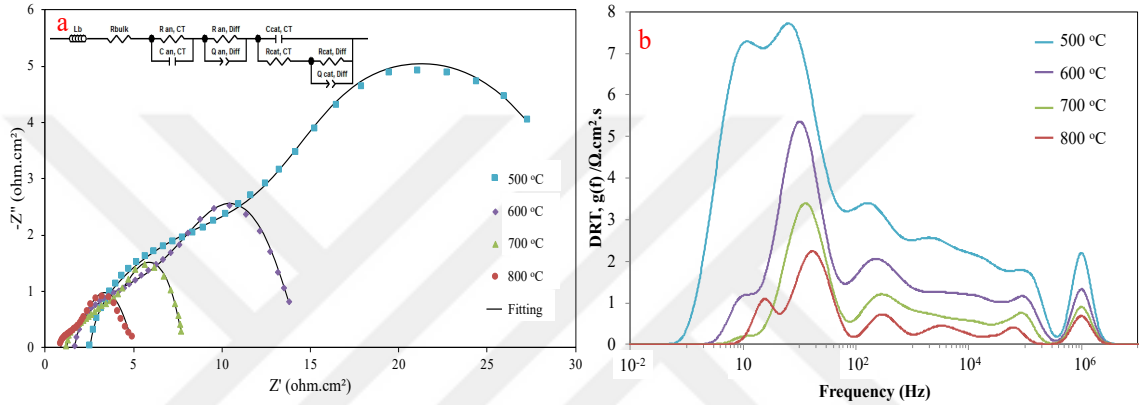


Figure 7.10. (a) Nyquist plots of LV05SM-YSZ-NiYSZ cell at OCV conditions, inset: Equivalent circuit model, (b) DRT curve of impedance spectra as a function of operating temperature at 500 - 800 °C.

The circuit enables the examination of EIS data and is an appropriate representation for this experimental system. These findings could be explained by the fact that oxygen reduction at mixed ionic-electronic conducting cathode films basically follows the bulk path method. According to this method, oxygen is adsorbed on the electrode surface initially, then it is incorporated as an oxide ion into the bulk and moved to the electrode/electrolyte phase boundary, where it ultimately reaches the electrolyte layer's crystal structure. The main resistive process $R_{cat,diff}$ in the bulk route is the electrochemical resistance related to the cathode surface oxygen exchange. The corresponding semicircle in the spectrum is seen at low frequencies, suggesting a capacitive-like characteristic. This behavior is referred to as a constant phase element and is associated with changes in the oxygen stoichiometry in the bulk of the electrode. It is labeled as $Q_{cat,diff}$. Consequently, the dominating low-frequency arc contains information on the bulk ($Q_{cat,diff}$) and surface ($R_{cat,diff}$) of the electrode. The resistive component of medium-frequency ($R_{cat,CT}$) relates to the transport of oxide ions across the electrode/electrolyte interface. The mid-frequency capacitance ($C_{cat,CT}$) is an

interfacial capacitance attached to the same boundary. The high-frequency intercept of the impedance spectra is caused by the ohmic resistance (Rbulk) of the electrolyte and non-zero electrical contact resistance of gold wires.

Grain boundary resistance becomes negligible with increasing temperature, therefore at high frequencies, one arc could be observed. Increased electrical conductivity and vacancy concentration with temperature are responsible for the enhanced electrochemical activity. These factors also enhance charge transfer and oxygen surface exchange in the cathode sample, which in turn enhances ORR at the cathode/electrolyte interface. Additionally, in every temperature range, the low-frequency arc showed higher values than the high-frequency semi-circle. The oxygen adsorption, dissociation, and diffusion process in the cathode sample is the rate-limiting stage of ORR, as evidenced by the significant low-frequency arc contribution to total resistance in the temperature range under investigation [146], [217]. Table 6.1 provides an overview of the electrochemical circuit characteristics that were determined by the fitting of impedance spectra.

Table 7.1. EIS Fitting values of LV05SM-YSZ-NiYSZ fuel cell at 500-800°C.

	500 ^{o}C	600 ^{o}C	700 ^{o}C	800 ^{o}C	Unit
Ran, Diff	16.475	4.695	2.1935	2.3315	ohm.cm^2
Lb	3.68E-07	3.56E-07	3.45E-07	3.62E-07	H
Rbulk	1.4165	0.9465	0.715	0.2047	ohm.cm^2
Rcat, Diff	14.225	7.06	3.189	1.5875	ohm.cm^2
Rcat,CT	0.000121	0.000129	0.00991	0.3656	ohm.cm^2
Ccat, CT	7.88E-09	2.05E-08	6.29E-08	1.2E-07	F
Qcat, Diff	0.001903	0.003188	0.00645	0.02821	S*s^a
a2	0.3152	0.3183	0.3039	0.689	
Qan, Diff	0.0098	0.011025	0.012955	0.018065	S*s^a
a1	0.5749	0.58	0.5181	0.2786	
Ran, CT	1.0405	1.9675	1.9025	0.608	ohm.cm^2
Can, CT	0.022435	0.0155	0.011755	0.030865	F

Impedance spectroscopy has been used to study electrochemical settings, despite its challenges in data interpretation. This approach is the best one currently available for assessing and identifying the operational cell's performance barriers. Typically, a sinusoidal

signal applied within a preset frequency range is used to measure the response. The kinetics of each distinct electrochemical process may be used to categorize them into different time domains, and using an equivalent circuit model can make it easier to identify each phase. Nevertheless, creating a model that fits the impedance data is sometimes arbitrary and based on individuals' preference. Consequently, several models can be successfully fitted to a single set of data.

As several models may fit the same impedance data and each model includes assumptions, a normal model fitting analysis of the EIS could not proceed and produce necessary data. The Distribution Relaxation Times (DRT) approach may be useful in this case. Examining the electrochemical processes in the system allows for the successful identification and effective resolution of the rate limiting phases. Concurrently, a clear overview of fundamental electrochemical processes could assist in the rational design of an appropriate model to assess the proper parameters. Impedance spectroscopy, equivalent circuit model analysis, and DRT were used in this investigation to fully describe the cell. DRT analysis was performed on the impedance data with a regularization value, λ, of 10^{-3}. The cell was investigated in the 500–800 °C temperature range in order to investigate the EIS and DRT dependency across operating temperatures (Figure 6.10b). The impedance spectra were also measured at different potentials at 800 °C using the values listed in Table 6.1 (Figure 6.11a).

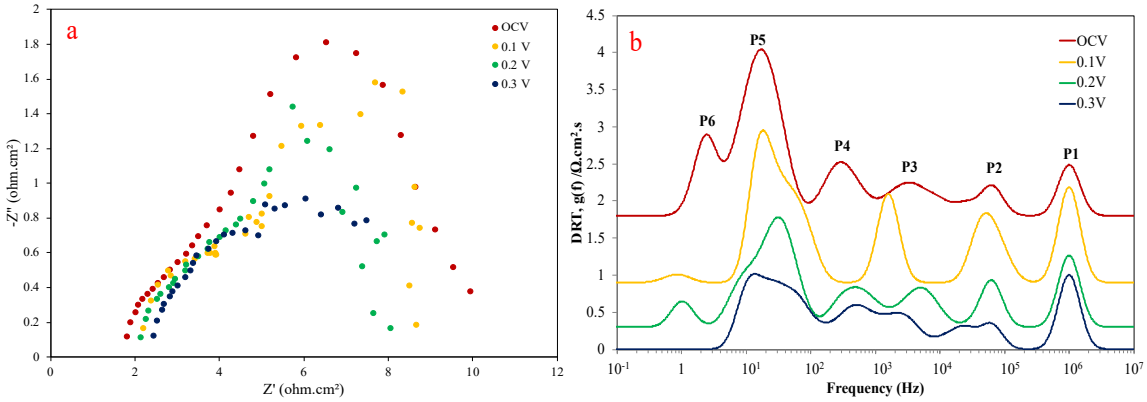


Figure 7.11. (a) Nyquist plots of LV05SM-YSZ-NiYSZ cell, (b) DRT patterns under different applied voltages at 800 °C.

Each electrode technique is represented by a distinct peak in the DRT. The electrode polarization resistance is indicated by the term "integral peak area." It is clear from Figure

6.10b that the high frequency response has less of an effect than the low frequency response. It is proposed that in these oxide materials, the high frequency peaks are caused by the charge transfer of oxide ions in electrodes, whereas the low frequency contribution comes from reactant flow or mass transport (gas diffusion) [91], [153], [218, 219]. The modest contributions that could not be detected and would require more experimental study, such as impedance analysis under different gas concentrations. However, it is essential and suggests the significance of using different and bi-layer electrolyte materials in order to reduce the total polarization resistance contribution of interfacial resistance.

Every parameter in the established equivalent circuit model shown in Figure 6.11a has a distinct DRT representation. Each reaction step in the cell can be identified by its label, P, which stands for resistance and capacitor and represents the adsorption, diffusion, and reaction processes, respectively. This helps to distinguish the contributions of each reaction step more noticeable. Six deconvoluted peaks, denoted P1 through P6, from high to low frequency, seemed to be visible in Figure 6.11b covering the examined frequency range of 1 MHz - 0.1 Hz, indicating six distinct electrochemical processes. P1, P3, P4, and P5 represent the four cathode processes in this model, whereas P2 and P6 represent the two anode processes. P2 represents hydrogen charge transfer, while P6 symbolizes gas diffusion in the anode [96], [220-223]. P1 represents the passage of oxide ions through the cathode's electrolyte network and across the cathode/electrolyte contact [224]. P4 indicates ORR at TPB areas, P5 displays oxygen gas diffusion in the cathode, and P3 is labeled for oxygen species (O^{-}/O_2^{2-}) diffusion to the TPBs [221–223]. Each process's resistance is linked to the accompanying step's activation energy. Resistance increases in direct proportion to activation energy.

The formula for the frequency (*f*), which is proportional to the response rate, is $f = 1/(2\pi RC)$. Greater values of *f* correspond to faster reaction rates. The processes and resistances at the low frequency area began to overlap with applied voltages, as seen in Figure 6.11b. As previously stated, low frequency deconvoluted peaks are associated with the mass transfer of reactants in the cathode, as well as the exchange and diffusion of oxygen species (O^{-}/O_2^{2-}) at the TPBs. It is evident that $R_{cat,diff}$, is the rate limiting step. This phenomenon was further confirmed by the comprehensive equivalent circuit fitting values in Table 6.1.

DRT result in Figure 6.11b was obtained using impedance data in Figure 6.11a, which was collected at various voltages. The significance of each peak is associated with a certain sub-step. The changes in P4, P5, and P6 become more noticeable as applied voltage increases, as seen in Figure 6.11b. Moreover, P4, P5, and P6 shift to lower frequencies whereas P1, P2, and P3 stay unchanged when the applied potentials rise. Consequently, P1–P3 are linked to the transport of oxide species through the electrolyte or across the interface, whereas P4–P6 are connected to the kinetics of the surface electrode, which reacts differently to applied potentials [225–227].

The performance of fuel cells made with various electrolyte materials was evaluated in order to validate the methods proposed in this research. The I-V and I-P curves for the LV05SC-GDC-NiGDC cell are shown in Figure 6.12. At 800 °C, the maximum power density of 76.70 mW/cm^2 was attained. The cell had a greater power density and current at 600 °C than at 700 °C. This demonstrates that the cell with the LV05SM-GDC composite cathode may provide results with greater power and current densities even while running at a lower temperature. The OCV values at 500, 600, 700, and 800 °C were found to be 0.51 V, 0.57 V, 0.65 V, and 0.60 V, respectively.

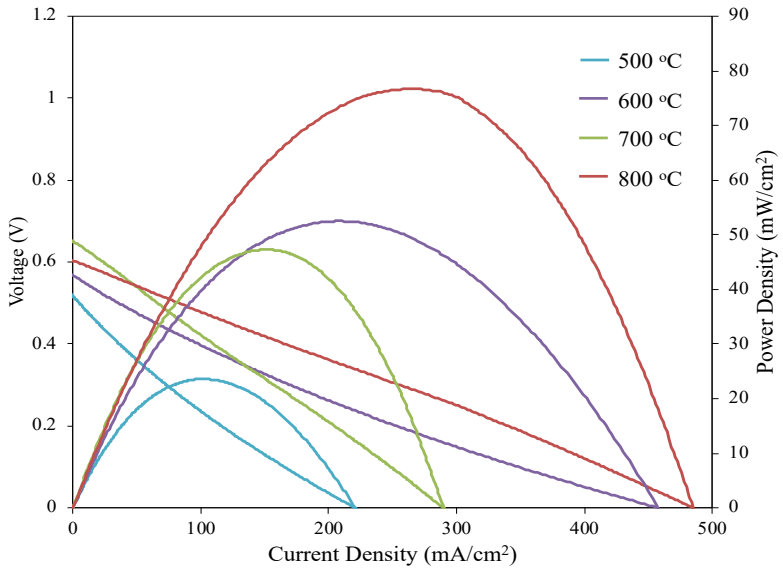


Figure 7.12. I-V curves and output power density of single cell with LV05SM-GDC-NiGDC at different temperatures.

The use of GDC as a single-layer electrolyte is limited by its partial reduction of Ce^{4+} to Ce^{3+}. The material's electrical conductivity, which is caused by the multivalency of the Ce

atom, reduces the OCV values and power density [230]. As a result, the single-layer GDC electrolyte, whose properties are investigated at temperatures no more than 650 ºC, is typically used to create intermediate temperature solid oxide fuel cells [231–236]. Nonetheless, certain research has suggested that a slight degree of electrolyte electrical conductivity may be helpful for improving processes on electrodes as the electrochemical reaction area grows. Furthermore, compared to traditional YSZ electrolyte, GDC electrolyte has a better ionic conductivity. By increasing oxide transport at the electrode/electrolyte interface as a result of the increased ionic conductivity, the charge transfer polarization resistance is reduced. Consequently, it may be possible to reduce the SOFC total polarization resistance, which would allow for even greater cell performance improvement [237, 238].

Figure 6.13a displays the impedance spectrum of the cell with GDC electrolyte examined at 500 - 800 oC, as shown by the Nyquist data. Semi-circle arcs are frequently observed in impedance spectra. The intercepts on the x-axis might be used to assess the polarization and ohmic resistance. With an increase in working temperature, total resistance decreases. This is because the high-frequency arc intensity improves and shifts into the lower frequency region as the temperature drops, increasing the cell's overall resistance. This pattern suggests that the reaction steps in the cell can be classified as physicochemical processes.

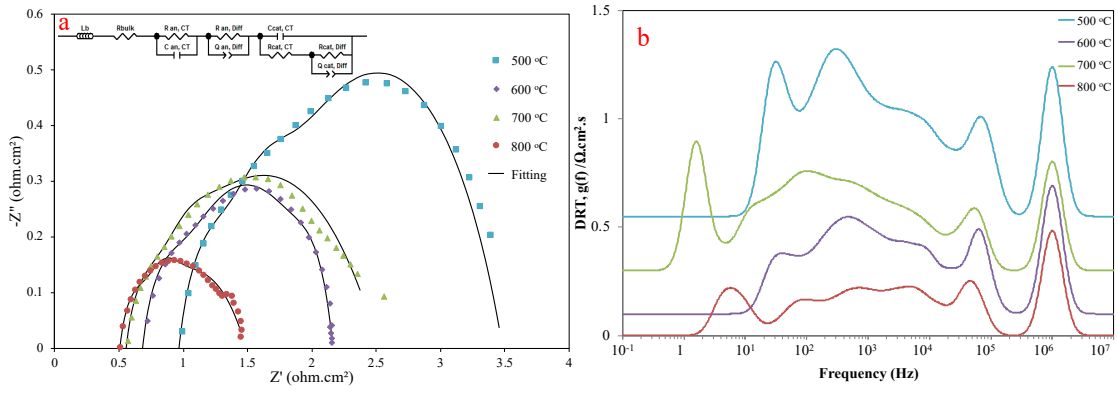


Figure 7.13. (a) Nyquist plots of LV05SM-GDC-NiGDC cell at OCV conditions, inset: Equivalent circuit model, (b) DRT curve of impedance spectra as a function of operating temperature at 500 - 800 ºC.

The low frequency arc intensity becomes greater below 700 ºC, indicating a behavior that is independent of temperature [239]. The cell exhibits the similar trend, with a lower

total resistance at 600 ºC, in Figure 6.13a. The related equivalent circuit model is shown in the inset of Figure 6.13a to further clarify the response process, and Table 6.2 contains the fitting values.

Table 7.2. EIS Fitting values of LV05SM-GDC-NiGDC fuel cell at 500-800ºC.

	500 ºC	600 ºC	700 ºC	800 ºC	Unit
Ran, Diff	0.615	0.42065	0.29715	0.2392	ohm.cm^2
Lb	3.75E-07	3.7E-07	3.78E-07	3.63E-07	H
Rbulk	0.3557	0.1874	6.32E-08	0.1309	ohm.cm^2
Rcat, Diff	1.8185	1.0205	1.6765	0.718	ohm.cm^2
Rcat,CT	0.47905	0.3931	0.4557	0.3022	ohm.cm^2
Ccat, CT	8.27E-08	1.16E-07	8.12E-08	1.71E-07	F
Qcat, Diff	0.004592	0.003809	0.02114	0.033855	S*s^a
a2	0.6118	0.6091	0.4379	0.4339	
Qan, Diff	0.000234	0.000373	0.001167	0.000494	S*s^a
a1	0.6515	0.6513	0.6042	0.6914	
Ran, CT	0.2166	0.14785	0.0891	0.09845	ohm.cm^2
Can, CT	0.000179	0.0273	0.001418	0.000808	F

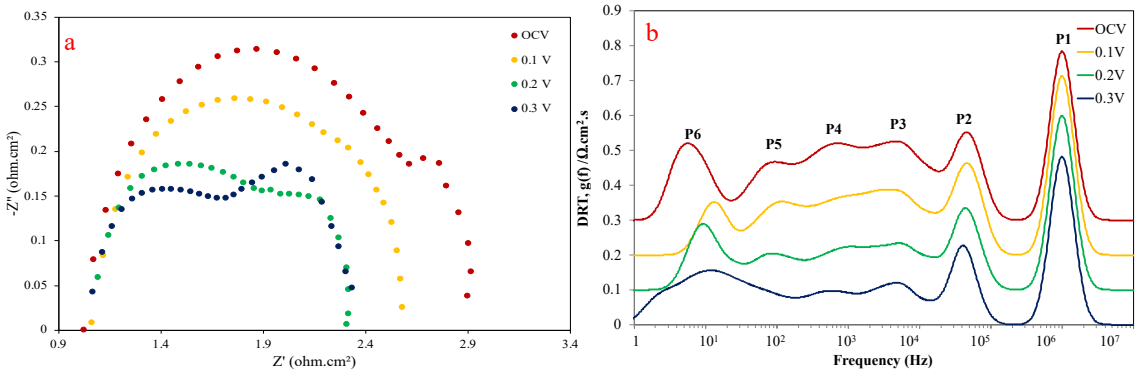


Figure 7.14. (a) Nyquist plots of LV05SM-GDC-NiGDC cell, (b) DRT patterns under different applied voltages at 800 ºC.

Figures 6.13b and 6.14b display the DRT spectra that were computed using the cell's impedance. Both the peak polarization and intensity decrease with increasing temperature in Figure 6.13b. The charge transfer process-related peak at high frequencies, however, is less temperature-dependent. The peaks at 600 ºC have lower values than the peaks at 700 ºC because the integral peak area indicates electrode polarization resistance. With the exception

of high frequency processes, it was unclear what to do next in order to decide. The DRT analysis of the impedance data under various applied potentials, which were obtained from the impedance data in Figure 6.14a, was displayed in Figure 6.14b.

Six distinct DRT peaks with individual electrode reaction processes can be shown in Figure 6.14b. The processes of charge transfer and oxide ion transfer were identified as the sources of two DRT peaks at high frequency, P1 and P2. Peaks in the mid-frequency range are associated with oxygen species exchange and diffusion at the TPBs. The changes in oxygen nonstoichiometric were structured below 1 Hz. For every cell response, there were a few comparable peaks that overlapped, though. As can be shown from the DRT analysis in Figure 6.14b, P5-P6 grew more dispersed and stacked on top of one another whereas P1 and P2 peaks remained unaffected by voltage variations. Due to this variation, the low frequency peaks strength increased to a more exquisite level at 10 Hz, which is known as the cathode oxygen gas diffusion.

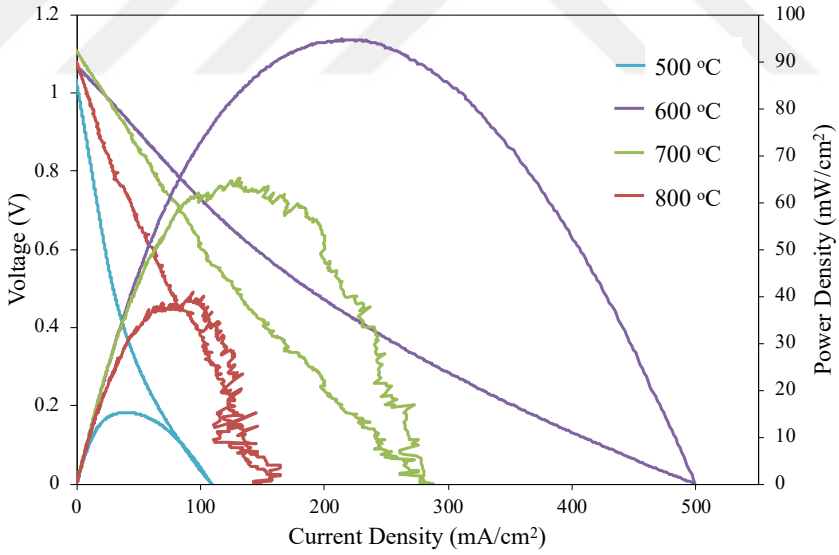


Figure 7.15. I-V curves and output power density of single cell with LV05SM-GDC (35 µm)-YSZ-NiYSZ at different temperatures.

Anode-supported double-layer electrolyte half-cell was then coupled with the produced cathode material. The I-V and I-P polarization curves of the LV05SC- GDC (35 µm)-YSZ-NiYSZ cell at different temperatures ranging from 500 to 800 oC are displayed in Figure 6.15. Peak power density of 98 mW/cm^2 with 1.07 V open circuit potential was attained at 600 °C. The cell exhibited unexpected behavior beyond 600 °C, as both the current

and power density decreased. Based on the IV characteristics and impedance data, the rate-determining mechanisms of this cell were the ohmic and concentration polarization under high current density. If the microstructures of the electrodes, particularly the cathode compartment and the electrolyte thickness, are modified, an improved cell should function even better at lower temperatures.

The observed polarization curves and cell potentials, however, only display the overall performance loss; exact details on the losses and fluctuations brought on by ohmic resistances and polarization during cell operation were not supplied. Thus, the EIS approach and equivalent model fitting were carried out in order to identify which sub-reaction is responsible for the cell degeneration, and the resulting values were shown in Table 6.3. Figure 6.16a presented the appropriate measured spectra. At both high and low frequencies, two distinct arcs may be seen in the Nyquist spectra. It is evident that when operating temperature increases, the ohmic resistance—the high frequency contact with the x-axis—decreases. In contrast, the high-frequency arcs in EIS spectra are similar and show very minor size changes over time. On the other hand, the low-frequency arc exhibits discernible changes. In anode-supported cells, the cathode influences the mid-frequency zone (1-400 Hz), whereas diffusion impacts the impedance spectrum below 10 Hz [221], [240-244]. The anode mostly primarily impacts the high frequency area (above 200 Hz).

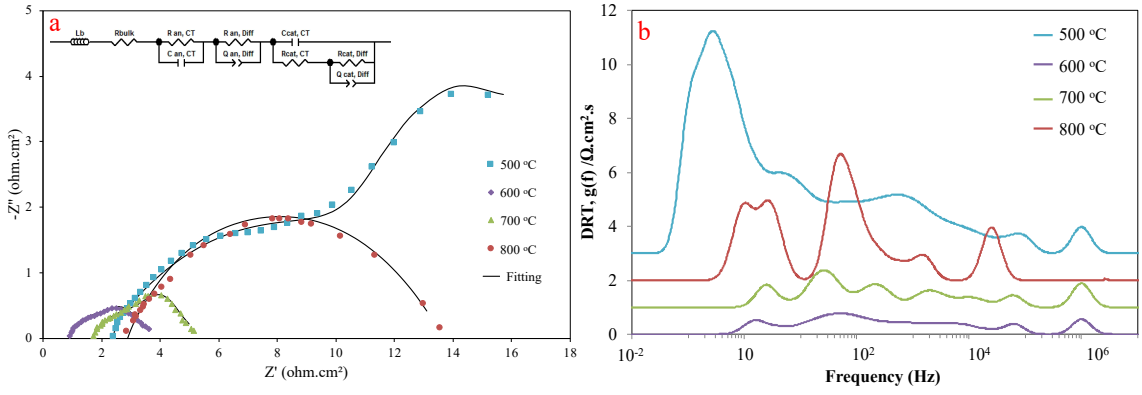


Figure 7.16. (a) Nyquist plots of LV05SM-GDC (35 µm)-YSZ-NiYSZ cell at OCV conditions, inset: Equivalent circuit model, (b) DRT curve of impedance spectra as a function of operating temperature at 500 - 800 °C.

The imaginary section of the spectrum, or y-axis, shows evidence of both cathode and anode impacts, even though the largest change in the spectrum is mostly observed at low

frequencies. However, the frequency zone corresponding to anode reaction processes altered rather negligibly when compared to the cathode reaction zone. This suggests that the anode was only slightly influenced, resulting in an incremental rise in the polarization, activation, and concentration resistances. The observed behaviors of the impedance spectra are caused by changes in the cathode that are connected to reactions, which suggests that cathode deterioration was the main factor influencing the degrading performance of the cell [244, 245].

Using the DRT technique, a number of cell sub-reaction pathways have been investigated. This strategy allowed the impedance components to be identified by their unique timings. Figure 6.16b shows the DRT results of the LV05SM-GDC (35 μm)-YSZ-NiYSZ cell at 500, 600, 700, and 800 °C. Most typically, the high frequency region is caused by charge transfer between the electrode and electrolyte. The middle frequency represents surface processes, whereas the low frequency region represents gas diffusion [246–248].

Table 7.3. EIS Fitting values of LV05SM-GDC (35 μm)-YSZ-NiYSZ fuel cell at 500-800°C.

	500 °C	600 °C	700 °C	800 °C	Unit
Ran, Diff	5.95E-05	0.000943	0.000105	1.372	ohm.cm^2
Lb	3.87E-07	3.7E-07	4.07E-07	3.84E-07	H
Rbulk	1.421	0.24415	0.5215	1.6375	ohm.cm^2
Rcat, Diff	11.66	2.9155	3.4335	9.475	ohm.cm^2
Rcat,CT	0.651	0.43605	0.9615	1.1945	ohm.cm^2
Ccat, CT	3.07E-08	5.4E-08	2.72E-08	3.78E-08	F
Qcat, Diff	0.004734	0.015475	0.0141	0.002545	S*s^a
a2	0.3593	0.3258	0.3147	0.4319	
Qan, Diff	0.000665	0.001238	0.001719	0.00106	S*s^a
a1	0.995	0.3757	0.3831	0.6284	
Ran, CT	5.895	0.25135	0.54	7.78E-07	ohm.cm^2
Can, CT	0.05275	0.028665	0.017065	11.48	F

The vast majority of impedance losses at 500 and 800 °C are likely caused by the sub-reactions in the mass flow and surface exchange domain, as shown by the largest intensity

peaks in Figure 6.16b. The peak at high frequency remains unchanged by the temperature differential, although they decreased between 600 and 700 ºC. The estimated DRT peaks in Figure 6.17b clearly show at least six independent reactions, in contrast to the impedance curve in Figure 6.17a, which shows overlap between the polarization processes. It is clear that under applied potentials as well as at high temperatures, process P1, which involves charge transfer processes, was inactive. In contrast, P4-P6 processes perform particular voltage dependence and heat activation. As the applied voltage increases, the peaks designated P4–P5 move to a lower frequency area and overlap. This demonstrates that at various temperatures and voltages, P4, P5, which were identified as surface exchange processes, remained resistant. Additionally, when voltages were applied, the low frequency P6 peak—which was ascribed to the mass transfer process of reactants in the cathode—became more resistive.

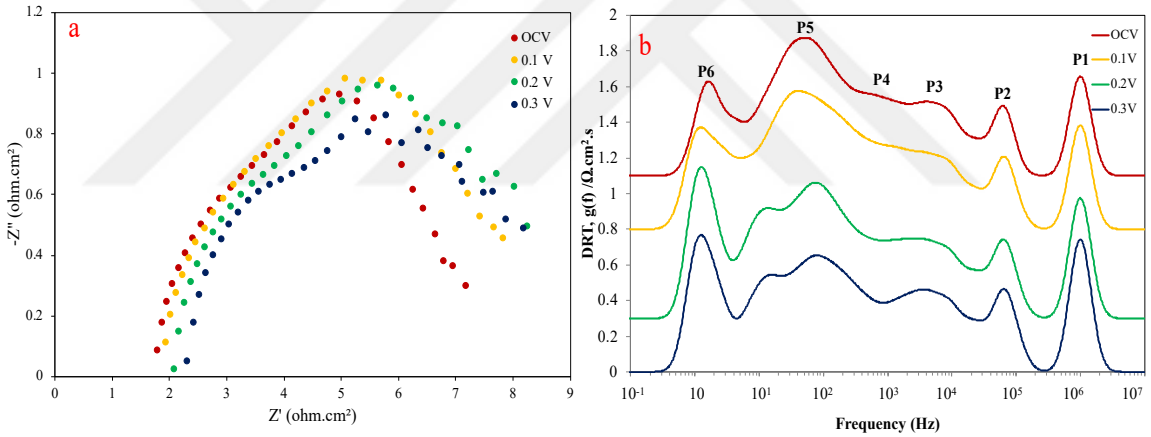


Figure 7.17. (a) Nyquist plots of LV05SM-GDC (35 µm)-YSZ-NiYSZ cell, (b) DRT patterns under different applied voltages at 600 ºC.

Cell potential and current-power density curves of the cell with a 5 µm GDC barrier layer at 500–800 ºC in H_2 fuel are displayed in Figure 6.18. The OCV readings were around 1V, which is slightly less than the value that would be predicted theoretically. The lower OCV readings might be the consequence of a minor short circuit caused by the thin GDC/YSZ double-layer electrolyte and imperfect sealing. Additionally, the open circuit potential in GDC material is decreased by partial reduction of Ce^{4+} to Ce^{3+}. Compared to the cell with the 35µm GDC/YSZ bi-layer electrolyte, the maximum power density of 20.85 mW/cm^2 is 80% lower. The cell performed best at 500 ºC after 800 ºC, a feature that was also evident in the DRT and EIS calculations. Performance measures may provide useful

insights into the structure of the cell, but more work has to be done to thoroughly examine the cell processes using DRT and impedance spectroscopy.

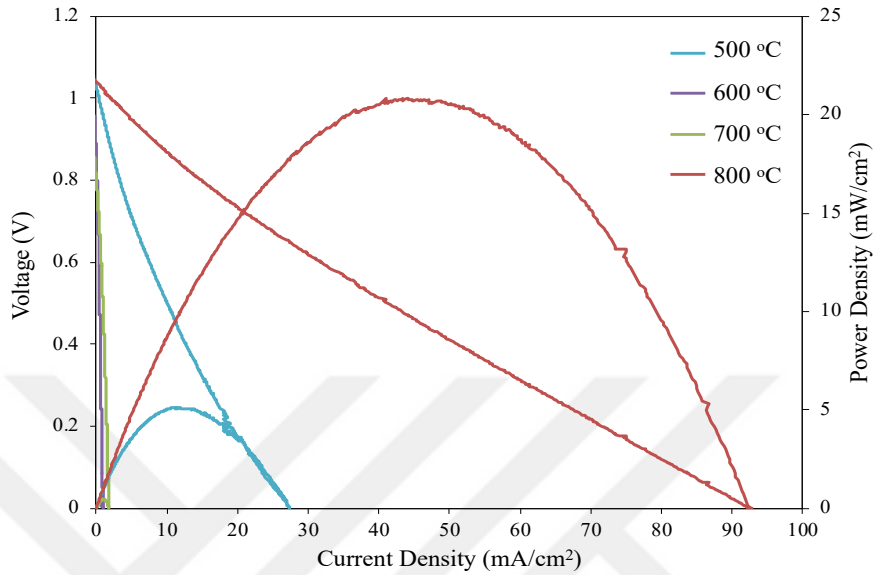


Figure 7.18. I-V curves and output power density of single cell with LV05SM-GDC (5 µm)-YSZ-NiYSZ at different temperatures.

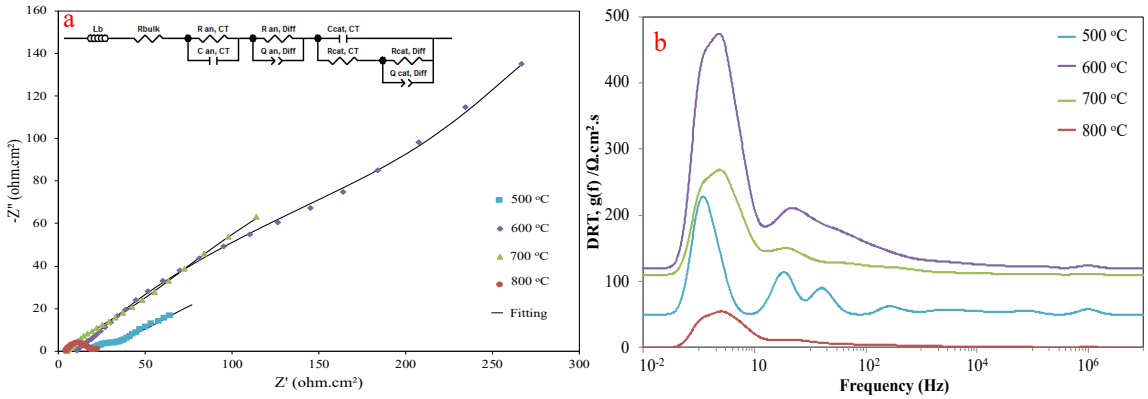


Figure 7.19. (a) Nyquist plots of LV05SM-GDC (5 µm)-YSZ-NiYSZ cell at OCV conditions, inset: Equivalent circuit model, (b) DRT curve of impedance spectra as a function of operating temperature at 500 - 800 °C.

The temperature range of 500 – 800 °C was used to record electrochemical impedance spectroscopy (EIS) measurements at open-circuit voltage for the LV05SM/GDC (5 µm)/YSZ/NiYSZ cell. Different electrochemical reaction processes, such adsorption, gas diffusion, and charge transfer, were examined in the studies. Figure 6.19a shows the Nyquist plots as a function of temperature. The resistance values that were obtained from the

impedance arc diameters have decreased with temperature, as expected. Due to several processes overlapping, only two semi-circle arcs could be seen.

Table 6.4 provides the fitting findings, and Figure 6.19a inset displays the corresponding circuit model. Among the many cell resistances, $R_{cat,diff}$ has the strongest polarization resistance, as can be observed. Fitting an impedance data, however, is a subjective problem. Therefore, in order to gain a deeper understanding of the electrode processes, the overlapping impedance arcs were deconvoluted by calculating the distribution of relaxation times. Figure 6.19b illustrates the results. Low frequency processes were more resistive at lower temperatures, as seen by the comparison of various temperatures in Figure 6.19b. The processes became less prominent as the working temperature increased, suggesting that mass transfer reactions were no longer resistive steps.

Table 7.4. EIS Fitting values of LV05SM-GDC (5 µm)-YSZ-NiYSZ fuel cell at 500-800°C.

	500 °C	600 °C	700 °C	800 °C	Unit
Ran, Diff	315.65	181.25	245.8	1.995	ohm.cm^2
Lb	2.08E-08	1.68E-07	3.07E-07	3.91E-07	H
Rbulk	19.035	9.975	4.1625	3.779	ohm.cm^2
Rcat, Diff	10.355	150.7	36.865	13.315	ohm.cm^2
Rcat,CT	2.3215	2.0545	0.7315	1.0965	ohm.cm^2
Ccat, CT	6.23E-08	1.15E-07	2.44E-07	6.76E-08	F
Qcat, Diff	0.000157	0.000541	0.001264	0.000155	S*s^a
a2	0.5437	0.4437	0.4478	0.6397	
Qan, Diff	0.005255	0.001221	0.0027	0.023145	S*s^a
a1	0.3485	0.583	0.5317	0.7624	
Ran, CT	1.8035	315.15	51.95	1.384	ohm.cm^2
Can, CT	0.00524	0.00505	0.028625	0.12185	F

Over the examined time scale, four DRT peaks obtained from Figure 6.20a were discovered in Figure 6.20b with several applied potentials. Each peak represents a rate-limiting electrode reaction, and the size of the peak indicates the resistance of the associated process. Bulk resistance, oxide ion incorporation at the electrode/electrolyte interface, and fuel charge transfer at the anode were all cited as causes of P1. It was also insensitive to variations in voltage. Additionally, the P2 peak at mid-frequency, which indicated the

transport of oxygen species to the TPBs, did not change. The P3 and P4 peaks, which were indicative of diffusion-related processes, maintained their independence from voltage variations in the low frequency range. As a consequence, the DRT results correlated well with the model fitting and previously suggested EIS.

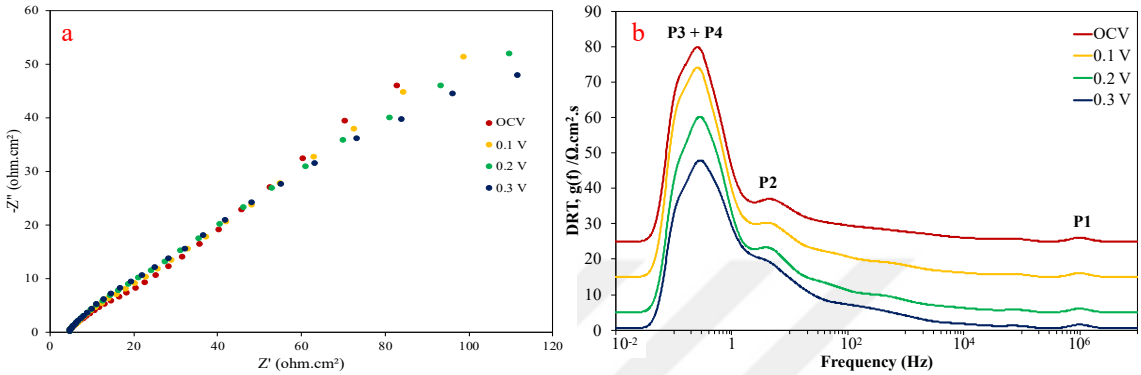


Figure 7.20. (a) Nyquist plots of LV05SM-GDC (5 µm)-YSZ-NiYSZ cell, (b) DRT patterns under different applied voltages at 800 °C.

7.5. Conclusion

As a conclusion to this chapter, single cells with YSZ, GDC and bi-layer electrolytes were produced and their performance, impedance and DRT behaviors under different temperature and voltages were reviewed. It was concluded that the cells with GDC (35µm)/YSZ double layer electrolyte exhibited highest power density with 98 mW/cm^2. In EIS plots, two separate arcs were visible showing highest polarization resistance contribution from mid and low frequency regions. Also, from the circuit model fitting results at Table 6.1 – 6.4, it could be reviewed that $R_{cat,diff}$ sub-reaction has the highest influence on total resistance with the values of 26.06, 5.23, 27.48 and 211.23 Ω/cm^2 for single cells with YSZ, GDC, GDC (35 µm)/YSZ and GDC (5µm)/YSZ electrolyte combinations, respectively.

From the DRT findings, charge transfer resistance contribution was neglected, because this peak is mostly labelled for transport of oxide ions through electrolyte network which is called as R_{bulk}. For single cell with YSZ electrolyte has performed largest resistance at diffusion and exchange of oxygen species (O^-/O_2^{2-}) at the TPBs and mass transfer of reactants in the cathode processes, and also the cell showed dependency on applied voltages

at low frequency. The mass transfer reactions such as oxygen and hydrogen gas diffusion in the electrodes have become more overlapped and shifted to higher frequencies. In the cell with only single layer GDC electrolyte, except charge transfer in electrolyte, different reaction steps were observed at each temperature differences. With increasing applied voltage, low frequency peaks which signify mass transport processes at cathode have become more spread and superimposed each other.

In order to compare bi-layer electrolyte influence in the cell performance, GDC layers were attached with different thicknesses on conventional YSZ electrolyte. In the first scenario, GDC layer with 35 μm thickness were tape casted and laminated, and the performance, EIS and DRT results were studied. It has highest power density among other combinations and lowest $R_{cat,diff}$ value in equivalent circuit fitting results. This estimation was also approved by DRT findings. Low and mid frequency peaks have the major effect on total cell resistance at 500 and 800 ^{o}C. At intermediate temperatures, cell processes have minor contributions to overall resistance. With applied potentials, surface exchange related processes were disturbed and have shifted towards lower frequencies showing contribution.

At the final case, a thin GDC layer were laminated with YSZ electrolyte and the cell was undertaken various experiments. The cell has exhibited similar behavior with the first cell prepared with YSZ electrolyte. Cathode mass transfer process has determined as rate limiting steps same as the case in the first cell. Moreover, with applied potentials gas diffusion processes developed higher resistances.

After all sets of analysis, modelling and calculations with different electrode and electrolyte material combinations, and their micro and 3D structures; the materials and interfaces could be manipulated and tailored on different length scales. Difficulties at the electrochemical interface can be identified by connected chemical, structural, and electrochemical characteristics in combination with comprehensive characterization approaches.

8. CONCLUDING REMARKS

In this thesis, the relations between the microstructures, processing parameters, and electrochemical performance of the SOFC components were examined. Through microstructural characterization and electrochemical investigations to identify the factors limiting the fuel cell material performance, this thesis produced a fundamental understanding of these relationships. The ultimate goal was to get further understanding of the characteristics of various cathode materials in order to enable advancements for future applications.

In Chapter 1, the aim was to address the chemistry and development of the state-of-the-art LSC perovskite materials with Vanadium doping. $La_{0.595}V_{0.005}Sr_{0.4}CoO_{3-\partial}$ (LV05SC) perovskite cathode was investigated as a novel cathode for intermediate temperature solid oxide fuel cells (IT-SOFC). Anode supported YSZ ($(Y_2O_3)_{0.08}(ZrO_2)_{0.92}$) and GDC ($Gd_{0.2}Ce_{0.8}O_{1.95}$) electrolytes were prepared by a multilayer tape casting and co-firing method. The green bi-layer tapes were co-fired at various temperatures with optimized electrolyte and anode slurries. X-Ray diffraction (XRD) and Scanning Electron Microscopy (SEM) were used to analyze the microstructures and the phase characterizations of the cathode material and single cell. EXAFS was recorded for V doping of 0.05%. The raw and calculated Co K-edge XAS spectra of LV05SC were analyzed. These findings showed that only partial doping into the A-site could be accomplished even at low metal concentrations such as 0.05% of V, and that the composition of the metals inside the crystal or the radius of the dopant metal may have a significant impact on the degree of substitution. The major result of V-doping into the perovskite lattice was the development of bulk oxygen vacancies, which improved the oxygen chemisorption characteristics of crystals. These properties play a key role in oxygen reduction reactions. At 1250 ^oC of the co-firing temperature, as prepared anode-supported cell showed no defects and excellent microstructural properties such as no gas permeability, good porosity, and sintered structure. The electrolytes with a thickness of almost 20 μm were fairly dense. The power densities were evaluated and anode-supported cell showed good electrochemical performance at intermediate temperatures. The peak power density of the cell reached to 5 mW/cm^2 for YSZ electrolyte, 340 mW/cm^2 for GDC electrolyte, 360 mW/cm^2 for GDC (35 μm)/YSZ electrolyte, and 90 mW/cm^2 for GDC (5

μm)/YSZ electrolyte at 800 °C. The online the distribution of relaxation times (DRT) Calculator generated by the German team at rhd Instruments was used to determine DRT with a regularization parameter of 10^{-3}. According to the EIS and DRT analysis, diffusion processes of oxide ions (O^{2-}) were found to be the limiting step for ORR. These findings suggest that the compound is a promising cathode material for IT-SOFCs.

In Chapter 2, it was studied certain perovskite oxides with substitution of Gd^{3+} substituted A-cations to understand ORR mechanism in the operation of SOFC in intermediate temperature range by employing the tape casting and co-firing procedures to generate the single cells as anode-supported with thin electrolytes to enhance the electrical characteristics of perovskite materials. The phase identifications and elemental composition of the produced $La_{0.5}Gd_{0.1}Sr_{0.4}CoO_{3-\partial}$ (LG10SC) perovskite cathode material was accomplished by XRD and XPS techniques. Both electrical and ionic conductivities, and the performances of perovskite materials have been measured for a variety of temperatures by employing EIS and DRT calculations. The maximum power densities of the single cells were 6.50 and 360 mW/cm^2 for single layer YSZ and GDC electrolytes, 415 and 170 mW/cm^2 for double layer GDC-YSZ electrolytes, respectively. According to EIS and DRT calculations, low frequency peaks have the major effect on total cell resistance. The mass transfer related processes were affected the most in high current regime with applied potentials and have shifted towards higher frequencies showing contribution originates from the flux of the reactants.

In Chapter 3, the effects of changes in the oxidation states of doped transition metals such as Vanadium were investigated to understand ORR mechanism in the operation of SOFC in intermediate temperature range. By employing the tape casting and co-firing procedures the single cells were produced as anode-supported thin electrolytes to enhance the electrical characteristics of perovskite materials. $La_{0.6-x}V_xSr_{0.4}FeO_{3-\partial}$ (LVxSF, x = 0.03) powders were synthesized by utilizing the sol-gel method. The phase identifications and diffraction patterns were recorded by XRD. XPS was used to analyze the elemental composition. For the morphology of surface and cross-section of the sintered cells, SEM analysis was conducted. Both electrical and ionic conductivities, and the performance of perovskite materials have been measured for a variety of temperatures by employing EIS and DRT calculations. The maximum power densities were 13.10, 182.20, 304 and 162.03

mW/cm^2 for LV3SF cathode on YSZ, GDC, and double layer electrolytes with two different thicknesses as 35 and 5 μm, respectively. As a result of these analysis, adsorption, dissociation, and diffusion processes were found to be the limiting steps of ORR. These findings suggest that this V-doped perovskite structure, LV3SF, is a promising cathode material for IT-SOFCs.

In Chapter 4, the effects of changes in the oxidation states of doped transition metals such as Vanadium were investigated to understand ORR mechanism in the operation of SOFC on intermediate temperature range. By employing the tape casting and co-firing procedures the single cells were fabricated as anode-supported with thin electrolytes to improve the electrical features of perovskite materials. V-doped perovskite structure, $La_{0.595}V_{0.005}Sr_{0.4}MnO_{3-\partial}$ (LV05SM), was studied in detail. The characterization techniques such as XRD, XPS and SEM were conducted for crystal diffraction patterns, elemental analysis and surface morphology of the single cell. Both the conductivity and performance analysis have been measured by impedance and linear sweep voltammetry analysis. The EIS data then was deconvoluted by DRT calculations. The maximum power densities were 95.32, 76.70, 98.10 and 20.85 mW/cm^2 for anode-supported cells with YSZ, GDC and double layer electrolytes with thicknesses of 35 and 5 μm, respectively. From DRT results, low frequency shows the highest intensity, suggesting that surface exchange processes and gas diffusion contribute the most to impedance losses, which is also consistent with the rate-limiting step of conventional LSM cathode.

Table 8.1. Comparison of relative surface concentration of the perovskite-type catalysts.

Materials	**Relative surface concentration of metals (%)**							**O (at%)**	**Performance**
	La	**$V^{4+/5+}$**	**Gd**	**Sr**	**$Co^{2+/3+}$**	**$Fe^{2+/3+}$**	**$Mn^{3+/4+}$**	**O_{ads}/O_{latt}**	**mW/cm^2**
LV05SC	37.9	0.9/1.4	–	12.2	14.5/33	–	–	1.49	360
LG10SC	38.6	–	4.8	9.2	15.3/32	–	–	1.63	415
LV3SF	41.6	7.5/3.7	–	19.6	–	4.3/23.2	–	1.20	304
LV05SM	58.5	2.8/4.9	–	23	–	–	4.6/6.1	1.13	98

The oxygen vacancy concentration is often correlated with the amount of O_{add} which is calculated by the deconvoluted area integrated [292, 293]. As a result, the development of oxygen vacancies from the partial replacement of La and Sr by other cations may lead to decrease in the lattice oxygen (O_{latt}) concentration. In general, oxygen vacancies caused by oxygen-deficient perovskite oxides result in unique oxidation states of transition metal ions, increasing the catalytic activity of perovskite-type catalysts. Table 7.1 provides the results from the XPS analysis of relative surface concentrations of transition metals, O_{ads}/O_{latt} ratios and performance results of anode-supported cells with GDC (35 μm)/YSZ electrolyte. Substitution of V^{4+}/V^{5+} or Gd^{3+} to the traditional cathode crystals LSC, LSF and LSM affects the characteristics of oxygen species inside the structure. The O_{ads}/O_{latt} ratio for Gd-doped LSC sample which is $La_{0.5}Gd_{0.1}Sr_{0.4}CoO_{3-\partial}$ (LG10SC) is the highest among other samples, hence better ORR catalytic performance. The performance experiments proves that LG10SC cathode material with GDC (35 μm)/YSZ electrolyte has the highest power density of 415 mW/cm^2.

There are several experimental research on cathodes for SOFCs that are reported in literature. The oxygen reduction reaction kinetics and the impact of various materials and their architectures on the air electrode's performance are highlighted. Further development of the cathodes will result from a greater knowledge of cathode dynamics.

REFERENCES

1. Silva-Mosqueda, D. M., F. Elizalde-Blancas, D. Pumiglia, F. Santoni, C. Boigues-Muñoz, and S. J. McPhail, "Intermediate Temperature Solid Oxide Fuel Cell Under Internal Reforming: Critical Operating Conditions, Associated Problems and Their Impact on the Performance", *Applied Energy*, Vol. 235, No. 1, pp. 625–640, 2019.

2. Choi, W., J. Kim, Y. Kim, and H. H. Song, "Solid Oxide Fuel Cell Operation in a Solid Oxide Fuel Cell–Internal Combustion Engine Hybrid System and the Design Point Performance of the Hybrid System", *Applied Energy*, Vol. 254, No. 1, pp. 113681, 2019.

3. Chen, B., H. Xu, and Q. Sun, "Syngas/Power Cogeneration from Proton Conducting Solid Oxide Fuel Cells Assisted by Dry Methane Reforming: A Thermal-Electrochemical Modelling Study", *Energy Conversion and Management*, Vol. 167, No. 1, pp. 37–44, 2018.

4. Liu, T., H. Liu, and X. Zhang, "A Robust Solid Oxide Electrolyzer for Highly Efficient Electrochemical Reforming of Methane and Steam", *Journal of Materials Chemistry A*, Vol. 7, No. 22, pp. 13550–13558, 2019.

5. Ni, M., M. Leung, and D. Leung, "Technological Development of Hydrogen Production by Solid Oxide Electrolyzer Cell (SOEC)", *International Journal of Hydrogen Energy*, Vol. 33, No. 9, pp. 2337–2354, 2008.

6. Van Biert, L., M. Godjevac, K. Visser, and P. V. Aravind, "Dynamic Modelling of a Direct Internal Reforming Solid Oxide Fuel Cell Stack Based on Single Cell Experiments", *Applied Energy*, Vol. 250, No. 1, pp. 976–990, 2019.

7. Haile, S. M., "Fuel Cell Materials and Components: The Golden Jubilee Issue—Selected Topics in Materials Science and Engineering: Past, Present and Future", *Acta Materialia*, Vol. 51, No. 19, pp. 5981–6000, 2003.

8. Chen, F. F., *The Future of Energy I: Fossil Fuels,* Springer, New York, 2011.

9. Cook, B., “Introduction to Fuel Cells and Hydrogen Technology”, *Engineering Science & Education Journal*, Vol. 11, No. 6, pp. 205–216, 2002.

10. Giorgi, J., and F. Leccese, “Fuel Cells: Technologies and Applications”, *The Open Fuel Cells Journal*, Vol. 6, No. 1, pp. 1-20, 2013.

11. Grove, W. R., “LXXII. On a Gaseous Voltaic Battery”, *The London, Edinburgh, and Dublin Philosophical Magazine and Journal of Science*, Vol. 21, No. 140, pp. 417–420, 1842.

12. Mond L., and L. Carl, “V. A New Form of Gas Battery”, *Proceedings of the Royal Society of London*, Vol. 46, No. 280–285, pp. 296–304, 1890.

13. Andújar, J. M. and F. Segura, “Fuel cells: History and Updating. A Walk Along Two Centuries”, *Renewable and Sustainable Energy Reviews*, Vol. 13, No. 9, pp. 2309–2322, 2009.

14. Gerhard, E., “Wilheim Ostwald: Founder of Physical Chemistry and Nobel Laureate 1909”, *Angewandte Chemie International Edition*, Vol. 48, No. 36, pp. 6600-6606, 2009.

15. Kunze, J., and U. Stimming, “Energietechnologie: Elektrochemie gegen Wärmekraftmaschinen ein Tribut an Wilhelm Ostwalds visionäre Aussagen”, *Angewandte Chemie*, Vol. 121, No. 49, pp. 9394–9401, 2009.

16. Nobel Prize, “Wilhelm Ostwald”, https://www.nobelprize.org/prizes/chemistry/1909/, accessed on December 3, 2023.

17. Eustice, A.L., *The Nernst Glower: Its Development, Characteristics and Application to Illumination Practice*, Forgotten Books, Illinois**,** 2018.

18. de Souza, S., “Thin-film Solid Oxide Fuel Cell with High Performance at Low-Temperature”, *Solid State Ionics*, Vol. 98, No. 1–2, pp. 57–61, 1997.

19. Gong, J., Y. Li, Z. Zhang, and Z. Tang, "AC Impedance Study of Zirconia Doped with Yttria and Calcia", *Journal of the American Ceramic Society*, Vol. 83, No. 3, pp. 648–650, 2004.

20. Baur, E. and H. Preis, "Über Brennstoff-Ketten mit Festleitern", *Zeitschrift für Elektrochemie und angewandte physikalische Chemie*, Vol. 43, No. 9, pp. 727–732, 1937.

21. Debe, M. K., "Electrocatalyst Approaches and Challenges for Automotive Fuel Cells", *Nature*, Vol. 486, No. 7401, pp. 43–51, 2012.

22. Wagner, F. T., B. Lakshmanan, and M. F. Mathias, "Electrochemistry and the Future of the Automobile", *The Journal of Physical Chemistry Letters*, Vol. 1, No. 14, pp. 2204–2219, 2010.

23. Zhang, H. and P. K. Shen, "Advances in the High-Performance Polymer Electrolyte Membranes for Fuel Cells", *Chemical Society Reviews*, Vol. 41, No. 6, pp. 2350-2382, 2012.

24. Xia, Z., S. Wang, and Y. Li, "Vertically Oriented Polypyrrolenano Wire Arrays on Pd-Plated Nafion Membrane and its Application in Direct Methanol Fuel Cells", *Journal of Material Chemistry A*, Vol. 1, No. 3, pp. 491–494, 2013.

25. Hsieh, S.S., I.C. Chen, and C.H. Hwong, "Development of a Four-Cell DMFC Stack with Air-Breathing Cathode and Dendrite Flow Field", *International Journal of Energy Research*, Vol. 38, No. 13, pp. 1693–1711, 2014.

26. McLean, G., "An Assessment of Alkaline Fuel Cell Technology", *International Journal of Hydrogen Energy*, Vol. 27, No. 5, pp. 507–526, 2002.

27. Kostowskyj, M., R. Gilliam, D. Kirk, and S. Thorpe, "Silver Nanowire Catalysts for Alkaline Fuel Cells", *International Journal of Hydrogen Energy*, Vol. 33, No. 20, pp. 5773–5778, 2008.

28. Ang, S. M., E. S. Fraga, N. P. Brandon, N. J. Samsatli, and D. J. Brett, “Fuel Cell Systems Optimization – Methods and Strategies”, *International Journal of Hydrogen Energy*, Vol. 36, No. 22, pp. 14678–14703, 2011.

29. Sammes, N., R. Bove, and K. Stahl, “Phosphoric Acid Fuel Cells: Fundamentals and Applications”, *Current Opinion in Solid State and Materials Science*, Vol. 8, No. 5, pp. 372–378, 2004.

30. Singhal, S., and K. Kendall, *High Temperature Solid Oxide Fuel Cells: Fundamentals, Design and Applications*, Elsevier, Oxford, 2003.

31. Dicks, A. L., “Molten Carbonate Fuel Cells”, *Current Opinion in Solid State and Materials Science*, Vol. 8, No. 5, pp. 379–383, 2004.

32. O’Hayre, R., W. Collela, and F. B. Prinz, *Fuel Cell Fundamentals*, Wiley, Hoboken, 2009.

33. Ormerod, R. M., “Solid Oxide Fuel Cells”, *Chemical Society Reviews*, Vol. 32, No. 1, pp. 17–28, 2003.

34. Stambouli, A. B. and E. Traversa, “Solid Oxide Fuel Cells (SOFCs): A Review of an Environmentally Clean and Efficient Source of Energy”, *Renewable and Sustainable Energy Reviews*, Vol. 6, No. 5, pp. 433–455, 2002.

35. Oryshchyn, D., N. F. Harun, D. Tucker, K. M. Bryden, and L. Shadle, “Fuel Utilization Effects on System Efficiency in Solid Oxide Fuel Cell Gas Turbine Hybrid Systems”, *Applied Energy*, Vol. 228, No. 1, pp. 1953–1965, 2018.

36. D.F. Chuahy, F. and S. L. Kokjohn, “Solid Oxide Fuel Cell and Advanced Combustion Engine Combined Cycle: A pathway to 70% electrical efficiency”, *Applied Energy*, Vol. 235, No. 1, pp. 391–408, 2019.

37. Singhal, S., “Advances in Solid Oxide Fuel Cell Technology”, *Solid State Ionics*, Vol. 135, No. 1–4, pp. 305–313, 2000.

38. Yang, C., Z. Yang, C. Jin, G. Xiao, F. Chen, and M. Han, “Sulfur-Tolerant Redox-Reversible Anode Material for Direct Hydrocarbon Solid Oxide Fuel Cells”, *Advanced Materials*, Vol. 24, No. 11, pp. 1439–1443, 2012.

39. Corigliano, O. and P. Fragiacomo, “Extensive Analysis of SOFC Fed by Direct Syngas at Different Anodic Compositions by Using Two Numerical Approaches”, *Energy Conversion and Management*, Vol. 209, No. 1, pp. 112559-112664, 2020.

40. Irshad, M., K. Siraj, and R. Raza, “A Brief Description of High Temperature Solid Oxide Fuel Cell’s Operation, Materials, Design, Fabrication Technologies and Performance”, *Applied Sciences*, Vol. 6, No. 3, pp. 70-75, 2016.

41. Dollard, W. J., “Solid Oxide Fuel Cell Developments at Westinghouse”, *Journal of Power Sources*, Vol. 37, No. 1–2, pp. 133–139, 1992.

42. Tesfai, A., P. Connor, J. Nairn, and J. T. S. Irvine, “Thermal Cycling Evaluation of Rolled Tubular Solid Oxide Fuel Cells”, *Journal of Fuel Cell Science and Technology*, Vol. 8, No. 6, pp. 28-35, 2011.

43. Laosiripojana, N., W. Wiyaratn, W. Kiatkittipong, A. Arpornwichanop, A. Soottitantawat, and S. Assabumrungrat, “Reviews on Solid Oxide Fuel Cell Technology”, *Engineering Journal*, Vol. 13, No. 1, pp. 65–84, 2009.

44. Gao, Z., L. V. Mogni, E. C. Miller, J. G. Railsback, and S. A. Barnett, “A Perspective on Low-Temperature Solid Oxide Fuel Cells”, *Energy & Environmental Science*, Vol. 9, No. 5, pp. 1602–1644, 2016.

45. Kendall, K., and K. Michaela, *High-Temperature Solid Oxide Fuel Cells for the 21st Century Fundamentals, Design and Applications*, Elsevier, Oxford, 2015.

46. Wachsman, E. D. and K. T. Lee, “Lowering the Temperature of Solid Oxide Fuel Cells”, *Science*, Vol. 334, No. 6058, pp. 935–939, 2011.

47. Fuel Cell Hand Book, *U.S. Department of Energy*, Washington, DC, 2004.

48. Steinberger-Wilckens, R., *Solid Oxide Fuel Cells: Fuel Cells Waste-to-Energy Chain,* Springer, Berlin/Heidelberg, 2012.

49. Bianchi, F. R., B. Bosio, A. Baldinelli, and L. Barelli, "Optimization of a Reference Kinetic Model for Solid Oxide Fuel Cells", *Catalysts*, Vol. 10, No. 1, pp. 99-104, 2020.

50. Adler, S. B., "Factors Governing Oxygen Reduction in Solid Oxide Fuel Cell Cathodes", *Chemical Reviews*, Vol. 104, No. 10, pp. 4791–4844, 2004.

51. Atkinson, A., S. Barnett, and R. J. Gorte, "Advanced Anodes for High-Temperature Fuel Cells", *Nature Materials*, Vol. 3, No. 1, pp. 17–27, 2004.

52. de Boer, B., *SOFC anode: Hydrogen Oxidation at Porous Nickel and Nickel/Zirconia Electrodes*, Ph.D. Thesis, University of Twente, 1998.

53. Minh N. Q. and Takahashi K, *Science and Technology of Ceramic Fuel Cells*, Elsevier, Amsterdam, 1995.

54. Fleig, J., "Solid Oxide Fuel Cell Cathodes: Polarization Mechanisms and Modeling of the Electrochemical Performance", *Annual Review of Materials Research*, Vol. 33, No. 1, pp. 361–382, 2003.

55. Istomin, S. Y. and E. V Antipov, "Cathode Materials Based on Perovskite-Like Transition Metal Oxides for Intermediate Temperature Solid Oxide Fuel Cells", *Russian Chemical Reviews*, Vol. 82, No. 7, pp. 686–700, 2013.

56. Virkar, A., "The Role of Electrode Microstructure on Activation and Concentration Polarizations in Solid Oxide Fuel Cells", *Solid State Ionics*, Vol. 131, No. 1–2, pp. 189–198, 2000.

57. Huang, Q. A., R. Hui, B. Wang, and J. Zhang, “A Review of AC Impedance Modeling and Validation in SOFC Diagnosis”, *Electrochimica Acta*, Vol. 52, No. 28, pp. 8144–8164, 2007.

58. Winter, M. and R. J. Brodd, “What Are Batteries, Fuel Cells, and Supercapacitors?”, *Chemical Reviews*, Vol. 104, No. 10, pp. 4245–4270, 2004.

59. Andersson, M., J. Yuan, and B. Sundén, “SOFC Modeling Considering Hydrogen and Carbon Monoxide as Electrochemical Reactants”, *Journal of Power Sources*, Vol. 232, No. 2, pp. 42–54, 2013.

60. Sreedhar, I., B. Agarwal, P. Goyal, and A. Agarwal, “An Overview of Degradation in Solid Oxide Fuel Cells-Potential Clean Power Sources”, *Journal of Solid-State Electrochemistry*. Vol. 24, No. 1, pp. 1020-1028, 2020.

61. Nelson, A. E., “Fundamentals of Industrial Catalytic Processes”, *The Canadian Journal of Chemical Engineering*, Vol. 85, No. 1, pp. 127–128, 2008.

62. Schroer, C. G., P. Boye, and J. M. Feldkamp, “Hard X-Ray Microscopy with Elemental, Chemical and Structural Contrast”, *Acta Physica Polonica A*, Vol. 117, No. 2, pp. 357–368, 2010.

63. Beale, A. M., A. M. J. Van der Eerden, K. Kervinen, M. A. Newton, and B. M. Weckhuysen, “Adding a Third Dimension to Operando Spectroscopy: A Combined UV-Vis, Raman and XAFS Setup to Study Heterogeneous Catalysts Under Working Conditions”, *Chemical Communications*, Vol. 1, No. 24, pp. 3015, 2005.

64. Clausen, B., “In-Situ Cell for Combined XRD and On-Line Catalysis Tests: Studies of Cu Based Water Gas Shift and Methanol Catalysts”, *Journal of Catalysis*, Vol. 132, No. 2, pp. 524–535, 1991.

65. Suib, S. L., *New and Future Developments in Catalysis: Batteries, Hydrogen Storage and Fuel Cells*, Elsevier, Amsterdam, 2013.

66. Le Pevelen, D. D., *X-ray Crystallography of Small Molecules: Theory and Workflow*, *In: Encyclopedia of Spectroscopy and Spectrometry*, Third Edition, Academic Press, Oxford, 2017.

67. Powell, C. J., "Improvements in the Reliability of X-Ray Photoelectron Spectroscopy for Surface Analysis", *Journal of Chemical Education*, Vol. 81, No. 12, pp. 1730-1734, 2004.

68. Bagus, P. S., E. S. Ilton, and C. J. Nelin, "The interpretation of XPS spectra: Insights into Materials Properties", *Surface Science Reports*, Vol. 68, No. 2, pp. 273–304, 2013.

69. Fadley, C. S., "X-Ray Photoelectron Spectroscopy: Progress and Perspectives", *Journal of Electron Spectroscopy and Related Phenomena*, Vol. 178–179, No. 1, pp. 2–32, 2010.

70. Greczynski, G. and L. Hultman, "X-Ray Photoelectron Spectroscopy: Towards Reliable Binding Energy Referencing", *Progress in Materials Science*, Vol. 107, No. 1, pp. 100588-100591, 2020.

71. Bu, Y., Q. Zhong, D. Xu, and W. Tan, "Redox Stability and Sulfur Resistance of $Sm_{0.9}Sr_{0.1}Cr_xFe_{1-x}O_{3-\delta}$ Perovskite Materials", *Journal of Alloys and Compounds*, Vol. 578, No. 1, pp. 60–66, 2013.

72. Puleo, F., L. F. Liotta, V. La Parola, D. Banerjee, A. Martorana, and A. Longo, "Palladium Local Structure of $La_{1-x}Sr_xCo_{1-y}Fe_{y-0.03}Pd_{0.03}O_{3-\delta}$ Perovskites Synthesized using a One Pot Citrate Method", *Physical Chemistry Chemical Physics,* Vol. 16, No. 41, pp. 22677–22686, 2014.

73. Powell, C. J. and A. Jablonski, "Surface Sensitivity of X-Ray Photoelectron Spectroscopy", *Nuclear Instruments and Methods in Physics Research Section A: Accelerators, Spectrometers, Detectors and Associated Equipment*., Vol. 601, No. 1–2, pp. 54–65, 2009.

74. Opitz, A. K., C. Rameshan, and M. Kubicek, "The Chemical Evolution of the La0.6Sr0.4CoO3−δ Surface Under SOFC Operating Conditions and Its Implications for

Electrochemical Oxygen Exchange Activity", *Topics in Catalysis*, Vol. 61, No. 20, pp. 2129–2141, 2018.

75. Nenning, A., A. K. Opitz, and C. Rameshan, "Ambient Pressure XPS Study of Mixed Conducting Perovskite-Type SOFC Cathode and Anode Materials under Well-Defined Electrochemical Polarization", *The Journal of Physical Chemistry C*, Vol. 120, No. 3, pp. 1461–1471, 2016.

76. Nenning, A. and J. Fleig, "Electrochemical XPS Investigation of Metal Exsolution on SOFC Electrodes: Controlling the Electrode Oxygen Partial Pressure in Ultra-High-Vacuum", *Surface Science*, Vol. 680, No. 1, pp. 43–51, 2019.

77. Park, J., M. Risch, and G. Nam, "Single Crystalline Pyrochlore Nanoparticles with Metallic Conduction as Efficient Bi-Functional Oxygen Electrocatalysts for Zn–Air Batteries", *Energy & Environmental Science*, Vol. 10, No. 1, pp. 129–136, 2017.

78. Sa, Y. J., D.-J. Seo, and J. Woo, "A General Approach to Preferential Formation of Active Fe–N_x Sites in Fe–N/C Electrocatalysts for Efficient Oxygen Reduction Reaction", *Journal of the American Chemical Society*, Vol. 138, No. 45, pp. 15046–15056, 2016.

79. Gorlin, Y., B. Lassalle-Kaiser, and J. D. Benck, "In Situ X-ray Absorption Spectroscopy Investigation of a Bifunctional Manganese Oxide Catalyst with High Activity for Electrochemical Water Oxidation and Oxygen Reduction", *Journal of the American Chemical Society*, Vol. 135, No. 23, pp. 8525–8534, 2013.

80. Park, J., M. Park, G. Nam, M. G. Kim, and J. Cho, "Unveiling the Catalytic Origin of Nanocrystalline Yttrium Ruthenate Pyrochlore as a Bifunctional Electrocatalyst for Zn–Air Batteries", *Nano Letters*, Vol. 17, No. 6, pp. 3974–3981, 2017.

81. Koningsberger, D. C., B. L. Mojet, G. E. van Dorssen, and D. E. Ramaker, "XAFS Spectroscopy; Fundamental Principles and Data Analysis", *Topics in Catalysis*, Vol. 10, No. 3/4, pp. 143–155, 2000.

82. Filez, M., E. A. Redekop, and J. Dendooven, “Formation and Functioning of Bimetallic Nanocatalysts: The Power of X-Ray Probes”, *Angewandte Chemie International Edition*, Vol. 58, No. 38, pp. 13220–13230, 2019.

83. Rehr, J. J., J. J. Kas, F. D. Vila, M. P. Prange, and K. Jorissen, “Parameter-Free Calculations of X-Ray Spectra with FEFF9”, *Physical Chemistry Chemical Physics*, Vol. 12, No. 21, pp. 5498-5503, 2010.

84. Bard, A. J., and L. R., Faulkner, *Electrochemical Methods: Fundamentals and Applications*, Wiley, New York, 2000.

85. Lasia, A., *Electrochemical Impedance Spectroscopy and its Applications, In: Modern Aspects of Electrochemistry*, Springer, Boston, 2002.

86. Macdonald, J. R. and W. B. Johnson, *Fundamentals of Impedance Spectroscopy, In: Impedance Spectroscopy*, Wiley, New York, 2005.

87. Lai, W. and S. M. Haile, “Impedance Spectroscopy as a Tool for Chemical and Electrochemical Analysis of Mixed Conductors: A Case Study of Ceria”, *Journal of the American Ceramic Society*, Vol. 88, No. 11, pp. 2979–2997, 2005.

88. Nenning, A., A. K. Opitz, T. M. Huber, and J. Fleig, “A Novel Approach for Analyzing Electrochemical Properties of Mixed Conducting Solid Oxide Fuel Cell Anode Materials by Impedance Spectroscopy”, *Physical Chemistry Chemical Physics*, Vol. 16, No. 40, pp. 22321–22336, 2014.

89. Jamnik, J. and J. Maier, “Generalized Equivalent Circuits for Mass and Charge Transport: Chemical Capacitance and its Implications”, *Physical Chemistry Chemical Physics*, Vol. 3, No. 9, pp. 1668–1678, 2001.

90. Chang, B.Y. and S.M. Park, “Integrated Description of Electrode/Electrolyte Interfaces Based on Equivalent Circuits and Its Verification Using Impedance Measurements”, *Analytical Chemistry*, Vol. 78, No. 4, pp. 1052–1060, 2006.

91. Chen, D., R. Ran, K. Zhang, J. Wang, and Z. Shao, “Intermediate-Temperature Electrochemical Performance of a Polycrystalline $PrBaCo_2O_{5+\partial}$ Cathode on Samarium-Doped Ceria Electrolyte”, *Journal of Power Sources*, Vol. 188, No. 1, pp. 96–105, 2009.

92. Vadhva, P., J. Hu, M. and J. Johnson, “Electrochemical Impedance Spectroscopy for All-Solid-State Batteries: Theory, Methods and Future Outlook”, *ChemElectroChem*, Vol. 8, No. 11, pp. 1930–1947, 2021.

93. Adler, S. B., J. A. Lane, and B. C. H. Steele, “Electrode Kinetics of Porous Mixed-Conducting Oxygen Electrodes”, *Journal of The Electrochemical Society*, Vol. 143, No. 11, pp. 3554–3564, 1996.

94. Schichlein, H., A. C. Müller, M. Voigts, A. Krügel, and E. Ivers-Tiffée, “Deconvolution of Electrochemical Impedance Spectra for the Identification of Electrode Reaction Mechanisms in Solid Oxide Fuel Cells”, *Journal of Applied Electrochemistry*, Vol. 32, No. 8, pp. 875–882, 2002.

95. Leonide, A., V. Sonn, A. Weber, and E. Ivers-Tiffée, “Evaluation and Modeling of the Cell Resistance in Anode-Supported Solid Oxide Fuel Cells”, *Journal of The Electrochemical Society*, Vol. 155, No. 1, pp. 29-36, 2008.

96. Sonn, V., A. Leonide, and E. Ivers-Tiffée, “Combined Deconvolution and CNLS Fitting Approach Applied on the Impedance Response of Technical Ni/8YSZ Cermet Electrodes”, *Journal of The Electrochemical Society*, Vol. 155, No. 7, p. 670-675, 2008.

97. Singhal, S., and K. Kendall, *High Temperature Solid Oxide Fuel Cells: Fundamentals, Design and Applications*, Elsevier, Oxford, 2003.

98. Doreau, F., G. Tarì, M. Guedes, T. Chartier, C. Pagnoux, and J. M. F. Ferreira, “Mechanical and Lamination Properties of Alumina Green Tapes Obtained by Aqueous Tape-Casting”, *Journal of the European Ceramic Society*, Vol. 19, No. 16, pp. 2867–2873, 1999.

99. Moon, H., S. Kim, S. Hyun, and H. Kim, “Development of IT-SOFC Unit Cells with Anode Supported Thin Electrolytes via Tape Casting and Co-Firing”, *International Journal of Hydrogen Energy*, Vol. 33, No. 6, pp. 1758–1768, 2008.

100. Gorte, R. J. and J. M. Vohs, “Catalysis in Solid Oxide Fuel Cells”, *Annual Review of Chemical and Biomolecular Engineering*, Vol. 2, No. 1, pp. 9–30, 2011.

101. Shaikh, S. P. S., A. Muchtar, and M. R. Somalu, “A Review on the Selection of Anode Materials for Solid Oxide Fuel Cells”, *Renewable and Sustainable Energy Reviews*, Vol. 51, No. 1, pp. 1–8, 2015.

102. Yamamoto, O., “Solid Oxide Fuel Cells: Fundamental Aspects and Prospects”, *Electrochimica Acta*, Vol. 45, No. 15–16, pp. 2423–2435, 2000.

103. Gao, Y., D. Chen, M. Saccoccio, Z. Lu, and F. Ciucci, “From Material Design to Mechanism Study: Nanoscale Ni Exsolution on a Highly Active A-Site Deficient Anode Material for Solid Oxide Fuel Cells”, *Nano Energy*, Vol. 27, No. 1, pp. 499–508, 2016.

104. Wincewicz, K. and J. Cooper, “Taxonomies of SOFC Material and Manufacturing Alternatives”, *Journal of Power Sources*, Vol. 140, No. 2, pp. 280–296, 2005.

105. Etsell, T. H. and S. N. Flengas, “Electrical Properties of Solid Oxide Electrolytes”, *Chemical Reviews*, Vol. 70, No. 3, pp. 339–376, 1970.

106. Badwal, S. P. S. and F. T. Ciacchi, “Oxygen-Ion Conducting Electrolyte Materials for Solid Oxide Fuel Cells”, *Ionics*, Vol. 6, No. 1–2, pp. 1–21, 2000.

107. Primdahl, S., “Mixed Conductor Anodes: Ni as Electrocatalyst for Hydrogen Conversion”, *Solid State Ionics*, Vol. 152–153, No. 1, pp. 597–608, 2002.

108. Basu, R. N., *Materials for Solid Oxide Fuel Cells: Recent Trends in Fuel Cell Science and Technology*, Springer, New York, 2006.

109. Han, L., J. Zhang, M. Zou, and J. Tong, “Toward Superb Perovskite Oxide Electrocatalysts: Engineering of Coupled Nanocomposites”, *Small*, Vol. 18, No. 50, pp. 1000-1013 ,2022.

110. Rodriguez J. A., Hanson J. C., and J. C. Peter, *In-Situ Characterization of Heterogeneous Catalysts*, Wiley, Hoboken, 2013.

111. Faes, A., A. Hessler-Wyser, D. Presvytes, C. G. Vayenas, and J. Van herle, “Nickel–Zirconia Anode Degradation and Triple Phase Boundary Quantification from Microstructural Analysis”, *Fuel Cells*, Vol. 9, No. 6, pp. 841–851, 2009.

112. Veen, A. C. van, M. Rebeilleau, D. Farrusseng, and C. Mirodatos, “Studies on the Performance Stability of Mixed Conducting BSCFO Membranes in Medium Temperature Oxygen Permeation”, *Chemical Communications*, Vol. 1, No. 1, pp. 32–33, 2003.

113. Li, S., Z. Lü, and B. Wei, “A Study of $(Ba_{0.5}Sr_{0.5})_{1-x}Sm_xCo_{0.8}Fe_{0.2}O_{3-\delta}$ as a Cathode Material for IT-SOFCs”, *Journal of Alloys and Compounds*, Vol. 426, No. 1–2, pp. 408–414, 2006.

114. Sun, L. P., M. Rieu, J. P. Viricelle, C. Pijolat, and H. Zhao, “Fabrication and Characterization of Anode-Supported Single Chamber Solid Oxide Fuel Cell based on $La_{0.6}Sr_{0.4}Co_{0.2}Fe_{0.8}O_{3-\delta}$–$Ce_{0.9}Gd_{0.1}O_{1.95}$ Composite Cathode”, *International Journal of Hydrogen Energy*, Vol. 39, No. 2, pp. 1014–1022, 2014.

115. Mogensen, M., D. Lybye, N. Bonanos, P. Hendriksen, and F. Poulsen, “Factors Controlling the Oxide Ion Conductivity of Fluorite and Perovskite Structured Oxides”, *Solid State Ionics*, Vol. 174, No. 1–4, pp. 279–286, 2004.

116. Kim, S., “Diffusion and Surface Exchange Coefficients in Mixed Ionic Electronic Conducting Oxides from the Pressure Dependence of Oxygen Permeation”, *Solid State Ionics*, Vol. 106, No. 3–4, pp. 189–195, 1998.

117. Lane, J., “Measuring Oxygen Diffusion and Oxygen Surface Exchange by Conductivity Relaxation”, *Solid State Ionics*, Vol. 136–137, No. 1–2, pp. 997–1001, 2000.

118. Zhang, H.M., N. Yamazoe, and Y. Teraoka, “Effects of B Site Partial Substitutions of Perovskite-Type $La_{0.6}Sr_{0.4}CoO_3$ on Oxygen Desorption”, *Journal of Materials Science Letters*, Vol. 8, No. 9, pp. 995–996, 1989.

119. Teraoka, Y., H.M. Zhang, and N. Yamazoe, “Oxygen-Sorptive Properties of Defect Pperovskite-Type $La_{1-x}Sr_xCo_{1-y}Fe_yO_{3-\delta}$”, *Chemistry Letters*, Vol. 14, No. 9, pp. 1367–1370, 1985.

120. Teraoka, Y., H.-M. Zhang, S. Furukawa, and N. Yamazoe, “Oxygen Permeation Through Perovskite-Type Oxides”, *Chemistry Letters*, Vol. 14, No. 11, pp. 1743–1746, 1985.

121. Tai, L., “Structure and Electrical Properties of $La_{1-x}Sr_xCo_{1-y}Fe_yO_3$. Part 1. The System $La_{0.8}Sr_{0.2}Co_{1-y}Fe_yO_3$”, *Solid State Ionics*, Vol. 76, No. 3–4, pp. 259–271, 1995.

122. Shao, Z. and S. M. Haile, “A High-Performance Cathode for the Next Generation of Solid-Oxide Fuel Cells”, *Nature*, Vol. 431, No. 7005, pp. 170–173, 2004.

123. Peña, M. A. and J. L. G. Fierro, “Chemical Structures and Performance of Perovskite Oxides”, *Chemical Reviews*, Vol. 101, No. 7, pp. 1981–2018, 2001.

124. Bhalla, A. S., R. Guo, and R. Roy, “The Perovskite Structure—A Review of Its Role in Ceramic Science and Technology”, *Materials Research Innovations*, Vol. 4, No. 1, pp. 3–26, 2000.

125. Sunarso, J., S. Baumann, J. M. Serra, et al., “Mixed Ionic–Electronic Conducting (MIEC) Ceramic-Based Membranes for Oxygen Separation”, *Journal of Membrane Science*, Vol. 320, No. 1–2, pp. 13–41, 2008.

126. Tejuca, L. G., J. L. G. Fierro, and J. M. D. Tascón, “Structure and Reactivity of Perovskite-Type Oxides”, *Advances in Catalysis*, Vol. 36, No. 1, pp. 237-328, 1989.

127. Goodenough J. B., S.L. Cooper, and T. Egami, *Localized to Itinerant Electronic Transition in Perovskite Oxides*, Springer, Berlin, 2001.

128. Megaw, H., *Crystal Structures: A Working Approach*, W. B. Saunders, Philadelphia, 1973.

129. Rao, C. N. R., J. Gopalakrishnan, and K. Vidyasagar, *Trends in Chemistry of Materials*, World Scientific Publishing, Bangalore, 2008.

130. Mizusaki, J., M. Yoshihiro, S. Yamauchi, and K. Fueki, "Nonstoichiometry and Defect Structure of the Perovskite-Type Oxides $La_{1-x}Sr_xFeO_{3-\delta}$", *Journal of Solid-State Chemistry*, Vol. 58, No. 2, pp. 257–266, 1985.

131. Fernández Sanjulián, J., M. Chennabasappa, and S. García-Martín, "Oxygen Vacancy Ordering in $SrFe_{0.25}Co_{0.75}O_{2.63}$ Perovskite Material", *Dalton Transactions*, Vol. 46, No. 5, pp. 1624–1633, 2017.

132. Zhou, W., R. Ran, and Z. Shao, "Progress in Understanding and Development of $Ba_{0.5}Sr_{0.5}Co_{0.8}Fe_{0.2}O_{3-\delta}$-Based Cathodes for Intermediate-Temperature Solid-Oxide Fuel Cells: A Review", *Journal of Power Sources*, Vol. 192, No. 2, pp. 231–246, 2009.

133. Zhou, W., Z. Shao, R. Ran, et al., "$Ba_{0.5}Sr_{0.5}Co_{0.8}Fe_{0.2}O_{3-\delta}$+$LaCoO_3$ Composite Cathode for $Sm_{0.2}Ce_{0.8}O_{1.9}$-Electrolyte Based Intermediate-Temperature Solid-Oxide Fuel Cells", *Journal of Power Sources*, Vol. 168, No. 2, pp. 330–337, 2007.

134. Eslem Kisa, A. and O. Demircan, "Synthesis and Characterization of $La_{0.595}V_{0.005}Sr_{0.4}CoO_{3-\delta}$ as a Novel Cathode Material for Solid Oxide Fuel Cells (SOFC)", *Journal of Sol-Gel Science and Technology*, Vol. 82, No. 2, pp. 352-360, 2017.

135. Kisa, A. E. and O. Demircan, "Erratum to: Synthesis and Characterization of $La_{0.595}V_{0.005}Sr_{0.4}CoO_{3-\delta}$ as a Novel Cathode Material for Solid Oxide Fuel Cells (SOFC)", *Journal of Sol-Gel Science and Technology*, Vol. 82, No. 2, pp. 352-360, 2017.

136. Kisa, A. E. and O. Demircan, "Transition Metal Doped Solid Oxide Fuel Cell Cathodes", *Journal of the Turkish Chemical Society Section A: Chemistry*, Vol. 5, No. 3, pp. 1153–1168, 2018.

137. la O', G. J., B. Yildiz, S. McEuen, and Y. Shao-Horn, "Probing Oxygen Reduction Reaction Kinetics of Sr-Doped $LaMnO_3$. Supported on Y_2O_3-Stabilized ZrO_2", *Journal of The Electrochemical Society*, Vol. 154, No. 4, p. B427, 2007.

138. Zhi, M., N. Mariani, R. Gemmen, K. Gerdes, and N. Wu, "Nanofiber Scaffold for Cathode of Solid Oxide Fuel Cell", *Energy and Environmental Science*, Vol. 4, No. 2, pp. 417–420, 2011.

139. Jun, A., J. Kim, J. Shin, and G. Kim, "Perovskite as a Cathode Material: A Review of its Role in Solid-Oxide Fuel Cell Technology", *ChemElectroChem*, Vol. 3, No. 4, pp. 511–530, 2016.

140. Steele, B. C. H., and A. Heinzel, "Materials for Fuel-Cell Technologies", *Nature*, Vol. 414, No. 1, pp. 345-352, 2001.

141. Tietz, F., I. Arulraj, M. Zahid, and D. Stover, "Electrical Conductivity and Thermal Expansion of $La_{0.8}Sr_{0.2}(Mn,Fe,Co)O_{3-\delta}$ Perovskites", *Solid State Ionics*, Vol. 177, No. 19–25, pp. 1753–1756, 2006.

142. Yamamoto, O., "Perovskite-Type Oxides as Oxygen Electrodes for High Temperature Oxide Fuel Cells", *Solid State Ionics*, Vol. 22, No. 2–3, pp. 241–246, 1987.

143. Petrov, A., "Crystal Structure, Electrical and Magnetic Properties of $La_{1-x}Sr_xCoO_{3-y}$", *Solid State Ionics*, Vol. 80, No. 3–4, pp. 189–199, 1995.

144. Perry Murray, E., "$(La,Sr)MnO_3$–$(Ce,Gd)O_{2-x}$ Composite Cathodes for Solid Oxide Fuel Cells", *Solid State Ionics*, Vol. 143, No. 3–4, pp. 265–273, 2001.

145. Jiang, S. P. and W. Wang, "Fabrication and Performance of GDC-Impregnated $(La,Sr)MnO_3$. Cathodes for Intermediate Temperature Solid Oxide Fuel Cells", *Journal of The Electrochemical Society*, Vol. 152, No. 7, p. A1398, 2005.

146. Jiang, S., “A Comparison of O_2 Reduction Reactions on Porous (La,Sr)MnO_3 and (La,Sr)(Co,Fe)O_3 Electrodes”, *Solid State Ionics*, Vol. 146, No. 1–2, pp. 1–22, 2002.

147. Kawada, T., J. Suzuki, and M. Sase, “Determination of Oxygen Vacancy Concentration in a Thin Film of La0.6Sr0.4CoO3−δ. by an Electrochemical Method”, *Journal of The Electrochemical Society*, Vol. 149, No. 7, p. E252, 2002.

148. Taskin, A. A., A. N. Lavrov, and Y. Ando, “Achieving Fast Oxygen Diffusion in Perovskites by Cation Ordering”, *Applied Physics Letters*, Vol. 86, No. 9, pp. 852-860, 2005.

149. Sansom, J. E. H., E. Kendrick, H. A. Rudge-Pickard, M. S. Islam, A. J. Wright, and P. R. Slater, “Synthesis and Characterization of the Perovskite-Related Cuprate Phases YSr2Cu2MO7+y(M = Co, Fe) for Potential Use as Solid Oxide Fuel Cell Cathode Materials”, *Journal of Materials Chemistry*, Vol. 15, No. 23, pp. 2317-2321, 2005.

150. Wan, J., J. Goodenough, and J. Zhu, “Nd2−xLaxNiO4+δ, a Mixed Ionic/Electronic Conductor with Interstitial Oxygen, as a Cathode Material”, *Solid State Ionics*, Vol. 178, No. 3–4, pp. 281–286, 2007.

151. K. T. Lee and A. Manthiram, “LaSr3Fe3-yCoyO10-δ ($0 \leq y \leq 1.5$) Intergrowth Oxide Cathodes for Intermediate Temperature Solid Oxide Fuel Cells”, *Chemistry of Materials*, Vol. 18, No. 6, pp. 1621–1626, 2006.

152. Xia, C., “Sm0.5Sr0.5CoO3 Cathodes for Low-Temperature SOFCs”, *Solid State Ionics*, Vol. 149, No. 1–2, pp. 11–19, 2002.

153. Peña-Martínez, J., D. Marrero-López, D. Pérez-Coll, J. C. Ruiz-Morales, and P. Núñez, “Performance of XSCoF (X=Ba, La and Sm) and LSCrX′ (X′=Mn, Fe and Al) Perovskite-Structure Materials on LSGM Electrolyte for IT-SOFC”, *Electrochimica Acta*, Vol. 52, No. 9, pp. 2950–2958, 2007.

154. Hansen, K. and K. Hansen, “A-Site Deficient (La0.6Sr0.4)1−sFe0.8Co0.2O3−δ Perovskites as SOFC Cathodes”, *Solid State Ionics*, Vol. 178, No. 23–24, pp. 1379–1384, 2007.

155. Hansen, K. K., M. Sø/gaard, and M. Mogensen, "Gd0.6Sr0.4Fe0.8Co0.2O3−δ: A Novel Type of SOFC Cathode", *Electrochemical and Solid-State Letters*, Vol. 10, No. 8, p. B119, 2007.

156. Bebelis, S., N. Kotsionopoulos, A. Mai, and F. Tietz, "Electrochemical Characterization of Perovskite-Based SOFC Cathodes", *Journal of Applied Electrochemistry*, Vol. 37, No. 1, pp. 15–20, 2006.

157. Lee, K. T. and A. Manthiram, "Comparison of Ln0.6Sr0.4CoO3−δ. (Ln=La, Pr, Nd, Sm, and Gd) as Cathode Materials for Intermediate Temperature Solid Oxide Fuel Cells", *Journal of The Electrochemical Society*, Vol. 153, No. 4, p. A794, 2006.

158. Taskin, A. A., A. N. Lavrov, and Y. Ando, "Fast Oxygen Diffusion in A-Site Ordered Perovskites", *Progress in Solid State Chemistry*, Vol. 35, No. 2–4, pp. 481–490, 2007.

159. Weber, A. and E. Ivers-Tiffée, "Materials and Concepts for Solid Oxide Fuel Cells (SOFCs) in Stationary and Mobile Applications", *Journal of Power Sources*, Vol. 127, No. 1–2, pp. 273–283, 2004.

160. Kojima, I., H. Adachi, and I. Yasumori, "Electronic Structures of the LaBO3 (B = Co, Fe, Al) Perovskite Oxides Related to Their Catalysis", *Surface Science*, Vol. 130, No. 1, pp. 50–62, 1983.

161. Jung, J., H. Y. Jeong, M. G. Kim, G. Nam, J. Park, and J. Cho, "Fabrication of $Ba_{0.5}Sr_{0.5}Co_{0.8}Fe_{0.2}O_{3-\delta}$ Catalysts with Enhanced Electrochemical Performance by Removing an Inherent Heterogeneous Surface Film Layer", *Advanced Materials*, Vol. 27, No. 2, pp. 266–271, 2015.

162. Suntivich, J., K. J. May, H. A. Gasteiger, J. B. Goodenough, and Y. Shao-Horn, "A Perovskite Oxide Optimized for Oxygen Evolution Catalysis from Molecular Orbital Principles", *Science*. Vol. 334, No. 6061, pp. 1383–1385, 2011.

163. Jung, J.I., M. Risch, and S. Park, “Optimizing Nanoparticle Perovskite for Bifunctional Oxygen Electrocatalysis”, *Energy & Environmental Science*, Vol. 9, No. 1, pp. 176–183, 2016.

164. Mangold, K.M., “Measurement Methods Structural Plus Electronic and Chemical Properties: X-Ray Absorption Spectroscopy”, *Journal of Power Sources*, Vol. 196, No. 10, pp. 4871–4872, 2011.

165. Nonaka, T., C. Okuda, Y. Seno, H. Nakano, K. Koumoto, and Y. Ukyo, “In-situ XAFS and Micro-XAFS Studies on LiNi0.8Co0.15Al0.05O2 Cathode Material for Lithium-Ion Batteries”, *Journal of Power Sources*, Vol. 162, No. 2, pp. 1329–1335, 2006.

166. Konishi, H., T. Hirano, D. Takamatsu, A. Gunji, X. Feng, and S. Furutsuki, “Effect of Composition of Transition Metals on Stability of Charged Li-rich Layer-structured Cathodes, Li1.2Ni0.2-xMn0.6-xCo2xO2 (x=0, 0.033, and 0.067), at High Temperatures”, *Electrochimica Acta*, Vol. 186, No. 1, pp. 591–597, 2015.

167. Haas, O., F. Holzer, S. Müller, et al., “X-Ray Absorption and Diffraction Studies of La0.6Ca0.4CoO3 Perovskite, Catalyst for Bifunctional Oxygen Electrodes”, *Electrochimica Acta*, Vol. 47, No. 19, pp. 3211–3217, 2002.

168. Müller, S., K. Striebel, and O. Haas, “La0.6Ca0.4CoO3: A Stable and Powerful Catalyst for Bifunctional Air Electrodes”, *Electrochimica Acta*, Vol. 39, No. 11–12, pp. 1661–1668, 1994.

169. Haas, O., R. P. W. J. Struis, and J. M. McBreen, “Synchrotron X-Ray Absorption of LaCoO3 Perovskite”, *Journal of Solid State Chemistry*, Vol. 177, No. 3, pp. 1000–1010, 2004.

170. Bu, Y., Q. Zhong, D. Xu, and W. Tan, “Redox Stability and Sulfur Resistance of Sm0.9Sr0.1CrxFe1−xO3−δ Perovskite Materials”, *Journal of Alloys and Compounds*, Vol. 578, No. 1, pp. 60–66, 2013.

171. Puleo, F., L. F. Liotta, V. La Parola, D. Banerjee, A. Martorana, and A. Longo, "Palladium Local Structure of $La_{1-x}Sr_xCo_{1-y}Fe_{y-0.03}Pd_{0.03}O_{3-\delta}$ Perovskites Synthesized Using a One Pot Citrate Method", *Physical Chemistry Chemical Physics*, Vol. 16, No. 41, pp. 22677–22686, 2014.

172. Mickevičius, S., S. Grebinskij, and V. Bondarenka, "Investigation of Epitaxial LaNiO3−x Thin Films by High-Energy XPS", *Journal of Alloys and Compounds*, Vol. 423, No. 1–2, pp. 107–111, 2006.

173. Li, J. P. H., X. Zhou, and Y. Pang, "Understanding of Binding Energy Calibration in XPS of Lanthanum Oxide by In-Situ Treatment", *Physical Chemistry Chemical Physics*, Vol. 21, No. 40, pp. 22351–22358, 2019.

174. Yousaf, A. Bin, M. Imran, M. Farooq, and P. Kasak, "Interfacial Phenomenon and Nanostructural Enhancements in Palladium Loaded Lanthanum Hydroxide Nanorods for Heterogeneous Catalytic Applications", *Scientific Reports*, Vol. 8, No. 1, p. 4354, 2018.

175. Bondarenka, V., Z. Martunas, S. Kaciulis, and L. Pandolfi, "Sol–gel Synthesis and XPS Characterization of Sodium–Vanadium Oxide Bronze Thin Films", *Journal of Electron Spectroscopy and Related Phenomena*, Vol. 131–132, No. 1, pp. 99–103, 2003.

176. Bondarenka, V. and R. Sereika, "XPS Study of Sol-Gel Synthesized Vanadium-Titanium-Hydroquinone Oxide Bronze Films", *International Letters of Chemistry, Physics and Astronomy*. Vol. 54, No. 1, pp. 201–207, 2015.

177. Iwanaga, S., M. Marciniak, R. B. Darling, and F. S. Ohuchi, "Thermopower and Electrical Conductivity of Sodium-Doped V2O5 Thin Films", *Journal of Applied Physics*. Vol. 101, No. 12, pp. 1050-1058, 2007.

178. Silversmit, G., D. Depla, H. Poelman, G. B. Marin, and R. De Gryse, "Determination of the V2p XPS Binding Energies for Different Vanadium Oxidation States (V5+ to V0+)", *Journal of Electron Spectroscopy and Related Phenomena*, Vol. 135, No. 2–3, pp. 167–175, 2004.

179. Biesinger, M. C., L. W. M. Lau, A. R. Gerson, and R. St. C. Smart, "Resolving Surface Chemical States in XPS Analysis of First Row Transition Metals, Oxides and Hydroxides: Sc, Ti, V, Cu and Zn", *Applied Surface Science*, Vol. 257, No. 3, pp. 887–898, 2010.

180. Shahid, M., J. Liu, Z. Ali, I. Shakir, and M. F. Warsi, "Structural and Electrochemical Properties of Single Crystalline MoV2O8 Nanowires for Energy Storage Devices", *Journal of Power Sources*, Vol. 230, No. 1, pp. 277–281, 2013.

181. Yamada, H. and Y. Ueda, "Magnetic, Electric and Structural Properties of β-$A_xV_2O_5$ (A = Ag)", *Journal of the Physical Society of Japan*, Vol. 68, No. 8, pp. 2735–2740, 1999.

182. Silversmit, G., D. Depla, H. Poelman, G. B. Marin, and R. De Gryse, "An XPS Study on the Surface Reduction of V2O5(001) Induced by Ar+ Ion Bombardment", *Surface Science*, Vol. 600, No. 17, pp. 3512–3517, 2006.

183. Sekiyama, A., S. Kasai, and M. Tsunekawa, "Technique for Bulk Fermiology by Photoemission Applied to Layered Ruthenates", *Physical Review B*, Vol. 70, No. 6, p. 060506, 2004.

184. Simner, S. P., M. D. Anderson, M. H. Engelhard, and J. W. Stevenson, "Degradation Mechanisms of La–Sr–Co–Fe–O3. SOFC Cathodes", *Electrochemical and Solid-State Letters*, Vol. 9, No. 10, p. A478, 2006.

185. Yokokawa, H., H. Tu, B. Iwanschitz, and A. Mai, "Fundamental Mechanisms Limiting Solid Oxide Fuel Cell Durability", *Journal of Power Sources*, Vol. 182, No. 2, pp. 400–412, 2008.

186. Cai, Z., M. Kubicek, J. Fleig, and B. Yildiz, "Chemical Heterogeneities on $La_{0.6}Sr_{0.4}CoO_{3-\delta}$ Thin Films—Correlations to Cathode Surface Activity and Stability", *Chemistry of Materials*, Vol. 24, No. 6, pp. 1116–1127, 2012.

187. Bertacco, R., J. P. Contour, A. Barthélemy, and J. Olivier, "Evidence for Strontium Segregation in La0.7Sr0.3MnO3 Thin Films Grown by Pulsed Laser Deposition:

Consequences for Tunnelling Junctions", *Surface Science*, Vol. 511, No. 1–3, pp. 366–372, 2002.

188. Pitale, S. S., I. M. Nagpure, V. Kumar, O. M. Ntwaeaborwa, J. J. Terblans, and H. C. Swart, "Investigations on the Low Voltage Cathodoluminescence Stability and Surface Chemical Behaviour using Auger and X-Ray Photoelectron Spectroscopy on LiSrBO3:Sm3+ Phosphor", *Materials Research Bulletin*, Vol. 46, No. 7, pp. 987–994, 2011.

189. Chen, Y., W. Jung, Z. Cai, J. J. Kim, H. L. Tuller, and B. Yildiz, "Impact of Sr Segregation on the Electronic Structure and Oxygen Reduction Activity of SrTi1−xFexO3 Surfaces", *Energy & Environmental Science*, Vol. 5, No. 7, p. 7979, 2012.

190. Kim, Y. S., D. J. Yun, S. H. Kim, Y. K. Kyoung, and S. Heo, "Damage-Free and Atomically Precise Surface Preparation of SrTiO3", *Current Applied Physics*, Vol. 16, No. 11, pp. 1464–1467, 2016.

191. Huang, Q., J. Zhang, Z. He, P. Shi, X. Qin, and W. Yao, "Direct Fabrication of Lamellar Self-Supporting Co3O4/N/C Peroxymonosulfate Activation Catalysts for Effective Aniline Degradation", *Chemical Engineering Journal*, Vol. 313, No. 1, pp. 1088–1098, 2017.

192. Wang, C., C. Zhang, and W. Hua, "Catalytic Oxidation of Vinyl Chloride Emissions over Co-Ce Composite Oxide Catalysts", *Chemical Engineering Journal*, Vol. 315, pp. 392–402, 2017.

193. Malkhandi, S., P. Trinh, and A. K. Manohar, "Design Insights for Tuning the Electrocatalytic Activity of Perovskite Oxides for the Oxygen Evolution Reaction", *The Journal of Physical Chemistry C*, Vol. 119, No. 15, pp. 8004–8013, 2015.

194. Moreno-Tost, R., J. Santamaría-González, P. Maireles-Torres, E. Rodríguez-Castellón, and A. Jiménez-López, "Cobalt Supported on Zirconium Doped Mesoporous Silica: A Selective Catalyst for Reduction of NO with Ammonia at Low Temperatures", *Applied Catalysis B: Environmental*, Vol. 38, No. 1, pp. 51–60, 2002.

195. Cheng, G., T. Kou, J. Zhang, C. Si, H. Gao, and Z. Zhang, "O_2^{2-}/O^- Functionalized Oxygen-Deficient Co3O4 Nanorods as High-Performance Supercapacitor Electrodes and Electrocatalysts Towards Water Splitting", *Nano Energy*, Vol. 38, No. 1, pp. 155–166, 2017.

196. Yao, C., J. Meng, and X. Liu, "Effects of Bi Doping on the Microstructure, Electrical and Electrochemical Properties of La2-xBixCu0.5Mn1.5O6 (x = 0,0.1 and 0.2) Perovskites as Novel Cathodes for Solid Oxide Fuel Cells", *Electrochimica Acta*, Vol. 229, No. 1, pp. 429–437, 2017.

197. Miao, J., J. Sunarso, C. Su, W. Zhou, S. Wang, and Z. Shao, "SrCo1−xTixO3−δ Perovskites as Excellent Catalysts for Fast Degradation of Water Contaminants in Neutral and Alkaline Solutions", *Scientific Reports*, Vol. 7, No. 1, p. 44215, 2017.

198. Maluf, S. S., P. A. P. Nascente, C. R. M. Afonso, and E. M. Assaf, "Study of La2−xCaxCuO4 Perovskites for the Low Temperature Water Gas Shift Reaction", *Applied Catalysis A: General*, Vol. 413–414, No. 1, pp. 85–93, 2012.

199. Tang, X., F. Gao, Y. Xiang, et al., "Effect of Potassium-Precursor Promoters on Catalytic Oxidation Activity of Mn-CoOx Catalysts for NO Removal", *Industrial & Engineering Chemistry Research*, Vol. 54, No. 37, pp. 9116–9123, 2015.

200. Steele, B. C. H. and A. Heinzel, "Materials for Fuel-Cell Technologies", *Nature*, Vol. 414, No. 6861, pp. 345–352, 2001.

201. Brandon, N. P., S. Skinner, and B. C. H. Steele, "Recent Advances in Materials for Fuel Cells", *Annual Review of Materials Research*, Vol. 33, No. 1, pp. 183–213, 2003.

202. Park, S., S. Choi, J. Kim, J. Shin, and G. Kim, "Strontium Doping Effect on High-Performance PrBa1-xSrxCo2O5+∂ as a Cathode Material for IT-SOFCs", *ECS Electrochemistry Letters*, Vol. 1, No. 5, pp. F29–F32, 2012.

203. Choi, S., J. Shin, K. M. Ok, and G. Kim, "Chemical Compatibility, Redox Behavior, and Electrochemical Performance of Nd1−SrCoO3−∂ Cathodes Based on Ce1.9Gd0.1O1.95 for

Intermediate-Temperature Solid Oxide Fuel Cells", *Electrochimica Acta*. Vol. 81, No. 1, pp. 217–223, 2012.

204. Ralph, J. M., A. C. Schoeler, and M. Krumpelt, "Materials for Lower Temperature Solid Oxide Fuel Cells", *Journal of Materials Science*, Vol. 36, No. 5, pp. 1161–1172, 2001.

205. Choi, S., S. Yoo, and J. Kim, "Highly Efficient and Robust Cathode Materials for Low-Temperature Solid Oxide Fuel Cells: PrBa0.5Sr0.5Co2−xFexO5+δ", *Scientific Reports*, Vol. 3, No. 1, p. 2426, 2013.

206. Kim, C., J. Kim, J. Shin, and G. Kim, "Effects of Composite Cathode on Electrochemical and Redox Properties for Intermediate-Temperature Solid Oxide Fuel Cells", *International Journal of Hydrogen Energy*, Vol. 39, No. 35, pp. 20812–20818, 2014.

207. Han, F., R. Mücke, and T. Van Gestel, "Novel High-Performance Solid Oxide Fuel Cells with Bulk Ionic Conductance Dominated Thin-Film Electrolytes", *Journal of Power Sources*, Vol. 218, No. 1, pp. 157–162, 2012.

208. Armstrong, T., "Synthesis, Crystal Chemistry, and Oxygen Permeation Properties of LaSr3Fe3−xCoxO10 (0≤x≤1.5)", *Solid State Ionics*, Vol. 140, No. 1–2, pp. 89–96, 2001.

209. Backhausricoult, M., "Interface Chemistry in LSM–YSZ Composite SOFC Cathodes", *Solid State Ionics*, Vol. 177, No. 19–25, pp. 2195–2200, 2006.

210. Grosjean, A., O. Sanseau, V. Radmilovic, and A. Thorel, "Reactivity and Diffusion Between La0.8Sr0.2MnO3 and ZrO2 at Interfaces in SOFC Cores by TEM Analyses on FIB Samples", *Solid State Ionics*, Vol. 177, No. 19–25, pp. 1977–1980, 2006.

211. Yang, K., J.H. Shen, K.Y. Yang, I.M. Hung, K.-Z. Fung, and M.C. Wang, "Formation of La2Zr2O7 or SrZrO3 on Cathode-Supported Solid Oxide Fuel Cells", *Journal of Power Sources*, Vol. 159, No. 1, pp. 63–67, 2006.

212. Yokokawa, H., “Thermodynamic Analysis on Interface Between Perovskite Electrode and YSZ electrolyte”, *Solid State Ionics*, Vol. 40–41, No. 1, pp. 398–401, 1990.

213. Su, C., W. Wang, R. Ran, Z. Shao, M. O. Tade, and S. Liu, “Renewable Acetic Acid in Combination with Solid Oxide Fuel Cells for Sustainable Clean Electric Power Generation”, *Journal of Materials Chemistry A*, Vol. 1, No. 18, p. 5620, 2013.

214. Zha, S. W., C. R. Xia, and G. Y. Meng, “Calculation of the E.M.F. of Solid Oxide Fuel Cells”, *Journal of Applied Electrochemistry*, Vol. 31, No. 1, pp. 93–98, 2001.

215. Boukamp, B. A., N. Hildenbrand, H. J. M. Bouwmeester, and D. H. A. Blank, “Impedance of Thin Film Cathodes: Thickness and Current Collector Dependence”, *Solid State Ionics*, Vol. 283, No. 1, pp. 81–90, 2015.

216. Baumann, F., J. Fleig, H. Habermeier, and J. Maier, “Impedance Spectroscopic Study on Well-Defined (La,Sr)(Co,Fe)O3−δ Model Electrodes”, *Solid State Ionics*, Vol. 177, No. 11–12, pp. 1071–1081, 2006.

217. Suzuki, T., M. Awano, P. Jasinski, V. Petrovsky, and H. Anderson, “Composite (La, Sr)MnO3–YSZ Cathode for SOFC”, *Solid State Ionics*, Vol. 177, No. 19–25, pp. 2071–2074, 2006.

218. Mauvy, F., C. Lalanne, and J.M. Bassat, “Electrode Properties of Ln2.NiO4+δ (Ln=La, Nd, Pr)”, *Journal of The Electrochemical Society*, Vol. 153, No. 8, p. A1547, 2006.

219. Escudero, M. J., A. Aguadero, J. A. Alonso, and L. Daza, “A Kinetic Study of Oxygen Reduction Reaction on La2NiO4 Cathodes by Means of Impedance Spectroscopy”, *Journal of Electroanalytical Chemistry*, Vol. 611, No. 1–2, pp. 107–116, 2007.

220. Ramos, T., J. Hjelm, and M. Mogensen, “Towards Quantification of Relations Between Electrode Polarization and Microstructure”, *Journal of The Electrochemical Society*, Vol. 158, No. 7, p. B814, 2011.

221. Barfod, R., M. Mogensen, T. Klemensø, A. Hagen, Y.L. Liu, and P. Vang Hendriksen, "Detailed Characterization of Anode-Supported SOFCs by Impedance Spectroscopy", *Journal of The Electrochemical Society*, Vol. 154, No. 4, p. B371, 2007.

222. Kornely, M., N. H. Menzler, A. Weber, and E. Ivers-Tiffée, "Degradation of a High Performance SOFC Cathode by Cr-Poisoning at OCV-Conditions", *Fuel Cells*, Vol. 13, No. 4, pp. 506–510, 2013.

223. Liu, B., H. Muroyama, T. Matsui, K. Tomida, T. Kabata, and K. Eguchi, "Analysis of Impedance Spectra for Segmented-in-Series Tubular Solid Oxide Fuel Cells", *Journal of The Electrochemical Society*, Vol. 157, No. 12, p. B1858, 2010.

224. Murray, E. P., T. Tsai, and S. A. Barnett, "Oxygen Transfer Processes in (La,Sr)MnO3/Y2O3-Stabilized ZrO2 Cathodes: An Impedance Spectroscopy Study", *Solid State Ionics*, Vol. 110, No. 3–4, pp. 235–243, 1998.

225. Yan, J., H. Chen, E. Dogdibegovic, J. W. Stevenson, M. Cheng, and X.-D. Zhou, "High-Efficiency Intermediate Temperature Solid Oxide Electrolyzer Cells for the Conversion of Carbon Dioxide to Fuels", *Journal of Power Sources*, Vol. 252, No.1, pp. 79–84, 2014.

226. Yan, J., Z. Zhao, L. Shang, D. Ou, and M. Cheng, "Co-Synthesized Y-Stabilized Bi2O3 and Sr-Substituted LaMnO3 Composite Anode for High Performance Solid Oxide Electrolysis Cell", *Journal of Power Sources*, Vol. 319, No. 1, pp. 124–130, 2016.

227. Zhang, X., L. Liu, and Z. Zhao, "Enhanced Oxygen Reduction Activity and Solid Oxide Fuel Cell Performance with a Nanoparticles-Loaded Cathode", *Nano Letters*, Vol. 15, No. 3, pp. 1703–1709, 2015.

228. Duncan, K. L., K.T. Lee, and E. D. Wachsman, "Dependence of Open-Circuit Potential and Power Density on Electrolyte Thickness in Solid Oxide Fuel Cells with Mixed Conducting Electrolytes", *Journal of Power Sources*, Vol. 196, No. 5, pp. 2445–2451, 2011.

229. Matsui, T., T. Kosaka, M. Inaba, A. Mineshige, and Z. Ogumi, “Effects of Mixed Conduction on the Open-Circuit Voltage of Intermediate-Temperature SOFCs Based on Sm-Doped Ceria Electrolytes”, *Solid State Ionics*, Vol. 176, No. 7–8, pp. 663–668, 2005.

230. Pikalova, E. Yu. and E. G. Kalinina, “Solid Oxide Fuel Cells Based on Ceramic Membranes with Mixed Conductivity: Improving Efficiency”, *Russian Chemical Reviews*, Vol. 90, No. 6, pp. 703–749, 2021.

231. Fu, C. J., S. H. Chan, X. M. Ge, Q. L. Liu, and G. Pasciak, “A Promising Ni–Fe Bimetallic Anode for Intermediate-Temperature SOFC Based on Gd-Doped Ceria Electrolyte”, *International Journal of Hydrogen Energy*, Vol. 36, No. 21, pp. 13727–13734, 2011.

232. Sivasankaran, V., L. Combemale, M. C. Pera, and G. Caboche, “Initial Preparation and Characterization of Single Step Fabricated Intermediate Temperature Solid Oxide Fuel Cells (IT-SOFC)”, *Fuel Cells*, Vol. 14, No. 3, pp. 533–536, 2014.

233. Shao, X., W. D. A. Rickard, D. Dong, et al., “High Performance Anode with Dendritic Porous Structure for Low Temperature Solid Oxide Fuel Cells”, *International Journal of Hydrogen Energy*, Vol. 43, No. 37, pp. 17849–17856, 2018.

234. Reolon, R. P., C. M. Halmenschlager, R. Neagu, C. de Fraga Malfatti, and C. P. Bergmann, “Electrochemical Performance of Gadolinia-Doped Ceria (CGO) Electrolyte Thin Films for ITSOFC Deposited by Spray Pyrolysis”, *Journal of Power Sources*, Vol. 261, No.1 , pp. 348–355, 2014.

235. Ding, C., H. Lin, K. Sato, and T. Hashida, “A Simple, Rapid Spray Method for Preparing Anode-Supported Solid Oxide Fuel Cells with GDC Electrolyte Thin Films”, *Journal of Membrane Science*, Vol. 350, No. 1–2, pp. 1–4, 2010.

236. Park, H. C. and A. V. Virkar, “Bimetallic (Ni–Fe) Anode-Supported Solid Oxide Fuel Cells with Gadolinia-Doped Ceria Electrolyte”, *Journal of Power Sources*, Vol. 186, No. 1, pp. 133–137, 2009.

237. Pérez-Coll, D., J. C. Ruiz-Morales, D. Marrero-López, P. Núñez, and J. R. Frade, “Effect of Sintering Additive and Low Temperature on the Electrode Polarization of CGO”, *Journal of Alloys and Compounds*, Vol. 467, No. 1–2, pp. 533–538, 2009.

238. Yamaji, K., Y. Xiong, H. Kishimoto, T. Horita, M. E. Brito, and H. Yokokawa, “Electronic Conductivity and Efficiency of SOFC Electrolytes”, *ECS Transactions*, Vol. 12, No. 1, pp. 317–322, 2008.

239. Riegraf, M., V. Yurkiv, R. Costa, G. Schiller, and K. A. Friedrich, “Evaluation of the Effect of Sulfur on the Performance of Nickel/Gadolinium-Doped Ceria Based Solid Oxide Fuel Cell Anodes”, *ChemSusChem*, Vol. 10, No. 3, pp. 587–599, 2017.

240. Hjelm, J., M. Soegaard, R. Knibbe, A. Hagen, and M. Mogensen, “Electrochemical Characterization of Planar Anode Supported SOFC with Strontium-Doped Lanthanum Cobalt Oxide Cathodes”, *ECS Transactions*, Vol. 13, No. 26, pp. 285–299, 2008.

241. Koch, S., P. V. Hendriksen, and M. Mogensen, “Solid Oxide Fuel Cell Performance Under Severe Operating Conditions”, *Fuel Cells*, Vol. 6, No. 2, pp. 130–136, 2006.

242. Hjelm, J., M. Sø gaard, M. Wandel, M. Menon, M. Mogensen, and A. Hagen, “Electrochemical Impedance Studies of SOFC Cathodes”, *ECS Transactions*, Vol. 7, No. 1, pp. 1261–1270, 2007.

243. Hagen, A., Y. L. Liu, R. Barfod, and P. V. Hendriksen, “Anode Supported Solid Oxide Fuel Cells - Deconvolution of Degradation into Cathode and Anode Contributions”, *ECS Transactions*, Vol. 7, No. 1, pp. 301–309, 2007.

244. Hagen, A., Y. L. Liu, R. Barfod, and P. V. Hendriksen, “Assessment of the Cathode Contribution to the Degradation of Anode-Supported Solid Oxide Fuel Cells”, *Journal of The Electrochemical Society*, Vol. 155, No. 10, p. B1047, 2008.

245. Nielsen, J., A. Hagen, and Y. L. Liu, “Effect of Cathode Gas Humidification on Performance and Durability of Solid Oxide Fuel Cells”, *Solid State Ionics*, Vol. 181, No. 11–12, pp. 517–524, 2010.

246. Chen, Y., Y. Choi, and S. Yoo, “A Highly Efficient Multi-Phase Catalyst Dramatically Enhances the Rate of Oxygen Reduction”, *Joule*, Vol. 2, No. 5, pp. 938–949, 2018.

247. Kromp, A., A. Leonide, A. Weber, and E. Ivers-Tiffée, “Electrochemical Analysis of Reformate-Fueled Anode Supported SOFC”, *Journal of The Electrochemical Society*, Vol. 158, No. 8, p. B980, 2011.

248. Huang, Y.L., A. M. Hussain, I. A. Robinson, and E. D. Wachsman, “Nanointegrated, High-Performing Cobalt-Free Bismuth-Based Composite Cathode for Low-Temperature Solid Oxide Fuel Cells”, *ACS Applied Materials & Interfaces*, Vol. 10, No. 34, pp. 28635–28643, 2018.

249. Ralph, J. M., C. Rossignol, and R. Kumar, “Cathode Materials for Reduced-Temperature SOFCs”, *Journal of The Electrochemical Society*, Vol. 150, No. 11, p. A1518, 2003.

250. Skinner, S., “Oxygen Diffusion and Surface Exchange in La2−xSrxNiO4+δ”, *Solid State Ionics*, Vol. 135, No. 1–4, pp. 709–712, 2000.

251. Perry Murray, E., “Electrochemical Performance of (La,Sr)(Co,Fe)O3–(Ce,Gd)O3 Composite Cathodes”, *Solid State Ionics*, Vol. 148, No. 1–2, pp. 27–34, 2002.

252. Ivers-Tiffée, E., A. Weber, and D. Herbstritt, “Materials and Technologies for SOFC-Components”, *Journal of the European Ceramic Society*, Vol. 21, No. 10–11, pp. 1805–1811, 2001.

253. Zhou, Q., T. He, and Y. Ji, “SmBaCo2O5+x Double-Perovskite Structure Cathode Material for Intermediate-Temperature Solid-Oxide Fuel Cells”, *Journal of Power Sources*. Vol. 185, No. 2, pp. 754–758, 2008.

254. Tarancón, A., J. Peña-Martínez, D. Marrero-López, A. Morata, J. C. Ruiz-Morales, and P. Núñez, "Stability, Chemical Compatibility and Electrochemical Performance of GdBaCo2O5+x Layered Perovskite as a Cathode for Intermediate Temperature Solid Oxide Fuel Cells", *Solid State Ionics*, Vol. 179, No. 40, pp. 2372–2378, 2008.

255. Tarancón, A., A. Morata, and G. Dezanneau, "GdBaCo2O5+x Layered Perovskite as an Intermediate Temperature Solid Oxide Fuel Cell Cathode", *Journal of Power Sources*, Vol. 174, No. 1, pp. 255–263, 2007.

256. Zhang, K., L. Ge, R. Ran, Z. Shao, and S. Liu, "Synthesis, Characterization and Evaluation of Cation-Ordered LnBaCo2O5+ as Materials of Oxygen Permeation Membranes and Cathodes of SOFCs", *Acta Materialia*, Vol. 56, No. 17, pp. 4876–4889, 2008.

257. Kim, J.H. and A. Manthiram, "LnBaCo2O5+δ Oxides as Cathodes for Intermediate-Temperature Solid Oxide Fuel Cells", *Journal of The Electrochemical Society*, Vol. 155, No. 4, p. B385, 2008.

258. Kim, G., S. Wang, A. J. Jacobson, L. Reimus, P. Brodersen, and C. A. Mims, "Rapid Oxygen Ion Diffusion and Surface Exchange Kinetics in PrBaCo2O5+x with a Perovskite Related Structure and Ordered A cations", *Journal of Materials Chemistry*, Vol. 17, No. 24, p. 2500, 2007.

259. Tarancón, A., S. J. Skinner, R. J. Chater, F. Hernández-Ramírez, and J. A. Kilner, "Layered Perovskites as Promising Cathodes for Intermediate Temperature Solid Oxide Fuel Cells", *Journal of Materials Chemistry*, Vol. 17, No. 30, p. 3175, 2007.

260. Li, W., L. Xie, L. Zhou, J. Ochoa-Lozano, C. Li, and X. Chai, "A Systemic Study on Gd, Fe and N Co-Doped TiO2 Nanomaterials for Enhanced Photocatalytic Activity Under Visible Light Irradiation", *Ceramics International*, Vol. 46, No. 15, pp. 24744–24752, 2020.

261. Gupta, J. A., D. Landheer, and G. I. Sproule, "Interfacial Layer Formation in Gd2O3 Films Deposited Directly on Si(0 0 1)", *Applied Surface Science*, Vol. 173, No. 3–4, pp. 318–326, 2001.

262. Tian, N., Y. Zhang, H. Huang, Y. He, and Y. Guo, “Influences of Gd Substitution on the Crystal Structure and Visible-Light-Driven Photocatalytic Performance of Bi $_2$ WO $_6$”, *The Journal of Physical Chemistry C*, Vol. 118, No. 29, pp. 15640–15648, 2014.

263. Zhang, N., D. Chen, F. Niu, S. Wang, L. Qin, and Y. Huang, “Enhanced Visible Light Photocatalytic Activity of Gd-doped BiFeO3 Nanoparticles and Mechanism Insight”, *Scientific Reports*, Vol. 6, No. 1, p. 26467, 2016.

264. Wattiaux, A., J. C. Grenier, M. Pouchard, and P. Hagenmuller, “Electrolytic Oxygen Evolution in Alkaline Medium on La1 − x Sr x FeO3 − y Perovskite-Related Ferrites: II . Influence of Bulk Properties”, *Journal of The Electrochemical Society*, Vol. 134, No. 7, pp. 1718–1724, 1987.

265. Traversa, E., S. Matsushima, G. Okada, Y. Sadaoka, Y. Sakai, and K. Watanabe, “NO2 Sensitive LaFeO3 Thin Films Prepared by R.F. Sputtering”, *Sensors and Actuators B: Chemical*, Vol. 25, No. 1–3, pp. 661–664, 1995.

266. Keplinger, F., R. Glatz, A. Jachimowicz, et al., “Thin-Film Ion-Selective Sensors Based on Neutral Carrier Membranes”, *Sensors and Actuators B: Chemical*, Vol. 1, No. 1–6, pp. 272–274, 1990.

267. Huang, K., H. Y. Lee, and J. B. Goodenough, “Sr- and Ni-Doped LaCoO3 and LaFeO3 Perovskites: New Cathode Materials for Solid-Oxide Fuel Cells”, *Journal of The Electrochemical Society*, Vol. 145, No. 9, pp. 3220–3227, 1998.

268. Tenelshof, J., H. Bouwmeester, and H. Verweij, “Oxygen Transport Through LaSrFeO Membranes II. Permeation in air/CO, CO Gradients”, *Solid State Ionics*, Vol. 89, No. 1–2, pp. 81–92, 1996.

269. Tenelshof, J., H. Bouwmeester, and H. Verweij, “Oxygen Transport Through LaSrFeO Membranes. I. Permeation in Air/He Gradients”, *Solid State Ionics*, Vol. 81, No. 1–2, pp. 97–109, 1995.

270. Mizusaki, J., T. Sasamoto, W. R. Cannon, and H. K. Bowen, "Electronic Conductivity, Seebeck Coefficient, and Defect Structure of La1-xSrxFeO3 (x=0.l, 0.25)", *Journal of the American Ceramic Society*, Vol. 66, No. 4, pp. 247–252, 1983.

271. Patrakeev, M. V., J. A. Bahteeva, E. B. Mitberg, I. A. Leonidov, V. L. Kozhevnikov, and K. R. Poeppelmeier, "Electron/Hole and Ion Transport in La1−xSrxFeO3−δ", *Journal of Solid State Chemistry*, Vol. 172, No. 1, pp. 219–231, 2003.

272. Teketel, B. S., B. A. Beshiwork, and X. Luo, "A-Site Doping Enabled Higher-Oxygen-Vacancy Cobalt-Free Layered Perovskite Cathode for Higher-Performing Protonic Ceramic Fuel Cells", *Ceramics International*, Vol. 48, No. 24, pp. 37232–37241, 2022.

273. Muñoz-García, A. B. and M. Pavone, "First-Principles Design of New Electrodes for Proton-Conducting Solid-Oxide Electrochemical Cells: A-Site Doped $Sr_2Fe_{1.5}Mo_{0.5}O_{6-\delta}$ Perovskite", *Chemistry of Materials*, Vol. 28, No. 2, pp. 490–500, 2016.

274. Aguilar, L., S. Zha, Z. Cheng, J. Winnick, and M. Liu, "A Solid Oxide Fuel Cell Operating on Hydrogen Sulfide (H2S) and Sulfur-Containing Fuels", *Journal of Power Sources*, Vol. 135, No. 1–2, pp. 17–24, 2004.

275. Yoon, S.-E., S.-H. Song, J. Choi, J.-Y. Ahn, B.-K. Kim, and J.-S. Park, "Coelectrolysis of Steam and CO2 in a Solid Oxide Electrolysis Cell with Ceramic Composite Electrodes", *International Journal of Hydrogen Energy*, Vol. 39, No. 11, pp. 5497–5504, 2014.

276. Manjunatha, K., I. C. Sathish, S. P. Kubrin, et al., "X-Ray Photoelectron Spectroscopy and Low Temperature Mössbauer Study of Ce3+ Substituted MnFe2O4", *Journal of Materials Science: Materials in Electronics*, Vol. 30, No. 11, pp. 10162–10171, 2019.

277. Sunarso, J., S. S. Hashim, N. Zhu, and W. Zhou, "Perovskite Oxides Applications in High Temperature Oxygen Separation, Solid Oxide Fuel Cell and Membrane Reactor: A Review", *Progress in Energy and Combustion Science*, Vol. 61, No. 1, pp. 57–77, 2017.

278. Ye, L., M. Zhang, P. Huang, et al., “Enhancing CO2 Electrolysis Through Synergistic Control of Non-Stoichiometry and Doping to Tune Cathode Surface Structures”, *Nature Communications*, Vol. 8, No. 1, p. 14785, 2017.

279. Kisa, A. E. and O. Demircan, “Fabrication and Electrochemical Performance of La0.595V0.005Sr0.4MnO3”, *Turkish Journal of Chemistry*, Vol. 42, No. 6, pp. 1479–1498, 2018.

280. Carpanese, M. P., D. Clematis, and A. Bertei “Understanding the Electrochemical Behaviour of LSM-Based SOFC Cathodes. Part I — Experimental and Electrochemical”, *Solid State Ionics*, Vol. 301, No.1, pp. 106–115, 2017.

281. Poulsen, F., “Defect Chemistry Modelling of Oxygen-Stoichiometry, Vacancy Concentrations, and Conductivity of (La1−xSrx)yMnO3±δ”, *Solid State Ionics*, Vol. 129, No. 1–4, pp. 145–162, 2000.

282. De Souza, R. A., J. A. Kilner, and J. F. Walker, “A SIMS Study of Oxygen Tracer Diffusion and Surface Exchange in La0.8Sr0.2MnO3+δ”, *Materials Letters*, Vol. 43, No. 1–2, pp. 43–52, 2000.

283. Chen, Y., J. Shen, G. Yang, W. Zhou, and Z. Shao, “A Single/Double-Perovskite Composite with an Overwhelming Single-Perovskite Phase for the Oxygen Reduction Reaction at Intermediate Temperatures”, *Journal of Materials Chemistry A*, Vol. 5, No. 47, pp. 24842–24849, 2017.

284. Woltermann, G. M., J. S. Magee, and S. D. Griffith, “Commercial Preparation and Characterization of FCC Catalysts”, *Studies in Surface Science and Catalysis*, Vol. 76, No. 1, pp. 105-144, 1993.

285. Centi, G., “Nature of Active Layer in Vanadium Oxide Supported on Titanium Oxide and Control of its Reactivity in the Selective Oxidation and Ammoxidation of Alkylaromatics”, *Applied Catalysis A: General*, Vol. 147, No. 2, pp. 267–298, 1996.

286. Bond, G. C., “Preparation and Properties of Vanadia/Titania Monolayer Catalysts”, *Applied Catalysis A: General*, Vol. 157, No. 1–2, pp. 91–103, 1997.

287. Wachs, I. E. and B. M. Weckhuysen, “Structure and Reactivity of Surface Vanadium Oxide Species on Oxide Supports”, *Applied Catalysis A: General*, Vol. 157, No. 1–2, pp. 67–90, 1997.

288. Yang, T. C. K., Y. L. Yang, R. C. Juang, T. W. Chiu, and C. C. Chen, “The Novel Preparation Method of High-Performance Thermochromic Vanadium Dioxide Thin Films by Thermal Oxidation of Vanadium-Stainless Steel Co-Sputtered Films”, *Vacuum*, Vol. 121, No. 1, pp. 310–316, 2015.

289. Lang, X., H. Mo, X. Hu, and H. Tian, “Supercapacitor Performance of Perovskite La $_{1-x}$ Sr $_{x}$ MnO $_{3}$”, *Dalton Trans,* Vol. 46, No. 40, pp. 13720–13730, 2017.

290. Ma, P., N. Lei, and B. Yu, “Flexible Supercapacitor Electrodes Based on Carbon Cloth-Supported LaMnO3/MnO Nano-Arrays by One-Step Electrodeposition”, *Nanomaterials*, Vol. 9, No. 12, p. 1676, 2019.

291. Lv, Y., Z. Li, and Y. Yu, “Copper/Cobalt-Doped LaMnO3 Perovskite Oxide as a Bifunctional Catalyst for Rechargeable Li-O2 Batteries”, *Journal of Alloys and Compounds*, Vol. 801, No. 1, pp. 19–26, 2019.

292. Zheng, S., Q. Hua, W. Gu, and B. Liu, “Catalytic Oxidation of CO on LaMn1−xFexO3 Perovskites Solid Solution”, *Journal of Molecular Catalysis A: Chemical*, Vol. 391, No. 1, pp. 7–11, 2014.

293. Zhan, H., F. Li, and C. Xin, “Performance of the La–Mn–Zn–Cu–O Based Perovskite Precursors for Methanol Synthesis from CO2 Hydrogenation”, *Catalysis Letters*, Vol. 145, No. 5, pp. 1177–1185, 2015.